Mechanical characterization of Linear Friction Welded Titanium alloys

Juan-Manuel Garcia

PSL
UNIVERSITÉ PARIS

THÈSE DE DOCTORAT

DE L'UNIVERSITÉ PSL

Préparée à MINES ParisTech

Mechanical characterization of Linear Friction Welded Titanium alloys

Caractérization mécanique d'alliages de titane soudés par friction linéaire

Soutenance de

Juan-Manuel GARCÍA

Le 21 Novembre 2019

École doctorale n°621

Ingénierie des Systèmes, Matériaux, Mécanique, Énergétique

Spécialité

Science et Génie des Matériaux

Composition du jury :

Aude SIMAR Professeur, UCLouvain (Belgique)	*Présidente*
Moataz ATTALLAH Professeur, Université de Birmingham (UK)	*Rapporteur*
Jean-Yves Buffière Professeur, INSA de Lyon (France)	*Rapporteur*
Salima BOUVIER Professeur, UTC (France)	*Examinatrice*
Guillaume ABRIVARD Docteur, Airbus	*Examinateur*
Bertrand FLIPO Ingénieur, TWI	*Examinateur*
Thilo MORGENEYER Maître de recherche, HDR, Mines ParisTech	*Directeur de thèse*

MINES ParisTech | PSL

Contents

The lack of your best hurts everything.

J.B. Peterson

Acknowledgements

In this project, I was meant to study the mechanical properties of titanium linear friction welded structures. As time went by, I realised that not only was I testing the strength, fatigue strength and toughness of my samples but also, I was testing myself. Indeed, I have learnt about my welds as much as I have learnt about myself. I have come a long way and I could never have fulfilled it without the help of a very substantial number of people. To all who have contributed I wholeheartedly thank you.

Yazid Madi, Marie-Thérèse Auclair and Henri Proudhon kindly and most vigourously favoured my application for this thesis. Thilo Morgeneyer took a non-neglectable risk of accepting me and then, he accompanied me all the way. Their contribution to my profesional project will have an effect in the rest of my profesional and personal life. Thanks to them I have been able to fulfil another dream. Yazid, Mariethé, Henry and Thilo: I will be grateful to you my entire life.

I kindly thank the members of the jury Aude Simar, Moataz Attallah, Jean-Yves Buffière, Salima Bouvier, Bertrand Flipo, Guillaume Abrivard and Thilo Morgeneyer for having read my manuscript and having attended my PhD defence. I enjoyed so much the discussion with you during my defence that I did not want it to end. I learnt many things that I will capitalise in my ongoing papers and in my future research on Linear Friction Welding.

I would like to thank the ANR for funding this project, ACB for providing my welds and the partners of the OPTIMUM project for all the kind discussions. Salima Bouvier is thanked for running the project. The kind discussions with Katia Mocellin, Lionel Fourment, Marion Risbet, Jérôme Favergeon, Guillaume Abrivard, François Bourdin, Xavier Boyat, Dorick Ballat-Durand and Antoine Potet are gratefully acknowledged. Jérôme Delfosse is kindly thanked for his keen insight concerning the dissimilar joints and prior to welding contamination. The help of Lukas Helfen and Andrew King concerning the non-destructive tomographic and laminographic observations are acknowledged. I also would like to thank *Universidad Nacional del Noroeste de Buenos Aires* (Junín, Argentine) and the EPF *École d'Ingeniéeur-e-s* (Sceaux, France) for giving me the opportunity of performing an international exchange during my engineering studies that finally led to this PhD thesis.

During the many conferences I have attended, I had the chance of meeting some important researchers among the communities of Linear Friction Welding, Fracture Mechanics and Titanium metallurgy. Achilleas Vairis, Anthony McAndrews, Bertrand Flipo, Joao Gandra, Steve Dodds, Jerry Gould, Aleksandar Sedmark, Robert Ritchie, Uwe Zerbst, Benoit Appolaire, Elisabeth Aeby-Gauthier and Yvon Millet are acknowledged for

the kind discussions concerning my results. I also would like to thank Elvi Dalgaard, Wenya Li, Philipp Frankel, Orest Ivasishin and Richard Turner for their answers to my several emails concerning their published papers.

Working at the *Centre des Matériaux*, I had many non-official supervisors that spared many hours of their time to teach and encourage me. Vladimir Esin and Anne-Françoise Gourges Lorenzon, thanks so much for your rigorous work and for the long discussions. Thanks for having taught me so much about metallurgy and fracture mechanics, I truly hope we will get to collaborate in the future. Henri Proudhon, you will always be a reference for me as a researcher and as a person, thanks for your kind friendship and for all that I have learnt with you. Loeiz Nazé, thanks for having shared with me your vast knowledge in metallurgy and its history. Yazid Madi, the strength with which you carry out your work is always inspiring to me, thanks for having given me so many ideas and opportunities. Jacques Besson, thanks for the time you spared me during my internship. Thanks André Pineau for your insight concerning the fracture mechanisms of my welds. I kindly thank Lucien Lairinandrasana for the discussions concerning the numerical simulations. Anthony Bunsell, thanks for the patience with which you corrected my English. Farida Azzouz, Samuel Forest, Djamel Missoum-Benziane, Kais Amar, Vladislav Yastebrov, Marie-Hélène Berger, Vincent Morel, Allain Köster and Fabrice Gaslain, thanks for the scientific discussions and the kind moments spent together in the daily life at the laboratory.

Je voudrais remercier tous les techniciens du Centre des Matériaux qui m'ont aidé à contourner les nombreuses difficultés techniques que j'ai rencontré en parcourant ce chemin. À mes amis de l'atelier, je suis un profond admirateur de la précision à laquelle vous travaillez. Réné, Fred, Vasco et les autres, merci pour tout ce que j'ai appris à vos côtés et merci pour la gentillesse et la bonne humeur que vous m'avez toujours gardées. Merci Maria pour toute ta gentillesse, pour m'avoir tant apporté en termes de microscopie, pour ton intelligence et surtout pour ton amitié, on a des encore des recherches à faire mais en Argentine. On y va ? Merci Antoine de m'avoir tant aidé, ceux qui travaillent au Centre des Matériaux ont vraiment la chance de t'avoir. Merci Abdennour et Régis pour votre soutien pendant mes longues campagnes expérimentales. Merci Stéphanie Dang pour m'avoir aidé à parcourir mes premiers pas dans la corrélation d'images que j'ai tant utilisé pendant ma thèse. Merci Cathérine pour ton *Buen día* de tous les jours. Merci Lynh-Thy, Yan, Zak, Jeando, Greg, Patrice et Olivier pour temps partagés au laboratoire. Merci Julie, Karine, Cécile, Anne, Gérard et Frank pour les bons moments passés ensemble, j'espère que ça continuera !

Je voudrais aussi remercier les nombreux amis que j'ai gagnés pendant ce voyage. Merci Francesco Deltoro pour ton amitié et pour les nombreux moments vécus ensemble. Grazie Luigi e Andreina di essere miei amici! Merci Bhimal de m'accompagner comme un frère, je suis vraiment chanceux et reconnaissant de toujours pouvoir compter sur toi. Merci Clément B de ton aide pendant mes essais, de toujours organiser des programmes sympas, pour t'être autant implique pour ma soutenance de thèse et d'être la personne que tu es, c'est rare de trouver des belles personnes comme toi. Merci Jean-Michel, de toujours une être référence pour moi, j'ai l'impression que tout ce que tu fais est juste, merci d'avoir corrigé mon papier sur l'alignement. Merci Quentin, j'ai vraiment beaucoup appris de toi. Merci Toba pour ta gentillesse aussi grande que controversée. Merci Sicong pour ton amitié. Merci Jonathan pour la bonne humeur que tu as toujours apportée à notre bureau et de m'avoir permis

d'apprendre sur tes recherches. Merci Thibault pour ton amitié et ta bonne humeur, j'ai toujours profité de nos belles discussions. Merci Pierre-Alexis del Infierno pour tous tes cours de français et pour ta belle amitié. Merci Aron (caro amico), Patrizio, Mohammed and Harris for your crazy personalities, you guys are the best. Anthony, keep up the good work in wood LFW joints. Merci Yannick pour la personne que tu es. Merci Julie, Aude, Chao et Nico J pour les bons moments passés dans notre bureau. Merci Vincent, Raphaël M, Raphaël C, Geoffrey B, Fabien, Hélène, Florent C, Frank, Constance, Lenny, Vincent H, Cholé, Lauranne, Louise, Eeva, Alexiane, Rossen, Laurent, Fang, Jan et Hanes pour les beaux moments vécu ensemble à l'heure de déjeuner.

Merci Gérard pour les bons moments vécus ensemble et de m'avoir aidé à commencer ma vie à Paris. J'espère t'avoir rendu fier, mon cher ami. Vielen Dank, Magdalena, für die vielen Diskussionen und für Deine ständigen ermutigenden Worte. Vielen Dank auch an Deine Familie und an Michael, dass Ihr Euer Zuhause zu meinem gemacht habt. Gracias Nics, por haberme influenciado hacia el camino de la ingeniería (y el de la música), siempre aprendo mucho de vos. Gracias Ñaki, Juan Martín, Verito y Daiana por tenerme siempre tanta confianza. Gracias Maryève, Amélie et Jonathan por creer siempre en mí y por acompañarme. Gracias a todos mis amigos de Junín. Gracias a mis amigos y profesores de la UNNOBA por su apoyo.

Merci Audrey pour m'avoir accompagné et avoir corrigé mon français et mon anglais. Tu m'as tellement lu que je suis convaincu que tu pourrais écrire un papier sur LFW et l'origine de l'univers de toi même ! Tu es vraiment une personne exceptionnelle, je te remercie aussi pour ton beau et constant sourire.

Merci Mariethé pour m'avoir ouvert les portes de ton cœur comme si j'étais un de tes enfants. Merci pour toute la gentillesse et la bienveillance que tu m'as manifestées de manière constante depuis qu'on s'est rencontrés. C'est vraiment très touchant.

Gracias a María, mi madre, por acompañarme en todos los proyectos que me he planteado. Gracias por haberme dado una vida increíble y gracias por ser una fuente inagotable de optimismo. Gracias, mamá. Te quiero.

1

Introduction

Résumé de chapitre

Le context et le project dans lequel cette thèse est inscrite sans décrits dans ce chapitre.

Chapter Abstract

The context of the project in which this PhD thesis is contained is described in this chapter.

Contents

Figures

1.1 Context

Diminishing greenhouse gas emissions (GHG) is a worldwide concern (Breidenich et al., 1998). The transport sector emitted 24% of the CO_2 world emissions in 2015, being the second one in the rank after electricity and heat production (Solaymani, 2019). Figs.1.1a and 1.1b show the evolution number of air transport passengers (pax) per country in Europe and in Asia over the last eleven years (2007-2018). For the sake of comparison, the count for each country was normalized with respect to the country maxima. The opacity of each curve represents the ratio between the country maxima and the maxima of all countries. The growth in number of pax is steady and its maxima was registered for 2018, for all countries in both continents. In the last eleven years, the number of pax was increased by factors of 1.33 and 4 in Europe and Asia, respectively. Compared to Europe, not only is the growth greater in the emerging economies, but also, the number of passengers is greater in its absolute value. This growing demand constitutes a constant challenge for manufacturers in the aerospace industry in terms of production time and production of greener technologies. Manufacturing technologies that enable the production of lighter planes, reduce production times and minimize raw material waste are required.

Titanium and titanium alloys are widespread in the aerospace industry (Boyer, 1996, 1995). Some of the most attractive characteristics of titanium are its strength/density ratio (Leyens and Peters, 2003), its corrosion resistance (Lütjering, 1998) and its capacity of being assembled with composites (Flipo et al., 2016). Titanium is the fourth most abundant structural metal in the Earth's crust exceeded only by aluminium, iron, and magnesium. Compared to other materials, its manufacturing costs are relatively high. Nevertheless, it was increasingly utilized in the aerospace industry. The usage of titanium in aircrafts has substantially increased by the end of the last century, as shown in Fig.1.2d. (Martin and Evans, 2000). It is interesting to note that the increment has also been substantial for composites. More recently, Chatterjee and Bhowmik (2019) claimed that from 1950 to 2019, the percentage in weight of titanium for aero-engines, evolved from 3% to 33%. These statistics reflect the increasing interest of aero-space manufacturers in titanium alloys.

A study on the environmental impact of metals production conducted by Norgate et al. (2007), showed that

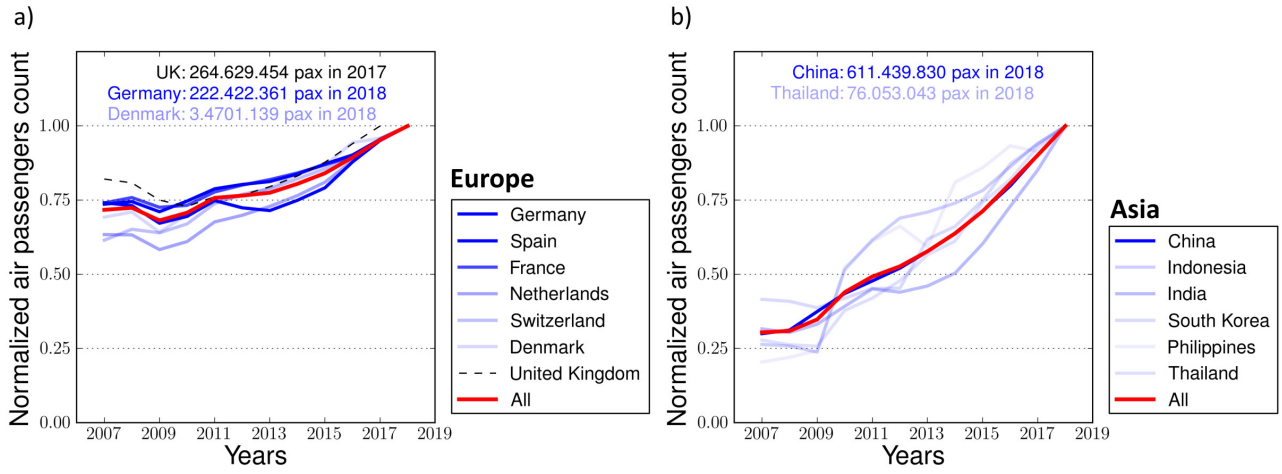

Figure 1.1: Evolution of the number of air transports passengers (pax) in countries of a) Europe and b) Asia normalized by country. The opacity level of each curve represents the ratio between the maximum number of passenger for a given country and the maximum number of passengers for all times and all countries. The count for United Kingdom was not available for the year 2018 and thus, it was plotted separately. Data extracted from Eurostat (data code: *TTR00012*) and The World Bank (data code: *AIR.PSGR*).

the production of 1 kg of titanium requires 361 MJ of non-renewable energy (Gross Energy Requirement (GER)), produces 22.4 kg of CO_2 (Global Potential Warming (GWP)) and 0.230 kg of SO_2 (Acidification potential (AP)) emissions. The values for other metals are shown in Fig.1.2a-e. It is remarkable that manufacturing titanium, which is produced by the Kroll (1940) process, is by far the most detrimental of manufacturing processes among all other metals. Notwithstanding, the use of titanium alloys substantially improves the autonomy and reduces the weight of aero-engines. For instance, in the Leap 2014 aero-engine produced by Safran Aircraft Engines in partnership with GE Aviation (CFM international), the Nickel-based material of the low pressure turbine blades was replaced by titanium aluminide (TiAl). With this feature, the Leap 2014 aero-engine exhibited a 50 % weight reduction, a 15 % reduction of GHG emissions and a 50 % reduction of NOx emissions. There is a trade-off between the environmental hazard of the manufacturing process of titanium and the environmental benefits of its utilization. Technologies that reduce titanium waste by reducing milling operations are required.

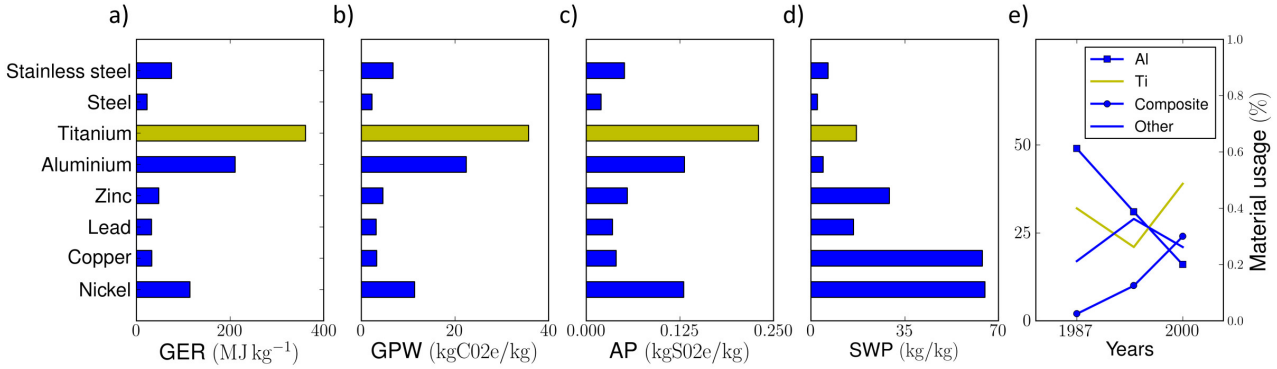

Figure 1.2: Environmental impact in terms of a) Gross Energy Requirement (GER), b) Global Warming Potential, c) Acidification Potential (AP) and d) Solid Waste Burden (SWB) for several metals (adapted from Norgate et al. (2007)). e) Evolution over the years of titanium usage in aircrafts (adapted from Martin and Evans (2000)).

Linear Friction Welding (LFW) is an innovative assembly process that consists in joining materials by solid state welding (Bhamji et al., 2011). This process exhibits several advantages that could be exploited in the aerospace industry to reduce gas emission. Some of these advantages are replacing rivets and other similar assembly technologies without adding weight to the structure, joining in times spans in the order of seconds and reducing material waste by the optimization of milling operations. LFW welded parts are candidates for mechanically loaded structural applications that may also involve cyclic loading. As most welding processes, LFW entails various concerns such as the characterization of the resulting microstructure, the numerical simulation of the welding process, the measurement of residual stresses and the mechanical characterization of the welded structure. Such a vast study requires various areas of expertise and associated involvement of research developments. It is in this context, that OPTIMUM ANR Project was proposed.

1.2 OPTIMUM ANR Project

The OPTIMUM ANR project was funded by the French National Research Agency (ANR) (see also: Project ID: ANR-14-CE27-0017 in https://anr.fr/Project-ANR-14-CE27-0017) and is an acronym for ***OPTIM****ization of* ***MU****lti-****M****aterials assemblies by Linear Friction Welding for Aerospace applications.* The main objective of Optimum is the experimental and numerical study of Titanium Linear Friction Welds (LFW). Four PhD students

in three different academics institutions were to study different aspects of LFW. All welding campaigns were designed and carried out by ACB. All the studied configurations were performed using the welding parameters of Table 1.1.

Friction pressure	Forging pressure	Amplitude	Frequency	Axial shortening
90 MPa	90 MPa	2 mm	50 Hz	3 mm

Table 1.1: Welding parameters for all configurations.

The project proposes an innovative approach which aims to establish a link between the welding process parameters, their effects on microstructure and subsequent mechanical properties, as well as the study of residual stresses and the numerical simulation of the process. The project was subdivided in fours work-packages that schematically shown in the diagram of Fig.1.3.

1.2.1 OPTIMUM work-packages

Work-package 1: Microstructural characterization

The first work-package aimed at the microstructural characterization of the LFW joints. This work-package was carried out by Dorick BALLAT-DURAND at *Université de Technologie de Compiègne (UTC)* at Compiègne (France), under the supervision of Prof. BOUVIER, Salima and Prof. RISBET Marion. Some of the main tasks assigned are: a parametric study of the effect of welding parameters in the microstructure and the microstructural characterization of Ti LFW joints.

Work-package 2: Measurement of residual stresses

The second work-package aimed at the measurement of residual stresses and was partially funded by the *Fondation de Recherche pour l'Aéronautique et l'Espace (FRAE)* and other third party funding. This work-package was carried out by Xavier BOYAT at *UTC* at Compiègne (France), under the supervision of Prof. BOUVIER, Salima and Prof. RISBET Marion. The main task of this work-package was the measurement of residual stresses and the microstructural characterization of some LFW joints made of Nickel-based alloys.

Work-package 3: Numerical simulation of the welding process

The third work-package aimed to the numerical simulation of the welding process. This work-package was carried out by Antoine POTET at *Centre de Mise en Forme de Matériaux (CEMEF)* (Sofia Antipolis, France), under the supervision of Prof. FOURMENT Lionel and Prof. MOCELLIN Katia. The main task of this work-package was to perform thermo-mechanical numerical simulations of the welding process, using the software for cold and hot forming process named Forge®.

Work-package 4: Mechanical characterization

The forth work-package aimed at the mechanical characterization of similar and dissimilar LFW joints in terms of monotonic, cyclic and fracture behaviour. This is the main topic of the present PhD thesis and it is detailedly described in Sections 1.3 and 1.5

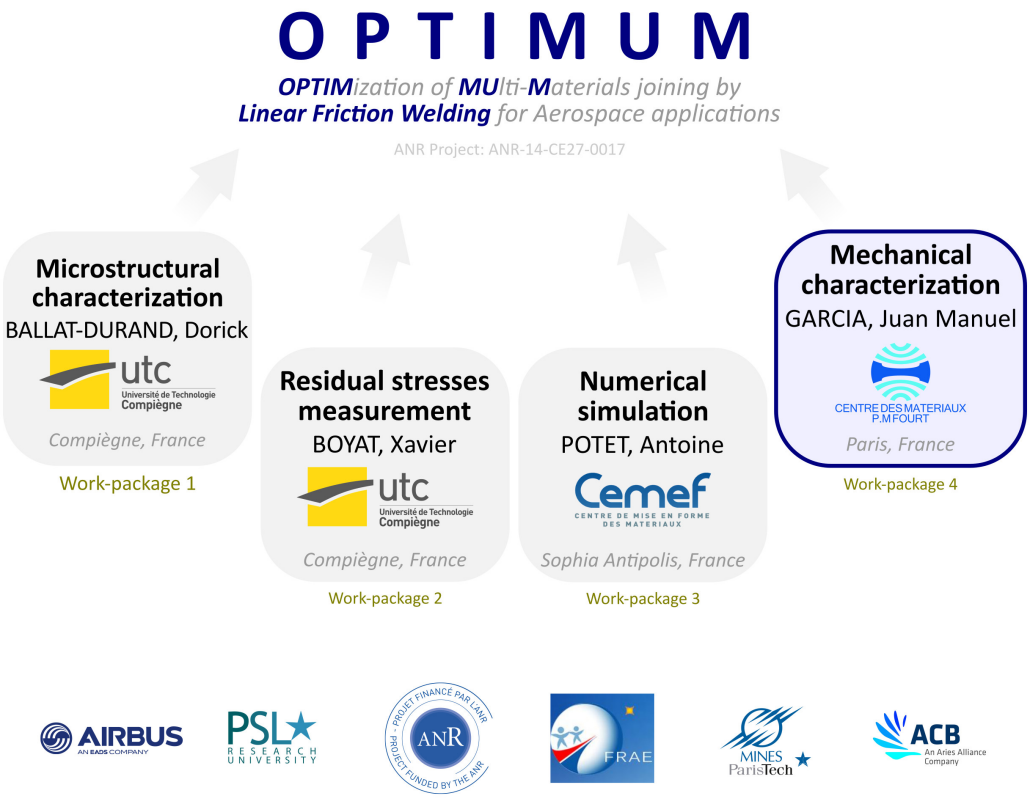

Figure 1.3: Organization of the ANR project in which this PhD thesis is inscribed.

The work-package 1 in the ANR project (see Fig.1.3), describes most of microstructural interpretations in which this work is based upon. These studies were also available in three scientific publications: *Multi-scale and multi-technic microstructure analysis of a linear friction weld of the metastable−β titanium alloy Ti–5Al–2Sn–2Zr–4Mo–4Cr (Ti17) towards a new Post-Weld Heat Treatment* (https://doi.org/10.1016/j.matchar.2018.08.013), *Through analysis of the microstructure changes during linear friction welding of the near−α titanium alloy Ti–6Al–2Sn–4Zr–2Mo (Ti6242) towards microstructure optimization* (https://doi.org/10.1016/j.matchar.2019.02.027) and *Contributions of an innovative post-weld heat treatment to the micro-tensile behavior of two mono-material linear friction welded joints using: The β–metastable Ti–5Al–2Sn–2Zr–4Mo–4Cr (Ti17) and the near–α Ti–6Al–2Sn–4Zr–2Mo (Ti6242) Ti–alloys* (http://doi.org/10.1016/j.msea.2019.138334). The interpretations in terms of microstructural characterization presented in the present PhD thesis account for the knowledge gathered in that work-package and the available open scientific literature. The analysis of residual stresses initially attributed to the work-package 2 in the OPTIMUM project turned out to be difficult. This is why I will discuss my results in light of results found in the open scientific literature.

1.3 Research objectives of this PhD Thesis

As described in the previous Sections, the main objective of this PhD thesis is to asses the mechanical behaviour of Titanium Linear Friction Welds. Specifically in terms of monotonic, cyclic and fracture behaviour in relationship with the underlying microstructure and potential defects associated to LFW.

Some of the most important questions that this PhD thesis tries to answer for each welding configuration are the following :

- Are there any defects ? What are their consequences in terms mechanical behaviour ?
- What is the strength of the joint ? Do the joints present overmatching or undermatching strength ? In other words, do the parent materials exhibit a higher or lower tensile strength than the weld zones ?
- Where in the welded structure does failure occur and what are the fracture mechanisms associated to the underlying microstructure ?
- What is the fatigue strength for a target life of 10^5 cycles ? Where does fatigue crack initiation take place in the welded structure and what are the fatigue crack propagation mechanisms associated to the underlying microstructure ?
- What is the local strain evolution and local strain to failure of the failure location ?

1.4 Approach

The mechanical characterization of LFW joints is carried out by performing mechanical tests using cross-weld specimens. The strength of the welds is measured by performing tensile tests using smooth samples and notched micro-tensile tests. The local measurements of strain are obtained by Stereo Digital Image Correlation and synchrotron tomography *in situ* and optical microscopy *in situ* observation. The spatio-temporal strain evolution in the cross-weld samples is assessed by using DIC strain-rate fields. The fatigue life is studied *via* an S–N approach on smooth samples. Complementary microstructural characterizations are performed on polished samples, using scanning electron microscopy techniques, such as EBSD and EDX. The damage mechanisms and fatigue crack propagation mechanisms are analysed through fractographic analysis by scanning electron microscopy. For selected weld configurations, non-destructive testing using synchrotron imaging was carried out to identify potential defects and *in situ* damage evolution.

1.5 Organization of this PhD thesis

Four chapters aim to be completed scientific contributions (Chapters 3, 4, 6 and 7) and one is presented in the form of an article project (Chapter 5). The first contribution (Chapter 3) is not directly related to LFW but still is an important part of the fatigue study that is carried out in the rest of the chapters. The studied assemblies are detailed in Table 1.2.

Weld	State	Chapter
Similar Ti6242 LFW joint	As welded	4
Similar Ti6242 LFW joint	As welded	5
Dissimilar Ti17-Ti64 LFW joint	As welded	6
Dissimilar Ti17-Ti64 LFW joint	Post weld heat treated	6
Similar Ti17 LFW joint	As welded	7
Similar Ti17 LFW joint	Post weld heat treated	7

Table 1.2: Studied LFW joints.

The five chapters that constitute our findings share a coherent narrative but are presented in the form of five isolated scientific contributions. I tried as much as possible to spare the reader of unnecessary repetitions but sometimes these were inevitable. I wholeheartedly thank the reader for going along with the eventual repetitions found in the reading of this document.

In **Chapter 2**, a literature review subdivided in three subsections is presented. The first subsection concerns a non-exhaustive review of Titanium metallurgy and mechanical behaviour elementary concepts. In the second subsection, some of the friction welding processes and linear friction welding are described. Finally in the third subsection, the state of the art in terms of mechanical characterization of linear friction welds and some other friction welds is presented.

In **Chapter 3**, a complementary study unrelated to Linear Friction Welding is presented. The main motivation of this work is to obtain reliable results during fatigue testing. At the beginning of this study, our laboratory was equipped with a set of new hydraulic grips for flat specimens. A procedure for the alignment of the load frame was required to ensure that our test procedures complied with international testing standards. This work concerns the use of Stereo Digital Image Correlation for the analysis and quantification of parasite loadings due to the misalignment of a load frame during fatigue specimen mounting. The aim of this work is to provide an easy way to estimate the parasite bending stresses induced by the load frame misalignment, using the out-of-plane displacement field obtained by SDIC and beam theory. Simple procedures to align of the commercial load frame are also provided.

In **Chapter 4**, the strength and fracture mechanisms under monotonic and cyclic loadings of a **similar Ti6242 LFW joint** with overmatching strength are studied. Potential defects are studied using 3D synchrotron imaging. Smooth cross-welded specimens are tested under monotonic and cyclic loading at room temperature in the as welded state. The local plastic activity is assessed by using DIC. The chronological order of deformation events is investigated using strain rate measurements. The fatigue crack initiation location in the welded structure and the fatigue crack propagation mechanisms in relationship with the underlying microstructure are studied. A dendritic defect at the WCZ that was related to prior to welding contamination was identified to be at the origin of a substantial reduction in fatigue life for a specimen.

In **Chapter 5**, the deformation and damage mechanisms under monotonic loading of both PM and WCZ of a **similar Ti6242 LFW joint** are assessed by synchrotron tomography and optical microscopy *in situ* notch tensile tests. Since this joint was observed to present overmatching strength, a notch was machined to micro-tensile specimens centred with respect to the WCZ. Furthermore, given the prior to welding contamination observed in Chapter 4, the effect of prior to welding contamination on the fracture mechanisms of the WCZ is studied by the analysis of two different joints welded in different conditions.

In **Chapter 6**, the effect of brass contaminants and weak zones on strength, fatigue resistance and toughness of a **dissimilar Ti17-Ti64 LFW joint** are studied. The effect of prior to welding contamination were staggeringly highlighted since, for the joint that was not cleaned prior to weld, an unexpected defect layer is identified. Conversely, for the joint that was cleaned prior to welding, the mechanical properties are remarkably better but compromised by a weak zone. The monotonic, cyclic and fracture behaviour of the weak zone are studied.

In **Chapter 7**, the tensile strength, fracture mechanisms, fatigue strength and fatigue crack propagation mechanisms of a **similar Ti17 LFW joint** in the as-welded state and post weld heat treated are studied

in relationship with the underlying microstructure and compared to the PM. This post weld hear treatment is intended to enhance the properties of the weak zone in the Ti17 TMAZ evidenced in Chapter 6. Tensile and fatigue tests were performed at room temperature using specimens made of PM and cross-weld specimens coming from three joints: the first was-welded in the as machined condition, the second was ground prior to weld and the third as-welded in the as machined condition and post weld heat treated. Special interest is drawn to the mechanical behaviour of the weak zones of the as-welded joint and to the effect of the post weld heat treatment on these zones' behaviour. Finally, an optimization of the post weld heat treatment is discussed.

In **Chapter 8**, a general discussion of all the results in this document, conclusions and perspectives are presented.

2

Literature Review

In this Chapter, a literature review containing three principal sections is presented. The first section contains a non exhaustive review on titanium metallurgy. The second section contains a review on solid stated friction joining processes and linear friction welding. Finally, the state of the art in mechanical characterization of LFW joints is presented for joints made of the near$-\alpha$ Ti6242 exhibiting α grains embedded in a β matrix, the α/β Ti64 exhibiting α grains and lamellar α/β microstructure and the $\beta-$metastable Ti17 alloy with large β grains and several forms of the α strengthening phase.

Résumé de chapitre

Une revue de la littérature contenant les trois axes principaux de cette thèse est présentée. La première section porte sur une revue non exhaustive de la métallurgie du titane. La deuxième section contient une revue des procédés de soudage à l'état solide et le soudage par friction linéaire. Finalement, l'état de l'art en termes de caractérisation mécanique de joints soudés par friction linéaire d'alliages de titane est présenté. Le premier alliage est le quasi–α Ti6242 ayant des grains α intégrés dans une matrice β, le deuxième est un alliage α/β TA6V ayant une microstructure composée par des grains α et des colonies lamellaires de phases α/β et le troisième est un alliage β–metastable Ti17 contenant de gros grains β et plusieurs formes de la phase durcissante α.

Chapter Abstract

A literature review containing three principal sections is presented in this chapter. The first section contains a non exhaustive review on titanium metallurgy. The second section contains a review on solid stated friction joining processes and linear friction welding. Finally, the state of the art in mechanical characterization of LFW joints is presented for joints made of the near$-\alpha$ Ti6242 exhibiting α grains embedded in a β matrix, the α/β Ti64 exhibiting α grains and lamellar α/β microstructure and the $\beta-$metastable Ti17 alloy with large β grains and several forms of the α strengthening phase.

Contents

Figures

2.1 Titanium

2.1.1 Pure titanium

Titanium is a light transition metal of remarkable mechanical properties. Titanium and its alloys have excellent corrosion resistance and a very high melting point (1678 °C), resulting in a very interesting material to work under strong loadings in a very wide temperature range (Leyens and Peters, 2003). Compared to industrial steels, its density is about a half and it exhibits almost twice their yield strength. Some titanium alloys are able to develop significant levels of work hardening by the retaining martensitic structures at room temperature, this property is also known as hardenability (Welsch et al., 1993). Due to its properties, titanium is largely used in several engineering applications such as aero-engine parts (Meetham, 1981), biomedical (Khorasani et al., 2015) and off-shore applications (Li et al., 2019). This element can be found in "black sands" containing ilmenite $FeTiO_3$ or rutile TiO_2 and it can be isolated following the Kroll process patented by Kroll (1940). Its production can only be achieved by batch process, and no continuous process resulting in a very expensive material Leyens and Peters (2003).

Crystal structure

At 882 °C, titanium undergoes an allotropic transformation from a low temperature hexagonal close-packed (h.c.p) crystal structure, to a high temperature body-centred cubic (b.c.c.), that remains stable up to the melting point. Low temperature h.c.p. crystal lattice is also known as the α phase and the high temperature b.c.c. crystal lattice is known as the β phase. The temperature to which titanium changes its crystal structure is called the $\beta-$transus temperature. The coexistence of both crystal lattice is fulfilled by the addition of alloying elements and thermo-mechanical processes results in a very large variety of properties (Leyens and Peters, 2003).

The lattice parameters of the hcp α phase are $a = 0.295\,\text{nm}$ and $c = 0.468\,\text{nm}$, giving a c/a ratio of 1.587. The lattice parameters of the bcc β phase is $a = 0.332\,\text{nm}$.

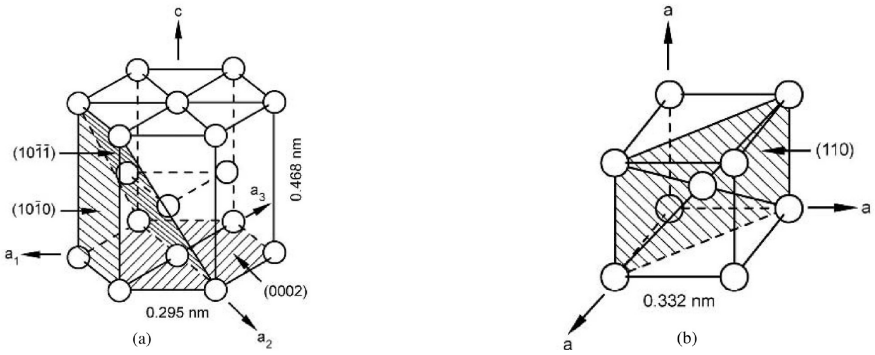

Figure 2.1: Unit cells of the a) α (h.c.p.) and b) β (b.c.c.) crystal lattices. (Polmear, 2005)

Elastic deformation in Titanium alloys

The elastic deformation of commercially pure titanium (CP-Ti) is a consequence of the elastic behaviour of the α and β phases (see Fig.2.1). The crystal lattices of these phases are anisotropic and their behaviour is

well documented in literature. For instance, Hayes (1972) proposed a mathematical formulation for describing the anisotropy of orthorhombic phases, in which the stress-strain relationship was expressed in therms of the angle between the orientation of the crystal lattice and the loading direction. The basic principle is to write the compliance tensor of elastic deformation and projecting it over a generic direction that represents the loading direction σ. The values for the compliance tensor are obtained experimentally and are often available in literature but exhibit some scatter, which leads to different results. Nevertheless, these computations give reliable information for analysing the global trends for the crystallographic directions of a given crystal lattice (Duval, 2013).

Based on this approach, Duval (2013) computed Young's Modulus of both α and β phases as a function of the angle between the loading direction and crystallographic directions (see Figs.2.2a and 2.2c). Furthermore, these computations were used to map Young's Modulus in the pole figure of each phase (see Figs.2.2b and 2.2d).

HCP crystal lattice (α phase) The symmetry around the c axis of the hcp crystal lattice simplifies this computation since the generic direction can be written as a function of a single geometric parameter. Young's Modulus is expressed as a function of the angle θ formed between the loading direction σ and the [1 0 0] (c) direction of the hcp crystal lattice, as shown by the overlaid schema in Fig.2.2a. The interval in which θ is contained is shown in Fig.2.2b. Young's Modulus varies from 100 GPa at $\theta = 90°$ to 145 GPa at $\theta = 0°$.

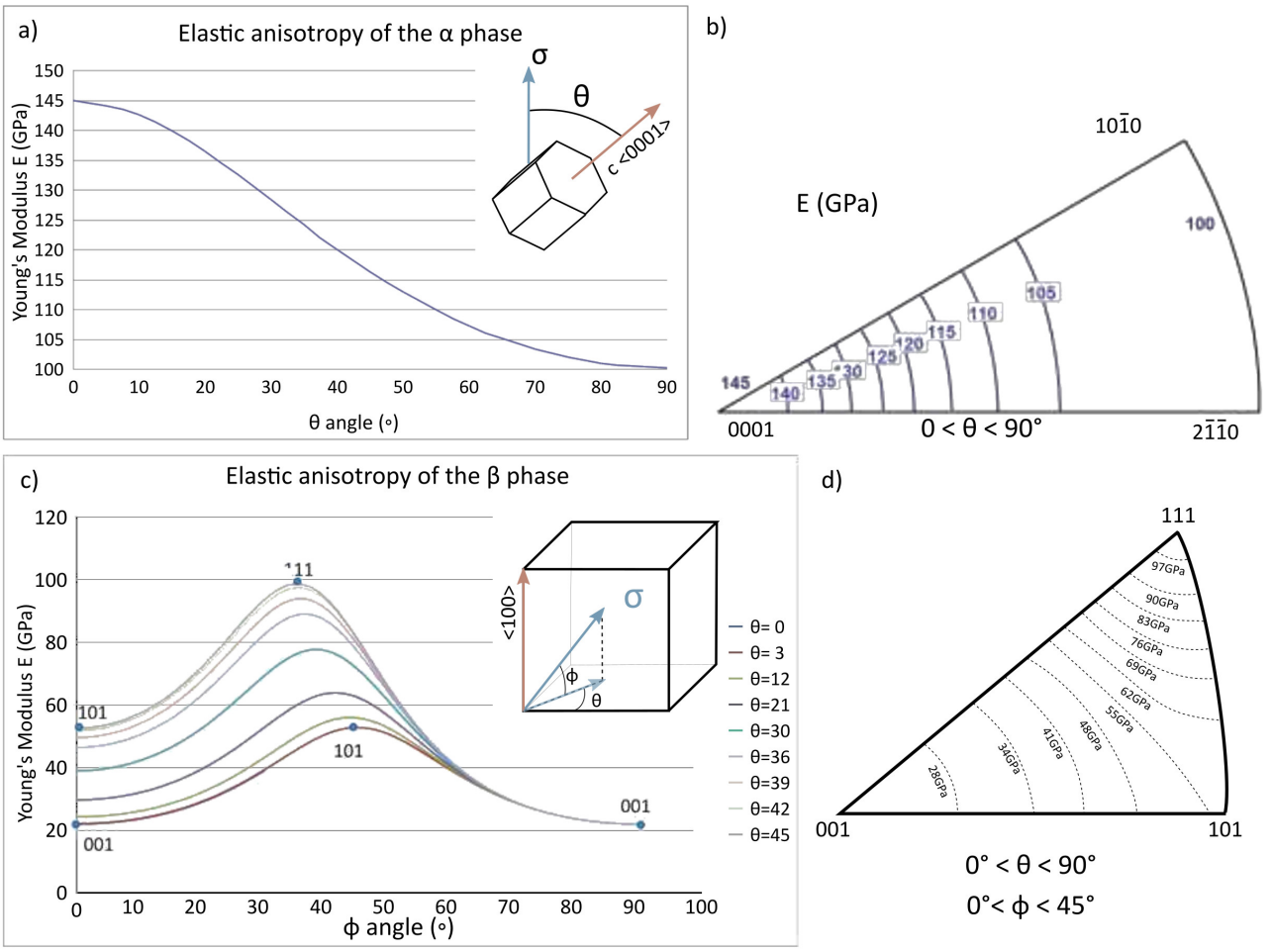

Figure 2.2: Graphical representation of the elastic anisotropy of the a-b) α (h.c.p.) and c-d) β (b.c.c.) phases as a function of the loading direction and crystallographic directions (Duval, 2013).

The ratio between the maximum and minimum Young's Modulus is 1.45 and the median is 122.5 GPa. Duval (2013) found a good agreement between these results and the experimental measurements available in literature (Roberts, 1962; Flowers et al., 1964; Gerday et al., 2011).

BCC crystal lattice (β phase) For this crystal lattice, Young's Modulus is expressed as a function of two angles ϕ and θ. The angle ϕ is formed by the loading direction σ and the (0 0 1) plane of the bcc crystal lattice. The angle θ is formed by the projection of the loading direction σ in the (0 0 1) plane of the bcc crystal lattice and the [1 0 0] direction of the bcc crystal lattice. The interval in which θ and ϕ are contained is shown in Fig.2.2d. In this manner, a set of curves are shown, one for each value of θ. As ϕ tends to 90, θ tends to 0 and Young's Modulus becomes independent of θ. In particular, if $\phi = 90$ loading is applied parallel to the [0 0 1] direction, in such case $\theta = 0$. The minimum and maximum value respectively are 25 GPa and 100 GPa. The ratio between the maximum and minimum is 4 and the median value is 62.5 GPa.

It is very interesting to note that, compared to the β phase, the median Young's Modulus of the α phase is substantially greater. This is also reflected by the fact that the minimum Young's Modulus of the α phase is equal to the maximum Young's Modulus of the β phase. It is also interesting to note that both phases exhibit a significant maximum/minimum Young's Modulus ratio. This is of particular interest for materials exhibiting texture.

Plastic deformation in Titanium alloys

The plastic deformation in a crystal depends on its lattice's slips systems and twinning modes. The number of slip planes multiplied by the number of slip directions determines the number of slip systems. This represents the number of dislocation glide opportunities. Plastic deformation by dislocation glide occurs in closely packed planes or directions, which minimize the required energy for undergoing deformation (Leyens and Peters, 2003).

HCP crystal lattice (α phase) The close packed plane is the the basal plane {0 0 0 1} and the closed packed direction are the prismatic directions $\langle 1\,1\,2\,0 \rangle$. Dislocation glide occurs with Burgers vectors of $\langle a \rangle$-type and $\langle a + c \rangle$-type contained in basal, prismatic, two first-order pyramidal and second-order pyramidal planes (see Fig.2.3a). There are five slip modes and thirty slip systems. The activation of these slip modes have been observed by several authors (Churchman and Allibone, 1954; Williams and Blackburn, 1968). For instance, Bridier et al. (2005) observed the coexistence of basal, prismatic and first-order slip modes of a Ti64 grade through scanning electron microscope *in situ* micro-tensile test.

BCC crystal lattice (β phase) In a bcc crystal lattice, dislocation glide occurs in the closed packed direction (1 1 1). The three planes containing this direction are {1 1 0}, {1 1 2} and {1 2 3}. The bcc crystal lattice exhibits a total of 3 slip modes and 48 slip systems (detailed in Fig.2.3b). A so called "pencil glide" mechanisms, first documented by Taylor (1928), has also been observed in material with a bcc crystal lattice. It consists in dislocation glide occurring by the activation of alternating slip system along (1 1 1) directions in planes with comparable packing densities containing, such as {1 1 0}, {1 1 2} and {1 2 3} (see schematic representation in Fig.2.4a). During the microscope scanning electron *in situ* micro-tensile test of a $\beta-$Ti21S grade performed by Ben Haj Slama et al. (2019), the authors observed slip traces that seem curvilinear at a mesoscopic scale (see

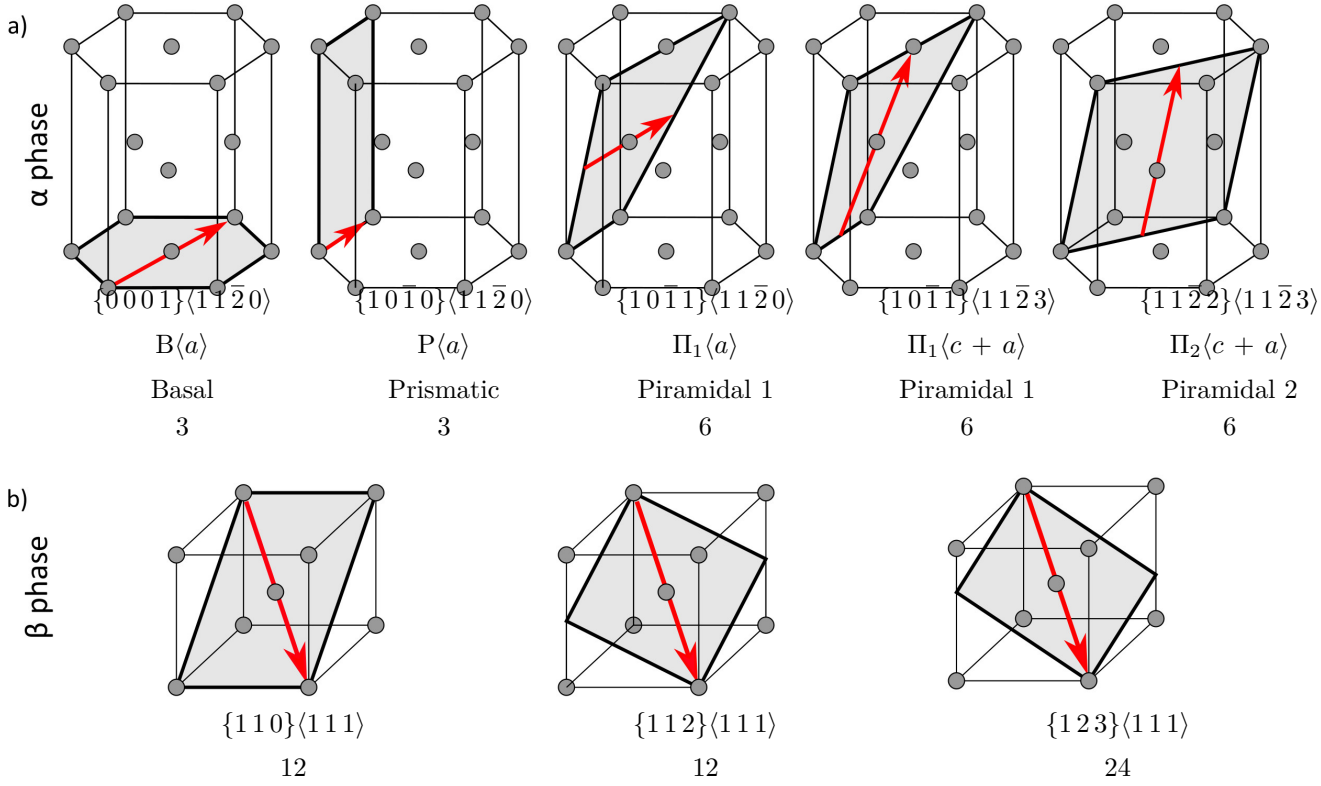

Figure 2.3: Graphical representation of the elastic anisotropy of the a) α (h.c.p.) and b) β (b.c.c.) phases as a function of the loading direction and crystallographic directions.

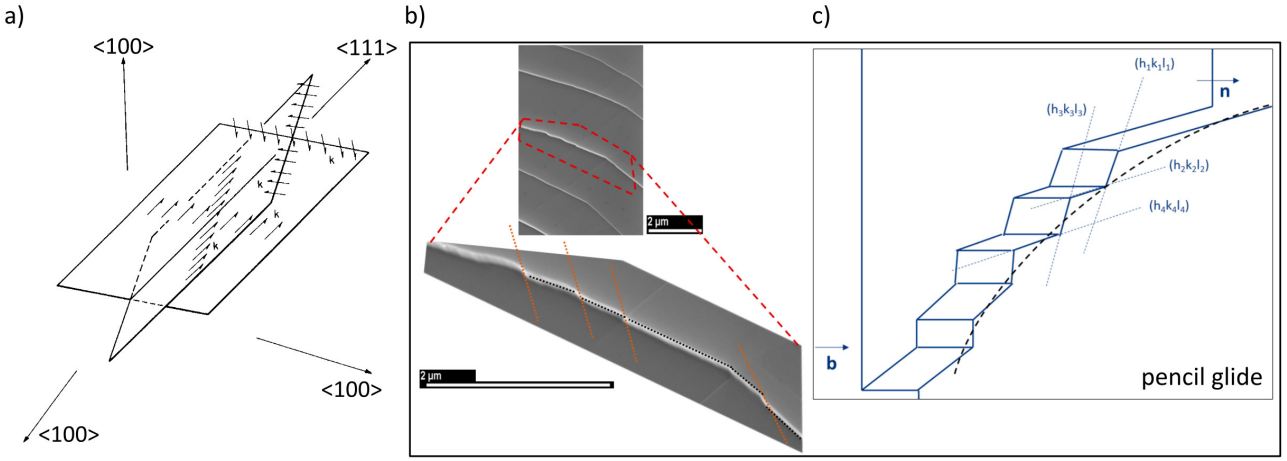

Figure 2.4: a) Geometric representation of the equivalence of slip with equal ease on any plane containing the (1 1 1) slip directions and slip with equal ease in any direction in the {1 1 1} slip planes (Piehler and Backofen, 1971). b) secondary electron micrographs showing curved slip lines resulting from pencil dislocation glide and (c) a corresponding schematic representation (Ben Haj Slama et al., 2019)

Fig.2.4b). Observations at higher magnification levels revealed zigzag slip traces (see Fig.2.4c). They claimed that dislocation can easily change plane during deformation but the mechanisms that drives that the change in slip system is still unknown (Ben Haj Slama et al., 2019).

2.1.2 Titanium alloys

Beyond a so called $\beta-$transus temperature of 882 °C, the crystal lattice of pure titanium undergoes an allotropic transformation from a low temperature α phase to a high temperature β phase (see Fig.2.5). This

transformation was first observed by Burgers (1934) in Zr single crystals. It consists in the transformation of the most densely packed planes and directions of the bcc β phase into the hexagonal α phase during cooling from temperature above the $\beta-$transus. These transformations are detailed in Eqs.2.1 and 2.2. Titanium has the following electronic configuration: [Ar] 3d2 4s2, resulting in an incomplete shell allowing to multiple solid solutions. The addition of alloying elements can increase, decrease or do not affect the $\beta-$transus temperature. Depending on these effects, alloying elements are respectively classified as $\alpha-$stabilizer, $\beta-$stabilizer and neutral elements. Fig.2.6 shows binary phase diagrams for solid solutions of the aforementioned alloying elements in a Ti metallic matrix. The existing phases are schematically mapped as function of the solid solution composition and temperature. The percentages in weight of Ti and each alloying element are laid in the horizontal axes. The solid solution temperature is laid in the vertical axis.

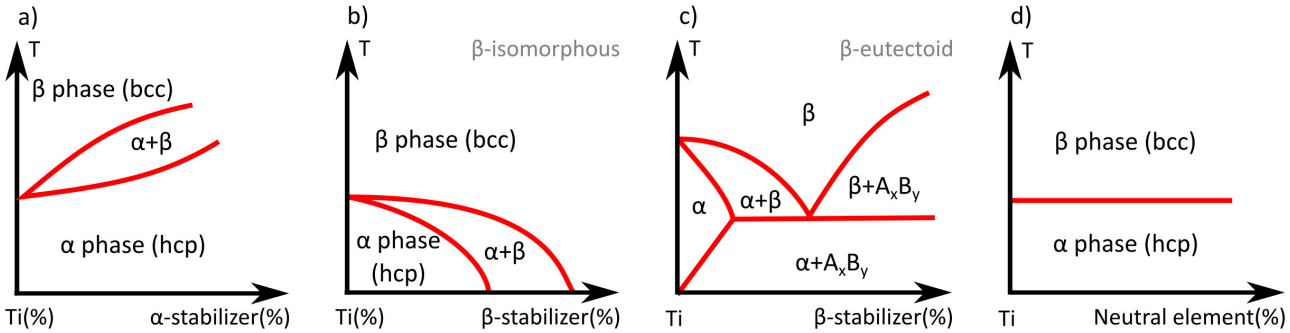

Figure 2.6: Light microscopy observation of the acicular martensite in Ti−6Al−4V quenched from the β phase field (Lütjering and Williams, 2003).

α stabilizers With the addition of $\alpha-$stabilizers not only is the $\beta-$temperature increased but also, a two-phase $\alpha+\beta$ field is developed, as shown in Fig.2.6a. These elements are classified in interstitial and substitutional elements, which exhibit different levels of solid solubility. Among the interstitial elements, O, N and C can be found. Elements such as B, Ga, Ge, and some other rare earth elements also stabilize the α phase but they exhibit low levels of solid solubility. Aluminium is the most important titanium $\alpha-$stabilizer since it exhibits large solubility in both the α and β phases (Lütjering and Williams, 2003).

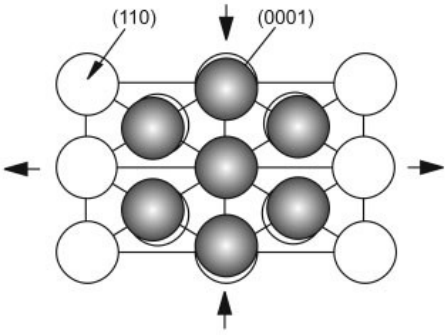

$$\{0\,0\,0\,1\}_\alpha \parallel \{1\,1\,0\}_\beta \quad (2.1)$$

$$\langle 1\,1\,2\,0\rangle_\alpha \parallel \langle 1\,1\,1\rangle_\beta \quad (2.2)$$

Figure 2.5: β/α transformation according to Burgers relationship (Leyens and Peters, 2003)

β stabilizers These elements decrease the $\beta-$transus temperature are subdivided in $\beta-$isomorphous and $\beta-$eutectoid elements and they shape differently the binary phase diagrams, as shown in Figs.2.6b and 2.6c. Some of the $\beta-$isomorphous alloying elements for Titanium are V, Mo, Ta, and Nb, being V and Mo the most frequently used due to their high solubility in the β matrix (Leyens and Peters, 2003). The β phase can be stabilized at room temperature with sufficient concentrations of the elements (Lütjering and Williams, 2003). The addition of low concentrations of $\beta-$eutectic elements such as Fe, Mn, Cr, Co, Ni, Cu, Si, and H, can induce the formation intermetallic compounds.

Neutral elements The most common neutral elements are Sn and Zr and are present in a large extent of commercial alloys (Lütjering and Williams, 2003). Compared with the elements mentioned above, the neutral elements have no significant effect in the $\beta-$transus temperature. Nevertheless, they are sometimes accounted as $\alpha-$stabilizers since, when alloyed with Al, they tend to replace it and stabilize in the hexagonal crystal lattice of the Ti_3Al, commonly known as α_2. Furthermore, they tend to strengthen the α phase (Lütjering and Williams, 2003).

Phase transformation in Titanium alloys

Titanium and titanium alloys undergo the transformation from β phase (bcc) to α phase (hcp) by a martensitic transformation or by a diffusion controlled nucleation and growth process. The nature of the transformation depends on the cooling rate and alloy composition (Lütjering and Williams, 2003). These transformation occur following the crystallographic relationships stated in Eq.2.1 and 2.2, were first observed in Titanium by Newkirk and Geisler (1953), and lead to 12 differently oriented hexagonal variants with respect to the β crystal lattice.

Martensitic transformation Titanium martensitic transformation is a displacive diffusionless process in which a β bcc crystal lattice transforms to a α hcp crystal lattice in given volume. The microstructure of titanium alloys undergoing this transformation often exhibit disk shaped geometries and is commonly known as α' Lütjering and Williams (2003). Two types of hexagonal α' martensite have been observed: massive martensite and acicular martensite (Williams, 1973). Pure titanium, titanium alloys with low alloying content or high martensitic transformation temperature exhibit massive martensite. Conversely, the acicular martensite is observed in alloys with higher solute content or lower martensitic transformation temperature and is formed by an entangled mixture of α plates, each one exhibiting different variants of the Burgers relationship (see 2.7). β stabilizers supersaturate the hexagonal α' martensite and precipitate into incoherent β particles decomposed to $\alpha + \beta$ at dislocations or β phase layers at plate boundaries, during annealing in the $(\alpha + \beta)$ phase field.

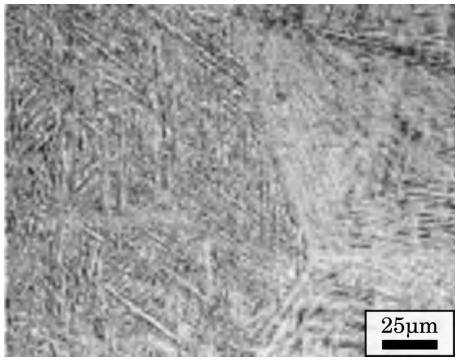

Figure 2.7: β/α transformation according to Burgers relationship (Leyens and Peters, 2003)

Nucleation and diffusional growth This process occurs when cooling from β field at sufficiently low cooling rates and it favours the continuous nucleation of the α phase at the β grain boundaries. As cooling continues, at the interface of the continuous α layer or at the β grain boundary, α plates grow into the β grain following some variant of the Burgers relationship Peters et al. (1983). These sets of α plates so called α colonies continue to grow until they meet other α colonies nucleating at other grain boundaries. These colonies should not be confused with the α and β plates developed within β grains, which are often called α and β lamellae. The microstructure containing these lamellae features is then designated as lamellar.

Metastable transformations

According to Froes (2015), the phases diagrams in Fig.2.10 are equilibrium phases diagrams. This means that the cooling rates are slowly enough to enhance diffusion. Conversely, if the cooling rate is too high diffusion is restricted and the phases so called metastable that exist in transition to an equilibrium can be developed. Some of the metastable phases that can be encountered in titanium alloys are martensite, metastable beta, omega, and beta prime (Froes, 2015). The apparition of these phases is often studied in the so called Continuous Cooling Transformation (CTT) diagrams. Sieniawski et al. (2013) documented the CCT diagrams for the alloys Ti6242 and Ti64 (see Fig.2.8), and showed that for cooling rates greater to 18 °C, an entangled martensitic α' was developed, as shown in Fig.2.9.

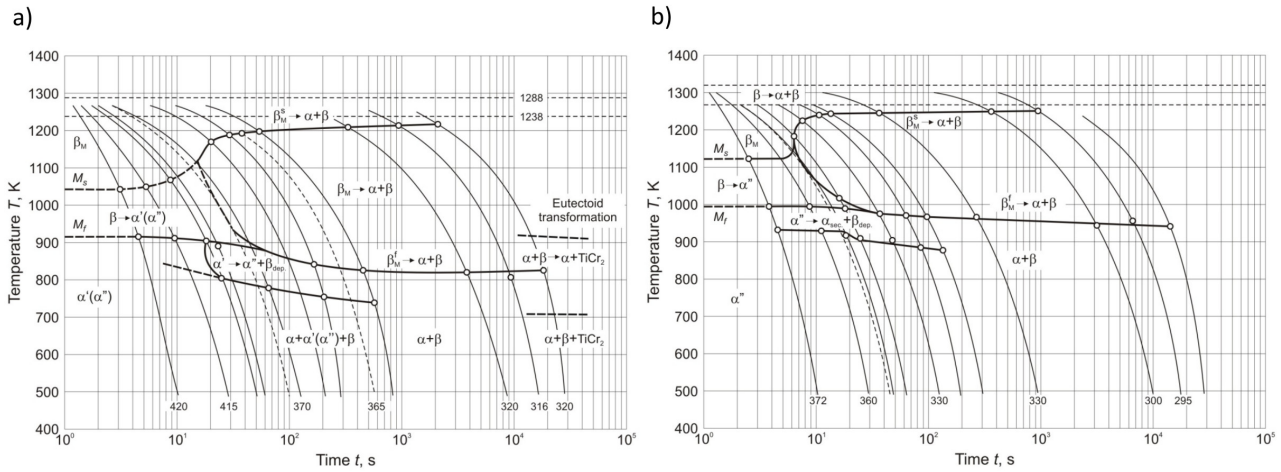

Figure 2.8: CCT diagram for a) Ti6242 and b) Ti64 titanium alloys (Sieniawski et al., 2013).

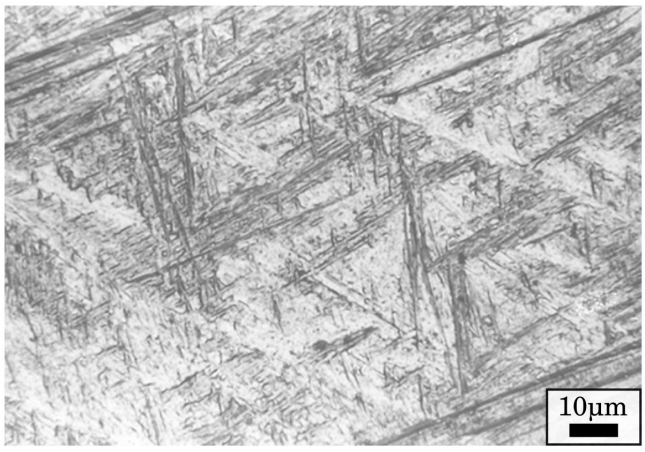

Figure 2.9: Martensitic microstructure of Ti6242 alloy after cooling from 1050 °C at a rate of 48 °C s^{-1} (Sieniawski et al., 2013).

Classification of Titanium alloys

Alloying titanium with different amounts of α and $\beta-$stabilizers followed by application of different thermo-mechanical processes has allowed a very vast spectre of titanium alloys to be developed. The most simple classification of commercial titanium alloys is formed by the following categories: $\alpha-$alloys, $\alpha+\beta-$alloys, $\beta-$metastable alloys, and $\beta-$stable alloys. The mechanical properties of some alloys within these categories are exhibited in Table 2.1. The classification of a given titanium alloy depends on its position in the horizontal axis in a pseudo-binary phase diagram of Fig.2.10. Each category of this alloys have different mechanical properties that briefly discussed hereafter.

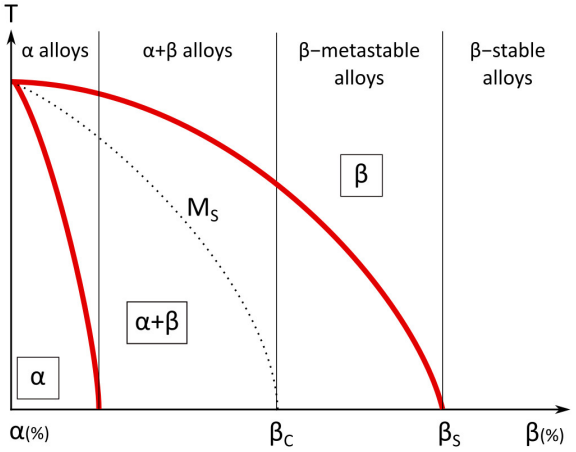

Figure 2.10: Schematic pseudo-binary phase diagram (adapted from (Leyens and Peters, 2003) and (Bania, 1994)).

α alloys Commercially pure and titanium alloys with very low $\beta-$stabilizer content $(2-5\,\%)$ are contained in this category. The β content is added to control the size of α grains and to improve the hydrogen tolerance (Lütjering and Williams, 2003). The CP-Ti alloys exhibit relatively low levels of strength (between 240 MPa and 740 MPa) which can be significantly improved by the addition of O. The commercially pure titanium alloys

Alloy	**Composition**	T_β(°C)	**E** (MPa)	**YS** (MPa)	**UTS** (MPa)	%**EI**
$\alpha-$alloys						
Grade 4	CP-Ti: 0.5Fe–0.4O	950	100-120	480-655	>550	15
Near$-\alpha$ alloys						
Ti6242	Ti–6Al–2Sn–4Zr–2Mo–0.1Si	995	114	990	1010	13
IMI834	Ti–5.8Al–4Sn–3.5Zr–0.5Mo–0.7Nb–0.35Si–0.06C	1045	120	910	1030	6-12
α/β alloys						
Ti64	Ti–6Al–4V	995	110-140	800-110	900-1200	13-16
Ti6246	Ti–6Al–2Sn–4Zr–6Mo	940	114	1000-1100	1100-1200	13-16
$\beta-$metastable alloys						
Ti17	Ti–5Al–2Sn–2Zr–2Mo–4Cr	890	112	1050	1100-1250	8-15
Ti5553(*)	Ti–5Al–5Mo–5V–3Cr	845	110	960-1100	1240	-

Table 2.1: Mechanical properties of various titanium alloys of different titanium categories (Leyens and Peters, 2003). (*Source: Clément et al. (2010))

	α	$\alpha+\beta$	β
Density	+	+	-
Strength	-	+	++
Ductility	-/+	+	+/-
Fracture toughness	+	-/+	+/-
Creep strength	+	+/-	-
Corrosion behaviour	++	+	+/-
Oxidation behaviour	++	+/-	-
Weldability	++	+/-	-
Cold formability	–	-	-/+

Table 2.2: Properties of α, $\alpha+\beta$ and β Ti alloys (Leyens and Peters, 2003).

are not heat treatable, hence they exhibit good weldability. These alloys are often used in applications that require high ductility and relatively high strength Davis et al. (1997).

Near$-\alpha$ alloys These alloys are preferentially used in high-temperature (up to 550 °C) applications due to its excellent creep behaviour and high strength (Leyens and Peters, 2003). The most used $\alpha-$stabilizer is Al since not only are the Young's modulus, tensile and creep strengths increased but also the density of the resulting alloy is reduced (Jaffee, 1958). At room temperature, these alloys contain both the α and β phases. Molybdenum is the primary beta stabilizer and it substantially increases the heat treatment response of the alloys (Froes et al., 1978). Silicon increases strength at all temperatures hence it improves the creep resistance of these alloys (Eylon et al., 1984). Given their strength in high-temperatures, these alloys are used in rotating components such as the hotter stages of compressors. For instance the blades of compressors in aero-engines are often made of Ti–5.8Al–4Sn–3.5Zr–0.5Mo–0.7Nb–0.35Si–0.06C (IMI834) and Ti–6Al–2Sn–4Zr–2Mo–0.1Si (Ti6242). As an interesting highlight, they significantly reduce weight compared to other alloys used in these applications (Postans and Jeal, 1981).

α/β alloys These alloys contain both α and β phases depending on the added content of each stabilizer and show high strength as moderate temperatures (Meetham, 1981). In comparison to near$-\alpha$ alloys, more β phase is retained at room temperature. Significant strengthening can achieved by solution treatment and ageing, being final quenching the most important instance of the heat treatment for fulfilling the β retention. Hardenability increases as the content of beta stabilizers increases (Donachie, 2000). Ti–6Al–4V (Ti64) and Ti–6Al–2Sn–4Zr–6Mo (Ti6246) are examples of these alloys. The most broadcast used alloy is Ti64 and will be further discussed in Section 2.1.2.

$\beta-$metastable alloys These alloys are rich in $\beta-$stabilizers and are said to be metastable because despite it is capable of retaining 100% of the β phase after quenching, they are susceptible of precipitating a secondary phase which is usually but not only α (Bania, 1994). These alloys are known for their hardenability on air cooling or water quenching (Donachie, 2000). The bcc β phase present in these alloys give them excellent forgeability properties. Ti–5Al–2Sn–2Zr–4Cr–4Mo (Ti17) and Ti–5Al–5Mo–5V–3Cr (Ti5553) are examples of these alloys and are often chosen for high strength applications.

Typical Titanium alloys microstructures

Depending of the thermo-mechanical history of a given titanium alloy, several microstructures can be obtained that lead to different mechanical properties.

Studied titanium alloys

Ti17 Ti$-$5Al$-$2Sn$-$2Zr$-$4Cr$-$4Mo, also known as Ti17, is $\beta-$metastable titanium alloy known for its deep hardenability and fatigue crack growth rates (Lütjering and Williams, 2003; Banerjee and Mukhopadhyay, 2010). Ti17 is used for gas turbine engine components and other applications demanding high tensile strength and good fracture toughness. It was invented in 1973 by General Electric for its utilization in fans and compressor discs (Meetham, 1981; Welsch et al., 1993). The most common microstructures are lamellar and bimodal which

respectively result of forging in the β and $\alpha + \beta$ fields (see Figs.2.11a and 2.11b) (Welsch et al., 1993). Its microstructure features large β grains namely 500 µm diameter containing different kinds of α precipitates: grain boundary α (α_{GB}), Widmanstätten lath colonies growing from the grain boundary (α_{WGB}) and two kinds of intergranular Widmanstätten laths (primary α^{p}_{WI} and secondary α^{s}_{WI}) Ballat-Durand et al. (2018). The macroscopic mechanical behaviour of $\beta-$metastable alloys is dependent on these microstructural features.

Under monotonic loading, ductility increases with increasing β grain size (Lütjering and Williams, 2003; Banerjee and Mukhopadhyay, 2010). The α precipitates are key in the strength of $\beta-$metastable alloys. Increasing volumetric fraction of intergranular α_{WI} increases strength (Aeby-Gautier et al., 2011). Increasing mean width of the α precipitates decreases tensile strength (Aeby-Gautier et al., 2013; Zhang et al., 2018), increases strain to failure and provokes intergranular fracture (Ivasishin et al., 2005). $\beta-$metastable alloys are known for their high specific strength, low elastic modulus, excellent fatigue/crack-propagation behaviour and excellent corrosion resistance (Boyer, 1996; Bania, 1994). Nonetheless, their application have found some limitations because of their high formulations and machining costs, complex processing (Eylon et al., 1994), low production volumes, and property scatter (Cotton et al., 2015). $\beta-$metastable alloys are often but not only used in structural applications such as the airframes (Banerjee and Williams, 2013). For instance, in 1973, General Electric patented the invention of Ti−5Al−2Sn−2Zr−4Cr−4Mo for its utilization in fans and compressor discs due to its deep hardenability, fracture toughness and fatigue crack growth rates (Welsch et al., 1993; Meetham, 1981). This alloy has several denominations such as UNS R58650 for the American Unified Numbering System of alloys, TA5CD4 for the French denomination, TC17 for the Chinese standards and it is commonly known as Ti17.

Ti6242 Ti–6Al–2Sn–4Zr–4Mo is a near$-\alpha$ alloy and was first developed by Timet but Bomberger and Seagle (1974) developed Ti–6Al–2Sn–4Zr–4Mo–0.1Si since the addition of low contents Si substantially increases its creep strength. This alloy is often used for high temperature applications.

Ti64 Ti−6Al−4V, commonly known as Ti64, is said to be an α/β alloy containing 10 µm diameter α grains and $\alpha + \beta$ colonies with big macro-zones sharing crystallographic orientations to a extent of roughly 100 times the apparent grain size (Le Biavant et al., 2002; Echlin et al., 2016; Kasemer et al., 2017). Nevertheless, it can be found in several metallurgical states, as shown in Fig.2.13. This alloys is known for its creep resistance up to a temperature of about 400 °C (Boyer, 1996) at the expense of a low resistance to crack propagation during the stage I of the fatigue life (Le Biavant et al., 2002; Bantounas et al., 2007). Ti64 was patented by (Stanley, 1959) at the end of the 1950s and until the end of the last century, it accounted for about 50% of the titanium tonnage of the world and up to 80% of the aerospace industry applications (Welsch et al., 1993).

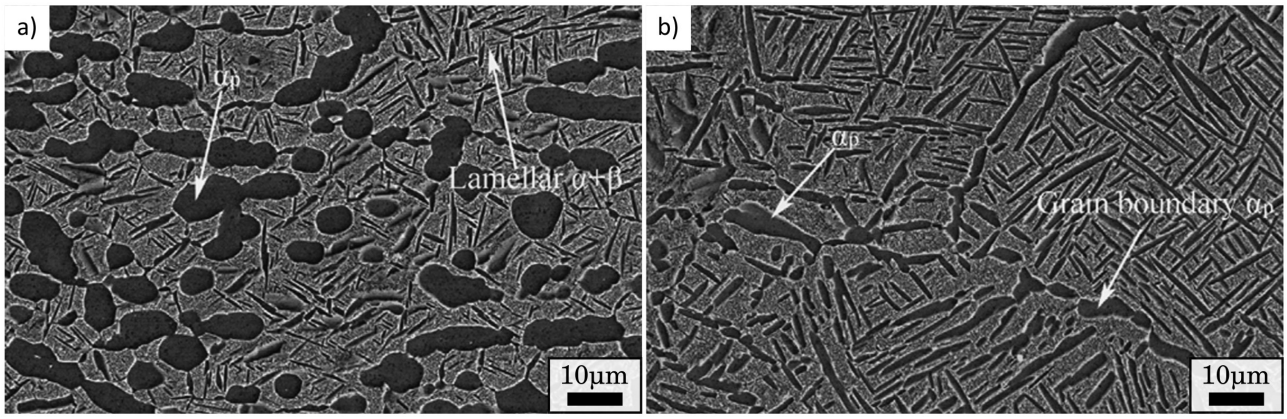

Figure 2.11: SEM observation of Ti17 with (a) lamellar and (b) bimodal microstructure. (Ji and Wu, 2014).

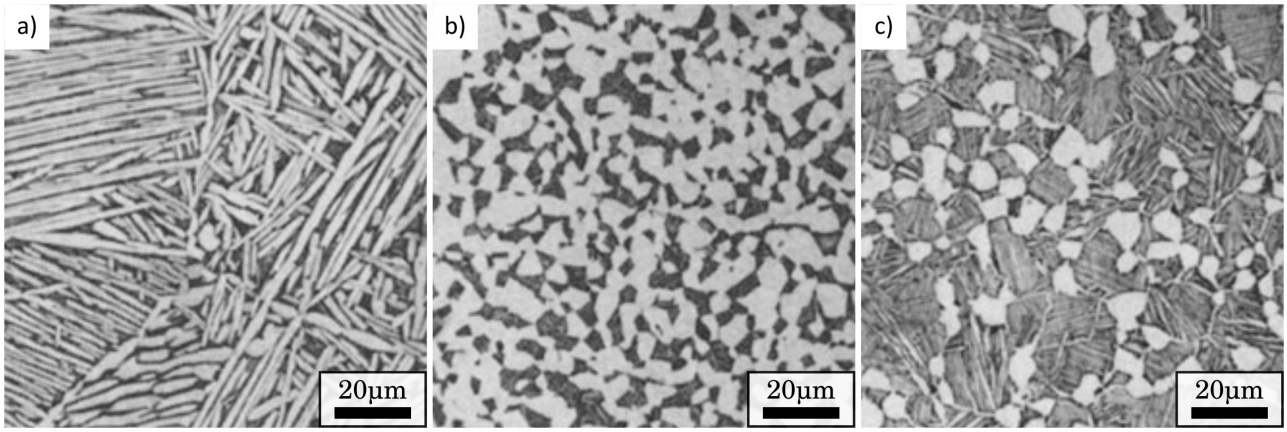

Figure 2.12: Microstructures of Ti6242 a) β solution treated (lenticular structure); b) $\alpha + \beta$ worked and $\alpha + \beta$ solution treated (primarily equiaxed α structure); and c) $\alpha + \beta$ worked and solution treated slightly below the β-transus temperature (low-volume fraction of equiaxed α in lenticular α matrix) (Eylon et al., 1984).

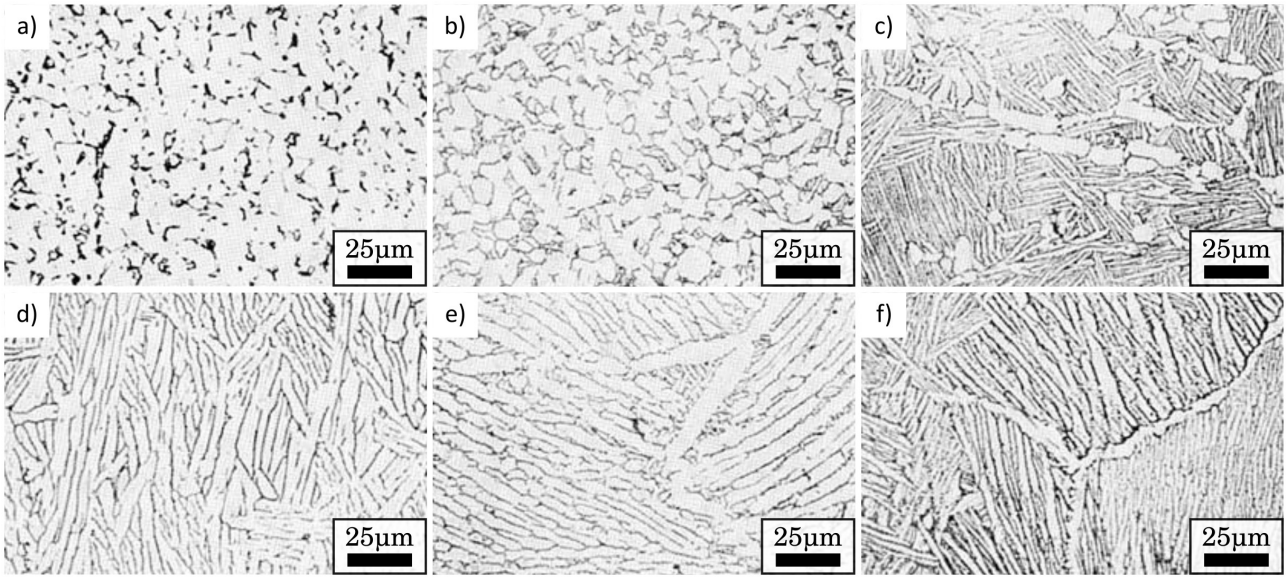

Figure 2.13: Microstructure of Ti64 in several conditions. a) Equiaxed α and a small amount of intergranular β. b) Equiaxed and acicular α and a small amount of inter-granular β. c) Equiaxed α in an acicular α (transformed β) matrix. d) Small amount of equiaxed α in an acicular α (transformed α) matrix. e) Plate-like acicular α (transformed β); α at prior β grain boundaries. f) Blocky and plate-like acicular α (transformed β); α at prior β grain boundaries. (Donachie, 2000)

2.2 Linear Friction Welding

2.2.1 Solid state welding processes

The verb to weld finds its etymology in the Old English word *weallan* and it means "to bubble" or "to boil", which are actions only observed in materials at liquid state. One might say that the concept of welding intrinsically implies melting. Indeed, the most well-known welding processes involve the junction of two pieces by a molten bridge. One of the first patents ever registered in the history of welding was the technique nowadays known as carbon arc-welding invented by de Benardos and Olszewski (1887). This technique consists in the formation of a voltaic arc between the metals to be operated and a conductor that leads to the local heating, softening and melting of the operated metals that bond during the solidification of the molten pool during cooling. Furthermore, some authors define the welding process explicitly using the concepts of melting and fusion (Ghosh et al., 2015).

According to The American Welding Society (1985), welding can be defined as following :

> *"a localized coalescence of metals or non-metals produced either by heating the materials to the required welding temperatures, with or without the application of pressure, or by the application of pressure alone, and with or without the use of filler materials"*

Several observations can be drawn from this definition. First, this definition involves the concept of coalescence. The etymology of the verb to coalesce unites the prefix *co–* ("together") and the Latin verb *alescere*, meaning to grow. Thus, in some sense, the materials to be welded become one. Second, welding extends to all kind of materials metallic or not. Indeed, nowadays a vast number of reports in scientific literature have registered welded joints made of different kinds of materials such as wood (Gfeller et al., 2003), ceramics (ichi Matsuoka, 1998), elastomers (Hollande et al., 1998), plastic and composites (Stokes, 1989). Third, welding is fulfilled by a combination of pressure and temperature which may or may not be provided by external agents. Fourth, welding does not necessarily imply the addition of filler material. Last but not least, the most interesting observation about this definition is that, despite its etymology, welding does not necessarily imply melting.

Solid state welding refers to a set of welding processes in which a melting-free bond between two materials is created. In friction welding processes, this is fulfilled by favouring the intimate contact between two materials through heat and significant plastic deformation during friction, and the application of an external pressure. The basic principle is to bring the joining surfaces close within interatomic distances to enhance the creation of a large number of interaction forces between atoms. If time was not an object bonding could occur only by proximity but this can be drastically accelerated by the application of heat. The transformation of mechanical energy into thermal energy due to friction was historically seen as an undesirable phenomenon. Conversely, in friction welding processes, the relative motion between the surfaces to be welded that can be rotary of linear rapidly produces friction heat drastically accelerate the joining process (Vill, 1962).

Friction welding processes exhibit several advantages:

- *Short welding times:* given that joining is often performed in a few seconds, high levels of productivity can be reached.
- *Absence of filler material:* unlike other types of welding, no material is added and as consequence, lighter

structures can be built. Furthermore, shielding gas is not required.

- *Efficiency:* The mechanical energy driving the motion of the workpieces to be welded is transformed into thermal energy directly in the surfaces to be welded, unlike other welding processes such as arc welding.
- *Optimizing milling operations:* workpieces with complex geometries are often produced by milling the bulk, this can lead to significant and expensive material loss.
- *Mechanical properties of the welded joint:* In some cases, the microstructures created in these processes exhibit better mechanical properties than the parent material.
- *Defects and microstructure:* Fusion welding processes are known for developing defects such as cast voids. Friction welding processes instead are less susceptible of showing this defects subject to proper welding parameters. Given that the melting temperature is not overreached, no poor recrystallized microstructures at equilibrium leading to macro segregations which are very detrimental for the mechanical properties.
- *Repeatability:* if suitable welding parameters are provided in an maintained manner, the process is very repeatable.
- *Dissimilar welds:* friction welded joints with different material can be created. Although, some metals combination seem still impossible.
- *Hygiene of the process:* Unlike other welding processes, no harmful gas emissions, ultra violets radiation or material spatter are produced.
- *Low surface preparation:* Compared to other processes, almost no surface preparation is required.
- *Self-cleaning:* For optimized welding parameters, most of the friction welding processes are known to be *self-cleaning*. This means that contaminants at the weld interface are extruded outside the weld into the so called flash.

Some of the disadvantages of friction welding processes are:

- *Geometrical constrains:* Each type of friction welding present some geometrical constrains that are discussed in Section 2.2.1.
- *Lack of standard:* Some of the friction welding processes are relatively new and standard is not still available. Some of the issues encountered to this matter are: standard geometries of the pieces to be welded, instrumentation such as piece-holder and surface preparation.
- *Size limitations:* Some of the friction welding processes can only perform welds within a certain maximum size threshold that, for the moment, do not seem scalable.
- *Cost:* the welding machine apparatus are too expensive and their acquisition remain interesting in high performance engineering application such as the aero-space industry.

These advantages and disadvantages are highly desirable for engineering applications and will be further discussed later in Section 2.2.1.

Types of Friction Welding

This Section introduces some of the most well-known friction welding processes are described. The main objective is to lay out the different friction processes, their characteristics, advantages and disadvantages. Special interest is drawn in Linear Friction Welding. Fig.2.14 schematically shows each process. Red arrows show rotations, blue allows show displacements and grey dashed point lines show rotation axis of symmetry.

Rotary Friction Welding (RFW) This is the first to be produced and most broadly used friction process. RFW consists in axially welding two axisymmetric workpieces. The first workpiece is called the fixed workpiece since it is clamped. The second workpiece describes an rotation movement around its main axis and is called the rotary workpiece. The rotary workpiece is axially pushed against the fixed workpiece with a so called friction pressure. After rotation, a final pressure so called forging pressure is applied. Two variants of this friction process exist, they differ in the energy input method, and they will be explained hereafter.

In the late nineteenth century, two patents were registered in USA proposing this technique for tubes (Bevington, 1891b), and for rods and cables (Bevington, 1891a). In the mid twentieth century, Vill (1962) claimed that this process did not find its way in industrial applications because the process received negative

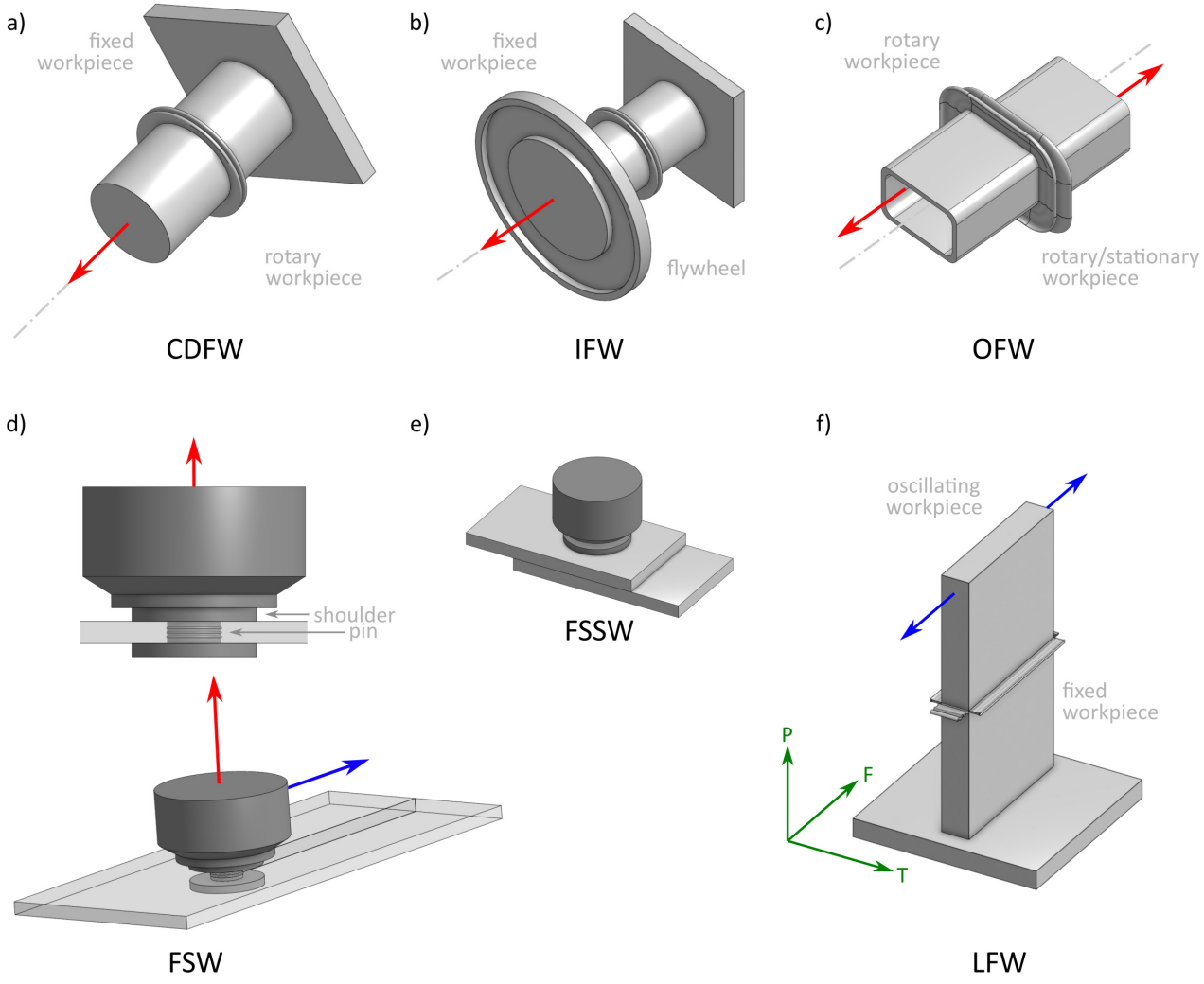

Figure 2.14

evaluations supported by scientists. The modifications proposed by Chudikov (1956) revealed better results that later were confirmed by Vill (1962). It was at that time that the process divulged into two variants each showing different energy input methods being one produced in the former USSR and the other in USA, which respectively are: Continuous Drive Friction Welding and Inertia Friction Welding.

Continuous Drive Friction Welding (CDFW) The rotation imposed to the rotary workpiece is provided by a motor and it is constant until achieving a target axial shortening (see Fig.2.14a). Once this is achieved, the rotation is stopped and the forging pressure is applied. The main feature of this process is that the energy utilised for welding is provided by a motor in a continuous matter (Chudikov, 1956). A schematic representation of the displacement, applied pressure and rotation speed is shown in Fig.2.15.

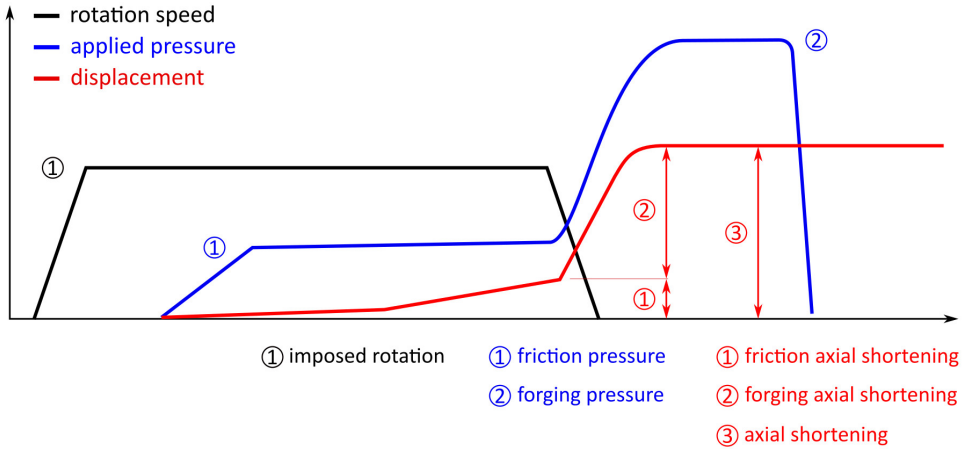

Figure 2.15: Typical sequences of CDFW.

Inertia Friction Welding (IFW) In this process, the rotary workpiece is attached to a flywheel (see Fig.2.14b) that is engaged to a motor. The flywheel is angularly accelerated up to a given angular velocity and disengaged from the motor. Thereafter, the rotating flywheel is pushed against the fixed workpiece until rotation is completely stopped by friction. Once the flywheel is stopped, the forging pressure is applied. This process was invented by Oberle et al. (1966). The main difference with CDFW is that the energy utilised for welding is provided by the kinetic energy of a flywheel.

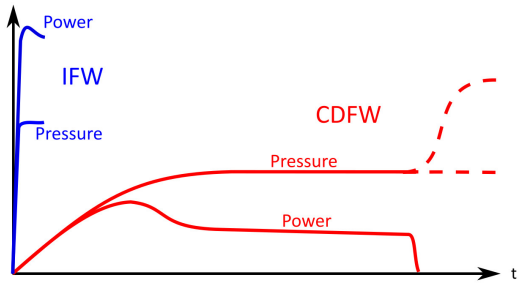

Figure 2.16: Time *vs.* Pressure and power for CDFW (blue) and IFW (blue) (Oberle et al., 1966)

Oberle et al. (1966) explained that the power required to perform a weld was not a concern for IFW since the flywheel should always be able to deliver it, unlike CDFW, in which power is limited by the power of the motor. Furthermore, the authors showed that the power and pressure over time required for performing a IFW join were lower that that required for performing CDFW.

Some of the applications of both CDFW and in IFW are vehicle axles and sub-axles made of carbon steel, suspension rods, steering columns, gear box forks and drive-shafts, as well as dissimilar engine valves Özdemir (2005). The process is very effective for performing butt-to-butt welds but it exhibits two important

disadvantages due to its circular nature. First, the heat generation is not homogeneous and second, the rotary workpiece must be axisymmetric.

Orbital Friction Welding (OFW) This process has three particularities. The first is that the weld can be performed by rotating one or both workpieces; the second particularity is that the workpieces rotate around an axis parallel yet non co-linear to their main axes; and third, the cross-section of the workpieces not necessarily must be circular. In Fig.2.14c, the workpieces exhibit a rectangular cross-section. The axis of the workpieces (grey dashed lines) are not co-linear with the angular velocities (red arrows). As a consequence of the orbital movement, the tangential velocity the weld interface is uniform. In theory, OFW produces uniform frictional heat at the interface as the velocity is uniform, which is not the case with RFW (Kallee et al., 2003). This process is particularly interesting for workpieces with not axisymmetric cross-sections yet it is not largely used. The limitation of CDFW, IFW, LFW and OFW is that the weld is confined to a very small area.

Friction Stir Welding (FSW) A rotating device formed by a pin and a shoulder is used as a non-consumable tool to be inserted between two sheets to be butt joined along the long or traverse directions. The angular velocity and displacement of the rotating tool are respectively shown by the red and blue arrows in Fig.2.14d. The friction generated by the tool heats and provokes a circular displacement of material around it. The shoulders serves as a containment of the hot material. The combined motion of rotation and displacement of the tool provokes an asymmetry of deformation in each plaque. Consequently, depending of the rotation of the tool, each side of the pin with respect to its displacement is often called the retreating or advancing side. FSW was invented by Thomas et al. (1995) at TWI in the United Kingdom. One of its advantages is that, technically, there is no limitation about the length of the welded joint and that various weld geometries can be produced.

Friction Stir Spot Welding (FSSW) This process is an upgrade of FSW and it is used to produced punctual joining in overlap configurations (see Fig.2.14e). The effect is localized in a single punctual weld so called spot. The non-consumable tool spins around an axis perpendicular to the sheets to be welded and is pushed against them. The material is softened by friction as the pin is plunged and the rotation stirs the material producing a spot weld. The most interesting aspect of FSSW is that rivets and other junctions can be replaced by hole-free FSSW joints with significant weight savings. This process was first invented by Iwashita (2003) for the Japanese company Mazda Motor Corporation.

Linear Friction Welding (LFW) The first patent that suggested this technique belongs to Ritcher (1929) but according to Bhamji et al. (2012), the description of the process was vague. At the mid twentieth century, Vill (1962) qualified this process as very doubtful. Later, a first patent proposing a machine capable of performing the linear reciprocation was produced by Maurya and Kauzlarich (1969) at Caterpillar Tractor Company. Later on, some other patents registered different aspects of LFW such as instrumentation and welding methods (Trask et al., 1998; Slattery, 2007). Although, according to Bhamji et al. (2012), no patent protecting the fundamentals of LFW were found. The first LFW machine for metals was produced at TWI in 1990 (see Fig.2.17). The uniaxial oscillation motion in LFW was an evolution of the orbital motion in OFW (Kallee et al., 2003).

Figure 2.17: TWI's electro-mechanically actuated linear friction welding machine (Kallee et al., 2003).

In this process, friction occurs due to the linear oscillating displacement of a so called oscillating workpiece against a fixed workpiece so called fixed workpiece (see Fig.2.18f). LFW is performed under force control and it occurs in 4 stages that are schematically shown in Fig.2.18f and it go as follows:

- *Conditioning Phase:* The two workpieces are put in contact and the oscillating workpiece begins to oscillate with an f frequency and an amplitude a.
- *Friction Phase:* A so called friction pressure $\mathrm{P_{fr}}$ is applied to generate heat at the weld interface. Vairis and Frost (1999) decomposed the friction phase in sub-phases:
  - *Initial Phase:* As the number of oscillations increases, the contact between the surfaces to be welded increases to 100 % true contact by reducing the asperities in the surfaces by a mechanism of wear.
  - *Transition Phase:* The increasing temperature at the weld interface softens the material at the weld interface and its vicinity and thus, the material is plastically deformed.
  - *Equilibrium Phase:* The oscillations of the oscillating workpiece and the forging pressure enhance the extrusion of plastically deformed material at the weld interface into the so called flash. Thus axial shortening begins to occur.
  - *Deceleration Phase:* The motion of the oscillating workpiece is gradually stopped to achieve a proper alignment of the workpieces.
- *Forging phase:* An additional increase in pressure so called friction pressure is sometimes applied to help consolidate the weld and achieving the target axial shortening Δh.
- *Release phase:* Both workpieces are removed from the welding machine.

In LFW, friction occurs parallel to the F axis, the friction and forging pressure are applied parallel to the P axis. The third direction corresponds to the thickness of the linear friction welded joint (see Fig.2.14g). Vairis and Frost (2000) proposed the specific energy input w delivered to the material that is measured in units of $\mathrm{kW/mm^4}$ and follows the expression of Eq.2.3:

$$w = \frac{a\, f\, \mathrm{P_{fr}}}{2\pi\, \mathrm{A}} \tag{2.3}$$

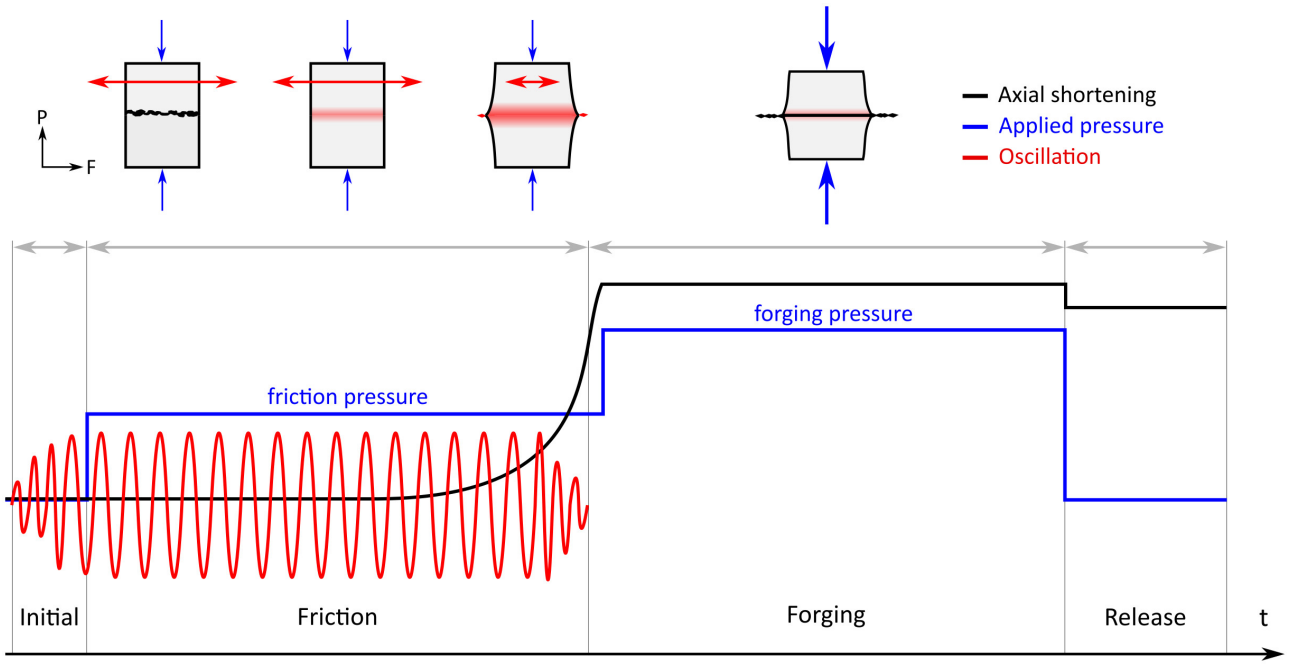

Figure 2.18: Phases in LFW (adapted from (Bhamji et al., 2012) and (Vairis and Frost, 1999)).

Where a stands for the oscillations amplitude in millimetres, f stands for oscillation frequency in Hz, P_{fr} stands for friction pressure in MPa and A stands for the cross-sectional surface to be welded in mm.

As most of the friction welding processes, linear friction welding is known to be self-cleaning since parent material and contaminants in the weld interface are extruded to form the so called flash. The high levels of plastic deformation and localized heat generated around the weld interface provoke microstructural changes, unknown mechanical properties and considerable levels of residual stresses that are comprised in four distinct welding zones (Vairis and Frost, 1998): the weld centre zone (WCZ), the thermo-mechanically affected zone (TMAZ), the heat affected zone (HAZ) and the parent material (PM). LFW exhibits some advantages such as very short welding times, typically in the order of some seconds and the reduction of bulk milling operations. Conversely, LFW requires some important investment and in some cases, compared to the PM, the weld can have inferior mechanical properties.

Applications of LFW

One of the most well known applications of LFW is the fabrication of the so called “Blisks” García (2011). This consist in replacing the mechanical fixings of blades in aero-engine compressors disks para LFWed blades, as shown in Fig.2.19a. The acronym “Blisk” is a composition of the words “blade” and “disk”, and it has been used in the three stages of the compressor of the Eurofighter’s EJ200 engine (MTU, 2001). Some of the advantages of this technology is the weight savings that is reports compared to other techniques that can reach up 30 % (Turner et al., 2011; MTU, 2001). Due to the moderate temperature undergone on the compressor, Blisks are often made of Ti64 or Ti6242 due to their resistance to low cycle fatigue and crack García (2011); MTU (2001); Turner et al. (2011). In aero-engines compressor, the disks are supposed to exhibit high tensile strength and high fatigue resistance and thus, they are often made of Ti17 of Ti6246.

Another application of LFW is the optimization of milling operations for the machining of complex work-

pieces. Instead of machining these workpiece from the bulk, some preform can be created using LFW that will optimize de milling operations. For instance, another aerospace applications is the production of titanium beams for rails with wings in their sides that are used for passenger seat attachment. The complex design of beams are extruded and the wings in their sides are obtained by very expensive machining in terms of material waste (see Fig.2.20a). The creation of simpler profiles followed by the addition of LFWed wings leads to important saving of material by preventing excessive milling (see Fig.2.20b) (Delfosse, 2012).

In aero-engines for instance, compressors are required to have disks with high resistance in both tensile strength and low cycle fatigue and blades with good resistance to high cycle fatigue and creep. The beams with LFWed wings can work under strong monotonic and cyclic loadings. The mechanical characterization of LFW joints in terms of monotonic, cyclic and fracture behaviour and its relationship with the underlying microstructure is highly required. Yet, few studies have been reported.

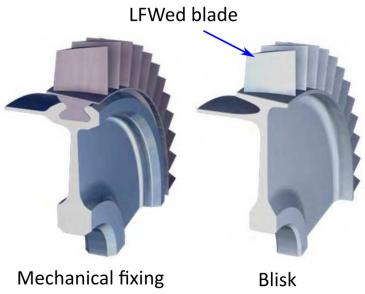

Figure 2.19: Illustration of the mechanical fixing of blade into a disks and the Blisks (Gar-

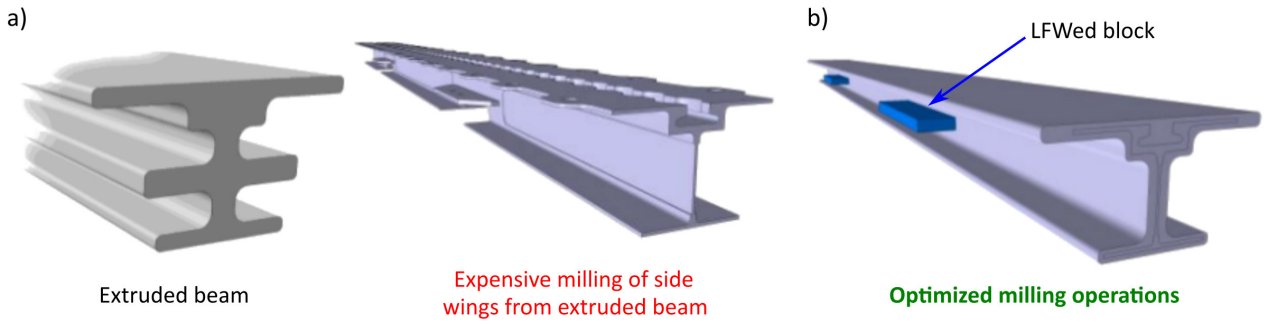

Figure 2.20: a) Machining of beams for aerospace applications by expensive milling operations and b) addition of LFWed wings to simpler extruded beams for optimizing milling operations (Delfosse, 2012).

2.3 Characterization of Ti LFW joints

In this Section, a literature review concerning the microstructural and mechanical characterization of similar and dissimilar LFW joints made of near$-\alpha$, $\beta-$metastable, and α/β titanium alloys is presented. Some work concerning other welding techniques and some other titanium alloys are also reviewed. The aim of this Section is twofold. First, to review the mechanical properties in terms of monotonic and cyclic loading for similar LFW joints made of the studied titanium alloys or comparable alloys. Second, to establish the state of the art in terms of friction welding characterizations.

2.3.1 Microstructural and defects characterization

Temperature evolution during LFW

During LFW joining, temperature at the weld interface can reach temperatures higher than the $\beta-$transus temperature. Researchers often instrument welding joints with thermocouples and register the temperature evolution over time in the vicinity of the weld interface. For instance, Ballat-Durand et al. (2019) carried out the microstructural characterization of the similar Ti6242 LFW joints studied in Chapters 4 and 5 and to do so, the authors instrumented the blocks to be welded with a system of thermocouples as shown in Fig.2.21b. The distance between the surface to be welded and the closest thermocouples was not specified. The thickness of the blocks was 15 mm (parallel to the T axis). The temperature evolution over time recorded during joining are shown in Fig.2.21a for the oscillating and fixed workpieces. In Figs.2.21c and 2.21d, similar measurements

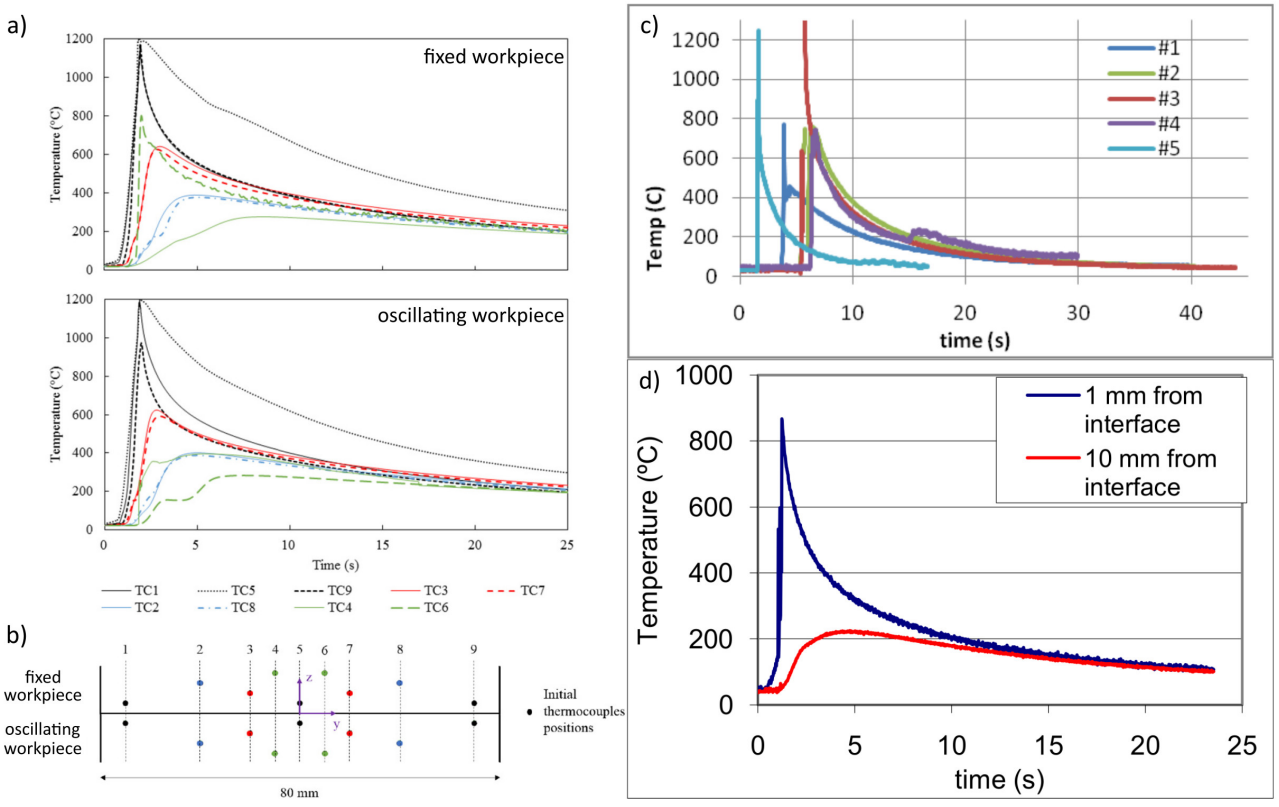

Figure 2.21: Thermal analysis during joining of a) a similar Ti6242 LFW joint (Ballat-Durand et al., 2019), b) a similar IMI–834 LFW joint (Dalgaard, 2011) and d) a similar Ti64 (Dalgaard, 2011) LFW joint. d) Schematic disposition of the system of thermocouples used for the thermal recording during welding used by Ballat-Durand et al. (2019).

are shown for the similar IMI-834 LFW joint and the similar Ti64 LFW joint studied by Dalgaard (2011). The distance between the surface to be welded and the closest thermocouples was 1 mm. The thickness of the blocks was 13 mm (parallel to the T axis). The geometries of the blocks to be welded, the thermal conductivity coefficient of the parent material and the welding parameters are not the same. Thus, only a qualitative comparison can be performed.

Temperature very rapidly reaches about ∼1200 °C for both the Ti6242 and the similar IMI–834 LFW joints, having each $\beta-$transus temperature of respectively $T_\beta = 990\,°C$ and $T_\beta = 1045\,°C$ (Ballat-Durand et al., 2019; Dalgaard et al., 2012a). For the similar Ti64 LFW joint, the peak temperature was about 850 °C. The cooling rates are quite different which can be explained by the aforementioned differences between the three configurations. Nonetheless, it is interesting to note that the order of magnitude of the cooling times is around some tenths of seconds. This suggests that the surrounding air leads to substantial cooling rates. A rough estimation of the cooling rate can be performed for the thermocouple #3 in Fig.2.21b that cooled from ∼1250 °C to 0 °C in about ∼37 s. The resulting mean cooling rate is about $\sim 33\,°C\,s^{-1}$, which is much bigger that the instantaneous cooling rate. As stated in Section 2.1.2, this cooling rate can lead to the formation of metastable phases such as martensitic microstructures.

Microstructural characterization

The microstructural characterization of similar Ti6242 and similar Ti17 LFW joints are described here. Most of the characterizations belong to the work-package 1 of the the ANR OPTIMUM Project in which this PhD Thesis is a part. These welds are further studied in following Chapters.

Similar Ti6242 LFW joints Fig.2.22a shows an polarized-light optical microscope observation with an overlaid microhardness profile for a similar Ti6242 LFW joint (Ballat-Durand et al., 2019). A higher magnification polarized-light optical microscope observation after etching is also shown. Using a microhardness profile combined with a polarized optical observation, Ballat-Durand et al. (2018) define the weld zones. The affected zone is highlighted by the increased microhardness which extends to a distance of about 4 mm. Etching revealed a vertical band of about 2 mm. The regions in which the microhardness is increased but that were not affected by etching are denominated as the Heat Affected Zone (HAZ). A polarized optical observation of the affected zone is shown in Fig.2.22b. The microstructure is similar to the Ti6242 PM at the vertical edges of the observation but it becomes increasingly deformed with the decreasing distance to the vertical band of Fig.2.22b. This contrast allowed the far thermo-mechanically affected zone (FTMAZ), near thermo-mechanically affected zone (NTMAZ) and WCZ to be defined. In the PhD thesis of Ballat-Durand et al. (2019), special attention is drawn the NTMAZ of the similar Ti17 LFW joint, which in the present document is referred as the TMAZ.

Fig.2.23 shows EBSD mappings at different magnification across the WCZ of the similar Ti6242 LFW joint. The objective of these EBSD mappings was to further study the microstructure developed in the affected zone and to study the formation of texture due to LFW. This texture was also documented in the WCZ of the similar IMI834 LFW joint studied by Dalgaard et al. (2012a).

Fig.2.23a shows the $\{0\,0\,0\,1\}$ crystal lattice orientation mapping on a PT plane. The authors claimed that the observed texture component in the WCZ was $\{0\,0\,0\,1\}\langle 1\,1\,\bar{2}\,0\rangle$ having the $\{0\,0\,0\,1\}$ slightly misaligned with the PT plane and the $\langle 1\,1\,\bar{2}\,0\rangle$ direction parallel to the F axis. The EBSD mapping of the WCZ in Fig.2.23b

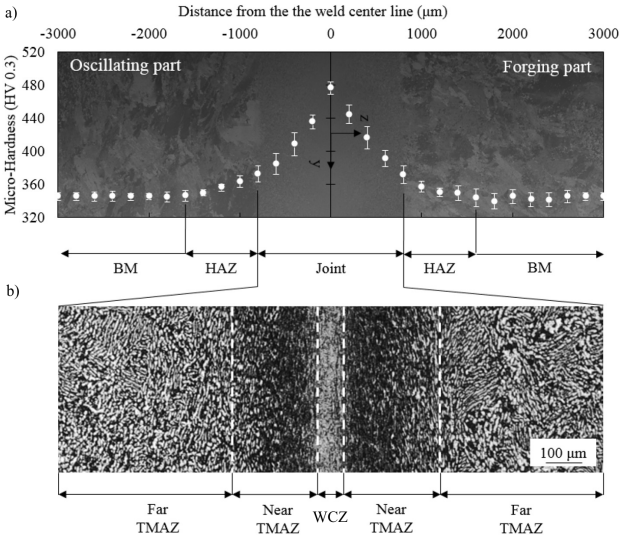

Figure 2.22: Combined data from optical observations with polarized-light and corresponding microhardness profile across the Ti6242 LFW joint detailing the characteristic macro-zones: the Welding Centre Zone (WCZ), the Thermo-mechanically Affected Zone (TMAZ) and the Heat Affected Zone (HAZ). The polarized-light showed the global microstructure refinement in the joint and etching revealed a further subdivision of the TMAZ into the far-TMAZ (FTMAZ) just deformed, the near-TMAZ (NTMAZ) heavily deformed and the WCZ fully transformed (Ballat-Durand et al., 2019).

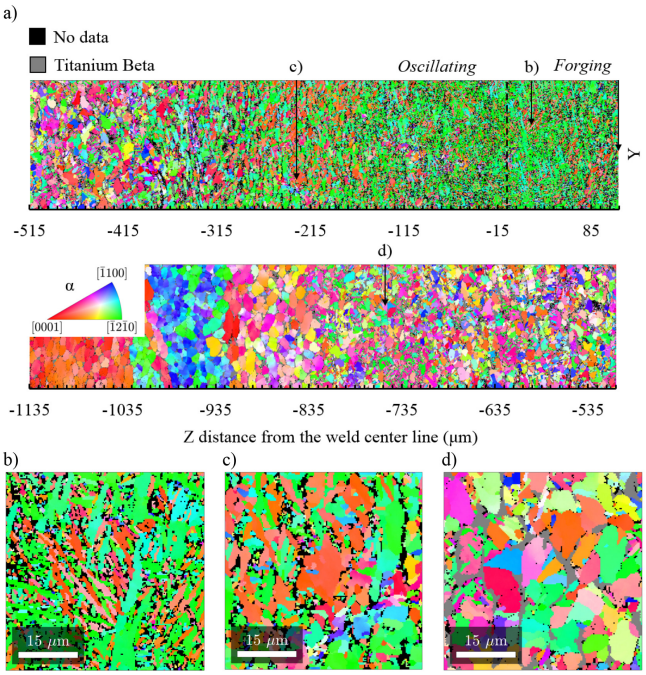

Figure 2.23: EBSD orientation map of the HCP phase within the WCZ of a similar Ti6242 LFW joint highlighting a) the microstructure refinement at the TMAZ/HAZ border (800 µm of the border in the F direction) and the change of microstructure in the joint from fragmented-like in the TMAZ to acicular in the WCZ. The arrows indicate the locations of the three magnifications, b) WCZ HCP entangled laths, c) NTMAZ deformed prior-nodular α and fine laths; d) FTMAZ showing fragmented-like coarse prior-nodular α within a β matrix (grey). The colours indicate the crystallographic directions of the HCP phase along the T direction. Grains formed by less than five measurement points were considered as not indexed. (step= 0.3 µm) (Ballat-Durand et al., 2019)

showed the formation of fine HCP entangled acicular α' microstructure without showing any traces of prior$-\beta$ grains. The microstructure of the FTMAZ displayed fine α precipitates and coarse α grains somewhat smaller than the α nodules observed in the PM embedded in a residual β matrix (see Fig.2.23d). The microstructure of the NTMAZ is seen in Fig.2.23 and it revealed a hybrid microstructure between the microstructures seen in the FTMAZ and WCZ.

α/β titanium alloys LFW joints Wanjara and Jahazi (2005) performed a parametric study on the effect of welding parameters on the microstructure and mechanical properties of similar Ti64 LFW joints. The authors observed Widmanstätten morphology at the WCZ.

Similar Ti17 LFW joints Fig.2.25 shows an observation across the affected zone by LFW with a microhardness profile of a similar Ti17 LFW joint. As for the aforementioned similar Ti6242 LFW joint, the heat affected zone (HAZ) is observed within the region in which, in the optical observation, does not seem to be

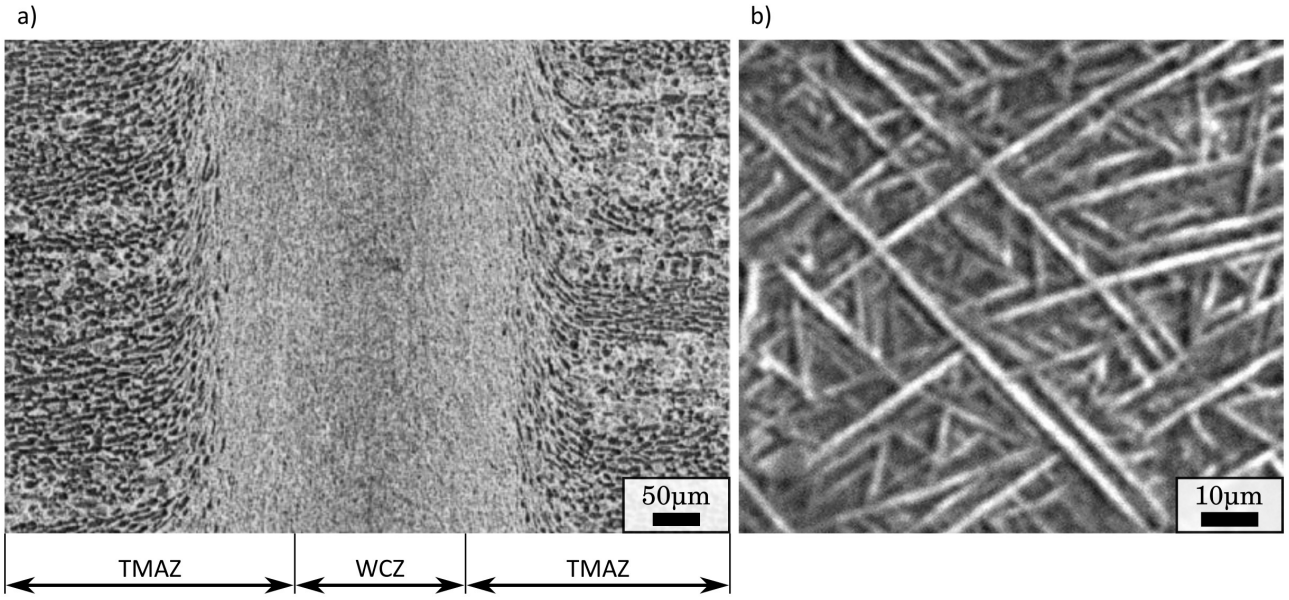

Figure 2.24: a) SEM/BSE observation of the WCZ and b) Widmanstätten morphology at the WCZ of a similar Ti64 LFW joint (Wanjara and Jahazi, 2005).

modified by LFW yet the microhardness is reduced. An optical contrast is observed containing a vertical line with features that are much smaller than PM β grains. This line allowed the WCZ to be identified. A well defined frontier can be observed between the WCZ and the TMAZ. Conversely, the frontier between the TMAZ and the HAZ is less easy identified. The extension of each TMAZ corresponds to the region in which the optical contrast gradient is observed. In Fig.2.26a, a high magnification observation of the WCZ is shown in which fine equiaxed α depleted distorted β grains are observed. Fig.2.26b shows an SEM/BSE observation of the TMAZ. It is interesting to note that features very similar to the $\alpha_{GB} + \alpha_{WGB}$ seen on the PM grains are observed.

Ballat-Durand et al. (2018) performed EBSD observations along the F direction in a region containing both the WCZ and TMAZ shown in Fig.2.27. Only the orientations of the bcc β phase were indexed. It is very interesting to note that, according to this observation and despite the presence of the features observed in Fig.2.26b, both the WCZ and TMAZ are purely β. This is consistent with the decreased microhardness measured in these locations.

Ballat-Durand et al. (2018) claimed that the features that convey the shape of the $\alpha_{GB} + \alpha_{WGB}$ phases in PM the microstructure exhibit a chemical contrast that corresponds to former $\alpha_{GB} + \alpha_{WGB}$ phases but given their β crystal lattice, they are denominated "traces of $\alpha_{GB} + \alpha_{WGB}$" or Ghost α phase. In the analyses of the elastic anisotropies of the Titanium α and β phases performed by Duval (2013), it has been shown that the softest orientation of the α phase exhibits the same Young's Modulus as the hardest orientation of the β phase, which means that β phase is much softer that the α phase (see Section 2.1.1).

Welding defects

Some authors claimed that LFW produces defect free joints (Guo et al., 2013; Ji et al., 2016b), yet some defects were observed in LFW joints made of Ti alloys (Ballat-Durand et al., 2019; Wanjara and Jahazi, 2005), as it can be seen in the SEM/BSE observations of Fig.2.28. For instance, in Fig.2.28a, the WCZ of a similar Ti6242 LFW joint that is constituted by an α' martensite microstructure, exhibits some spherical voids. These

voids seem to have a distribution of diameters that are in the order of hundreds of nm. Similarly, Wanjara and Jahazi (2005) observed some spherical voids in the WCZ of a similar Ti64 LFW joint that exhibited a diameter in the order of a few microns. Furthermore, Wanjara et al. (2014) observed an oxide layer at the centre of the WCZ that was also observed for a similar LFW joint made of Waspaloy Chamanfar et al. (2012a).

Wanjara and Jahazi (2005) observed that the oxides at the centre of the WCZ appear if a certain power input threshold was not overreached. Recently, McAndrew et al. (2015) carried out experiments and numerical simulations to understand better the self-cleaning mechanisms of LFW. They performed four welds with increasing axial shortening and investigated the weld interface for detecting unsuccessful contaminants removal. As it can be seen in Fig.2.29a, 2.29c and 2.29e, increasing the axial shortening favoured the extrusion of the

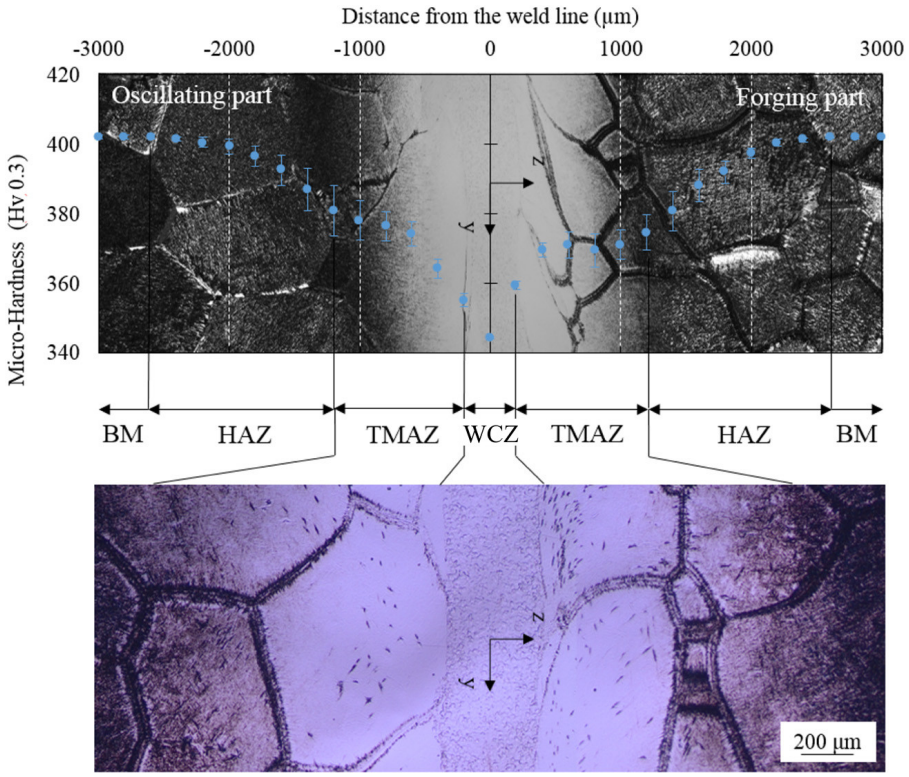

Figure 2.25: Combined presentation of the OM observations and the corresponding local hardness measurements across the Ti17 LFW joint detailing the characteristic macroscopic zones: the Welding Line (WCZ), the Thermo-Mechanically Affected Zone (TMAZ) and the Heat Affected Zone (HAZ) Ballat-Durand et al. (2018).

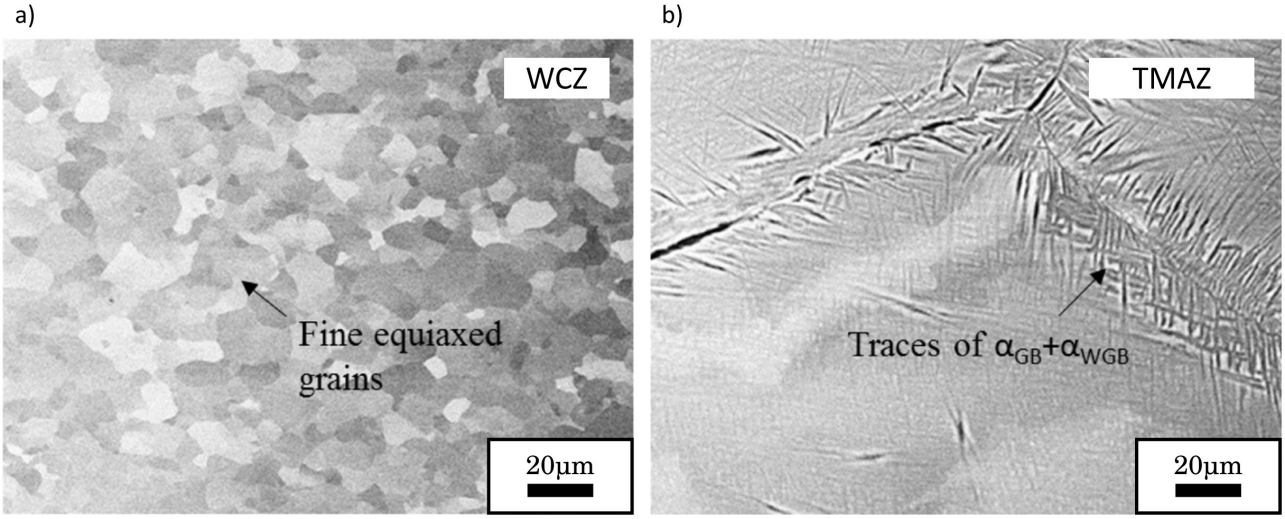

Figure 2.26: SEM/BSE observations of a similar Ti17 LFW joint showing a) fine equiaxed α depleted β grains at the WCZ and b) retained "Ghost" $\alpha_{GB} + \alpha_{WGB}$ and α^{p}_{WI} in the form of faded laths with a blur contrast with the matrix in the TMAZ. Ballat-Durand et al. (2019).

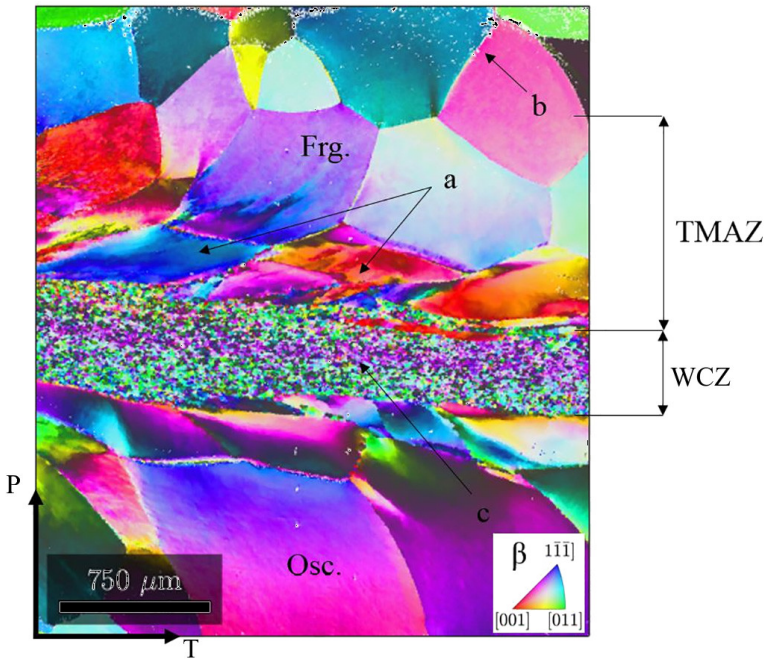

Figure 2.27: EBSD orientation map of the β phase (step= 1.7 µm) within the similar Ti17 LFW joint in the as welded state highlighting: a. the deformation endured by the PM prior$-\beta$ grains in the TMAZ; b. the position of the HCP α indexed points recovered at the very end of the TMAZ starting with the α_{GB} + α_{WGB} morphology then the α_{WI} laths; c. the grain refinement and the apparent texturation in the WCZ. The colour indicates the crystallographic directions of the β phase along the F axis.

contaminants at the weld interface. These observations were in agreement with the numerical simulations in Fig.2.29b, 2.29d and 2.29f. Yet, the mechanisms at the origin of these voids has not yet been explained.

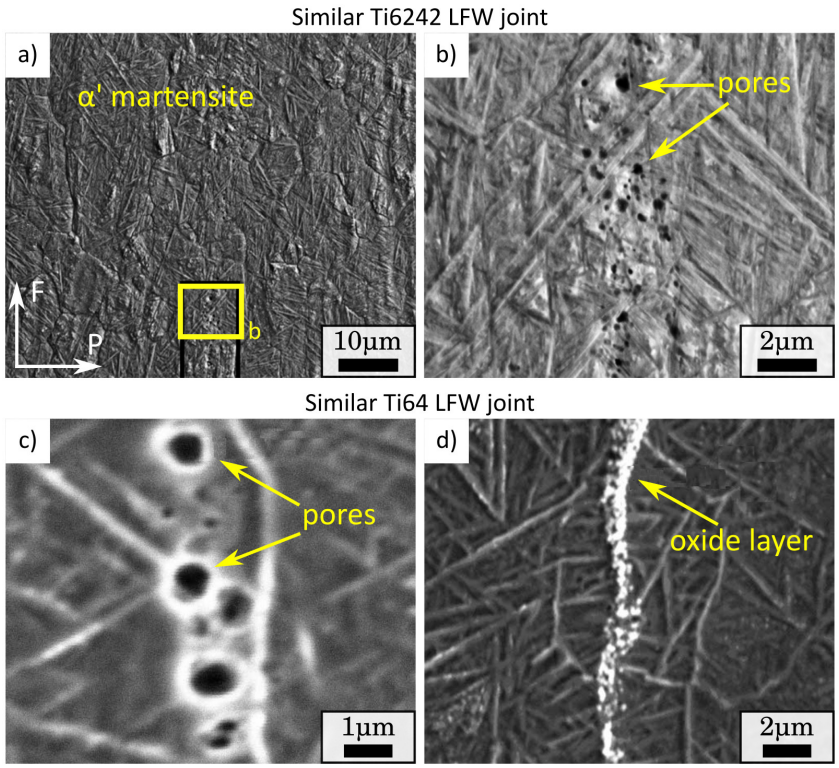

Figure 2.28: a) Acicular entangled α' martensite and b) pores in the WCZ of a similar Ti6242 LFW joint. c) Pores and d) oxide layer at the WCZ of similar Ti64 LFW joint (Wanjara and Jahazi, 2005).

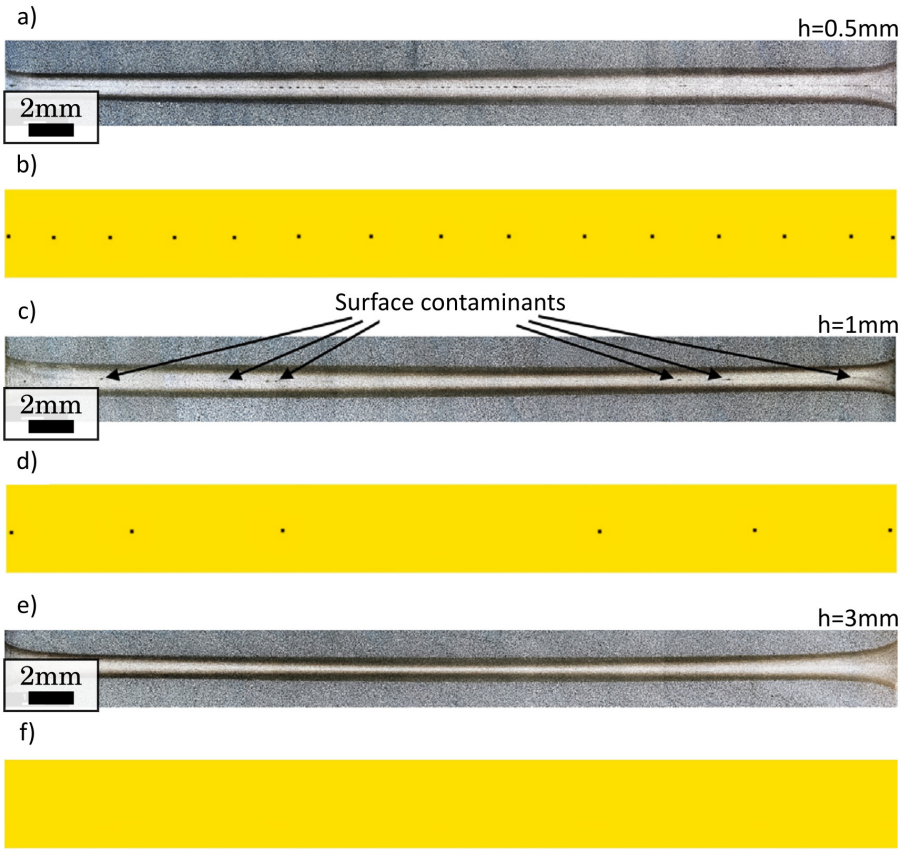

Figure 2.29: Numerical simulation of the self-cleaning mechanisms for a similar Ti64 LFW joints (McAndrew et al., 2015).

2.3.2 Residual stresses

In this Section, a brief review on the techniques for residual stresses measurement techniques and the measurements performed for the studied alloys is presented.

Measurement techniques

Residual stresses are measured using several techniques that can be classified in mechanical and diffraction techniques.

Diffraction techniques The interplanar atomic spacing along different directions is obtained by the scattering phenomena induced diffraction using Bragg's law. The residual stresses are computed by using the generalized Hooke's law, using the elastic constants of the studied alloy and the crystal lattice parameters in the undeformed state as a reference. This implies that a precise measurement of the undeformed state of the crystal lattice needs to be known. This is one of the main drawbacks of using this technique for cross-welded structures, given that sometimes metastable phases with unknown crystal lattice parameters can be produced (see Section 2.1.2).

- **X-ray radiation** Diffraction is given by the interaction between the crystal lattice of the studied alloy and a X-ray beam. The advantage of this technique is that a fairly high spatial resolution can be obtained with decreasing thickness of the X-ray beam and it is available in laboratory scale but in can also performed at synchrotron (Fitzpatrick and Lodini, 2003). The wavelength of X-rays is typically $0.1 < \lambda < 0.2\,\text{nm}$, which implies a low penetration. Subsequently, the measurement is performed only on the surface of the specimen (a few nanometres) (Withers and Bhadeshia, 2001).

- **Neutron radiation** Diffraction is given by the interaction between the crystal lattice of the studied alloy and a neutron beam. Given that the neutron's wavelength is at the atomic scale, lower absorption occurs compared to the X-ray diffraction. Often the studied depth is a few centimetres (Withers and Bhadeshia, 2001). The disadvantage is that the source of neutrons comes from a nuclear reaction which is often not available at the laboratory scale (Fitzpatrick and Lodini, 2003).

Mechanical techniques The residual stresses computations are obtained by the measurement of a relaxation displacement after material removal that is compared to a reference geometry. Despite these techniques are destructive and that they exhibit a low spatial resolution, most of them are accessible in laboratory scale.

- **Hole drilling** This technique consists in drilling a hole and measuring the spring-back displacement with a rosette of strain gauges or optical measurements. The standard for the the utilization of this technique is given by The American Society for Testing and Materials (ASTM) (1992). This method is cheap, standardized and damage is localized within the hole area. However, only provides low spatial resolution residual stresses measurements in the surface of the studied specimen. The measurement is often limited by the size of the drilled hole, which is very big compared to the typical welding zones sizes developed in linear friction welded structures.

- **Contour method** This method was introduced by Prime (2000) and it consists in cutting a section of structure containing residual stresses and measuring the relaxation displacement field by optical means. The measured displacement field is used as boundary conditions for back-calculating the out-of-plane residual stresses using as a reference the geometry of the equivalent cut structure containing no residual stresses. The calculation can be performed analytically or by finite elements analysis. The advantage of this method is that it gives a good spatial resolution and it is rather cheap. Nevertheless, it provides the out-of-plane residual stress field and the Young's modulus of the studied structure needs to be know, which often is not the case for the metastable phases developed in linear friction welded structures.

Residual stresses in friction welded structures

Near$-\alpha$ titanium alloys LFW joints Frankel et al. (2009) measured the residual stress field of a similar Ti6242 using Synchrotron X-ray diffraction. The F axis was parallel to the short axis of the block to be welded. For the computation of the residual stresses, the initial crystal lattice parameters was corrected as function of the P coordinate depending on the chemical variation of the α phase. Fig.2.30 shows residual stresses profiles across axis parallel to each welding direction (see Fig.2.30). Tensile residual stresses of about ~800 MPa are measured in the TMAZ. The zone containing residual stresses extents up to 2.5 mm away from the WCZ. It is interesting to note that the residual stresses profiles are slightly asymmetric, being higher for coordinates with positive values of P.

α/β titanium alloys LFW joints Frankel et al. (2009) also measured the residual stresses of a dissimilar Ti64A-Ti64B LFW joint using Synchrotron X-ray diffraction that compared to measurements obtained by the contour method. The microstructures of both Ti64 grades, Ti64A and Ti64B, and the residual stresses profiles across the WCZ are exhibited in Fig.2.31. Compared to the Ti6242 specimen, the residual stresses peak parallel to the P direction was lower (~700 MPa) and the zone affected by residual stresses was slightly narrower (~2 mm). The asymmetry in the residual stresses profile is more pronounced but it seems to be related to to the different microstructures presented between the blade and the disk, which was not the case for the Ti6242 LFW

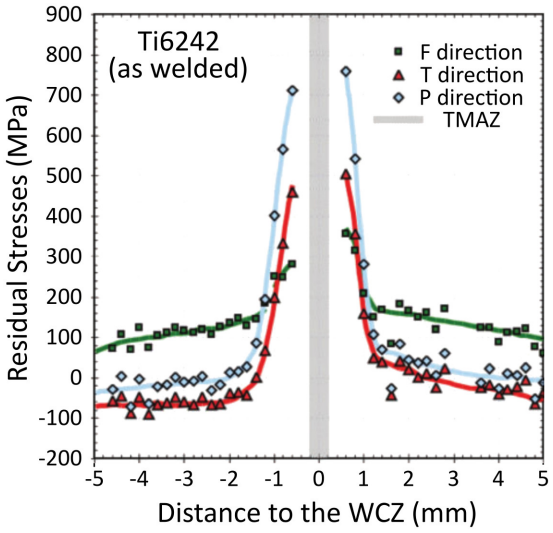

Figure 2.30: Residual stress in three principal directions for a similar Ti6242 LFW joint (Frankel et al., 2009).

joint. It worthy of being noticed that a strong peak of −200 MPa compressive residual stresses is measured at the coordinate P = 2 mm.

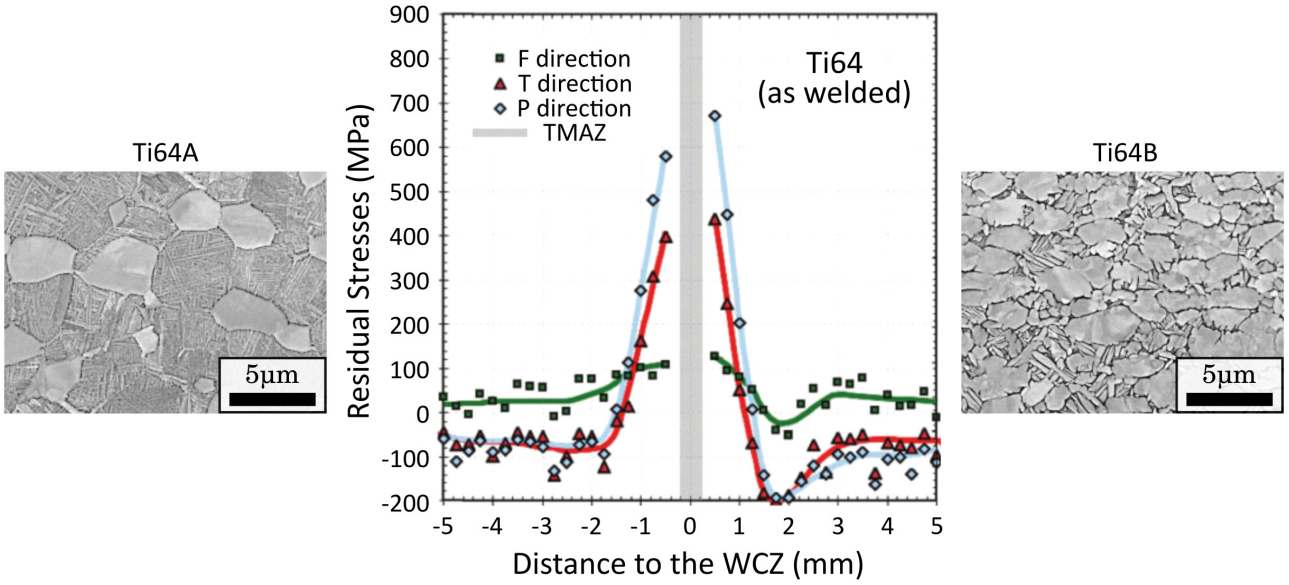

Figure 2.31: Residual stress in three principal directions for a similar Ti64 LFW joint (Frankel et al., 2009).

Romero et al. (2009) studied the effect of the forging pressure in residuals stresses field in dissimilar Ti64 LFW joints. Two grades of Ti64 titanium alloys were used to generate LFW joints with 4 different forging pressures (P, 2.2P, 5P and 9P). Energy dispersive synchrotron X-ray diffraction experiments were performed on the high-energy beamline 15A at the ESRF to measure the strained α lattice parameters. Residual stresses were computed with the unstrained reference parameters. Fig.2.32d shows the measured stress fields. Maximal stresses are found in the specimen welded with reference pressure at a distance of ∼0.5 mm of the WCZ. Its values are 670 MPa in the T direction, 380 MPa in F direction and 320 MPa in P direction. At a distance of 2 mm some compression residual stresses can be found. Romero et al. (2009) found that the residual stresses peak in the vicinity of the WCZ decreases with increasing forging pressure.

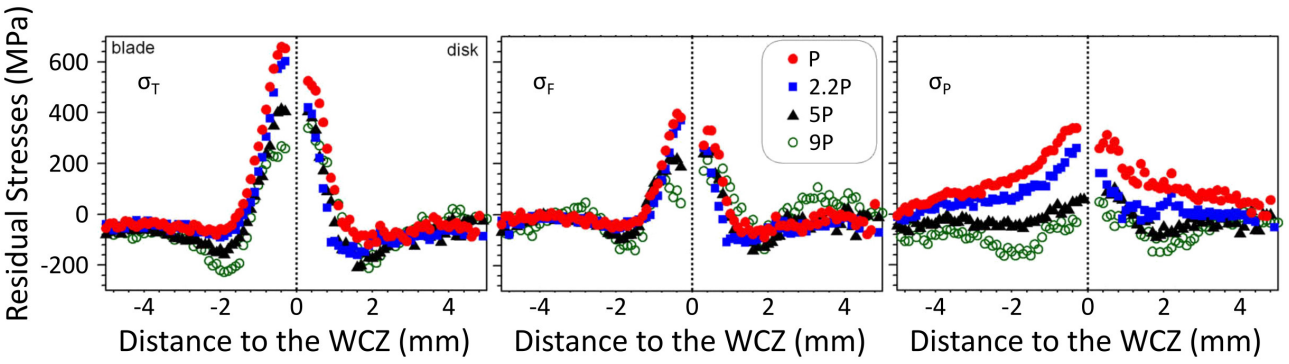

Figure 2.32: Residual stress in three principal directions for a similar Ti64 LFW joint (Romero et al., 2009).

Frankel et al. (2009) compared the residual stresses measurements performed by Synchrotron X-ray radiation with measurements carried out with the Contour Method using Stereo Digital Image Correlation for obtaining the spring-back displacement of the cut surface. The authors also studied the effect of two post weld heat treatments in terms of residual stresses. Fig.2.33a shows the topography of the cross-weld specimen highlighting the spring-back displacement for the joint in the as welded state and the two post weld heat treatment. Fig.2.33b

shows the finite elements analyses computation for residual stress. The peak maximum residual stress field is 500 MPa which was not in agreement with the Synchrotron X-ray radiation measurements. The authors attributed this difference to possible measurements artefacts in the displacements field obtained by Stereo Digital Image Correlation and to artefacts introduced by texture in the diffraction measurements through X-ray measurements.

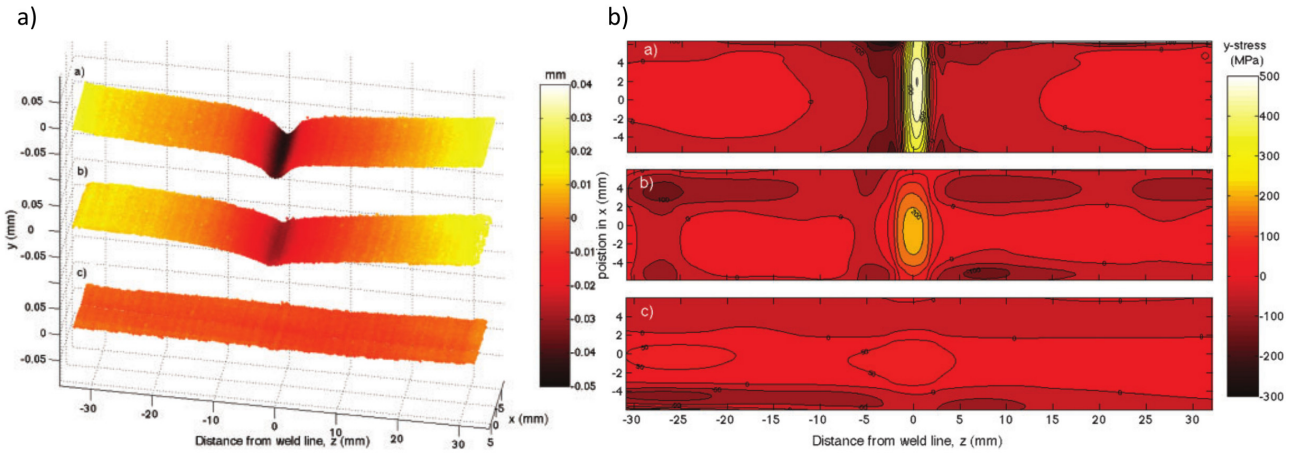

Figure 2.33: a) Displacement field for Ti64 cross-weld samples cut by EDM in the as welded sate, after PWHT1 and after PWHT2. b) Residual stresses fields for Ti64 samples obtained by contour method of a sample in the as welded condition, after PWHT1 and after PWHT2 (Frankel et al., 2009).

$\beta-$metable titanium alloys LFW joints Xie et al. (2016) measured the residual stresses of a dissimilar Ti17(β)-Ti17($\alpha+\beta$) LFW joint by Synchrotron X-ray diffraction and the contour method. They claimed that X-ray diffraction exhibits a low spatial resolution for LFW joints but nevertheless, it served well for comparison and validation of the contour method measurements. It should be pointed out that, for the FEA computation of the welded structure residual stresses, the Young's modulus of the PM was used for the entire cross-welded structure (Xie et al., 2016). This is quite arguable since. It has been shown that $\beta-$metastable titanium alloys undergo a α depletion in the TMAZ and WCZ during LFW (Ballat-Durand et al., 2018; Dalgaard et al., 2012a; Wanjara et al., 2014) and, as shown established by (Duval, 2013), pure β phases exhibit lower Young's modulus that two-phases alloys (see Section 2.1.1).

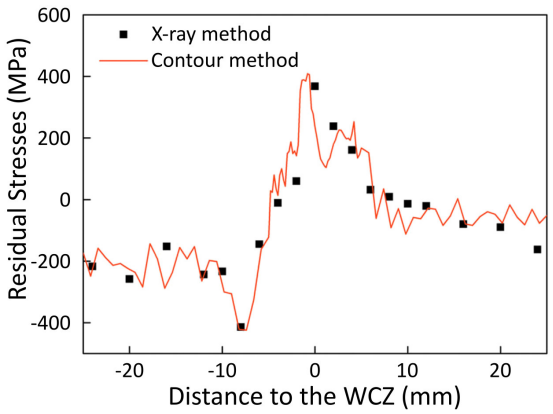

Figure 2.34: Comparison of residual stresses measurements by the contour method and X-ray diffraction (Xie et al., 2016) of a dissimilar Ti17(β)-Ti17($\alpha+\beta$) LFW joint.

Friction welds in general an other materials Daymond and Bonner (2003) measured the residual stresses in a dissimilar titanium LFW joint using neutron diffraction. Fig.2.35 shows the residual stresses profile across each axis as a function of the distance to the WCZ along the P axis. The maximum stresses is found parallel to the T and F axes with a value of 400 MPa. Stress parallel to the P axis is about 100 MPa. It should be noticed that the residual stresses in the three components are positive. The WCZ undergoes a significant hydrostatic pressure. Far from the weld (~ 20 mm) some compression can be found parallel to the T axis. As shown in the previous residual stresses profiles, residual stresses are not symmetric.

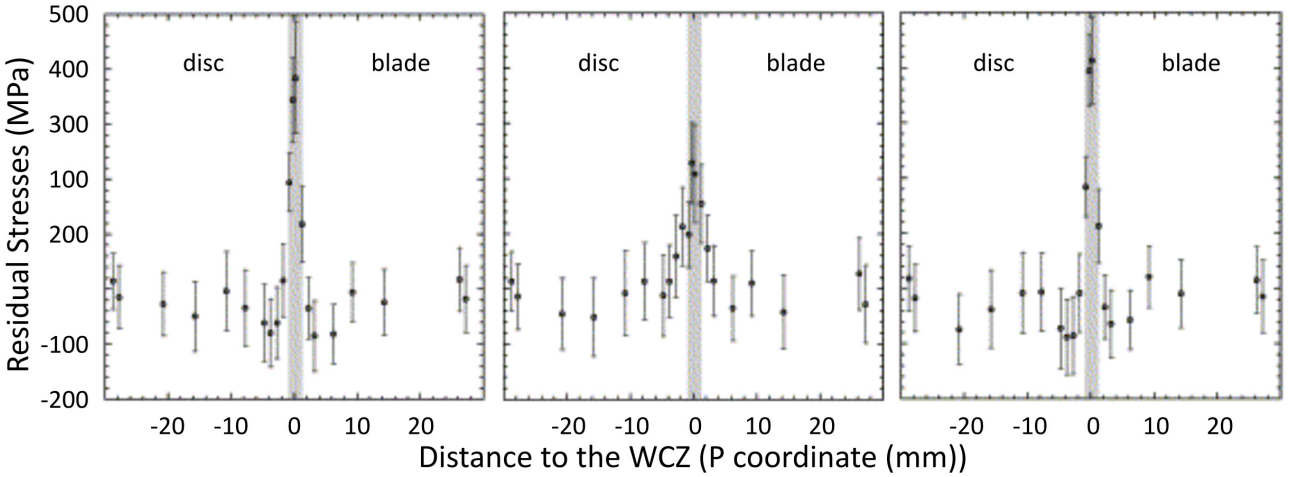

Figure 2.35: Residual Stresses parallel to the (a) T axis, (b) P axis, and (c) F axis, as a function of position along the P axis (Daymond and Bonner, 2003).

Kim et al. (1995) computed an approximation of residual stresses for the three directions z (the specimen main axis), r (radial coordinate) and θ (tangential component) for a dissimilar AISI 340L-Titanium RFW joint. Fig.2.36 shows the residual stress as function of z. Residual stress are tensile near to the centre and become compressive in the surroundings. Residual stresses profiles are asymmetric since the welded alloys exhibit different values of thermal expansion coefficients. It is noteworthy that the residual stress in the r and θ direction are greater and that the maximal stress is shifted from the weld centre. This asymmetry is similar to the one observed in linear friction weld and suggests that the RFW is not symmetric.

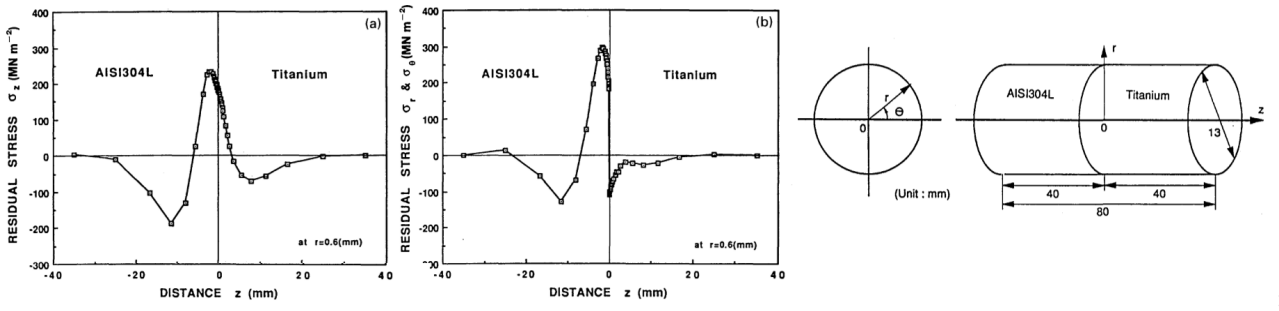

Figure 2.36: a) Residual stresses profiles of a) σ_z and a) σ_r and σ_θ in axial direction near centre of welded component ($r = 0.6$ mm) (Kim et al., 1995).

Some of the residual stresses measurements are gathered in Fig.2.37 for a qualitative comparison, since these measurements were performed used different residual stresses measurements techniques and over different weld configurations. Despite the differences in the absolute value of each measurement, it seems that authors agree

about the existence of tensile residual stresses parallel to the P axis. These residual stresses might play a role in the mechanical behaviour of the cross-welded structures. For instance, the presence of residual stresses could lead to an early plastic activity in the vicinity of the weld at positions under tensile residual stresses close to the local yield strength.

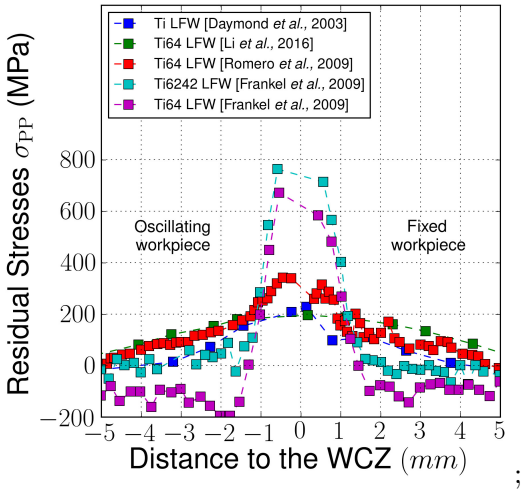

Figure 2.37: Residual stresses measurement literature review.

2.3.3 Mechanical Characterization

In terms of mechanical characterization of welds, The American Welding Society (1985) has introduced the term "joint efficiency", which represents the ratio of the strength of a joint to the strength of the parent material. According to Funderburk (1999), the AWS D1.1 Structural Welding Code – Steel introduced the terms of matching and undermatching to refer to various mechanical properties of welds such as yield and tensile strength with respect to the parent material. If a weld exhibits a lower strength than the parent material, the joint efficiency can easily be computed by comparing the strength of a specimen made of parent material to the strength of a cross-weld specimens. For smooth cross-weld tensile specimen exhibiting a higher tensile strength than the parent material, failure occurs at the parent material and the tensile strength registered is that of the parent material. Several authors have preferred the use of the terms "undermatching" and "overmatching" strength to qualify welds specifically in terms of their strength with respect to the strength of the parent material. The term overmatch is not defined in the Standard Welding Terms and Definitions given by The American Welding Society (1985) and is often used to characterize welds exhibiting failure far from the weld during monotonic tensile testing or Vickers microhardness profiles across the weld showing increased local microhardness at the weld.

Microhardness

Microhardness profiles are carried out following ASTM E384-17. The standards requires that the distance between two microhardness indentation should be greater that 2.5 times the diagonal of a single indentation. Using loads of 200 g, 300 g and 500 g, indentations in Titanium alloys exhibit diagonals of about $40-70\,\mu m$. This implies a sufficient spatial resolution for analysing friction welded structures. Therefore, Vickers microhardness is

the preferred technique in microhardness testing for the mechanical characterization of friction welded structures. Welds exhibiting local increased microhardness exhibit an overmatching strength, whereas welds with reduced microhardness exhibit undermatching strength. Microhardness testing is mostly performed by analysing the microhardness profile along the P axis, although some authors 2D perform microhardness mappings.

Near$-\alpha$ titanium alloys LFW joints Ballat-Durand et al. (2019) performed microhardness profiles across the WCZ over parallel to the P axis (see Fig.2.22). The WCZ exhibits a local microhardness maximum of 480 HV. Microhardness gradually increases from the PM to the WCZ over a distance of less than 2 mm. Combining the microhardness profile with microscopic observations, Ballat-Durand et al. (2019) defined weld zones that extent over a distance of less than 4 mm. The increased microhardness at the WCZ suggests a overmatching strength. During tensile testing, failure should occur far from the WCZ.

$\beta-$metastable titanium alloys LFW joints As stated in Section 2.3.1, $\beta-$metastable titanium alloys undergo an α depletion during linear friction welding (Ballat-Durand et al., 2018; Dalgaard, 2011; Wanjara et al., 2014). The absence of the strengthening α precipitations hits to a softening of the WCZ and TMAZ for linear friction welded joints.

Ballat-Durand et al. (2018) proposed a post weld heat treatment consisting in solutionizing and ageing for favouring the precipitation of the α strengthening phase in the α depleted WCZ and TMAZ. Fig.2.38 shows the microhardness profile across the weld in three conditions: as welded (cyan markers), annealed (orange markers) and annealed+aged condition (black markers). The load used for the microhardness measurements was 300 g.

The microhardness profile of the as welded joint shows that the α depleted β microstructures of the TMAZ and WCZ exhibit reduced microhardness along a distance of about 2 mm centred with respect to the WCZ. The PM exhibited a microhardness of 403 HV, whilst the WCZ in the as welded condition exhibited a local minima of about 343 HV. During monotonic loading, failure should take place in the vicinity of the weld. It is interesting to know that the post weld heat treatment proposed by Ballat-Durand et al. (2018) homogenized the microhardness profile across the weld up to 97 % of the microhardness exhibited by the PM. This suggests that the post weld heat treatment might have restored the mechanical properties in the vicinity of the WCZ and that, for the post-weld heat treated joint, failure might occur elsewhere than at the vicinity of WCZ during monotonic loading. This also suggests that the *alpha* depletion in the TMAZ and WCZ is undesirable since it seems to induce undermatching strength.

The microstructure of a dissimilar Ti17(lamellar)-Ti17(equiaxed) LFW joint exhibited a fine recrystallized zone at the WCZ with significant reduced microhardness (Ji and Wu, 2014). The microhardness profile across the WCZ is shown in Fig.2.39. The reduced microhardness extents up to a distance of 1 mm around the WCZ exhibiting a local minima of about 320 HV at the WCZ. The microhardness of the PM is about 360 HV. Notice that by the application of an annealing post weld heat treatment, not only is the WCZ microhardness increased but also it is greater than that of the PM (420 HV).

Dalgaard (2011) weld two similar Ti5553 LFW joints with two different set of welding parameters. The reference joint was performed with undisclosed pressure P and frequency f. The second joint was performed with undisclosed pressure 1.5P and frequency 0.6. Microhardness profiles across the weld were performed over each LFW joint and are respectively shown in Figs.2.40a and 2.40b. The WCZ exhibits a microhardness minimums

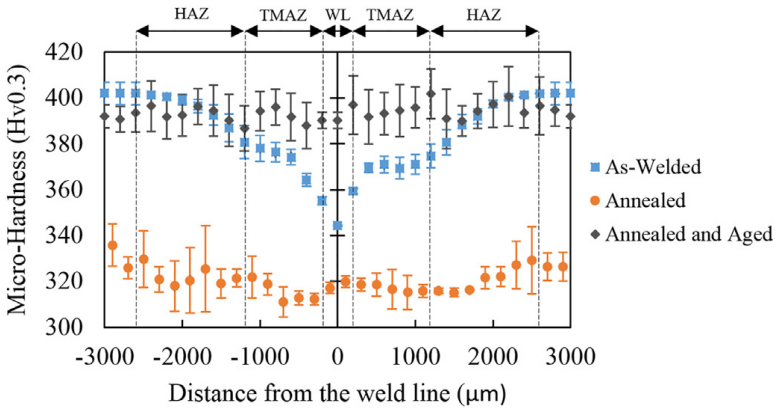

Figure 2.38: Microhardness profiles across the WCZ of a similar Ti17 LFW joint through an axis parallel to the P axis for the joint in the as welded condition (cyan markers), annealed (orange markers) and annealed+aged condition (black markers). Load: 300 g Ballat-Durand et al. (2018).

at the WCZ of 300 HV and 280 HV of each joint. It interesting note that the microhardness profile for the second joint exhibits microhardness measurements that are below the microhardness of the PM.

α/β titanium alloys LFW joints Schroeder et al. (2015) proposed a model for the numerical simulation of the LFW process and validated its properties with several experimental sources of data such as thermal data, axial shortening, and weld microstructure for several welding geometries. Fig.2.41 shows one of the studied geometries so called block-to-plate, in which the oscillating workpiece had a shorter welding length compared to the fixed workpiece. Microhardness at the WCZ is about 425 HV where the for the PM it is 300 HV. The similar Ti64 LFW joint exhibits an overmatching strength. It is interesting to see that the microhardness mapping allows the curved shape of the WCZ to be seen.

The microhardness profiles of both similar α/β titanium alloys LFW joints and he similar Near$-\alpha$ titanium alloys LFW joints exhibited overmatching strength. Failure during monotonic loading should occur far from the WCZ. The similar $\beta-$metastable titanium alloys LFW joints exhibiting α depleted WCZ and TMAZ exhibit undermatching strength. Failure during monotonic and cyclic loadings should take place in the vicinity of the WCZ and TMAZ.

Tensile behaviour

Determining the tensile properties by standard tensile testing on smooth cross-weld tensile specimens reports two difficulties that are related the characteristic heterogeneity of the cross-welded structures.

First, the measurement of the Ultimate Tensile Strength (UTS). In the case of undermatching strength, failure occurs at the WCZ or TMAZ under complex heterogeneous strain fields that will induce to a underestimation of the UTS of the WCZ or TMAZ. In such cases, the joint efficiency parameter introduced at the beginning of this Section is used. Therefore, tensile testing specimens made of PM are of primary importance for better understanding the monotonic response of cross-weld tensile specimens. In the case of a weld with overmatching strength, failure occurs at the PM for smooths tensile specimens making impossible to determine the UTS of the WCZ. Hence, accurately determining the failure location in the welded structure during monotonic loading is highly required.

Second, the measurement of macroscopic total strain with standard extensometers. The measured total

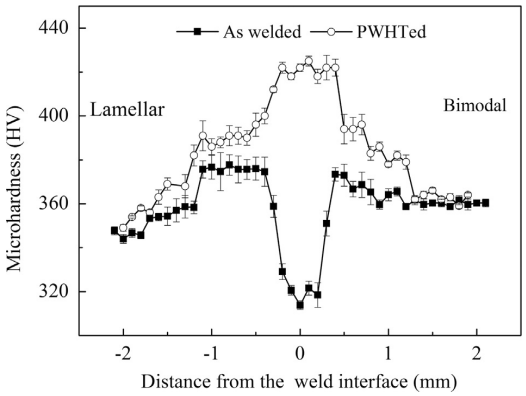

Figure 2.39: Microhardness profiles across the WCZ through an axis parallel to the P axis for the joint in the as welded condition (black markers) and the post weld heat treated joint (white markers). Load: 500 g Ji and Wu (2014)

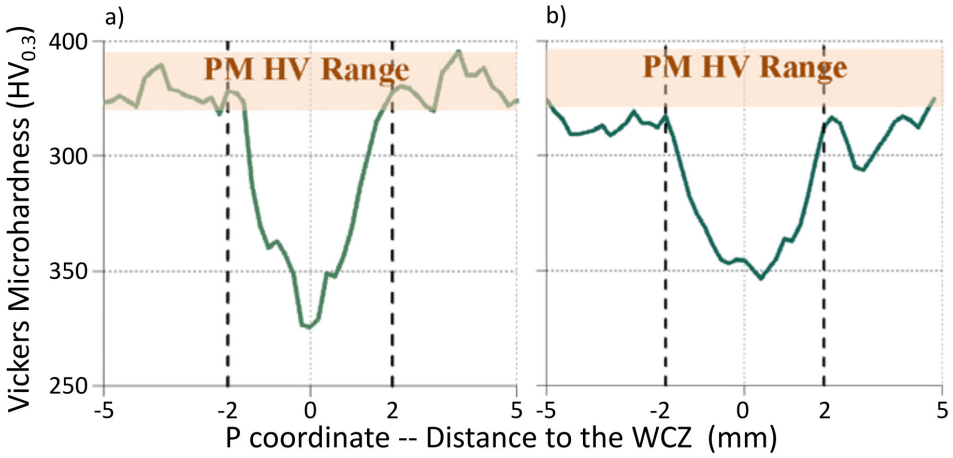

Figure 2.40: Vickers microhardness profile across the WCZ for two similar Ti5553 LFW joints welded with a) undisclosed forging pressure P and frequency f, and b) undisclosed forging pressure 1.5P and frequency $0.6f$. Load: 300 g (Dalgaard, 2011).

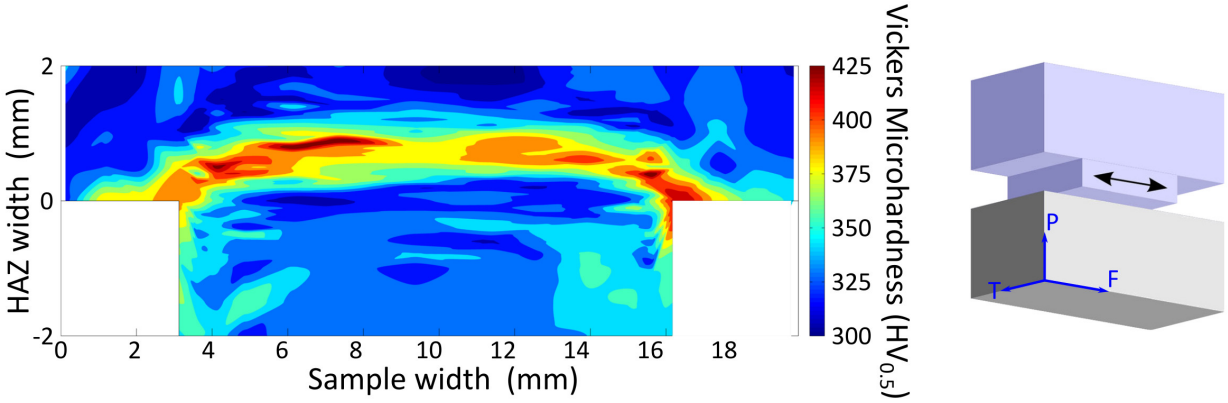

Figure 2.41: Vickers microhardness mapping. Load: 1 kg. (Schroeder et al., 2015).

strain is dependent of the measure basis or initial gauge length. The measurement of total strain tends to the total strain of the WCZ when the initial gauge length tends to the WCZ, which, given the size of the welding zones, is often limited by the available instrumentation. Conversely, the measurement of total strain tends to the total strain of the PM for increasing initial gauge length. This is a contentious issue since sometimes, the measurements of total strain are provided without specifying the initial gauge length Ma et al. (2012). The complex strain field in welded structures can also be addressed by monitoring the displacement field over the specimen surface with a standard system of Digital Image Correlation or Stereo Digital Image Correlation.

In this Section, a literature review on the mechanical properties of linear friction welded structures of the

studied titanium alloys is presented. Special interest is drawn in the ratio between the mechanical properties of the cross-weld structures and the PM, particularly: UTS, strain to failure, failure location and fracture mechanisms. Some other material and friction welded structures are also reviewed.

Near$-\alpha$ titanium alloys LFW joints In the mechanical characterization of the similar IMI834 LFW joint performed by Dalgaard et al. (2012b), three joints were produced with three different values of friction pressure. The forging pressure for the LFW-1, LFW-2 and LFW-3 joint respectively were P_{fr}, $1.5P_{fr}$ and $2P_{fr}$. Smooth cross-weld tensile specimens of each joint were compared to a specimen made of PM. The tensile specimen cross-section area was 6 mm × 4 mm. Macroscopic engineering strain was measured with a initial gauge length of 25 mm. The tensile test curves are shown in Fig.2.42a. Fig.2.42b shows the strain fields obtained by DIC just before failure for the aforementioned tensile specimens. The position of the WCZ is shown by a grey dashed line on the background. The colour bar of each map is placed at its right.

The macroscopic engineering stress of the cross-weld specimen is the same as the one of the PM sample. This suggests that failure occurred at the PM. As shown by the strain maps of Fig.2.42b, localization occurs at the PM for the cross-weld specimens. Notice that the local strain failure ε_{PP} for the three tensile specimen are comparable, which is consistent with failure at the PM. The WCZ exhibits higher strength than PM. This findings confirm the weld overmatching strength.

The LFW-3 cross-weld tensile specimen exhibited a lower macroscopic strain. It seems that the contribution of the WCZ to the total strain is lower. This should be easy to verify by comparing the strain fields obtained by DIC but given that the extent of the colour bar is not the same, it is difficult to precisely determine this.

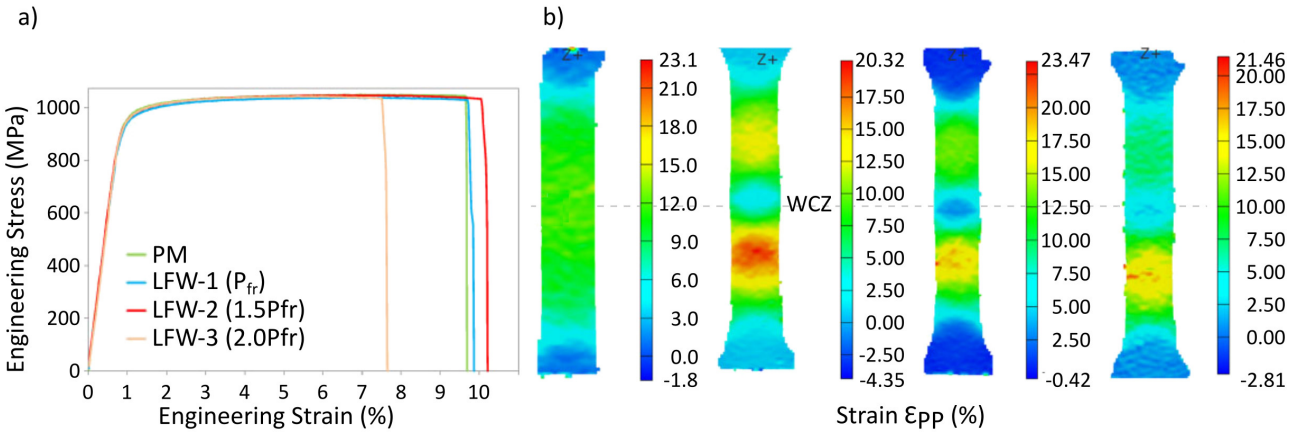

Figure 2.42: a) Tensile curves for on specimen made of IMI834 PM and three cross-weld tensile specimens of a three similar IMI834 LFW joints with different friction pressures. b) Strain fields obtained by DIC just before failure for the aforementioned tensile specimens. (Dalgaard et al., 2012b).

β−metastable titanium alloys LFW joints Wanjara et al. (2014) and Dalgaard et al. (2012a) carried out the mechanical characterization of a similar Ti5553 LFW joint. Two joints were produced with undisclosed forging pressures of P_{fr}, $1.5P_{fr}$. The mechanical properties of the cross-weld specimens were compared to a specimen made of Ti5553 PM. Only the mechanical properties of the cross-weld specimen and the specimen of PM were disclosed and are shown in Table 2.3. The gauge length for the macroscopic strain measurement was 25 mm. The specimen made of PM showed a strain to failure of 11.2 % and a UTS of 1108 MPa. The cross-weld specimen showed a strain to failure of 3 % and a UTS of 17.4 MPa. Unlike the similar near$-\alpha$ titanium alloys

LFW joints, not only is the UTS of the cross-weld specimen lower that than of the PM, but also the macroscopic strain to failure is substantially lower. This suggest that failure occurred at the WCZ.

Dalgaard et al. (2012a) claimed that failure should occur in the vicinity of the WCZ and TMAZ due to the α depletion provoked by the welding process in this location. Fig.2.43 shows the ε_{PP} fields obtained by DIC just before failure for a specimen made of PM and a cross-weld specimen. The colour bar corresponding to each strain field is shown at the left of each map. Notice that, compared to the PM, the values of local strain are quite lower for the cross-weld specimen. The local strain for the cross-weld specimen is localized at WCZ. It is also interesting to note that the localization occurs in diagonal band for the PM, whilst it is localized on the WCZ for the cross-weld specimen. This findings clearly highlight the undermatching strength of the joint.

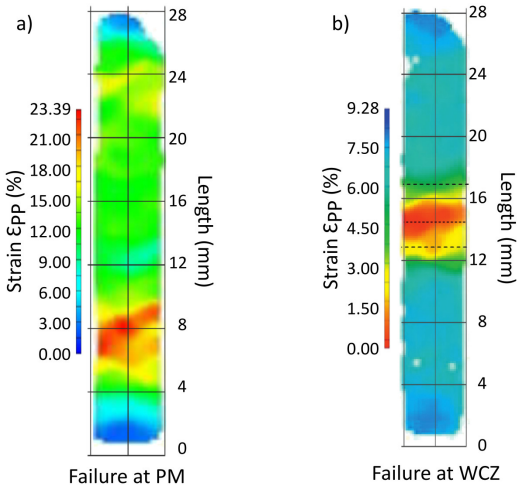

Figure 2.43: ε_{PP} fields for a PM Ti5553 specimen and a cross-weld Ti5553 specimen Dalgaard et al. (2012a).

Wanjara et al. (2014) studied the effect of two pre-weld heat treatment and two post-weld heat treatments.

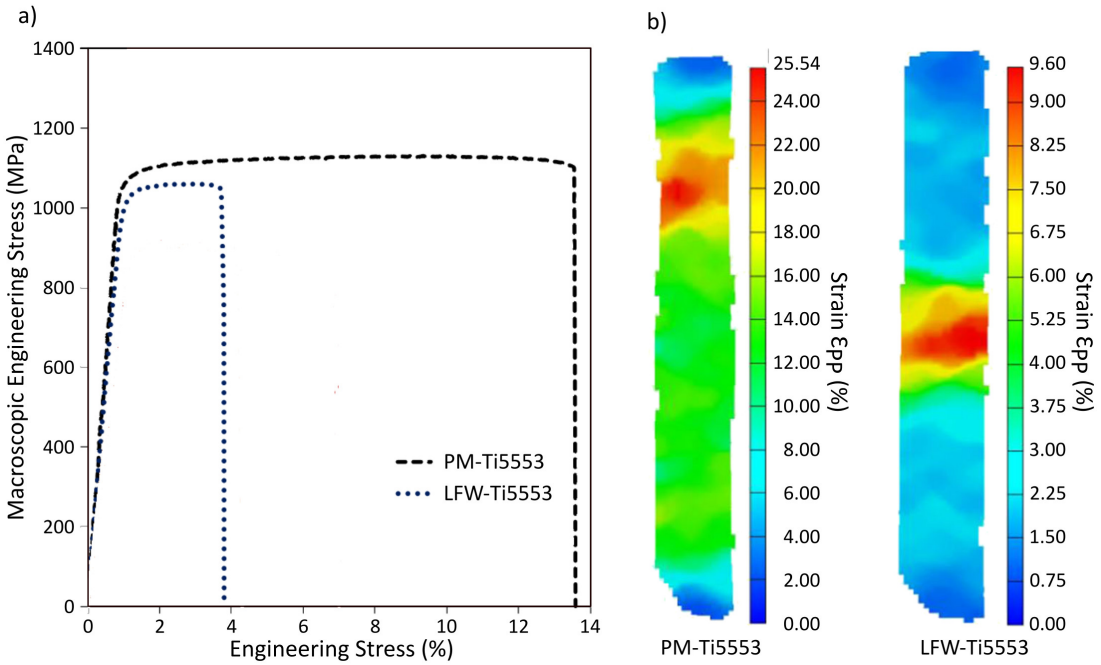

Figure 2.44: a) Tensile curves for a specimen made of Ti5553 PM and a cross-weld tensile specimens of a similar Ti5553 LFW joint in the as welded condition. b) Strain fields obtained by DIC just before failure for the aforementioned tensile specimens. (Wanjara et al., 2014)

Fig.2.44a shows the tensile curves for a specimen made of Ti5553 PM (blue dots) and a cross-weld specimen (black dashed line). As previously mentioned for the results reported by Dalgaard et al. (2012b), the UTS and total strain are lower for the cross-weld specimen compared to PM specimen. Is should also be noted that the Young's of the PM sample seems to be slightly higher than that of cross-weld specimen. It seems that the depletion of the α phase in the vicinity of the weld reduced the local Young's Modulus. This effect would be amplified as the initial gauge length of the extensometers approaches to the length of the WCZ and TMAZ welded zones.

Fig.2.44b shows the strain maps just before failure for the specimens of Fig.2.44a. The same localization over a band is observed for the specimen made of Ti5553 PM and the same localization on the α depleted WCZ and TMAZ are observed. It is worthwhile of being noticed that the levels of local strain are much smaller for the cross-weld specimen. It is very interesting of noticing that the hottest colours are localized close to the specimen surface. This suggest a structural effect as a result of the strain distribution between the TMAZ and WCZ.

The mechanical properties of different tensile test reported in literature were gathered in Table 2.3. The reduced macroscopic strain and UTS of the similar $\beta-$metastable LFW joints is encountered for several tests. As announced by the microhardness profiles in Section 6.3.2, the similar $\beta-$metastable titanium alloys similar LFW joints often exhibit a undermatching strength.

Alloy	**Condition**	**YS** (MPa)	**UTS** (MPa)	**El.** (%)	**Failure location**	**Source**
LFW Ti17	As welded	1028.0	1057.0	2.0	TMAZ	(Li et al., 2010)
LFW Ti17	As welded	1029.0	1105.7	4.2	PM	(Li et al., 2010)
LFW Ti17	As welded	1016.0	1076.1	2.2	PM	(Li et al., 2010)
PM Ti5553	Lamellar	1046.0	1108.0	11.2	N/A	(Dalgaard et al., 2012a)
LFW Ti5553	W. parameters: P_{fr}, a	1019.0	1058.0	4.0	TMAZ	(Dalgaard et al., 2012a)
LFW Ti5553	W. parameters: $1.5P_{fr}$, $0.6a$	988.0	1013.0	2.9	TMAZ	(Dalgaard et al., 2012a)
PM Ti17	Bimodal	1191.0	1210.0	8.7	N/A	(Ma et al., 2012)
LFW Ti17	As welded	991.0	1076.0	4.9	Not specified	(Ma et al., 2012)
LFW Ti17	Annealing 530 °C/4 h	979.0	1093.0	5.4	Far from former WCZ	(Ma et al., 2012)
LFW Ti17	Annealing 610 °C/4 h	979.0	1221.0	7.3	Far from former WCZ	(Ma et al., 2012)
LFW Ti17	Annealing 670 °C/4 h	1222.0	1262.0	7.1	Far from former WCZ	(Ma et al., 2012)

Table 2.3: Literature review on tensile properties of similar β titanium alloys LFW joints.

By instrumenting the tensile test with a DIC system, Dalgaard et al. (2012b) has showed that the similar IMI834 LFW joint exhibits overmatching strength. Furthermore, the ε strain field was measured with a reasonable spatial resolution. The tensile tests results of the $\beta-$metastable clearly highlighted that the depletion of the α in the WCZ and TMAZ is detrimental for the monotonic behaviour of the cross-welded structure. As for the similar near$-\alpha$ titanium alloys LFW joints, the strain fields obtained by DIC properly highlighted the structural behaviour of the cross-welded structure. These studies were focussed on determining whether the welds exhibit overmatching or undermatching strength and on highlighting the overall strain behaviour of the welded structure. Nonetheless, further studies are required.

For instance, the local UTS and the determination of whether the WCZ of the near$-\alpha$ titanium alloys LFW joints underwent plastic deformation or not is still missing. Moreover, the chronological evolution of plastic activity is not observed. More explicitly, even if failure occurs at PM, the first stages of plastic may have occurred at the WCZ or its vicinity. Finally, the damage mechanisms of the WCZ can not be assessed since failure occurred elsewhere.

Failure location under monotonic loading of LFW joints

The determination of failure location is important for judging the quality of a weld in terms of mechanical properties. Fig.2.45a shows two optic observations of the surface of the specimen coming from the similar Ti5553 LFW joint studied by Dalgaard et al. (2012b). Failure occurred at the Ti5553 TMAZ for two specimens. As stated previously on this Section, the α depleted β grains of the TMAZ and WCZ in a similar $\beta-$metastable titanium alloy LFW joint represent a threat for the integrity of the welded structure. Dalgaard et al. (2012b) attributed the failure location to the heterogeneity in grain size between the grains at the TMAZ and the grains at the WCZ. A sound understanding of the mechanisms leading to this failure location are still required.

Mateo et al. (2009) proposed the use of LFW for the reparation of damaged blades of Ti6246 titanium alloy in gas turbines of aeroengines. The particularity of this work is that several LFW joints form a single welded structure. Joints containing two of three WCZ in series were characterized in terms of microstructure and mechanical properties. As for similar Ti64 LFW joints, the similar Ti6246 LFW joints exhibited an overmatching strength. This is clearly seen in the *post mortem* SEM observation of a tensile specimen containing three WCZ of Fig.2.45b. The three WCZ are indicated by yellow arrows and the crack is clearly seen half-way between two of the WCZs. The same phenomenon is observed for the similar Ti64 LFW joint characterized by Li et al. (2008) (see Fig.2.45d). The graph of Fig.2.45c shows the failure location of tensile specimens made of Ti64 PM (open markers) and cross-weld tensile specimens coming from a similar Ti64 LFW joint (filled markers) (Wanjara and Jahazi, 2005). It is worthwhile of being noticed that no specimen failed at the WCZ nor the TMAZ.

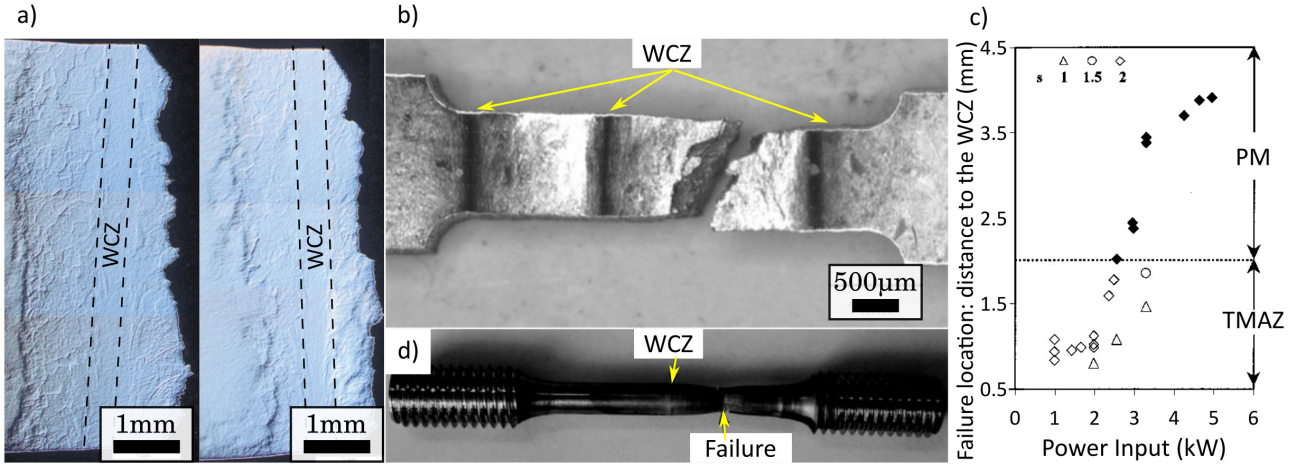

Figure 2.45: a) Optic observations of the surface of specimen made of similar Ti5553 LFW joint showing the failure location on the welded structure of tensile specimen coming from a similar Ti5553 LFW joint (Dalgaard et al., 2012b); b) SEM observation of a specimen containing three similar Ti6246 LFW joints (Mateo et al., 2009); c) failure location for a the tensile specimens made of PM (open markers) and tensile specimens coming from a similar Ti64 LFW joint (filled markers) (Wanjara and Jahazi, 2005) and d) photograph of a tensile specimen coming from a similar Ti64 LFW joint (Li et al., 2008).

Both the similar IMI834 LFW joint and the similar Ti64 failed at the PM (see Figs.2.42, 2.45c, and 2.45d). The similar Ti5553 LFW joint failed at the TMAZ (see Fig.2.45a). No specimen failed at the WCZ. This implies that for studying the damage mechanisms of the WCZ for any of theses joints, the utilization of notched tensile specimens is required. Yet, no reports were found in literature addressing this study.

Fatigue

Aircraft structures undergo several cyclic loads such as loading actions, manoeuvre loads, turbulence and landing loading cycles (Payne, 1976). The study of cyclic behaviour concerns the fatigue strength up to a target fatigue life, fatigue crack propagation mechanisms and fatigue crack propagation rate. In the case of linear friction welded structures, special interest is drawn on the location in the welded structures of fatigue crack initiation. In this Section, the available literature on the cyclic behaviour of linear friction welded structures is presented.

Kuroki et al. (2020b) studied and compared the cyclic behaviour with an S–N approach (see Fig.2.46a) over smooth fatigue specimens coming from a grade of Ti64 (PM), a similar Ti64 LFW joint in the as welded condition (LFW–AW) and one after following an undisclosed post weld heat treatment (LFW–PWHT). The failure location on the welded structure is shown in Fig.2.46b. The curves of the PM and the cross-weld fatigue specimens are very similar. The cross-weld fatigue specimens exhibit a comparable fatigue strength. The LFW process seems to slightly affect the fatigue strength of the PM. Concerning the failure location on the welded structure, the distance to the WCZ should be disregarded for the PM fatigue specimens but interesting to see that there is a considerable scatter. For the PM fatigue specimens, fatigue crack initiation occurs at different positions of the gage length. The authors did not disclose the microstructure of the WCZ and TMAZ for the LFW fatigue specimens in the as welded state (red triangles). The sizes of the weld zones are unknown. It is hence difficult to draw conclusions about the failure location. McAndrew et al. (2014) performed a similar LFW joint with a comparable grade of the PM in which the WCZ and TMAZ extended to a distance of about 1 mm. If this value is used to analyse the results presented in Fig.2.46b, it could be said that only one specimen failed at the TMAZ and the other failed far from it. This could explain the similarity on the fatigue strength between the PM and LFW–AW fatigue specimens. Unfortunately, Kuroki et al. (2020b) did not relate the date in both graphs of Fig.2.46, thus conclusions about the specimen that failed in the vicinity of the WCZ and its number of cycle to failure can not be drawn from this information. It could be interesting to precisely define where in the welded structure failure did failure occur for this specimen and to thoroughly study its propagation mechanisms. Nevertheless, the results provided by Kuroki et al. (2020b) show that failure location of the LFW–PWHT fatigue specimens exhibit a very similar scatter to that of the PM fatigue specimens. This suggests that the behaviour of the LFW–PWHT joint is similar to the PM during cyclic loading.

In addition to the tensile tests explained in Section 2.3.3, Mateo et al. (2009) studied the cyclic behaviour of single, double and triple welds with and S–N approach (see Fig.2.47a). The stress ratio was R= 0.1 and the target fatigue life was 10^7. For the target fatigue life, the fatigue strength of the PM and cross-weld fatigue specimens is about 640 MPa. The S–N curves for the PM and the cross-weld fatigue specimens are very similar. This suggests that failure occurred at the PM. Mateo et al. (2009) claimed that failure occurred at a distance comprised between 4 mm and 12 mm sometimes internally and sometimes at the surface. Fig.2.47b shows the fracture surface for a cross-weld fatigue specimen tested at a maximum fatigue stress of 800 MPa that exhibited a fatigue life of $N_f = 1211600$ cycles. In Fig.2.47c, the fatigue crack initiation site is shown. An object with an elliptical shape having the larger semi-axis of about 120 mm is seen. The authors claimed that this object was an α nodule in the PM microstructure.

As for the results of Kuroki et al. (2020a), fatigue crack initiated at the PM. It seems that similar LFW

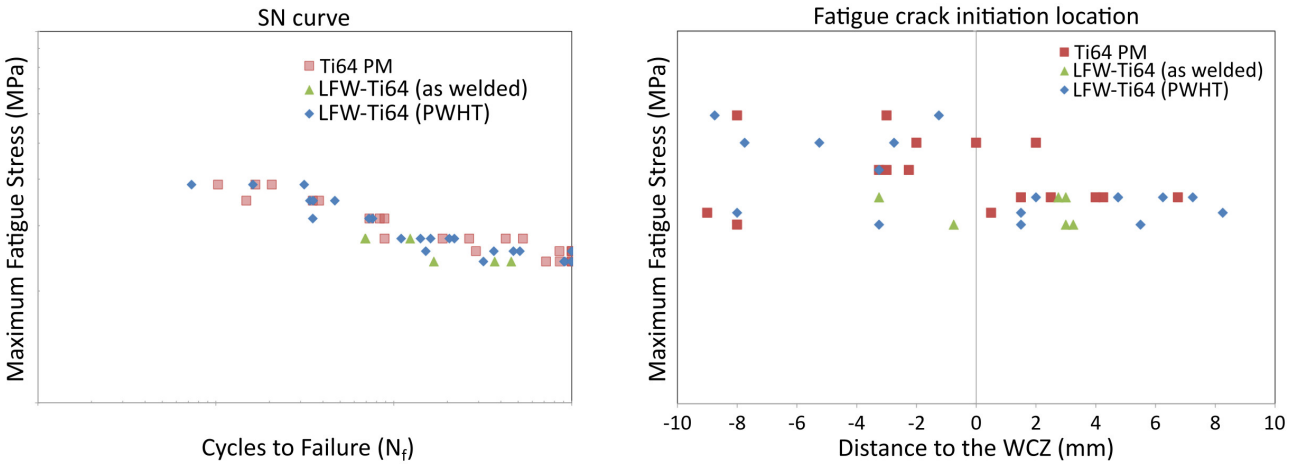

Figure 2.46: a) Curve S–N (R=0.1) and b) failure location for a grade of Ti64 (red rectangles), a similar Ti64 LFW joint in the as welded condition (green triangles) and one after following an undisclosed post weld heat treatment (blue diamonds). The cycles to failure and the maximum applied stress were not disclosed (Kuroki et al., 2020b).

joints made of α/β titanium alloys leads to joints with overmatching strengths and fatigue crack initiation occurs far from the affected zone.

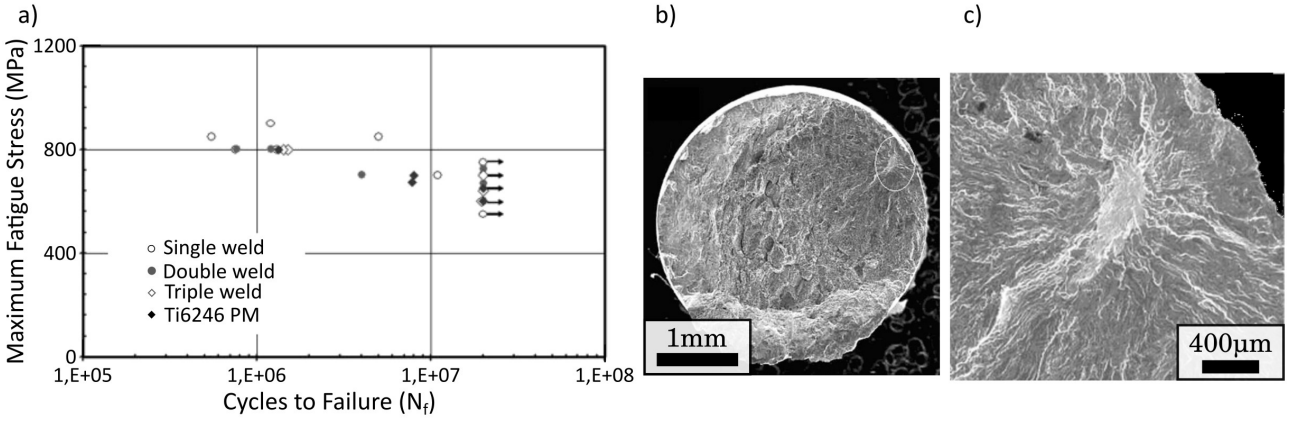

Figure 2.47: SN curve for Ti6246 PM, cross-weld fatigue specimens containing a single weld (one WCZ, empty circles), double welds (two WCZ, filled diamond) and triple welds (three WCZ, empty diamonds) Mateo et al. (2009).

2.4 Conclusions

Literature concerning the near–α, α/β and β–metastable LFW joints was reviewed in this Chapter. The main points of interest were microstructure, potential defects, residual stresses, microhardness profiles, monotonic behaviour, fracture mechanisms, fatigue strength, fatigue crack initiation site and fatigue crack propagations mechanisms.

During cooling after overreaching the $\beta-$transus temperature during joining, metastable microstructures are developed in the WCZ of titanium LFW joints. For the similar LFW joints made of near–α IMI834 and α/β Ti64 titanium alloys, α' martensite microstructures are developed (Wanjara and Jahazi, 2005; Dalgaard et al., 2012b). For the $\beta-$metastable Ti5553 and Ti17 titanium alloys, a depletion of the α phase is observed in the WCZ and TMAZ. The microstructure of the WCZ is formed by fine equiaxed α depleted distorted β grains of about $\sim$10 µm and the TMAZ is formed by α depleted deformed β grains (Ballat-Durand et al., 2018; Wanjara et al., 2014).

The results available in literature concerning the residual stresses do not agree. Measurements vary between 500 MPa and 700 MPa (Frankel et al., 2009; Romero et al., 2009) parallel to the P axis, which represents about two thirds of the yielding limit of the PM's. There is nonetheless a common ground between these findings. The application of post weld heat treatments tends to effectively reduce the present residual stresses.

Microhardness increases with decreasing distance to the WCZ of LFW joints made of near–α and α/β titanium alloys (Schroeder et al., 2015; Ji et al., 2016b; Li et al., 2008; Ballat-Durand et al., 2019; Dalgaard et al., 2012b), whilst it decreases for the $\beta-$metastable titanium LFW joints (Li et al., 2010; Ballat-Durand et al., 2018; Dalgaard et al., 2012a). LFW joints made of near–α and α/β titanium alloys exhibit overmatching strength. Conversely, for $\beta-$metastable titanium alloys, the welds exhibit undermatching strength. These findings are in agreement with the documented tensile tests results. For LFW joints made of near–α and α/β titanium alloys, failure never occurred in the WCZ and macroscopic strain was slightly reduced (Wanjara and Jahazi, 2005; Dalgaard et al., 2012b; Li et al., 2008). For $\beta-$metastable LFW joints, failure occurs at the WCZ-TMAZ frontier and macroscopic ductility is highly compromised (Wanjara et al., 2014; Dalgaard et al., 2012a). Strain fields obtained by DIC clearly show localization at the PM for the similar IMI834 LFW joint (Dalgaard et al., 2012b) and at the WCZ for the similar Ti5553 LFW joints (Dalgaard et al., 2012a). In terms of cyclic behaviour, the fatigue strength of similar α/β LFW joints is comparable to the parent materials (Mateo et al., 2009; Kuroki et al., 2020b).

A certain understanding about the mechanical properties has been established in literature. It seems that, despite the presence of residual stresses, the martensitic microstructures developed in near–α and α/β LFW joints seem to constitute a sound weld. Conversely, the α depletion in the WCZ and TMAZ of $\beta-$metastable LFW joints seems more critical. There are nevertheless several questions that remain open in literature.

The strain fields obtained by DIC by Dalgaard et al. (2012b) and Dalgaard et al. (2012a) gave a first estimation of the local strain for the WCZ and TMAZ. These measurements are particularly relevant for the $\beta-$metastable LFW joint studied by Dalgaard et al. (2012a), since failure occurs at the TMAZ. Thus, the plastic behaviour of the TMAZ and WCZ can be studied and most importantly, strain to failure can be measured. In the case of near–α LFW joints, this was not possible since failure occurred at the PM. Therefore, the plastic behaviour, strain to failure and fracture mechanisms of the WCZ for near–α LFW joints is still unknown. A

study in which the mechanical behaviour of these joints is studied through notched micro-tensile tests seems necessary.

Very few studies have studied in depth the fracture mechanisms and its relationship with the underlying microstructure. For the $\beta-$metastable LFW joints, a depletion of the α strengthening phase has been observed (Dalgaard et al., 2012a; Ballat-Durand et al., 2018) that lead to failure at the TMAZ (Li et al., 2010; Dalgaard et al., 2012a). In the fractographic analysis reported by Li et al. (2010), elongated features were observed and qualified as brittle fracture. The macroscopic deformation was 2 % and failure occurred at the TMAZ. This suggests that local deformation at the TMAZ was greater. Similarly, Dalgaard et al. (2012a) measured a local deformation of 9.28 % at TMAZ just before failure. Considering this local deformation, it seems unlikely that the elongated fracture features observed by Li et al. (2010) were at the origin of a brittle fracture. A better understanding of the relationship between these elongated features and the α depleted β microstructure of the TMAZ is required.

Some authors claimed that LFW is self-cleaning process ref, how ever several authors have found defects in terms of voids and oxides at the weld interface.

The most common utilization of LFW is for the fabrication of "Blisks" (see Section 2.19), for which fatigue is one of the main mechanical loadings that these LFW structures undergo (Kuroki et al., 2014; García, 2011). There is a lack of studies in literature concerning cyclic behaviour, fatigue strength and fatigue crack initiation of LFW joints. First, it seems very important to precisely define the fatigue crack initiation site location on the welded structure. Second, understanding the fatigue crack initiation mechanisms and its relationship with the underlying microstructure is of primary interest.

3

On the use of Stereo Digital Image Correlation for the alignment of fatigue testing machines

In the approach of this thesis work, tensile and fatigue testing of flat samples will be a major part. At the beginning of our project, our laboratory was equipped with a set of new hydraulic grips for flat specimens. To ensure that our test procedures for tensile and particularly fatigue testing of cross-weld specimens complies with international testing standards, a procedure for aligning the load frame was required.

In this Chapter, an experimental procedure for the alignment of fatigue testing machines based on Stereo Digital Image Correlation measurements is presented and an analytical expression for the computation of bending stresses in fatigue specimens to compare with the criteria given by international standards is developed.

This work will be submitted as following: *On the use of Stereo Digital Image Correlation for the alignment of fatigue testing machines in accordance with International standards. Juan–Manuel García, Marie–Thérèse Auclair and Thilo–Frank Morgeneyer. Experimental Mechanics.*

Résumé de chapitre

La Stéréo Corrélation d'Images (SDIC) est utilisée pour l'analyse et la quantification des chargements parasites provoqués par une machine de fatigue non alignée sur des éprouvettes de fatigue. Des solutions analytiques sont fournies pour des éprouvettes ayant a) des rayons d'entaille tangents à la section utile et b) des rayons continus entre les têtes. L'objet de ce travail est de fournir un outil simple pour estimer les contraintes parasites de flexion dues au désalignement de la machine de fatigue, en utilisant les déplacements hors plan mesurés par SDIC et la théorie des poutres. De plus, des procédés simples pour aligner une machine de traction commerciale sont proposés. Les contraintes parasites de traction obtenues par des simulations numériques sont en accord avec celles résultant des solutions analytiques.

Chapter Abstract

Stereo Digital Image Correlation (SDIC) is used for the analysis and quantification of parasite loadings due to the misalignment of a load frame during fatigue specimen mounting. Analytical solutions are provided for fatigue specimens having a) tangentially blending fillets between the uniform test section and the ends, and b) continuous radius between the ends. The aim of this work is to provide an easy way to estimate the induced parasite bending stresses due to the load frame misalignment, using the out-of-plane displacement measurements obtained by SDIC and beam theory. Simple procedures for aligning a commercial load frame are also provided. The bending stresses profile along the specimen main axis obtained by numerical simulations have shown a very good agreement with the analytical models.

Contents

Figures

Keywords

Fatigue, Load frame alignment, Stereo digital image correlation, Experimental mechanics

Nomenclature

x, position on the fatigue specimen main axis;

y, position on the thickness of the fatigue specimen;

z, position on the width of the fatigue specimen;

The origin is set at the specimen surface having the origin at the lower grip of the fatigue specimen;

L_t, span between clamps;

L, gage length for the TF fatigue specimen;

D, length of the transition zone (fillets) for the TF fatigue specimen;

W, specimen minimum width;

t, specimen minimum thickness;

C, width of the specimen heads;

b, distance between the gripped zones and the transition of the fatigue specimen;

R, radius of the transition zone of the fatigue specimen;

E, Young's modulus;

δ_F, bending deflection imposed by the misaligned load frame;

θ_{xy}, rotation around the z axis imposed by the clamps;

θ_{yz}, torsion angle of twist imposed by the non co-planarity of the upper and lower clamps;

$\sigma_f^{\max}$, maximum fatigue stress imposed during uniaxial fatigue test;

F, reaction shear force on the clamps;

M, bending moment imposed by the clamps;

I_z, area moment of inertia of the cross-section of the specimen with respect to the z axis;

K_t, stress concentration factor;

ΔK, stress intensity factor;

m_i, stiffness correction factor for fatigue specimens;

σ, component of the stress field parallel to the loading direction on the faces perpendicular to the specimen main axis;

δ_F^{adm}, maximum admissible bending deflection parallel to the y axis (v displacement) according to the ASTM E 466-07 (2007) international standard.

3.1 Introduction

Fatigue characterization is a mainstream issue for a large number of engineering applications as it still causes most of the failure cases in service (Suresh, 1998). The development and optimization of new materials, workpieces and structures demands reliable experimental results. The fatigue life and fatigue strength of materials is assessed by the application of cyclic uniaxial loading on standard specimens such as the flat fatigue specimen with tangentially blending fillets between the uniform test section and the ends (TF) shown in Fig.3.1a and the flat fatigue specimen with continuous radius between ends (CR) shown in Fig.3.1b. The stress field developed in these specimens is more complex than the stress field in a beam with constant section (CS) shown in Fig.3.1c but the imposed loading should be uniaxial. Nevertheless, the application of a pure uniaxial loading is often difficult. Mounting specimens on misaligned load frames can induce severe parasite loadings. The lack of co-planarity and parallelism between the load frame grips induces parasite bending and torsion stresses. A specimen mounted in non coplanar grips works as a fixed-guided beam under bending stresses which will added to the imposed fatigue stresses. The subsequent mean stress increase results in a reduction of the fatigue life (Suresh, 1998). For instance, Eichlseder (2002) showed that the presence of a constant bending moment can significantly reduce the fatigue strength of a material and Lee et al. (2005) gave some factor corrections to the

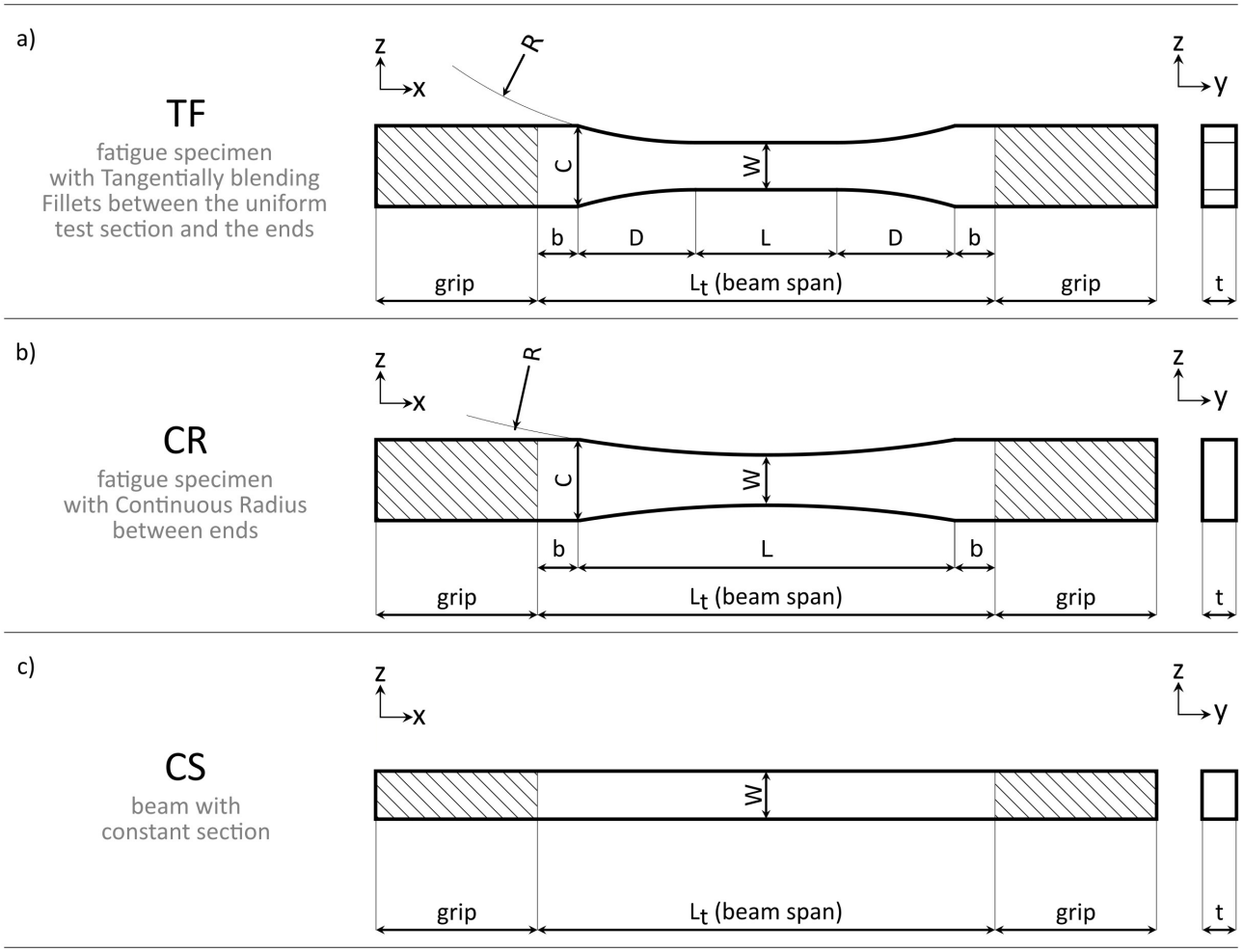

Figure 3.1: View of the specimen geometry for flat fatigue specimens a) with tangentially blending fillets between the uniform test section and the ends (TF) ; b) with continuous radius between ends (CR) and c) a beam with constant cross-section (CS).

fatigue life and fatigue strength as function of the imposed bending. It seems self-evident that the alignment of the load frame requires special attention.

A misaligned load frame will induce parasite bending stresses on the fatigue specimen. The standards give a tolerance for these bending stresses. According to the ASTM E 466-07 (2007) standard:

> *"The bending stresses (strains) so determined on either the cylindrical or rectangular cross section specimen should be limited to less that* 5 % *of the greater of the range, maximum or minimum stresses (strains), imposed during any test program."*

The standard refers to strains since the stresses are computed using Hooke's law and the lecture of strain gages placed in several positions on the specimen surface. A detailed procedure is proposed in the ASTM E1012-14e1 (2014) standard. The alignment is assessed by the use of device called the alignment transducer that consists in a standard specimen instrumented with several strain gages. This practice entails three issues. First, the misalignment of the load frame must be such that the imposed deformation will not plastically deform the trial specimen of the alignment transducer. This would require the replacement of the transducer of the trial specimen which is time consuming and expensive. Second, it assumes that the Young's modulus of the studied material is known and constant, which is not the case, for instance, for the cross-weld specimens studied by Ambriz et al. (2011). Third, the disposition of the strain gage system for highlighting both parasite bending and torsion stresses which needs to be adapted for each specimen geometry seems burdensome. For instance, for flat fatigue specimens such as the CR or TF, a trial fatigue specimen should be taken having several longitudinal strain gages centred with respect to the minimal cross-section. The trial specimen must be rotated around its main axis several times to check different orientations. The number of strain gages and turns depends on whether the specimen has a rectangular or a circular cross-section. For CR or TF fatigue specimens, both bending and torsion should be highlighted by two or three axial strain gages without further specifications. Not only are these methods cumbersome but also the information they provide is difficult to interpret in terms of misalignment. A more straightforward method is needed to address the issue of parasite stresses induced by misaligned load frames.

During the twentieth century, researchers in the field of experimental mechanics took advantage of the advancements in the field of digital image recording and processing for the implementation and development of image processing algorithms for performing measurements (Schreier et al., 2009). Namely, W. H. Peters (1982) proposed a basic algorithm to analyse digital images and track the planar displacement field of pixel subsets on the surface of a tensile specimen using digital image techniques. Sutton et al. (1983) improved the aforesaid algorithm to take into account the deformation of the tracked subsets and the inclusion of splines to get a sub-pixel resolution. Later on, the 2D standard correlation techniques were extended to a 3D displacement-strain field by the use of stereo-vision. By the inclusion of a second camera, Luo et al. (1993); Perng-Fei Luo (1994) succeeded to measure the complex three dimensional displacement field at the surroundings of the crack tip of a propagating fatigue crack on a surface of 13.2 mm × 16.8 mm with an outstanding accuracy of 3.7 µm.

In this work, the use of SDIC is proposed for studying, correcting, verifying and analysing the consequences of a misaligned load frame in terms of parasite stresses when mounting fatigue specimens. First, the bending deflection and torsion angle of twist imposed by the misaligned load frame are measured using SDIC and a TF fatigue specimen made of a titanium alloy. Second, simple procedures for the alignment of the load frame are

proposed. Third, using beam theory, the bending stresses for fatigue specimens having a) tangentially blending fillets between the uniform test section and the ends, and b) continuous radius between the ends are written as a function of the bending deflection and the specimen geometry. The aim is to determine in a simple manner if the potential parasite stresses induced by the load frame alignment respect the standard requirements without performing finite elements simulations. Finally, boundary conditions are applied to a numerical fatigue specimen to match the displacement fields measured by SDIC for validating the analytical model and studying the stress fields induced by the load frame misalignment. The analytical model is validated by comparing with the stress profiles along the specimen main axis obtained by finite elements simulations. The consequences of the load frame misalignment are discussed in terms of parasite stresses.

3.2 Experimental

Fatigue specimen A smooth TF fatigue specimen made of Ti6242 titanium alloy was machined following the ASTM E 466-07 (2007) international standard. The specimen geometry is shown in Fig.3.1a. The width and length of the uniform test section were respectively $W = 7\,\text{mm}$ and $L = 21\,\text{mm}$. Specimen thickness was $t = 3\,\text{mm}$. The width of the ends was $C = 12\,\text{mm}$. The radius and length of the transition zone were $R = 63\,\text{mm}$ and $D \approx 17.57\,\text{mm}$. The distance to the grip area was $b \approx 3.13\,\text{mm}$. The beam span was $L_t \approx 62.6\,\text{mm}$. Ti6242 titanium alloy Young's modulus is $E = 118\,\text{GPa}$. The microstructural and tensile properties of Ti6242 were documented by García and Morgeneyer (2019).

Load frame and specimen mounting A MTS 250 kN servo-hydraulic load frame with a set of MTS 647.10 hydraulic planar wedge grips with diamond serrations were used to clamp the specimens during fatigue tests. The load frame workbench, the load line and the standard SDIC strain monitoring system used in Section 3.2.1 were aligned with respect to gravity (see Fig.3.2a). The load frame workbench was aligned using a high precision water level. The load line and the SDIC strain monitoring system were aligned with respect to a self-levelling laser level, as shown in Fig.3.2b. Specimen mounting on the load frame upper clamp was performed using a laser level as a vertical reference. The force offset was set to zero having the lower grip open. After commanding a zero force, the closing of the lower clamp was commanded. This ensures that the specimen will not be exposed to compression loadings during the lower grip closing.

Clamping the specimen at both sides imposes boundary conditions to both ends. Displacement is fixed to zero in all directions. As shown in Fig.3.2d, rotations in the xy plane are fixed to zero ($\theta_{xy} = 0$). During testing, the loading of the specimen takes place by the displacement of the lower grip parallel to the x axis.

The position of the upper grip in the y axis must be adjusted so both grips will be coplanar. If this alignment is not properly achieved, a bending deflection δ_F parallel to the y axis is imposed to the fatigue specimen when clamped at both sides (see Figs.3.2c and 3.2d).

The lower grip is free to rotate around the x axis but some resistance to rotation may persist due to friction. This rotation is often driven by the torsional stiffness of the grips and the mounted specimens. If the grips torsional stiffness is considerably bigger than the specimen torsional stiffness, grips may remain non-parallel introducing a torsion angle of twist θ_{yz} (see Figs.3.2d). The settlement of both grips is primary since it prevents the introduction of parasite bending and torsion loadings. Methods for correcting the lack of both co-planarity

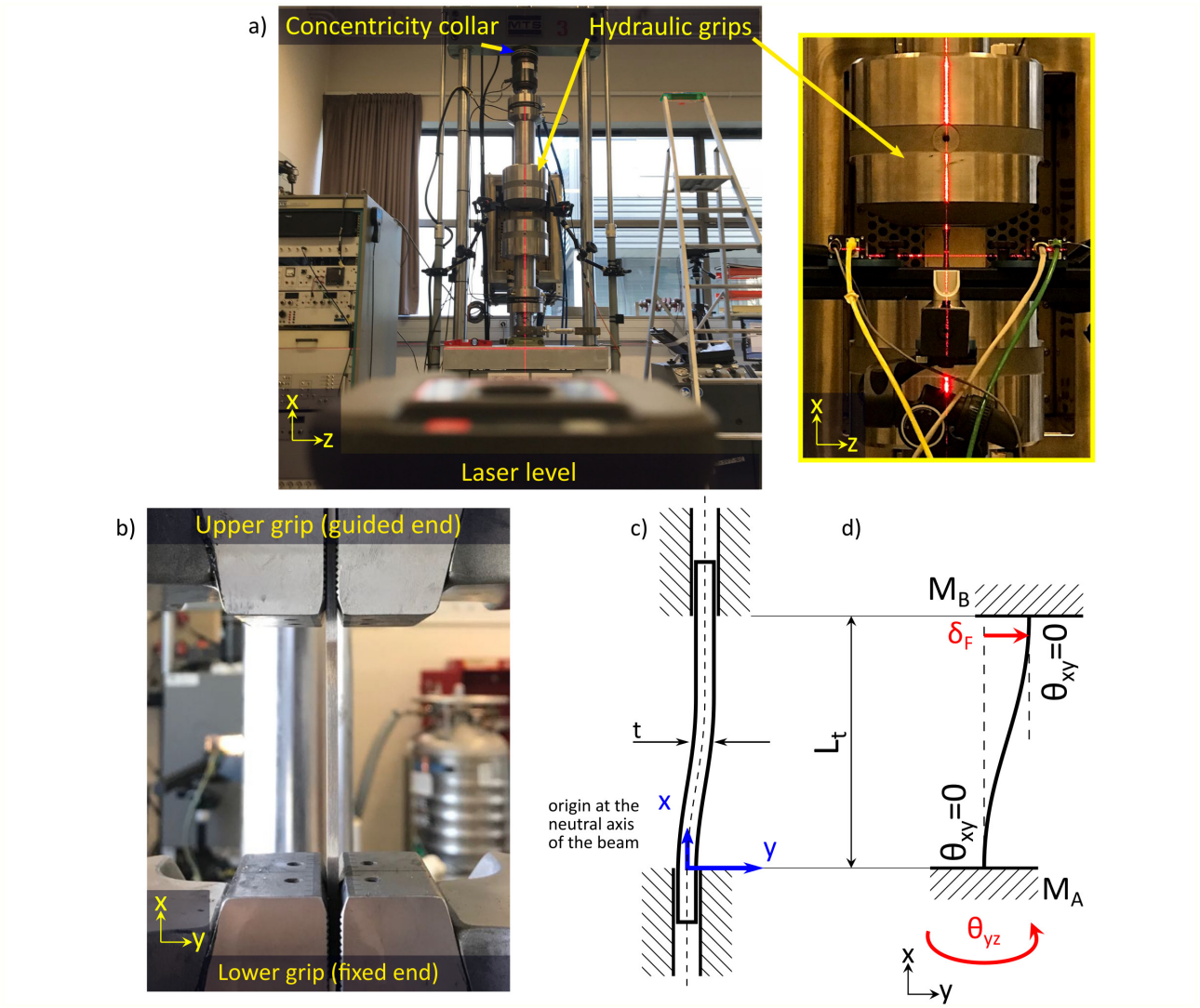

Figure 3.2: a) front view of the testing machine (xz plane) showing its alignment with respect to gravity using the laser level (red lines); b) side view of the mounted specimen (xy plane) in the closed-closed configuration; c) Schematic view of the mounted specimen in the closed-closed configuration (xy plane) and d) fatigue specimen modelled as a beam with imposed bending deflection δ_F and torsion angle of twist θ_{yz} (red arrows). Figs.3.2c and 3.2d share the frame of reference.

and parallelism of the grips are proposed in Section 3.2.2.

3.2.1 3D displacement field measurement using SDIC

The specimen out-of-plane displacement w during mounting was monitored using a standard system of SDIC. Two 2048 px × 2048 px Manta G-419B cameras were placed to follow the displacement of an artificial random black and white speckle depicted on the specimen surface. The cameras were aligned to gravity using a water level. The distance between the cameras was 26 cm and the camera-object distance was 31 cm, leading to a field of view of 65 mm × 65 mm. Images were exploited with Vic-3D™ from Correlated Solutions, Inc. (version 7.2.4, 2014). Subset size was 35 px ≈ 175 µm, step size was 9 px and filter size was 15 px. The spatial resolution was 160 µm. The uncertainty in the in-plane and out-of-plane displacements were respectively 0.2 µm and 0.4 µm.

The SDIC system was used to perform a two step stereo-correlation. The reference image was the specimen in the closed-open configuration (upper clamp only) and the final image was in the closed-closed configuration

(both clamps). The w out-of-plane displacement mappings of Fig.3.4 show the load frame in the initial state (Fig.3.4a), the load frame after the torsion correction (Fig.3.4b) and the load frame after the torsion and bending corrections (Fig.3.4c). Both corrections are explained in Sections 3.2.2. After the torsion correction, only the vertical gradient remains, indicating the parasite torsion loading was successfully eliminated (see Fig.3.4b). Finally, after both corrections, only very slight gradients are seen in Fig.3.4c meaning that the bending deflection was also eliminated.

Accurately measuring the bending deflection δ_F and the torsion angle of twist θ_{yz} from these mappings is quite difficult. To simplify this, the ξ and ζ axis in Fig.3.5a are introduced to measure the bending deflection δ_F and the torsion angle of twist θ_{yz} for the load frame in all states. Thick lines shown the displacement profiles of the load frame in the initial state, thin lines after torsion correction and dashed lines after bending-torsion correction. These axes show the same information as the mappings of Fig.3.4a-c, but reading the displacement magnitudes is simpler and more accurate. The mean value of the out-of-plane displacement profile for the τ axis represents the δ_F bending deflection and its slope the θ_{yz} torsion angle of twist (thick blue line in Fig.3.5b). From this graph it can be read that the load frame imposes a bending deflection of $\delta_F = 222.4\,\mu m$ and a torsion angle of twist of $\theta_{yz} = 1.9°$ when the specimen is set in the closed-closed configuration. The torsion correction led to a negligible torsion angle of twist and had barely no effect on the bending deflection (thin lines in Figs.3.5b and 3.5c). After the bending-torsion correction, both bending deflection and torsion angle of twist were negligible.

3.2.2 Alignment of the load frame

Torsion correction. Given that the lower grip is free to rotate around the x axis, if the torsional stiffness of the specimen is high enough, initially non parallel grips should auto-align during cycling. This practice is not recommended since, the application of a torsion angle of twist could deform plastically or damage specimens in some cases. Instead, prior to testing, the torsional auto-alignment should be done with a structure of higher torsional stiffness. In this study, a nickel-based alloy block of 120 mm × 120 mm × 10 mm and Young's modulus of 200 GPa, was cycled for 15 min with a maximum force 20 kN and a stress ratio of 0.1. The slope of the blue dashed line in Fig.3.5b is almost zero, exhibiting that the torsional stiffness of the Ni block was enough to self-align the load frame.

Bending moment correction. The elimination of the parasite bending loading is fulfilled by correctly positioning the upper grip along the y axis. The difficulty of this alignment is twofold. First, the determination of the required displacement is not easy to measure. Second, displacing a macroscopic structure such as the upper grip through a microscopic distance can be quite burdensome. In this work, the displacement of the upper grip was set to be equal to the bending deflection δ_f measured by SDIC in Section 3.2.1. For the load frame used in this study, the column holding the upper grip describes a pure translation parallel to the y axis by the adjustment of the four screws placed in the concentricity collar shown in Fig.3.2 and Fig.3.3. Once the target translation is determined, the required number of turns on the screws can easily be computed by knowing their pitch. The violet dashed line on Fig.3.5c shows that, after both corrections, a bending deflection of a 9 µm is applied to the specimen when mounted.

3.3 Analytical estimation of the parasite bending stresses

The aim of this section is to propose a simple tool for computing the induced bending stresses as a function of the bending deflection δ_F and the geometry of of two different geometries of standard fatigue specimens using beam theory. In Section 3.2.2, it was shown that the torsion correction of Section 3.2.2, leads to a negligible torsion angle of twist ($\theta_{yz} \approx 0$). On the other hand, despite both corrections, some bending remains. International standards require that bending stresses should not exceed 5 % of the imposed maximum fatigue stress $\sigma_f^{\max}$ (ASTM E 466-07, 2007). Hence, the question about the maximum admissible bending deflection

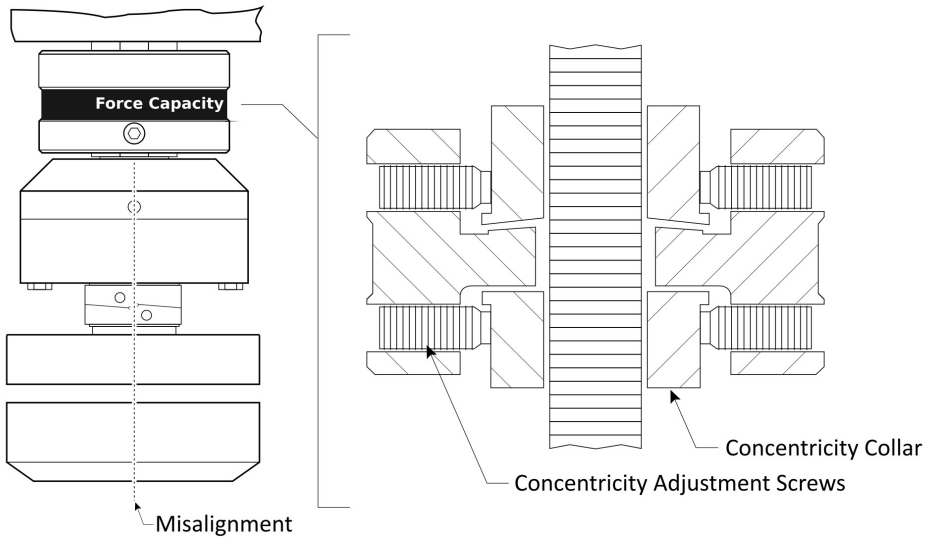

Figure 3.3: Schematic view of the concentricity collar of Fig.3.2 for the MTS 250 kN servo-hydraulic load frame showing the concentricity adjustment screws (MTS Systems Corporation, 2008) and the out-of-plane misalignment.

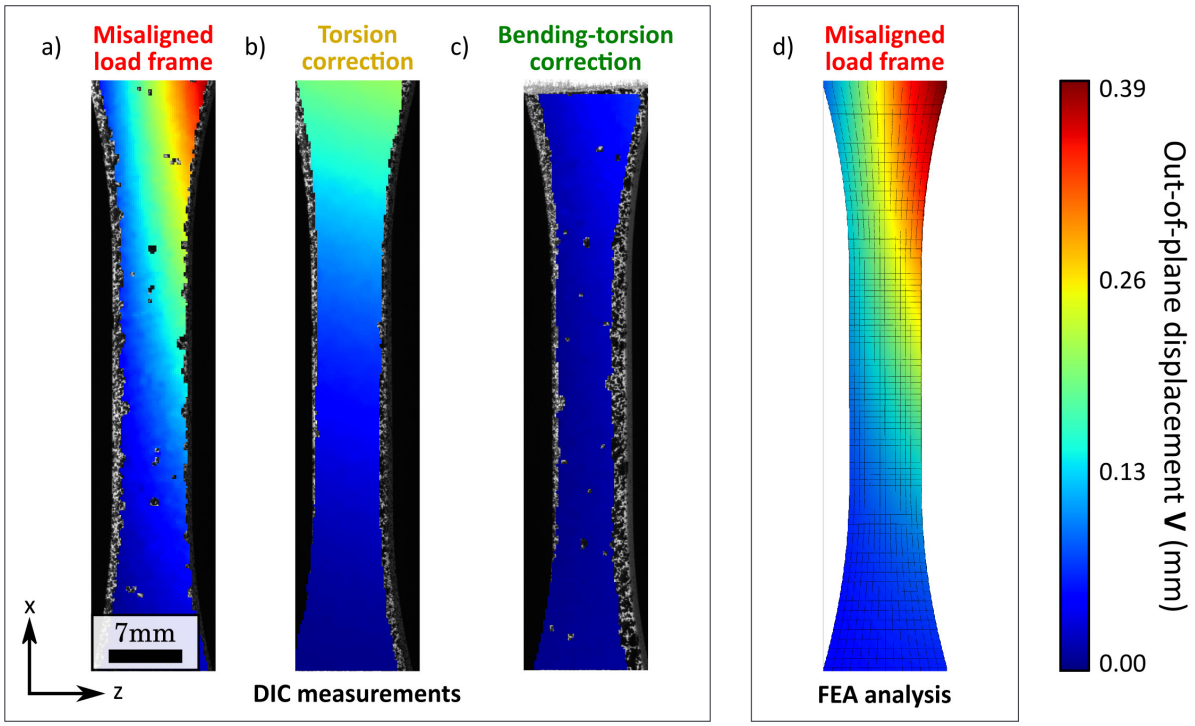

Figure 3.4: View of the fatigue specimen in the closed-closed configuration with the overlaid out-of-plane displacement field w obtained by DIC having the load frame in the a) initial state; b) after torsion correction; c) after torsion and bending correction and d) out-of-plane displacement field v obtained by Finite Elements Analysis.

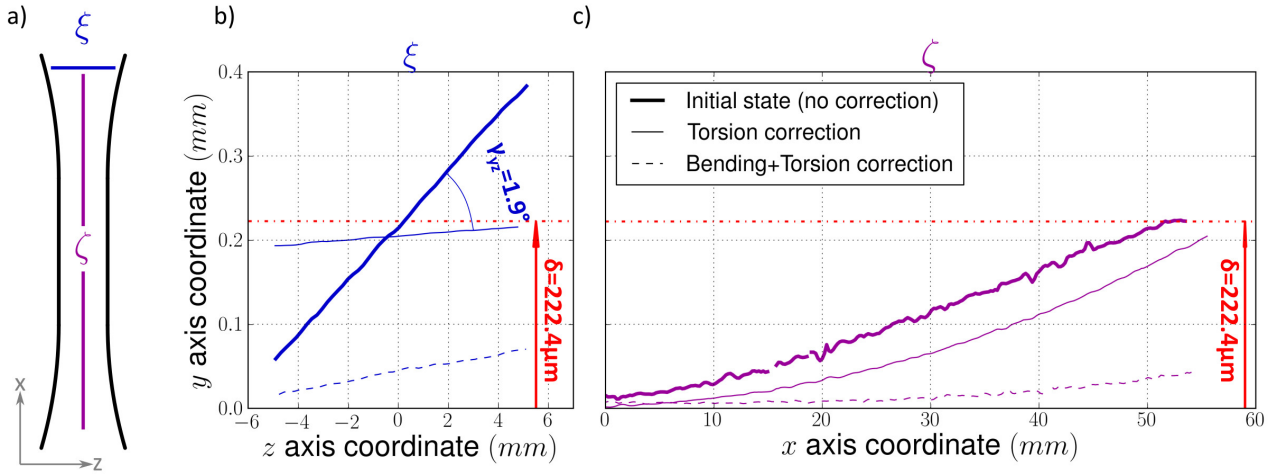

Figure 3.5: a) Schematic view of the fatigue specimen showing the location of the axis ξ and ζ (blue and violet, respectively) ; fatigue specimen w out-of-plane displacement in the closed-closed configuration obtained by SDIC for the load frame in the initial state (thick lines), after torsion correction (thin lines) and after bending+torsion correction (dashed lines) for b) the ξ axis and c) the ζ axis.

may arise.

If the torsion angle of twist is zero, the fatigue specimen works as a fixed-guided beam under bending stresses due to a bending deflection δ_F (see Fig.3.2d). The bending moment of such beam is given by Eq.3.1.

$$M(x) = F \times (x - L_t/2) \tag{3.1}$$

Where L_t represents the beam span and F the reaction force on the clamps which are function of the bending deflection δ_F and the bending stiffness of the specimen. The fixed-guided beam is supported by two clamps imposing two rotation and four displacement boundary conditions to the beam. Statically over-determined beams such as this one can be studied using energy based approaches such as Castigliano (1873)'s method. For example, the bending deflection δ_F can be computed by taking the partial derivative of the energy balance between the beam internal strain energy and the work of external forces with respect to the force on the clamps F, as shown in Eq.3.2.

$$\delta_F = \int_{L_t} \frac{M(x)}{E\,I_z} \frac{\partial M}{\partial F} dx \tag{3.2}$$

Where E stands for Young's modulus and I_z for the area moment of inertia of the cross section. By introducing the expression of the bending moment in Eq.3.1 and considering the elementary case of a beam with rectangular and constant cross-section, the bending form of Hooke's law can be written as stated in Eq.3.3 (for its detailed deduction, see Appendix A).

$$F = \frac{EWt^3}{L_t^3}\,\delta_F \tag{3.3}$$

This expression is a particular case of the results exhibited by Oberg et al. (2004) and stands for beams having constant width W. For its utilisation in fatigue specimens, a correction needs to be introduced.

3.3.1 Introduction of stiffness correction factor m_i to easily calculate parasite stresses

Fatigue specimens' moment of inertia is a function of the position on the beam main axis (x coordinate) due to their variable width. Hence, the resolution of the integral in Eq.3.1 becomes a little bit more unwieldy. The structural effect introduced by the specimen variable width can be taken into account by multiplying Eq.3.3 by a dimensionless correction factor m_i, where i stands for the type of fatigue specimen (TF or CR). This factor represents the ratio between the stiffness of the studied specimen and the equivalent constant section beam both having a thickness t, a span L_t and a minimal section of width W. Its analytical computation can be fulfilled by solving Eq.3.2 considering the area moment of inertia as a function of the x coordinate $I_z(x)$.

The ASTM E 466-07 (2007) standard establishes constrains concerning the design of fatigue specimens which are meant to reduce the stress concentration factor K_t. The main feature to fulfil this is the design of transition zones having very big radius ($R > 8W$). In this instance, the circular transition zone can reasonably be approximated with polynomials. In this work, the TF and CR fatigue specimens are studied by approximating the transition zones with both first and second degree polynomials. The choice of the polynomial degree undertakes a trade-off between simplicity and precision. When using first degree polynomials, the computation is very straightforward at the stake of some precision and contrarily, second degree polynomials are somewhat more laborious but give instead a very accurate solution.

3.3.2 Stiffness correction factor for fatigue specimens

Approximation of transition zones using first degree polynomials

The approximation of the transition zone using straight lines can be performed by using geometrical ratios. For both the TF and the CR fatigue specimens, the ratio between the widths of the gripped zones and the test uniform zone is $k_1 = C/W$. For the TF fatigue specimen, the ratio between the length of the transition zone and the test uniform zone is $k_2 = D/L$. The geometry of the fatigue specimens using the straight lines is shown in Figs.3.6a and 3.6c. The detailed resolution of Eq.3.2 considering linear transition zones is described in Appendix A.2.1 and A.3.1. For the sake of simplicity, this computation was performed considering that the distance between the grip and the beginning of the transition zone is null ($b = 0$).

TF fatigue specimen Having the values of k_1 and k_2, the value of stiffness correction factor m_{TF} can be computed using Eq.3.4. This expression is obtained by applying Castigliano (1873)'s method as detailed in Section A.2.1. In a simpler manner, the values of k_1 and k_2 can be read from the abacus of Fig.3.6a which was plotted using Eq.3.4. The contour levels of the stiffness correction factor are close to vertical lines when k_1 tends to 1 revealing that the influence of k_2 is very small. For decreasing values of k_1, the geometry of the specimen tends to the CS beam. Indeed, for the particular case of $k_1 = 1$, the contour level of m_{TF} is a vertical line of level 1 and Eq.3.6 takes the bending form of Hooke's law for the CS beam, as stated in Eq.3.3. For increasing values of k_1, the stiffness correction factor m_{TF} becomes increasingly sensitive to the value of k_2. The vertical and horizontal dashed black lines in Fig.3.6a reference to the values of k_1 and k_2 for the TF fatigue specimen of Section 3.2. The corresponding stiffness correction factor values is $m_{\mathrm{TF}} = 1.4$.

CR fatigue specimen With the value of k_1, the value of the stiffness correction factor m_{CR} can be read from the abacus of Fig.3.6d that was obtained by means of Eq.3.5. The dashed lines represents solution for $k_1 > 0$. The black line represents the stiffness correction factor for CR fatigue specimens $k_1 > 1$. As it can be seen in Appendix A.3.1, the function is not defined at $k_1 = 1$ but the function converges to $m_{\mathrm{CR}} = 1$ as k_1 tends to 1 which represents the case of the CS beam. A linear regression for the solution described in the Appendix A.3.1 is overlaid in Fig.3.6. The determination coefficient is $R^2 = 0.98$.

$$m_{\mathrm{TF}} = (2k_2+1)^3 : \left\{ \frac{12\,k_2^3}{(1-k_1)^3} \left[(1-k_1)^2 - (1-k_1)\left(2\,\frac{(k_2+1/2)(1-k_1)}{k_2} + k_1 \right) + \left(\frac{(k_2+1/2)(1-k_1)}{k_2} + k_1 \right)^2 \ln\left(\frac{1}{k_1} \right) \right] + 1 \right\} \tag{3.4}$$

$$m_{\mathrm{CR}} = \left\{ \frac{12}{(1-k_1)} \left[\left(\frac{1}{2} + \frac{k_1}{2(1-k_1)} \right)^2 \ln\left(\frac{1}{k_1} \right) - \left(\frac{3}{8} + \frac{k_1}{4(1-k_1)} \right) \right] \right\}^{(-1)} \tag{3.5}$$

Approximation of transition zones using second degree polynomials

Considering the centre of curvature defined by Cauchy (1826), the circular shape of the transition zones can be approximated by second degree polynomials having the same radius of curvature. In behalf of simplicity, the integral in Eq.3.2 is solved using second order polynomials with quadratic coefficients of $\frac{1}{2R}$. The accuracy of this approximation increases with increasing R. The resolution for both geometries is detailed in the Appendix A. The expression of the m_i factor depends on the fatigue specimen geometry and it can be read from Table 3.1.

3.3.3 Computation of the maximum admissible bending deflection $\delta_F^{\mathbf{adm}}$

Eq.3.3 states the bending form of Hooke's law for a CS beam. The introduction of the aforementioned stiffness correction factor m_i allows the bending form of Hooke's law for fatigue specimens to be written (see Eq.3.6).

$$F = m_i \frac{EWt^3}{L_t^3} \delta_F \tag{3.6}$$

As explained in Timoshenko (1956), one can compute the bending stresses σ_{xx} as a function of x by substituting Eq.3.6 and Eq.3.1 in Eq.3.7.

$$\sigma_{xx}(x) = \frac{M(x)\,y}{I_z(x)} \tag{3.7}$$

By replacing the expressions of the bending moment (Eq.3.1) and the corresponding moment of inertia in Eq.3.7, the general expression for the bending stress is obtained. Under bending, the bending stresses are maximum at the specimen surface ($y = t/2$) (Timoshenko, 1956).

$$\sigma_{xx}(x) = m_i \left(\frac{EWt^4\delta_F}{2L_t^3} \right) \frac{(x - L_t/2)}{I_z(x)} \tag{3.8}$$

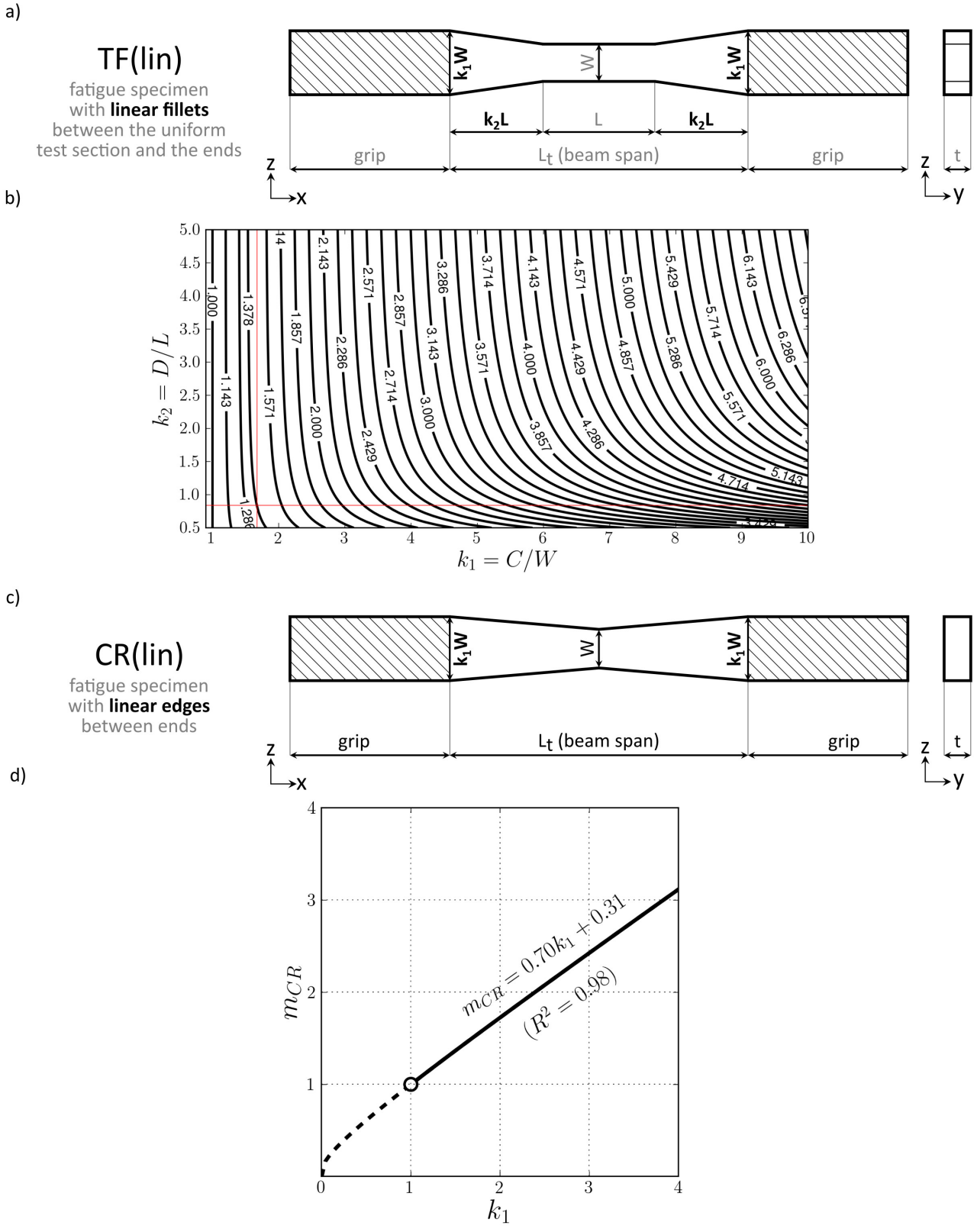

Figure 3.6: a) Simplification of TF fatigue specimen using first with linear fillets between the ends; b) abacus for the simplified TF fatigue specimen stiffness correction factor m_{TF}; c) simplification of CR fatigue specimen using first with linear edges between the ends; d) abacus for the simplified CR fatigue specimen stiffness correction factor m_{CR}. All transition zones are approximated using first degree polynomials.

The standard establishes the maximum admissible bending stresses with a poor precision about the location of its measurement. Considering that the maximum bending moment is located at the clamps ($x = 0$ and

Specimen	m_i
TF	$\left\{\frac{8W}{CL_t^3}\left[\left(\frac{L_t}{2}\right)^3-\left(D+\frac{L}{2}\right)^3\right]-\frac{24RW}{L_t^3}\left[\frac{L}{2}\ln\left(\frac{RW}{D^2+RW}\right)-\frac{(L^2-4RW)}{4\sqrt{RW}}\tan^{-1}\left(\frac{D}{\sqrt{RW}}\right)-D\right]+\frac{L^3}{L_t^3}\right\}^{-1}$
CR	$\left\{\frac{W}{CL^3}\left[\frac{b^3}{3}+\frac{b^2L}{2}+\frac{bL^2}{4}\right]+\frac{RW}{L^3}\left[\frac{L}{2}-\sqrt{RW}\tan^{-1}\left(\frac{L}{2\sqrt{RW}}\right)\right]\right\}^{-1}$
CS	1

Table 3.1: Stiffness correction factor m_i for the computation of the reaction force on the clamps for different fatigue specimens using second degree polynomials for the transition zones.

$x = L_t$, see Eq.3.1), the authors have chosen to take the bending stresses at these locations as a reference for comparing with the standard requirements. On this case, the maximum admissible bending deflection δ_F^{adm} can be computed using Eq.3.9

$$\frac{M(L_t)\,t/2}{I_z(L_t)} \leq 0.05\sigma_f^{\max} \qquad \delta_F^{\text{adm}} \leq \frac{\sigma_f^{\max} L_t^2 C}{60 m_i E W t} \tag{3.9}$$

Example

The study conducted by García and Morgeneyer (2019) had as aim the assessment of the strength and fatigue strength of Ti6242 linear friction welded joints using the load frame and the fatigue specimen described in Section 3.2. The maximum fatigue stress during the fatigue trials was $\sigma_f^{\max} = 700\,\text{MPa}$. By the use of Eq.3.9 and the computation of m_{TF} taken from Table 3.1, it can be calculated that the maximum admissible bending deflection was $\delta_F^{\text{adm}} = 160\,\mu\text{m}$ which is lower than the $\delta_F = 222.4\,\mu\text{m}$ measured in Section 3.2.1. If the torsion and bending corrections of Section 3.2.2 had not been performed prior to the fatigue trials, the results would not had been in agreement with the standard requirements.

3.4 Finite element analysis verification

The purpose of this Section are to validate the analytical model proposed in Section 3.3, and to further study the effects of the bending and torsion stress fields on a fatigue specimen mounted on a misaligned load through Finite Element Analysis (FEA). The Zset FE software (Besson and Foerch, 1998) was used to perform 3D linear elastic simulations over meshes of the CS beam and the CR and TF fatigue specimens using eight-node brick elements. The geometrical parameters of the TF specimen are described in 3.2. The values of the width of the minimal cross-section W, the thickness t and the beam span L_t for both the CR fatigue specimen and

the CS beam are those of the TF specimen described in Section 3.2. The radius of the CR specimen was $R = 159\,\text{mm}$. Boundary conditions were applied at both endings of each mesh to simulate the closing of both grips. The bottom and top grips worked respectively as the fixed and guided ends. During mounting, both bending and torsion occur at the same time. In furtherance of the analysis, these loadings were uncoupled. For each geometry, displacement boundary conditions were applied to the top grip to simulate four stages: the application of the maximum admissible bending deflection δ_F^{adm}, the application of the bending deflection δ_F measured in Section 3.2.1, the torsion angle of twist θ_{yz} measured in Section 3.2.1 and finally, the application of the maximum fatigue stress $\sigma_f^{\max} = 700\,\text{MPa}$ studied in section 3.3.

3.4.1 Validation of the analytical model

Figs.3.7, 3.9 and 3.8 show the stress profile over the ζ axis at the first simulation stage (application of the theoretical maximum admissible bending deflection δ_F^{adm}) for the CS beam and the TF and CR fatigue specimens. The horizontal axis corresponds to the x coordinate in the ζ axis. On top of every graph, a view of each mesh can be seen. Notice that these views were scaled to match the graph horizontal axis. The red line represents the stress profile obtained by simulations. The dashed lines represent the stress profiles obtained by the analytical model of Section 3.3 computed using Eq.3.7. The blue and black dashed lines represent the stress profile of the fatigue specimen having transition zones approximated with first degree polynomials and second degree polynomials, respectively. The standard maximum admissible bending stress is plotted in horizontal dashed red lines. The theoretical analysis proposed in Section 3.3 is validated by two features. First, the application of the maximum admissible bending deflection computed in Section 3.3 leads to the standard maximum admissible stress ($0.05\sigma_f^{\max} = 35\,\text{MPa}$) at both ends of the specimen. Second, far from the boundary conditions, there is a strong agreement between the stress profiles obtained by the simulation and the analytical model using second degree polynomials. Furthermore, it should be pointed out that, for the geometrical parameters used here, the proximity of the analytical model with both approximations and the simulated one reveals that having replaced the circular transition zones by polynomials is a very good approximation.

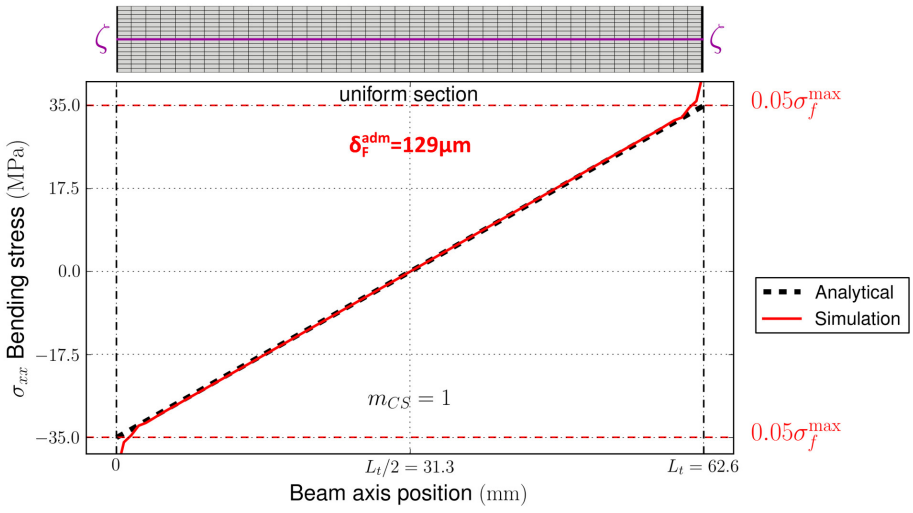

Figure 3.7: Bending stress σ_{xx} profile over the ζ axis for the CS beam comparing the results for the analytical solution (dashed black line) and the numerical solution (red line).

The stress profile of the CS beam is linear (see Fig.3.7). This is expected since having a constant moment of

inertia, the bending stress is proportional to the linear bending moment (see Eq.3.7). The stress profiles of the TF and CR fatigue specimens are more complex (see Figs.3.9 and 3.8). Despite of that, in the zones where the width is constant, the stress profile remains linear. As explained in Section 3.3, the stiffness correction factor for the CS beam is $m_{\text{CS}} = 1$ and since the width is constant ($C = W$), the bending stress profile is independent of the width of the specimen (see Eq.3.9). Hence, comparing the stress profile of the CS beam to the TF or CR fatigue specimens is unintuitive.

Comparing the TF and CR fatigue specimens seems more relevant. In the graphs of the TR and CR fatigue specimens, the value of m_i and the maximum admissible bending deflection are indicated. Having that m_{CR} is bigger than m_{TF}, it can be said that the bending stiffness of the CR specimen is bigger that the TF specimen. Thus, a smaller deflection is required to reach the same level of bending stress. Indeed, the maximum bending deflection for the TF specimen is smaller than the one of the CR specimen.

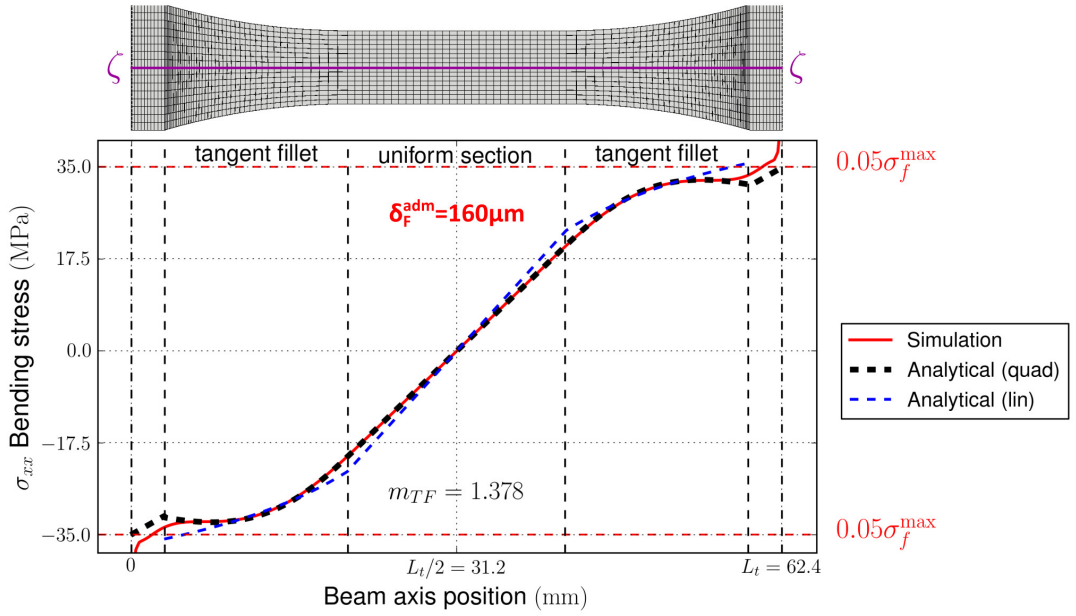

Figure 3.8: Bending stress σ_{xx} profile over the ζ axis for the CR fatigue specimen comparing the results for the analytical solution with a first degree polynomial on the transition zone (dashed blue line), analytical solution with a second degree polynomial on the transition zone (dashed black line) and the numerical solution (red line).

3.4.2 Effect of parasite torsion loading

Fig.3.10 shows the stress field at the end of the gage length and at the end of the specimen span for the three stages mentioned in Section 3.4. The linearity of the stress as function of y predicted in Eq.3.7 is observed in Fig.3.10a. The colour bar of Fig.3.10a and Fig.3.10b were fixed at the same range. This highlights the fact that some stress in the loading direction is added by the torsion angle of twist rotation. The scale of Fig.3.10c was shifted to the values around the applied fatigue stress. One can see that torsion increases stress at the corners.

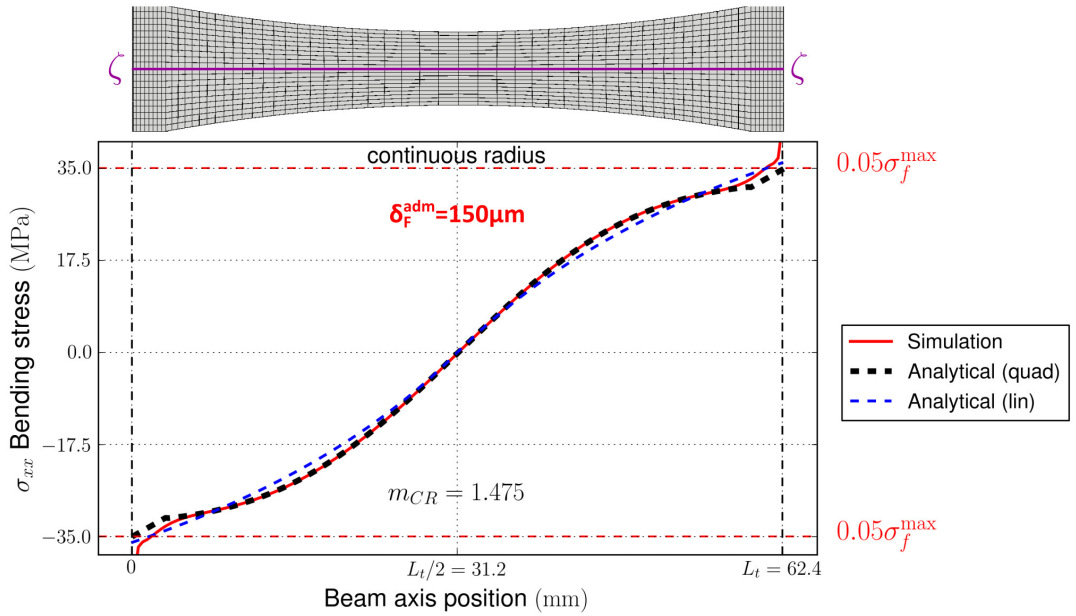

Figure 3.9: Bending stress σ_{xx} profile over the ζ axis for the TF fatigue specimen comparing the results for the analytical solution with a first degree polynomial on the transition zone (dashed blue line), analytical solution with a second degree polynomial on the transition zone (dashed black line) and the numerical solution (red line).

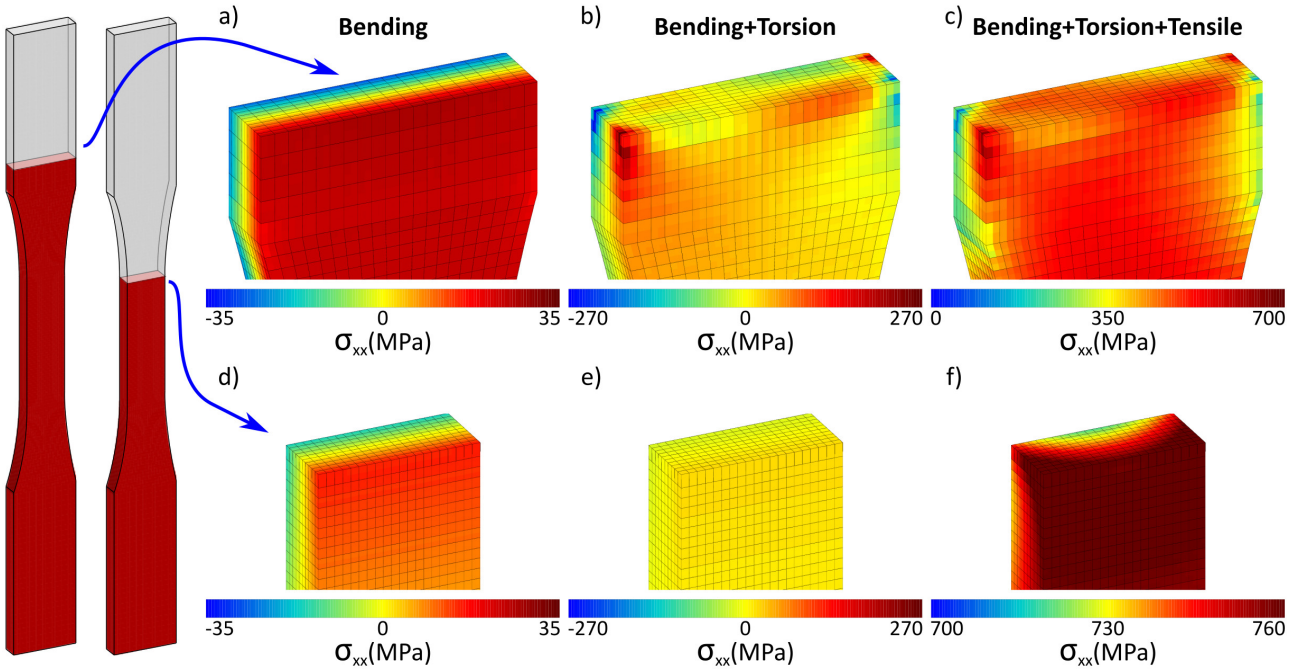

Figure 3.10: Maps of the σ_{xx} stress for the sections at the end of the gage length (a, b and c) and at the end of the span (c, d and e) for : pure bending (a and d), bending and torsion (c and e) and bending, torsion and the application of the maximum fatigue stress $\sigma_{max} = 750\,\text{MPa}$.

3.5 Procedure for the use of SDIC on the alignment of a load frame

In this Section, a brief description of the procedure for the alignment of a load frame prior to fatigue trials is described using the tools presented in this paper that can be used by technicians, engineers and researchers instead of the strain gage based procedure. The steps to be followed are summarised in Fig.3.11 and described hereafter:

1. *Compute the stiffness correction factor m_i for the specimen to be used.*

   The stiffness correction factor can be calculated using the approximations of first or second degree polynomials. The first degree approximation will give a rough approximation with very simple computations. Its value can be read from the abacus of Figs.3.6. For a better approximation, compute using the formulas shown in Table 3.1.

2. *Compute the maximum admissible bending deflection δ_F^{adm}*

   For its computation, use the formula in Eq.3.9 and the following parameters:

   - Stiffness correction factor: m_i

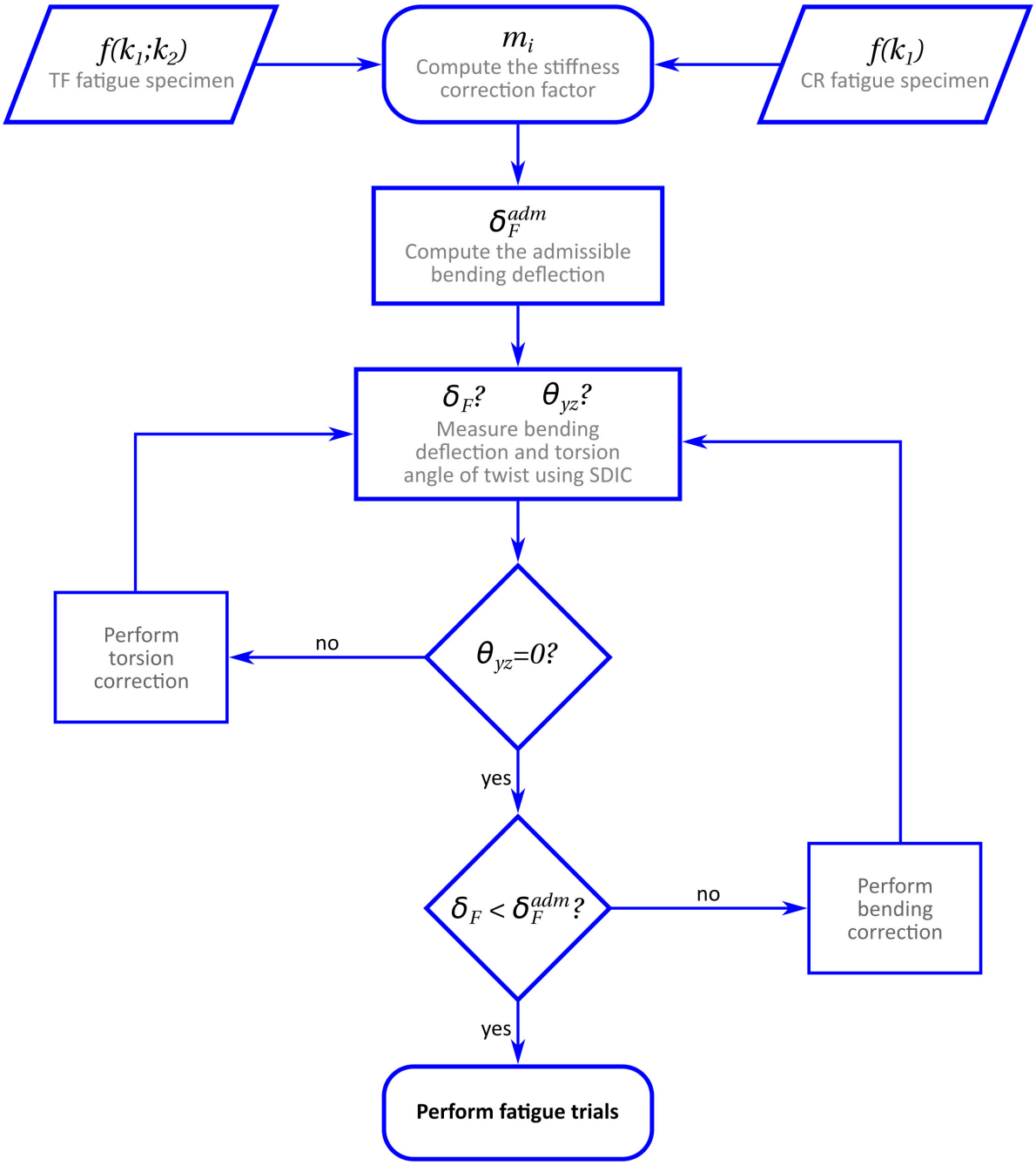

Figure 3.11: Procedure for the alignment of a load frame using SDIC.

- Widths at the gripped areas and minimal cross-section: C and W.
- Fatigue specimen span: L_t
- Fatigue specimen thickness: t
- Maximum fatigue stress to be applied during the trials: $\sigma^f_{\max}$
- Material's Young's modulus: E

3. *Measure bending deflection δ_F and torsion angle of twist θ_{yz} using SDIC.*
   Set the SDIC strain monitoring system, depict a black and white speckle over the surface of a trial specimen o as plane cut-off of comparable dimensions, mount the specimen and perform a two step correlation. Reference image: specimen clamped only on one side. Deformed image: specimen clamped at both sides.

4. *Verify SDIC measurements.*
   The torsion angle of twist should be barely 0 and the measured bending deflection δ_F should be at least inferior to the admissible bending deflection δ_F^{adm}. In the ideal case, it should also be 0. If this is not the case, perform torsion and bending correction as described in Section 3.2.2.

5. *Performe fatigue trials.*

3.6 Discussion

3.6.1 Structural effect introduced by the variable width of the fatigue specimen

In Eq.3.9 the widths of the specimen at the grips and at the minimal section are respectively in the numerator and denominator. In the particular case of a beam with constant cross-section, not only these factors would simplify but also m_i would be unitary. It is interesting to note that, if the beam has a constant section, the bending stresses and consequently the maximum admissible bending deflection are independent of the width of the beam, within the hypotheses of beam theory. This fact highlights the structural effect that the variable width introduces to the stiffness of the fatigue specimen.

In Section 3.3.3, the bending stress to be compared with standards requirements was taken at the both clamps ($x = 0$ and $x = L_t/2$). The width of the fatigue specimen at this locations is $C > W$. It could be argued that since the cross-section surface is bigger, the applied normal stress during the fatigue test is lower and therefore, the contribution of the bending stress to the total stress could be neglected. By the use of Eq.3.1, it can be shown that the bending stress increases with decreasing span (L_t) or decreasing width at the gripped zones (C). This is particularly important to consider since sufficiently small values of L_t and C not only would imply important bending stresses but also plasticity could be reached for fatigue tests having values of maximum fatigue stress close to the yielding limit.

It should be noticed that since the bending moment is zero at the centre of the beam ($x = L_t/2$), the bending stresses are zero as well. Thus, if the misalignment of the grips were to be measured using a strain gage system

as advised by the standard ASTM E 466-07 (2007), it is recommended to use initial gage lengths as long as possible to capture the strain due to the stresses far from the centre. Moreover, if a SDIC system is not available, a rough measure of out-of-plane displacement could be performed using a probe for later comparison with the maximum bending deflection stated in Eq.3.9. The out-of plane displacement fields exhibited in Section 3.2.1 have shown that the measure should be done close to the clamps on the specimen main axis.

3.6.2 Surface fatigue crack initiation and parasite bending stresses

Fatigue crack initiation occurs often but not only at defects on the fatigue specimen surface (Le Jolu et al., 2015). In some materials, fatigue crack initiation can take place internally in the surroundings of inclusions (Abdesselam et al., 2018; Pineau and Antolovich, 2016), dendritic defects (García and Morgeneyer, 2019), oxides (Wang et al., 2006), etc. A misaligned load frame induces bending stresses which depend on x and y, as it can be seen in Eq.3.7. Furthermore, the bending stress profile is linear with the coordinate parallel to the specimen thickness y, having its maximum at the surface ($\|y\| = t/2$). This implies that the bending stresses favour the fatigue crack initiation at the surface of the specimen. These considerations underline the importance of load frame alignment prior to fatigue trials, specially in the case of materials having potential internal crack initiation sites.

3.6.3 Parasite torsion loading and axisymmetric specimens

If a cylindrical rod is exposed to a torsion loading around its main axis x, the stress field turns out to be pure shear in perpendicular yz planes (Timoshenko, 1956). For the fatigue specimens in this work, the vertex on the rectangular cross-sections add a structural effect that leads to some stress parallel to the loading direction, as it can be seen in Figs.3.10c-d. Thus torsion favours fatigue crack initiation on the corners of rectangular specimens.

Even if this torsion effect could be abated by choosing fatigue specimens with circular cross-section, it is advisable to eliminate parasite torsion stresses since they add components to the deviatoric part of the stress tensor that could lead to a premature yielding. As a consequence, the fatigue life would be shortened.

3.6.4 The use of SDIC for the alignment on fatigue assessments

The most remarkable advantage of using SDIC for analysing the alignment of a load frame is exhibited in the out-of-plane mapping of Fig.3.4a. In contrast with the standard strain gage system proposed by the standards, SDIC captures and clearly highlights the existence of both bending and torsion parasite loadings by the horizontal and vertical gradients on the out-of-plane mapping. The effectiveness of both corrections seen in Figs.3.4b-c is also worthy of being noticed.

In this paper, the importance of the alignment of the load frame for the fatigue life and fatigue strength assessments was shown. The alignment of the loading frame is also very important for other fatigue assessments. For instance, in study of fatigue crack propagation the alignment is major concern. These trials are often performed by applying a uniaxial cyclic loading on compact tension specimens or biaxial cyclic loadings on cruciform specimens. Researchers on this domain, control the alignment of the load frames by the use of

systems of strain gages as proposed by the standards (Covey and Bartolotta, 2000; McMaster and McKeighan, 2004). Notwithstanding, SDIC could also be used for the alignment of these load frames.

For the assessment of the fatigue life and fatigue strength, the effect of the bending stresses and their subsequent influence on the mean fatigue stress were discussed. In fatigue crack propagation, the key variable is the stress intensity factor ΔK which is a function of the stress amplitude $\Delta\sigma$ applied parallel to the loading direction during cycling. Fatigue crack initiation occurs during cycling when the stress intensity factor reaches a certain threshold value ΔK_{th} and its increase during cycling is the driving force for the fatigue crack propagation Suresh (1998). Applying parasite bending stresses to a compact tension or a cruciform specimen under biaxial loading can have several consequences. First, the computation of the stress intensity factor would be distorted. Second, the application of an asymmetrical loading will drive the fatigue crack propagation path in unwanted directions. Finally, the application of bending stresses implies compression stress on one side favouring crack closing and tensile stress on the other increasing the stress intensity factor.

Seemingly, parasite torsion stresses would remain unseen in the computation of the stress intensity factor. Nonetheless, as explained in Section 3.6.3, shear could imply premature yielding.

3.7 Summary and conclusions

The parasite stresses during fatigue specimen mounting in a misaligned load frame were studied through and experimental, analytical and numerical approach. Out-of-plane displacement fields obtained by SDIC are a very innovative and simple tool to analyse the alignment of a load frame prior to fatigue trials. A very accurate analytical model is proposed for calculating the maximum admissible bending deflection δ_F^{adm} for flat CR and TF fatigue specimens using first degree and second degree polynomials for approximating the geometry of the transition zones. The numerical results validated the analytical models.

This approach is exemplified thanks to a study conducted by García and Morgeneyer (2019). For the target maximum fatigue stress and the geometry of TF fatigue specimen, the maximum admissible bending deflection was $\delta_F^{\text{adm}} = 160\,\mu\text{m}$ which was higher than the initially measured $\delta_F = 222.4\,\mu\text{m}$ by SDIC. Simple procedures were established for the alignment of the load frame which led to final bending deflection of $\delta_F = 16\,\mu\text{m}$ and neglectable torsion angle of twist.

A misaligned load frame induces parasite stress on fatigue specimens that favour fatigue crack initiation on the specimen surface and corners. The effect of torsion stress is lower in axisymmetric fatigue specimens compared to the rectangular section specimens.

Acknowledgements

Abdennour Meddour and Alain Köster at *Centre des Matériaux (Paris, France)* are gratefully acknowledged for their kind help on the alignment of the loading frame. Vladislav Yastrebov and Samuel Forest at *Centre des Matériaux (Paris, France)*, and Sebastian Nievas at *UNNOBA (Junín, Argentine)* are kindly thanked for their insight on the mathematical formulations. The authors acknowledge the financial support from the French National Research Agency (ANR) and FRAE through OPTIMUM ANR-14-CE27-0017 project.

4

Strength and fatigue strength of a similar Ti6242 LFW joint

In the previous chapter, a procedure for aligning the load frame was proposed and applied.

In this chapter, the strength and fatigue strength of a similar Ti6242 LFW joint is studied. Tensile tests instrumented with SDIC over smooths cross-weld specimens are performed to track plastic activity in the welded structure in time and space. The fatigue crack initiation location in the welded structure and the associated fatigue crack propagation mechanisms are assessed by SEM observations.

This work was published in the Journal Fatigue & Fracture of Engineering Materials & Structures under the title *Strength and fatigue strength of a similar Ti6242 LFW joint* and is available in https://doi.org/10.1111/ffe.12973.

Résumé de chapitre

Les résistances en traction et en fatigue de joints mono-matériau Ti6242 soudés par friction linéaire (LFW) ont été étudiées et comparées au matériau de base (MB). Des observations non destructives ont révélé la présence de pores dans l'interface de la soudure. Le noyau de la soudure a montré une résistance supérieure au matériau de base provoquant une ductilité macroscopique réduite. La déformation locale et la vitesse de déformation normalisée ont été abordées par SDIC et elles ont souligné une activité plastique précoce dans le voisinage du noyau de la soudure qui a été attribuée aux contraintes résiduelles. Pour la durée de vie visée de 10^5 cycles, la résistance en fatigue a légèrement été réduite mais elle a également été mise en péril par une forte dispersion. En effet, un amorçage interne de fissure de fatigue en œil de poisson a été observé autour d'un défaut dendritique inattendu. Ce défaut a été associé à une fusion localisée lors du soudage, dû à la présence de laiton émanant de l'usinage par électroérosion.

Chapter Abstract

Strengths for monotonic and cyclic loadings of similar overmatching Ti6242 Linear Friction Welds (LFW) were studied and compared to the parent material (PM) behaviour. Non destructive synchrotron observations revealed the presence of pores in the weld interface. The Weld Centre Zone (WCZ) showed a higher strength leading to lower macroscopic ductility of the cross-weld samples. Local strain and normalized strain rate have been assessed by stereo Digital Image Correlation (DIC) and revealed an early plastic activity at yielding in the vicinity of the WCZ attributed to residual stresses. For the target life, the fatigue strength was slightly reduced but compromised by a strong scatter. Indeed, an internal fish-eye fatigue crack initiation was found on an unexpected dendritic defect that was very different from the PM microstructure and the known martensitic α' in the WCZ. The dendritic defect was linked to surface contamination prior to welding and led to melting.

Contents

Figures

Keywords

Titanium alloy, Linear friction welding, Mechanical properties.

Nomenclature:

α (h.c.p.), hexagonal closed packed titanium crystal lattice; β (b.c.c.), body centred cubic titanium crystal lattice; F, friction axis; P, pressure axis; T, thickness axis; E, Young's modulus; Y, yield strength; UTS, Ultimate Tensile Strength; $\varepsilon_{\mathrm{macro}}$, macroscopic engineering strain; $\varepsilon_{\mathrm{PP}}$, local strain following the P axis; $\dot{\varepsilon}_{\mathrm{PP}}$, local strain rate following the P axis; $\sigma_{\varepsilon_{\mathrm{PP}}}$, standard deviation on the local strain following the P axis during rigid body displacement; $\sigma_{\max}$, maximum fatigue stress; R, fatigue stress ratio; N_f, fatigue life; ΔK, stress intensity factor; a, crack size; da/dN crack growth per cycle.

4.1 Introduction

Titanium alloys are widely used in the aerospace industry (Boyer, 2010). An increasing demand of titanium and composite materials has recently been observed (Gabriele, 2016) due to the progressive growth of air traffic (Airbus, 2017) and their high compatibility of working together, such as galvanic and thermal expansion coefficients compatibility and corrosion protection (Boyer, 1995). Titanium's excellent corrosion resistance, mechanical resistance and low density give them increasing importance. Ti6242 highlights a very good creep resistance and it enables working in high temperature environments (Chen, 1982).

A need to improve the buy-to-fly ratio is raising and it could be satisfied, *e.g.* by the use of novel joining techniques (Boyer, 2010). Linear Friction Welding (LFW) is a solid-state joining process which was first suggested by (Ritcher, 1929) and it works as follows: A cantilever workpiece, also known as stationary workpiece, is in contact with a second piece named the oscillating workpiece which follows a linear oscillatory motion. After a fraction of a second of friction, a forging pressure is applied to achieve a target axial shortening. High levels of plastic deformation and localized heat are generated around the weld interface following four distinct phases. Microstructural changes, unknown mechanical properties and considerable levels of residual stresses are found in four distinct welding zones (Vairis, 1997) : the weld centre zone (WCZ), the thermo-mechanically affected zone (TMAZ), the heat affected zone (HAZ) and the parent material (PM). This process is very quick, reduces bulk milling operations, enables the conception of dissimilar welds and, in some cases, enhanced weld mechanical properties.

LFW joints may be subjected to strong mechanical and cyclic loadings (Flipo et al., 2016; García, 2011; Mateo et al., 2009; Kuroki et al., 2014). Understanding their mechanical properties in monotonic and cyclic loadings is fundamental for its industrial application. Several authors studied the tensile properties of similar LFW joints using as parent material comparable alloys to Ti6242, such as Ti64 and IMI-834 (Flipo et al., 2016; Mateo et al., 2009; Kuroki et al., 2014; Li et al., 2012, 2008; Debeugny and Racineux, 2013; Dalgaard, 2011; Dalgaard et al., 2012a; Wen et al., 2014; Meshram and Mohandas, 2010; Zhao and Fu, 2015). Some similar and dissimilar joints failed far from the WCZ (Mateo et al., 2009; Li et al., 2012; Debeugny and Racineux, 2013; Dalgaard, 2011; Wen et al., 2014; Meshram and Mohandas, 2010). For instance, Dalgaard et al. (2012b) observed that the formation of a fine microstructure in the WCZ of a similar IMI-834 LFW joint led to overmatching strength. In a similar manner, (Li et al., 2008) documented the overmatching strength of a Ti64 LFW joint.

During tensile tests, the macroscopic strains are typically measured using standard extensometers. This measurement represents a limited relevance while testing cross-weld specimens due to the heterogeneous material microstructure, associated strain heterogeneity and presence of residual stresses. Advancements on experimental mechanics such as Digital Image Correlation (DIC) shed new light on the strain monitoring. The assessment of the strain fields on cross-weld specimens has already been exploited by several authors (Dalgaard, 2011; Chamanfar et al., 2016; Stinville et al., 2015; De Strycker et al., 2011). For the last 20 years a large number of authors have used spatio temporal graphs to highlight the presence of strain bands due to instabilities of Portevin's Le Chatelier effect and the Lüders bands. Yet, very little attention has been given to the chronological strain evolution and strain rate in the weld zones during tensile test.

Friction Stir Welding (FSW) is one of the most broadcast solid state joining processes and it is known for having different kind of *defects*. The most common defect is called joint line remnant, "lazy S" or "zig-zag curve"

(Zhou et al., 2006) and it consists on a line of oxides that zigzags along the thickness of the weld. Another typical defect is called "kissing bond" or "root flaw" and consists of the final part of the JLR remaining open, due to an insufficient penetration of the tool pin (Le Jolu et al., 2015). The two sheets to be welded by FSW must be closer than a given threshold distance, when this distance is not respected, another kind of defect called the "GAP" takes place leading to the presence of cavities (Le Jolu et al., 2015). Some surface defects related to excessive heat input have also been observed such as flash formation, surface galling and nugget collapse.

Concerning the documented defects in *LFW*, literature is less abundant. Some of the documented defects are porosity, oxides and the formation of an abnormal microstructure (Wanjara and Jahazi, 2005; Li et al., 2014). (Wanjara and Jahazi, 2005) found that either oxides or porosity could appear in the WCZ as a function of the chosen LFW parameters.

Some authors studied the effects of *FSW* welds defects on the *tensile properties* (Lang et al., 2010). For instance, (Le Jolu et al., 2014), (Elangovan et al., 2008) and (Nakata et al., 2000) documented the effect of defects on the tensile strength of FSW joints. The weld properties of sound welds and welds containing defects were similar even if surface defects such as kissing bond acted as crack initiation site during tensile tests. Despite the existence of pores and oxides, some resistance to a monotonic loading can be obtained. (Wanjara and Jahazi, 2005) observed the presence of oxides and pores in the WCZ of similar Ti−6Al−4V LFW joints and yet failure always occurred in the TMAZ or the PM. (Li et al., 2012) and (Li et al., 2014) reported the presence of *abnormal microstructures* in the WCZ of similar Ti alloys LFW joints which resulted into failure in the elastic domain with a quasi brittle fracture.

The consequences of *FSW* defects in terms of *fatigue life* and *fatigue crack propagation* have been documented to some extent. (Le Jolu et al., 2015) and (Lomolino et al., 2005) found surface defects on a similar FSW joint that may have diminished the fatigue strength. (Lombard et al., 2008) found that surface defects played a significant role in the crack initiation stage. (Di et al., 2007) and (Ceschini et al., 2007) observed that the zig-zag defect of FSW joints also known as joint line remnant acted as a crack initiation site during fatigue tests diminishing the fatigue life compared to sound welds. James et al. (2003) observed that that the kissing bond defect on a similar aluminium FSW joint shorten the overall fatigue life of the specimen by favouring the link between two cracks. A considerable understanding of the role of defects on the fatigue crack propagation mechanisms of FSW joints can be found in literature whilst the defects' effects on the fatigue crack initiation and propagation mechanisms of *LFW joints* seem poorly documented.

A certain agreement about the presence of *residual stresses* in LFW joints can be found in literature (Frankel et al., 2009; Romero et al., 2009). Compared to the parent material, LFW joints exhibit a reduced fatigue lifetime due to the presence of tensile residual stresses (Webster and Ezeilo, 2001). (Romero et al., 2009) have studied similar Ti6242 and Ti64 LFW joints and reported that residual stresses decrease with increasing forging pressure. Despite these evidences, little research has been carried out on the relationship between the fatigue strength and the residual stresses for LFW welds.

In this paper, strength and fatigue strength of the little studied similar Ti6242 LFW joint are studied. The originality of this work relies on three major highlights. Firstly, the presence of defects at the microscopic scale has been assessed using non-destructive observations techniques such as synchrotron laminography. Secondly, a new analysis of the strain fields obtained by DIC has been proposed. Normalized strain rate spatio-temporal graphs were used to detect an early plastic activity in the surroundings of the WCZ and to foresee the fatigue

crack initiation site on the welded structure. Finally, the fatigue life scatter and fatigue crack propagations mechanisms are studied. In particular, the effect of the workpiece surface contamination prior to welding on fatigue life has been assessed. In the experimental part, materials, welds and experimental details will be given. In the following section, results will be given in terms of weld microstructure, defects analysis, tensile tests on smooth specimens with additional DIC analysis. In particular, the normalized DIC strain rate fields are analysed to get insight about the potential fatigue crack initiation site. In the last part, the results of an S-N fatigue approach are presented. Particular attention is drawn to fatigue crack initiation sites and fatigue crack initiation mechanisms and their resulting fatigue scatter. The results and in particular the effect of defects is discussed.

4.2 Experimental and materials

Parent material (PM) Ti−6Al−2Sn−4Zr−2Mo−0.1Si titanium alloy was used as PM in this study. Ti6242 is a near–α alloy with a α grains (h.c.p.) embedded in a β matrix (b.c.c.). The nominal chemical composition is exhibited in Table 4.1. Billets of a 250 mm diameter produced by Timet were forged in the $\alpha+\beta$ domain. Blocks with 80 mm × 70 mm × 15 mm dimensions have been machined using Electrical Discharge Machine (EDM) for LFW. The long and short direction coincided with the rolling direction (RD) and transverse direction (TD) of the billet, respectively. The EDM cutting tool was a brass wire composed of Zinc and Copper.

Al	Sn	Zr	Mo	Si
6	2	4	2	0.1

Table 4.1: Nominal chemical composition (%*wt.*) of the Parent Material.

Linear Friction Welds Similar Ti6242 LFW joints were produced by ACB. During joining, friction occurred along the F axis and a forging pressure was applied along the P axis, as shown in Fig.4.1. F and P axes were parallel to the long and short directions of the blocks, respectively. The third direction corresponds to the thickness (T). All specimens were machined by EDM parallel to a PT plane and tested in the as welded condition (See Fig.4.2). A burn-off of about 2.76 mm was achieved.

Microscopic observations The samples were prepared by standard metallographic procedure consisting in mounting, grinding and polishing to a mirror like quality. The parent material and welded joint were observed in a ZEISS DSM982 Gemini Scanning Electron Microscope (SEM) operated at 15 keV using backscattered electrons (BSE) detector. The fractographic analysis was carried out at low and high magnification using secondary electron detector in both LEO 1450VP SEM and ZEISS DSM982 Gemini SEM.

Laminography A 500 µm thick sheet-like specimen parallel to a the PT plane was machined, as shown in Fig.4.2. Laminographic observations were performed at the European Synchrotron Radiation Facility (ESRF) on the beamline ID19. A monochromatic beam of 36 keV X-ray energy was used to observe a volume of 1664 µm × 1664 µm × 500 µm. Voxel size was 0.65 µm resulting in a final reconstructed volume of size 2560 px × 2560 px × 770 px. The normal to the specimen surface and the axis of rotation held an angle of about 30° to the X-ray beam.

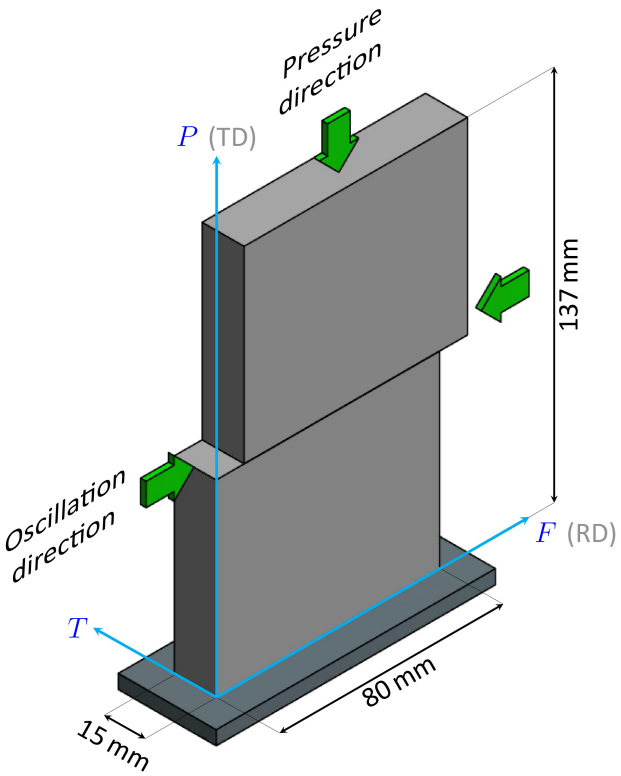

Figure 4.1: A schematic view of the welded joint showing the friction direction (F), the forging pressure direction (P) and the thickness direction (T).

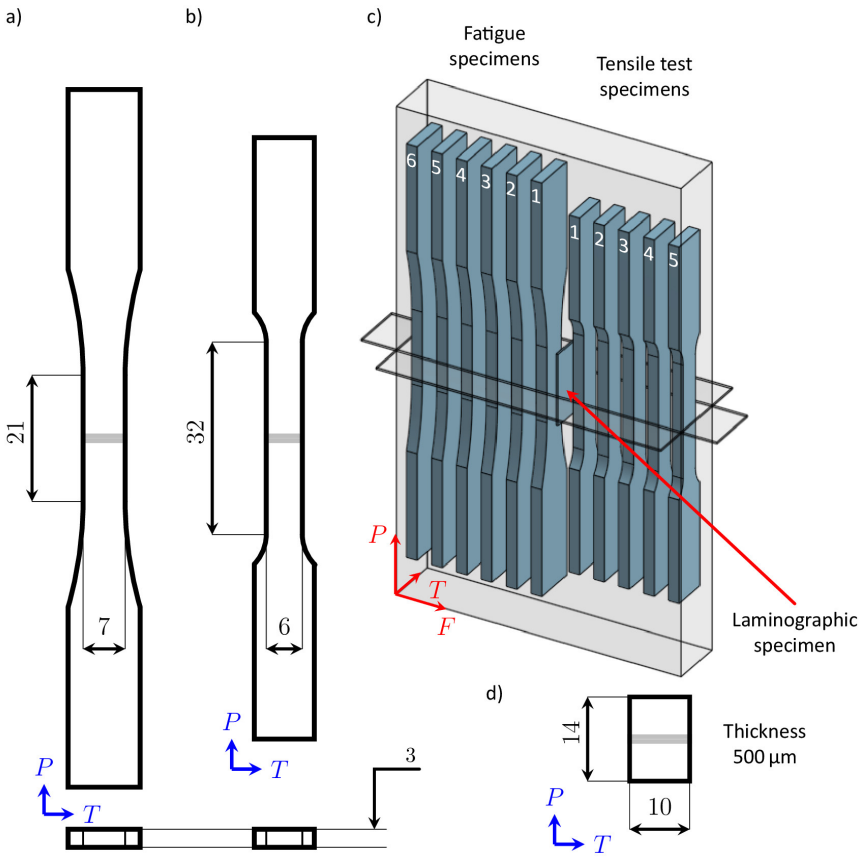

Figure 4.2: a) Geometry of the fatigue specimen; b) geometry of the tensile specimen; c) schematic view of the specimen location in the welded joint and d) laminography specimens. All measures are given in mm.

Microhardness Vickers microhardness tests were carried out across the weld with a 100 µm step size, a 500 g load and a dwell period of 15 s. Tests were conducted following the ASTM E384-17 (2017) international standard.

Tensile test Nine smooth cross-weld specimens were machined. Four PM specimens and five cross-weld specimens were tested. Tensile tests were conducted following the ASTM E384-17 (2017) international standard with a MTS 250 kN load frame at room temperature. Load frame cross-head speed was $0.032\,\mathrm{mm\,s^{-1}}$. The specimen geometry is shown in Fig.4.2. The tensile test specimens were machined parallel to a PT plane and were tested having the stationary workpiece on the upper grip of the load frame. Load was applied parallel to the P direction. Elongation was measured with optical extensometers. Gage length was 25 mm and cross section was 3 mm × 6 mm.

Digital image stereo correlation During tensile test, weld zones local strain has been monitored using a standard system of Digital Image Stereo Correlation. A system of two 2048 px × 2048 px Manta G-419B cameras was placed to follow the displacement of an artificial random black and white speckle depicted on the specimen surface (see Fig.4.3). The distance between the cameras was $a = 26\,\mathrm{cm}$ and the camera-object distance was $b = 31\,\mathrm{cm}$ (see Fig.4.3a), leading to a field of view of 40 mm × 40 mm. Images were exploited with Vic-3D™ from Correlated Solutions, Inc. (version 7.2.4, 2014). Acquisition was carried out taking 2 frames per second. Subset size was 35 px ≈ 175 µm, step size was 9 px and filter size was 15 px. Before tensile testing, the displacement and the Hencky $\varepsilon_{\mathrm{PP}}$ measurements uncertainty were determined by correlating two consecutive images of the static specimen. Uncertainty in displacement measurements turned out to be 0.1 µm. This corresponds to a Hencky strain uncertainty of $\Delta\varepsilon_{\mathrm{PP}} = 0.0002$ with a standard deviation of $\sigma_{\varepsilon_{\mathrm{PP}}} = 9.56 \times 10^{-5}\%$. As shown is Fig.4.3b, the load line, the specimen and the cameras frame were aligned using a laser level (red lines in Fig.4.3b). Both cameras were aligned to gravity using a water level.

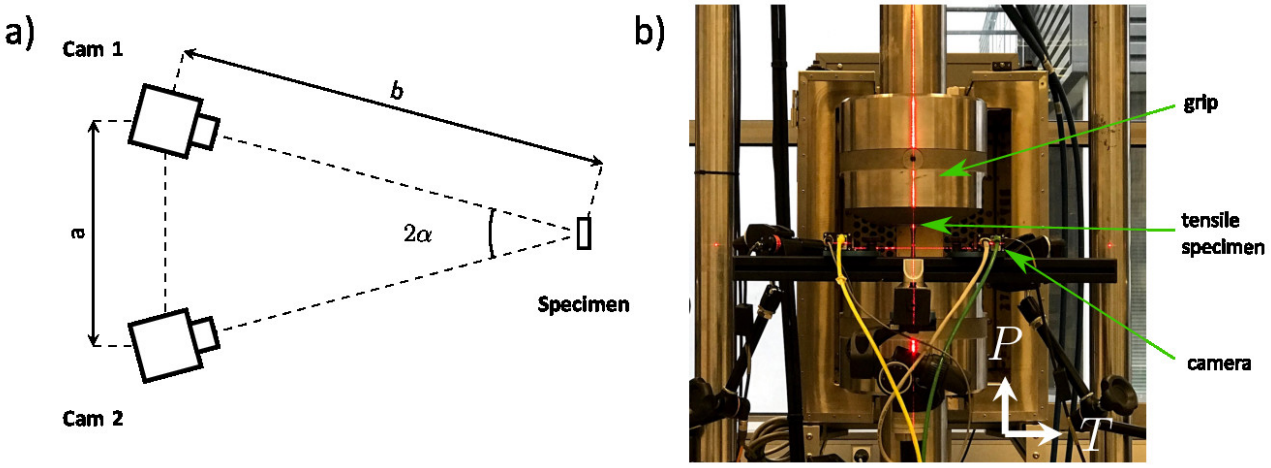

Figure 4.3: a) Schematic top view of the experimental setup for performing stereo correlation with a standard DIC system. b) Specimen, camera frame and load line aligned to gravity using a laser level (red laser lines).

Fatigue test Standard fatigue test using smooth specimens have been carried out following the ASTM E 466-07 (2007) international standard. Two sets of specimens have been tested: fatigue specimens made of parent

material and cross-weld specimens. PM samples have been machined in a perpendicular plane to the extrusion axis of the billet having its principal axis tangential to the billet section. Cross-weld specimens were machined parallel to a PT plane of the joint, having its principal axis parallel to the P direction, as shown in Fig.4.2. Cross-weld samples have been labelled from 1 to 7, being 1 the one on the centre of welded joint. The uniaxial tension zone had a length of 21 mm and a constant gage section of 3 mm × 7 mm. A sinusoidal waveform was imposed using a MTS 250 kN servo-hydraulic load frame. The stress ratio was $R = 0.1$ and the test frequency was 20 Hz. Specimens corners were rounded with a lime and their surface were polished to a mirror-like state. Targeted fatigue life was $N_f = 10^5$ cycles.

4.3 Results

4.3.1 Microstructure

Fig.4.4a shows a micrograph obtained using BSE detector for the PM. One can see that the microstructure consists of equiaxed α grains and lamellar α situated in a β matrix. The Average Grain Intercept method was performed using SEM/BSE observation of the PM microstructure (not shown here) to compute the average grain size of the α grains. The resulting average grain size was about 10.7 µm. Fig.4.4b shows the microstructure observed in the cross section of the welded joint on a PT plane. The presence of the WCZ is observed within the horizontal ∼100 µm thick band. Microstructure in the surroundings of the WCZ shows indications of strong levels of plastic deformation and the fragmentation of former α grains. The level of plastic deformation is higher close the WCZ. Fig.4.4c shows a high magnification view of the WCZ. A very fine recrystallization is observed. Needle shape like grains of ∼150 nm thickness are observed. An acicular entangled α' martensite is formed within prior-β RX grains (Ballat-Durand et al., 2019). This microstructure is comparable to the one observed in Ti64 and IMI-834 similar LFW joints (Dalgaard et al., 2012b; McAndrew et al., 2014) and, as for these joints, enhanced UTS is expected to be found in the WCZ.

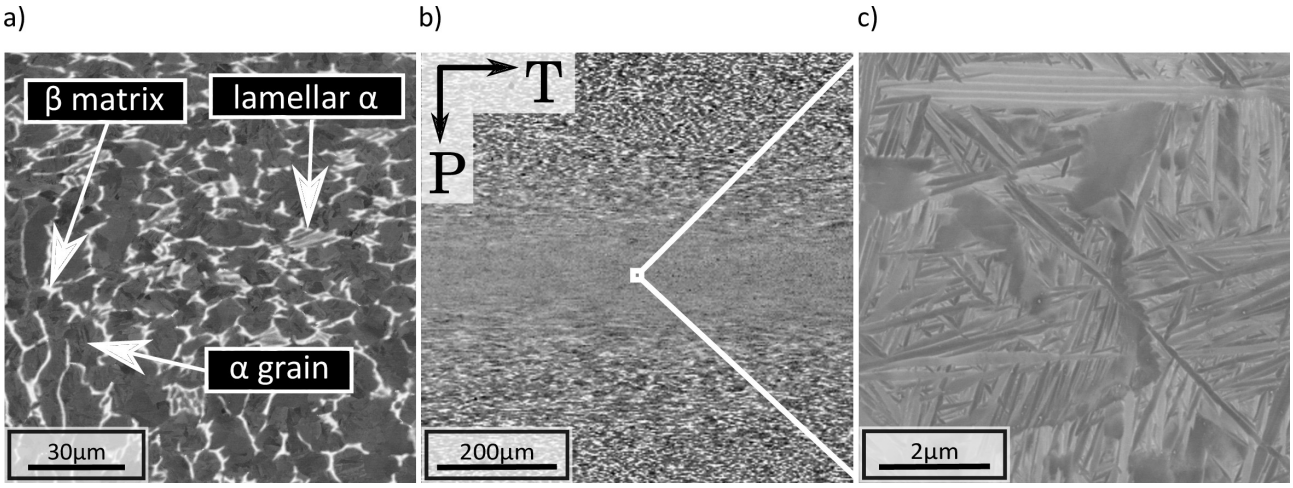

Figure 4.4: SEM/BSE observation of a) PM microstructure, b) the affected zone containing the WCZ and the TMAZ and c) the very fine entangled acicular α' martensite in the WCZ.

4.3.2 Defects observation

Fig.4.5a shows a $2D$ section parallel to a PT plane taken from the 3D laminographic volume. In absorption laminography, contrast is mainly based on the mean atomic number of the observed object. Increasing mean atomic number leads to brighter grey levels. Ti6242 is two-phase titanium alloy. Aluminium content stabilizes the α phase increasing the β-transus temperature while molybdenum content stabilizes the β phase decreasing the β-transus temperature. Tin and Zirconium are neutral elements and they can be found in solid solution in both phases (Leyens and Peters, 2003). The equiaxed dark features represent the lighter aluminium rich α grains and the brighter features the heavier molybdenum rich β matrix. The parent material microstructure is observed in Fig.4.5b. The absence of the brighter features in Fig.4.5c reveals the WCZ and thermo-mechanically affected zone. Fig.4.5d shows a very low atomic number object with a circular shape surrounded by a very bright

white line in its border. This edge enhancement is known to be evidence of a strong phase contrast revealing interfaces between different microstructural entities (Shen et al., 2013; Helfen et al., 2013). These findings suggests the presence of voids. Using image processing through Python scripts based on the *pymicro* library

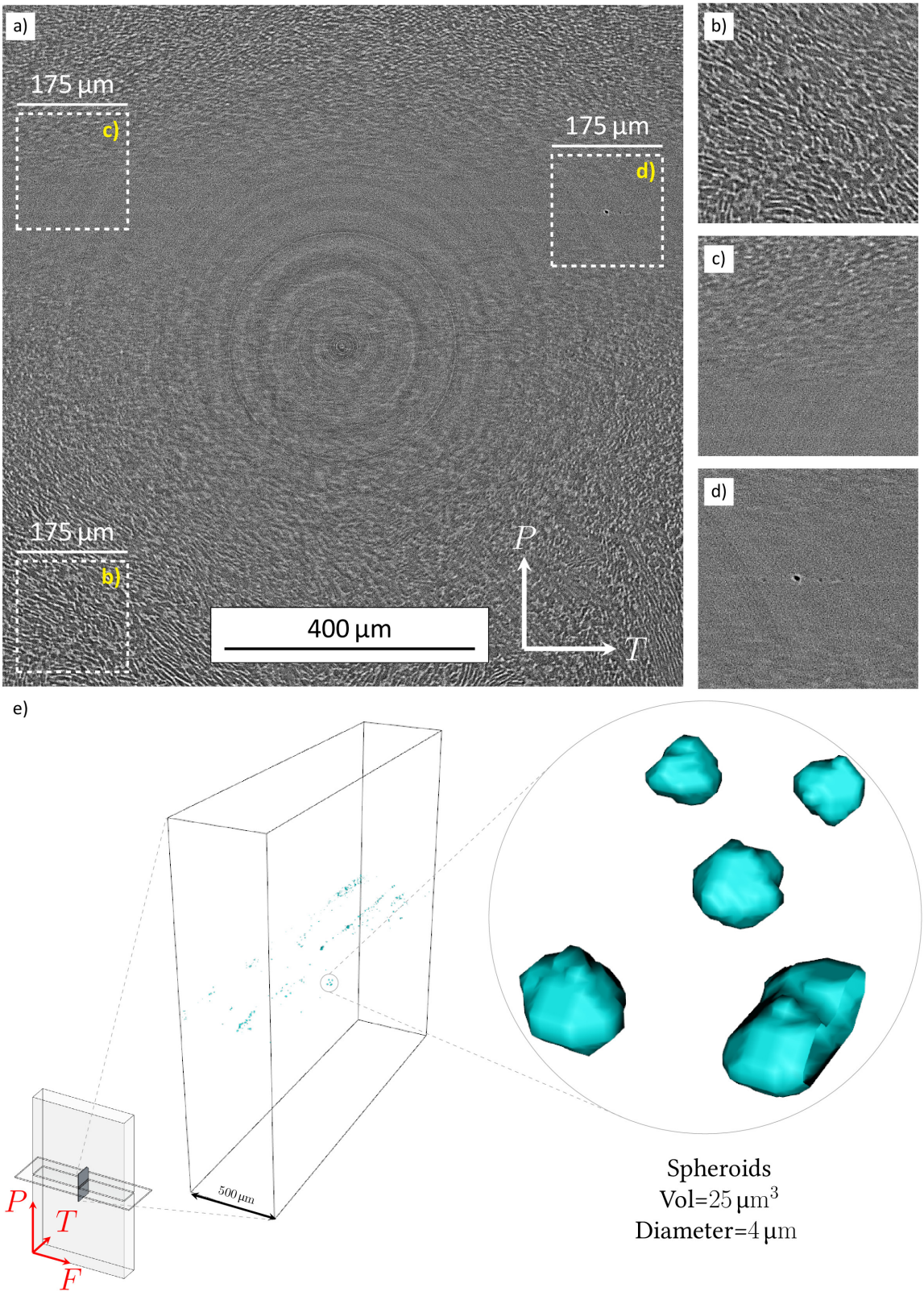

Figure 4.5: a) A $2D$ view of a PT section of the reconstructed laminographic volume. b) PM microstructure, α grains and the β matrix are observed in the darker and brighter phases, respectively. c) TMAZ. d) Cavities in the weld. e) 3D visualisation of the micrometric cavities population.

(http://github.com/heprom/pymicro), a 3D visualization of the voids population has been performed. A colour has been given to the cavities in the weld interface and all other features have been set in absolute transparency (see Fig.4.5). Voids typical diameter was 4 µm and they were located at the centre of the WCZ, at the frontier between both welded blocks following lines perpendicular to the friction direction.

4.3.3 Microhardness evolution

Fig.4.6 shows the average microhardness profile over three lines perpendicular to the WCZ. The measurement standard deviation for the three indentation lines is represented with vertical error bars. Microhardness showed a maximum of 420 $HV_{0.5}$ at the WCZ centre. Indentations further than 2.5 mm to the WCZ presented an average microhardness of 330 $HV_{0.5}$. Compared to the PM, microhardness on the WCZ is about 27 % higher.

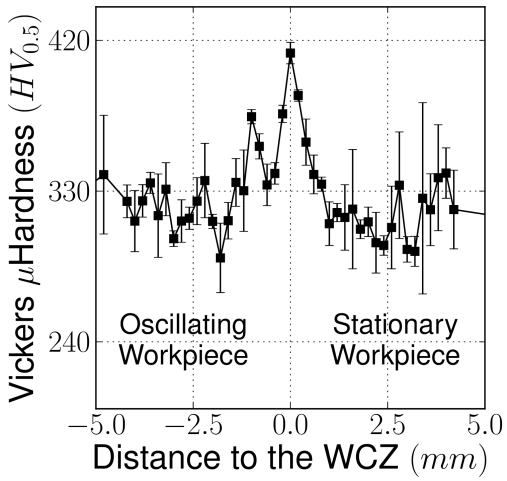

Figure 4.6: Mean Vickers microhardness over 3 profiles along the WCZ, having in vertical error bars the measurements standard deviation.

The standard deviation in microhardness measurements (see Fig.4.6) is strongly decreased in the WCZ which is consistent with a reduced grain size in this area. The increased microhardness at the WCZ is consistent with the formation of a metastable martensitic phases (see Section 4.3.1). The affected zone by the welding process can be estimated to be 5 mm wide. Increased microhardness on the WCZ suggests enhanced UTS thus, During tensile test, failure should occur at the PM.

4.3.4 Tensile properties

The macroscopic engineering stress-strain curves for the PM and cross-weld specimens are plotted in Fig.4.7a. The tensile test curves for the PM and cross-weld tensile specimens are respectively plotted in grey and in colours. The position of every cross-weld tensile specimen on the F axis is indicated in the overlaid schematic drawing of the welded block. Failure location for the cross-weld specimens is shown in Fig.4.7b. Average total strain measured over a 25 mm basis was 9.2 % for the cross-weld specimens and 14.0 % for the PM specimens. Young's modulus and UTS were respectively $E = 118$ GPa and $UTS = 960$ MPa for both sets of specimens with a very limited scatter. The mechanical resistance of the LFW joint showed a weld efficiency of 100 %.

All cross-weld specimens failed far from the WCZ in the oscillating work-piece side suggesting that the WCZ has a higher UTS (see Fig.4.7). These findings are in agreement with the increased microhardness measured in Section 4.3.1, revealing overmatching strength.

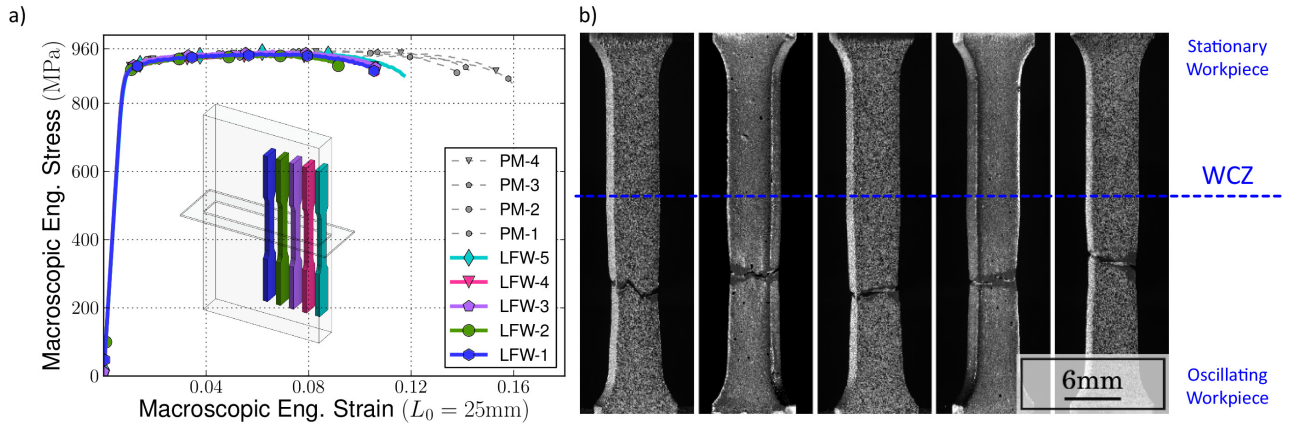

Figure 4.7: a) Engineering strain-stress curves for the LFW cross-weld (colour) and PM specimens (grey) b) Macroscopic *post mortem* view of the LFW cross-weld specimens showing failure location.

4.3.5 DIC analysis

Cumulated strain

Fig.4.8a shows the specimen and its black and white speckle to perform the local strain monitoring. The overlaid green rectangle in transparency depicts the region of interest (ROI for DIC). Fig.4.8b shows nine steps of the cumulated strain map within the ROI. The colour bar is shared with Fig.4.8c. To illustrate the temporal strain cumulation, the strain history of a generatrix line (vertical white line in Fig.4.8a is plotted in the so called spatio-temporal graph (Besnard et al., 2011; Ren et al., 2017; Chmelík et al., 2007) of Fig.4.8c. Macroscopic strain and P coordinates are given in the horizontal and vertical axis, respectively. The mapped variable is the strain field following the load direction ($\varepsilon_{\mathrm{PP}}$). The maximum strain level in the colour bar is set to the maximum local strain found during the test. The WCZ is placed at 0 mm of the P coordinate. The oscillating workpiece side of the weld is placed in the negative values of the P axis. The macroscopic engineering stress-strain curve is plotted in white. The nine strain maps of Fig.4.8b are taken in the nine characteristic instants (white squares) of the macroscopic engineering stress-strain curve of Fig.4.8c. Tensile tests give information about the macroscopic engineering stress and uniform strain for an uniaxial stress state up to necking. Given the heterogeneity of the welded structure, local information is required. The surface 3D displacement and 2D strain fields are obtained by Stereo Digital Image Correlation. Plastic strain for the PM is higher and slightly asymmetrical. Macroscopic engineering stress reaches the UTS at a macroscopic engineering strain of 0.08. Afterwards, localization takes place at a distance of 10 mm in the oscillating workpiece side reaching a local strain of 0.36.

Strain profiles

To investigate further the heterogeneous strain distribution, Fig.4.9 shows the strain profiles for three cross-weld and one PM tensile test specimens at three different characteristic instants of the macroscopic tensile test curve: at yielding (dashed lines), at UTS (thin lines) and at failure (thick lines). Strain profiles at yielding show heterogeneous levels along the ROI. The strain profile at UTS for the PM sample is shown. The Failure strain profile for the PM sample shows the strain localization with a maximum local strain of 0.4 and a neck that affects 10 mm of the gage length. The PM in the cross-weld specimen showed a higher local strain than

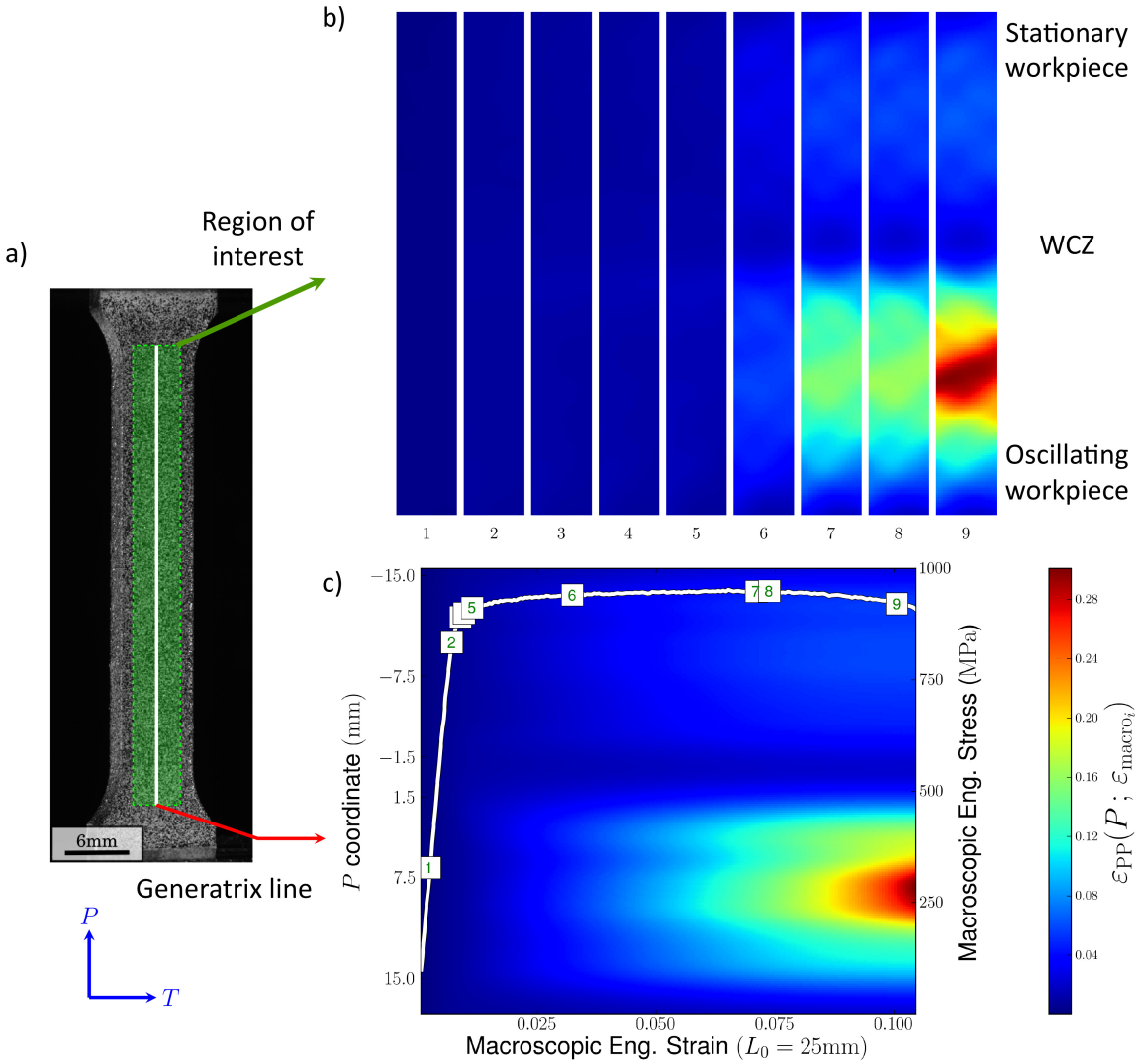

Figure 4.8: a) LFW cross-weld tensile specimen in the load frame showing the region of interest (ROI) (green rectangle) and a generatrix line (white line); b), nine steps of the strain field in the ROI; and c) a cumulated strain spatio-macroscopic deformation graph and the macroscopic engineering strain-stress curve.

the WCZ for the strain profile at UTS. WCZ mean strain at UTS is 0.018. Localization takes place at PM on the oscillating workpiece side of the specimen at a distance of 10 ± 2 mm.

The homogeneity of the strain profiles at the yielding strength suggests that the WCZ Young's modulus is the comparable to the PM. Maximum local ε_{PP} strain at fracture was comparable between PM and the PM in the cross-weld specimens. No significant strain increment was observed for the WCZ between UTS and failure. First, it should be pointed out that the WCZ strain contribution to the cross-weld total macroscopic strain is lower that that of PM. Thus PM samples show a higher ductility, as pointed out in Section 4.3.4. Secondly, it would be interesting to determinate whether the WCZ has reached plasticity or not. Using Hooke's law and the values of E and UTS presented in Section 4.3.4, it could be calculated that the WCZ elastic strain was 0.008, which was smaller than the measured total strain. Hence, the WCZ had deformed plastically. Since the minimum strain was found at the WCZ, it could be concluded that plasticity takes places in the entire gage length. Understanding the chronological order of the plastic activity at the welding zones can be particularly relevant for the early stages of plasticity that govern low cycle fatigue behaviour.

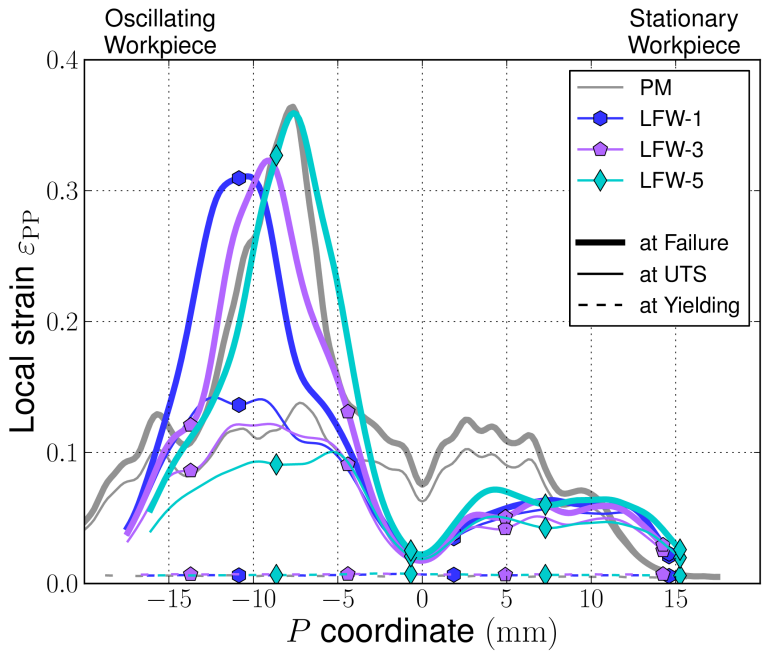

Figure 4.9: Strain profiles obtained by DIC for PM (grey) and LFW cross-weld (colours) tensile specimens at yielding, at UTS and at failure.

Incremental strain

Whilst in previous sections the total cumulated strain was investigated, here the instantaneous strain activity will be assessed. Fig.4.10a shows a view of the specimen surface showing its black and white speckle for DIC strain monitoring. In Fig.4.10b, the same nine instants as analysed in Fig.4.8b-c are now analysed in terms of incremental strain. This incremental strain $\Delta\varepsilon(t_i)$ for a given time interval Δt_i is an approximate measure of the local strain rate for a given time $\dot{\varepsilon}(t_i)$. Given that the $\varepsilon(t_i)$ signal was weaker for the initial correlation steps, the measurement noise became comparable to the $\Delta\varepsilon(t_i)$ signal. Different time steps were taken to ensure the same signal-noise ratio: $\Delta t_i = 2000\,\text{ms}$ for the elastic domain and $\Delta t_i = 500\,\text{ms}$ for the plastic domain. Notice that the strain rate over the generatrix line has been normalized by the maximum strain rate found on the line for a given t_i. Consequently, the colour bar has been scaled from 0 to 1. This information permits the instantaneous maximum strain rate to be followed. Fig.4.10b and Fig.4.10c share the colour bar.

The macroscopic engineering stress-strain curve was linear and the normalized strain rate map was homogeneous until $\varepsilon_{\text{PP}}^{macro} \sim 0.0065$. The second map has been taken at the beginning of the non-linearity of the macroscopic engineering stress-strain indicating the onset of plasticity. Some localized plastic activity is observed in the vicinity of the WCZ ($P = 1.5\,\text{mm}$). The strain rate maps 3 to 9 shows that plastic activity shifted from the WCZ to the oscillating workpiece side. Fig.4.10c shows that the maximum strain rate shifted from the WCZ to the PM where final localization took place, leading to failure. The most astonishing fact is that, even if failure takes place far from the WCZ, plastic activity initiates at its vicinity despite the overmatching strength of the WCZ. This behaviour could be linked to the presence of residual stresses (Frankel et al., 2009; Romero et al., 2009; Kim et al., 1995). Fatigue failure is known to initiate where the first stages of plastic activity take place. Therefore, fatigue crack initiation should take place in the vicinity of the WCZ. Residual stresses may have relief at yielding (Fratini et al., 2009) but they are likely to induce fatigue crack initiation at this location (Zerbst et al., 2014).

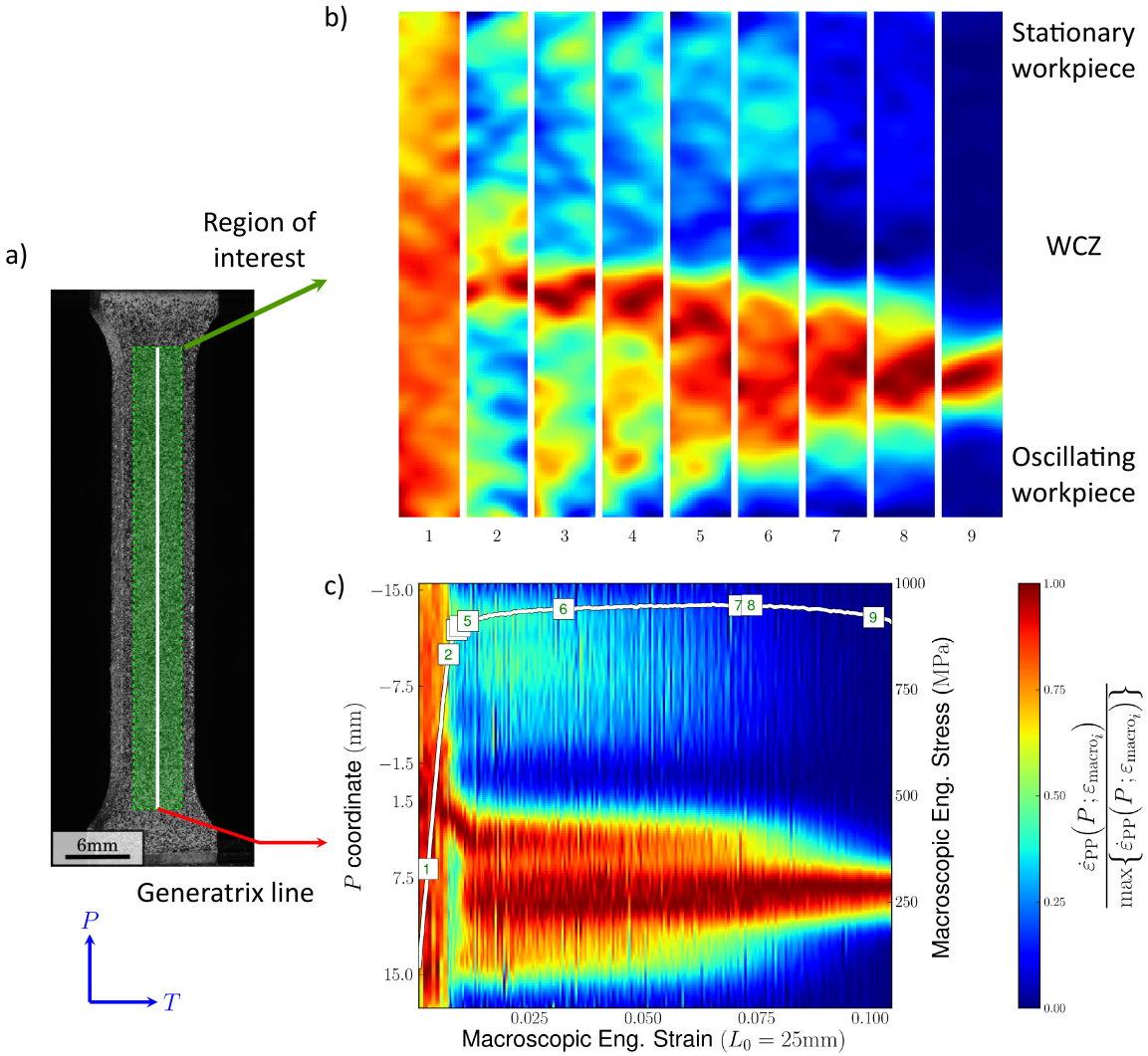

Figure 4.10: a) LFW cross-weld tensile specimen in the load frame showing the ROI (green rectangle) and a generatrix line (white line); b) nine steps of the instantaneously normalized strain rate field in the ROI; and c) a normalized strain rate spatio-macroscopic deformation graph with the overlaid macroscopic engineering strain-stress curve.

4.3.6 Fatigue

Wöhler curves

Fig.4.11 shows the S-N curve for the PM fatigue specimens (white triangles) and the cross-weld fatigue specimens (yellow triangles) specimens. For the sake of simplicity, only the LFW-1 and LFW-3 fatigue specimens have their label next to its marker on the S-N curve. For the target fatigue life of 10^5 cycles, fatigue strength of PM and LFW joint are $\sim$ 600 MPa and $\sim$625 MPa, respectively. The LFW-1 and LFW-3 fatigue specimens were both tested at a maximum stress of 500 MPa. Compared to the PM samples, fatigue resistance of cross-weld specimens is slightly reduced. However, cross-weld specimens present significant fatigue life scatter.

Crack initiation site

The specimen surface parallel to the PT plane was observed *post-mortem* using BSE detector for five cross-weld fatigue specimens. Fig.4.12 shows the distance between the crack initiation site and the WCZ for five cross-weld fatigue specimens. The WCZ of every specimen was aligned to the vertical green dashed line

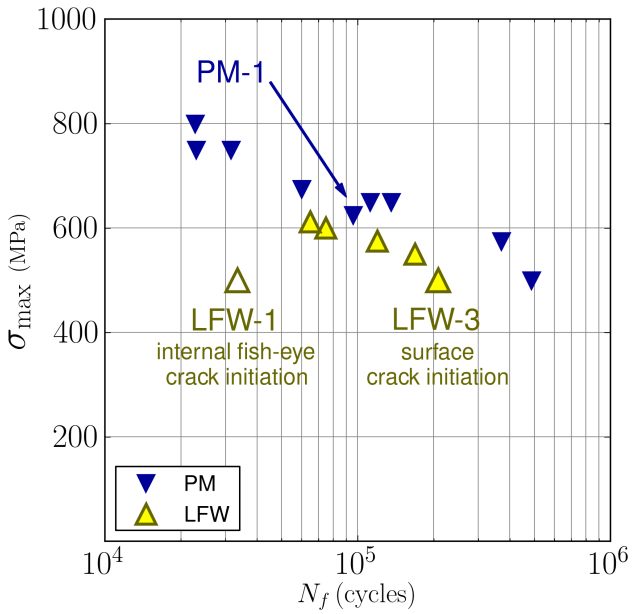

Figure 4.11: S-N curve for the PM (blue) and LFW cross-weld (yellow) fatigue specimens ($R = 0.1$).

on the right. Red crosses indicate the crack initiation site for every specimen. The LFW-1 fatigue specimen presented its crack initiation site at the WCZ. The distance from the WCZ to the crack initiation site for the cross-weld fatigue specimens ($i = 2, 3, 4, 5$) specimens occurred at a mean distance of 1.5 mm. The LFW-6 fatigue specimen failed at a distance of 2.8 mm. As anticipated in Section 4.3.5, all cross-weld specimens had its fatigue crack initiation in the vicinity of the weld possibly due to the presence of residual stresses (Romero et al., 2009; Frankel et al., 2009).

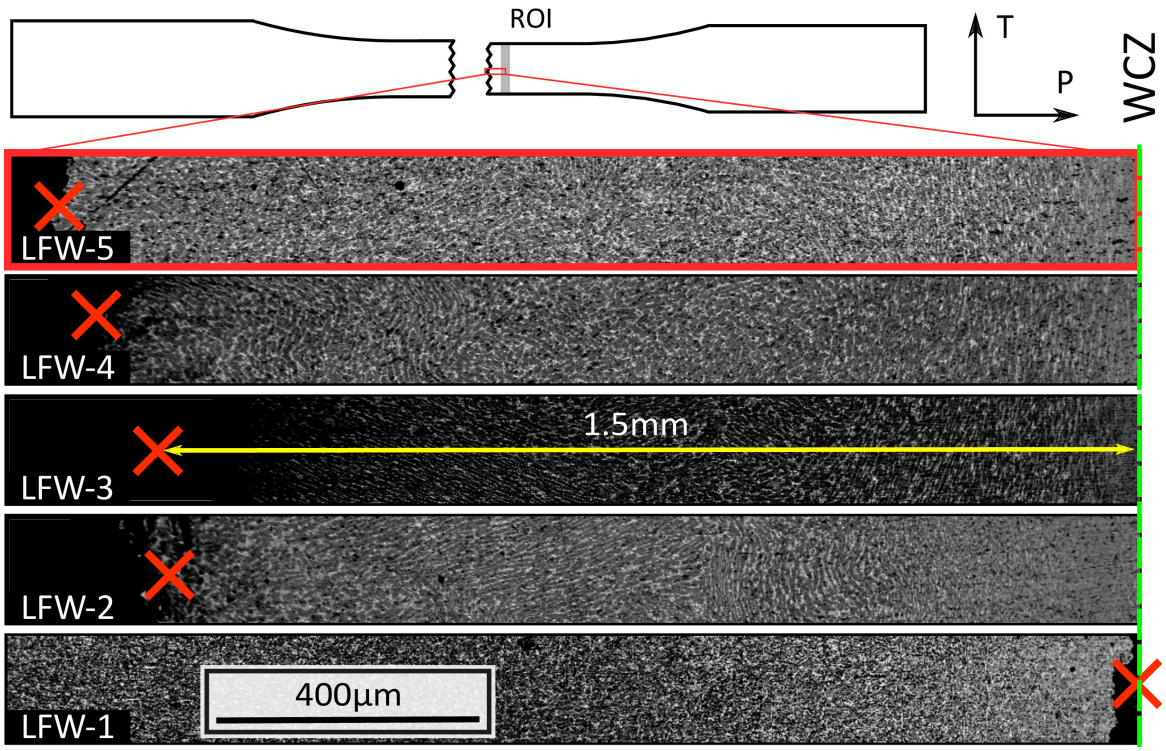

Figure 4.12: *Post mortem* SEM/BSE observation of the specimen surface on a PT plane showing with a red cross the location of the fatigue crack initiation site and its distance to the WCZ for five LFW cross-weld fatigue specimens.

4.3.7 Fractographic observations

The fatigue crack propagation mechanisms of the PM and LFW cross-weld fatigue specimens are studied through SEM and SEM/BSE fractographic observations of the PM-1, LFW-1 and LFW-3 fatigue specimens fracture surfaces. Surface crack initiation site of the PM-1 fatigue specimen is shown in Fig.4.13a-b. Long fatigue crack propagation ridges converge to a point at the specimen surface. Fig.4.13c and Fig.4.13d respectively show high magnification SEM and SEM/BSE observations of the crack initiation site. Features of a comparable size to the PM underlying microstructure, i.e. α grains, are seen. The orientation of the crack propagation plane seems to change at the boundaries of α grains. The crystallographic facets indicate a stage I fatigue initiation mechanism for the PM.

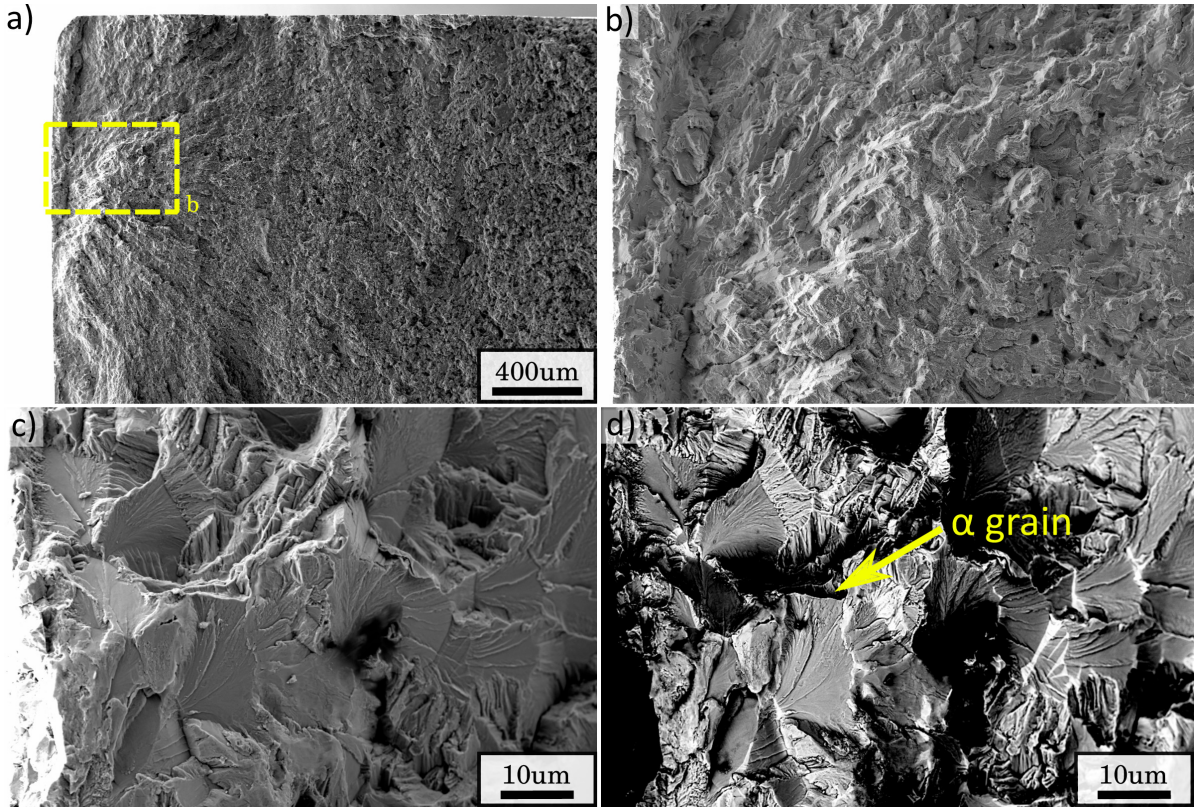

Figure 4.13: Fractograph of the PM-1 fatigue specimen, showing a) fracture surface; b) low magnification micrograph of the crack initiation site; c) SEM high magnification observation; and d) SEM/BSE observation of the crack initiation site.

Figs.4.14a-b show the surface crack initiation site of the LFW-3 fatigue specimen. The fracture surface is located at a distance of ~1.5 mm from the WCZ as shown in Fig.4.12. Several fatigue ridges converge to a region at the specimen surface. Following the zoom of Fig.4.14b, it seems that the crack initiated at several closely spaced sites. Figs.4.14c-d show SEM and SEM/BSE high magnification micrographs of the central crack initiation site, respectively. Three features resembling to PM α grains are seen. A stage I fatigue crack propagation similar to the PM is observed. This is consistent with the fact that microstructure similar to the PM is found this location. However, it seems that the residual stresses in this location, as registered by (Frankel et al., 2009; Romero et al., 2009; Kim et al., 1995), were sufficient to trigger the onset of plastic activity in several sites of this area.

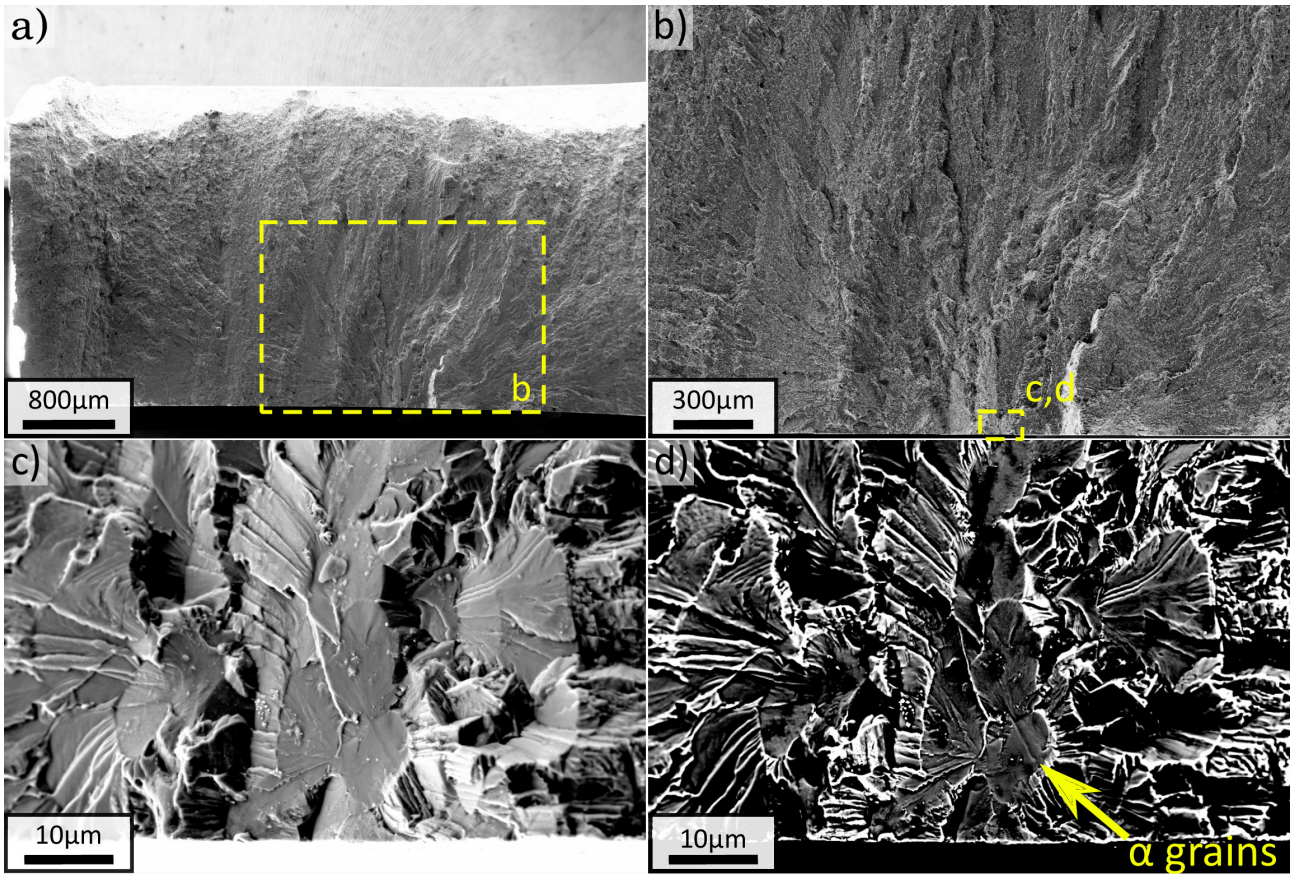

Figure 4.14: Fractograph of the LFW-3 fatigue specimen, showing a) fracture surface; b) SEM low magnification micrograph of the crack initiation site; c) SEM high magnification observation; and d) SEM/BSE observation of the crack initiation.

Defect induced internal crack initiation

Fig.4.15a shows the fracture surface of the short fatigue life LFW-1 fatigue specimen. Fatigue ridges converge to a line in the centre. Up to the dashed green line, the surface roughness around the fatigue ridges was smooth; afterwards, surface became rougher. It seems that fatigue crack propagation happened in vacuum up to the point it reached the specimen surface allowing the air to enter. The entering air may have changed the surface roughness during fatigue crack growth, due to the influence of oxidation layers in the crack tip (see Fig.4.16e). This phenomena is known as 'fish-eye' and has already been documented for martensitic steel by (Naito et al., 1984; Murakami et al., 2000; Abdesselam et al., 2018). A high magnification image at the centre of the central line is shown in Fig.4.15b. Three main features are observed: grey round-cornered features resembling to dendrites (see Figs.4.16a-c), a population of nanometric black voids and flat surfaces reminding cleavage facets (see Fig.4.16b). It should be recalled that the LFW-1 fatigue specimen had its fatigue crack initiation site in the WCZ (see Fig.4.12) and that the microstructure in this location is typically an acicular entangled α' martensite (see Fig.4.4). In contrast, the round-cornered features seen in Figs.4.16a-c are very different from the underlying microstructure in this location. These features resemble to dendrites as *e.g.* described by (Polmear, 2005) and (Hayakawa et al., 1991a) and hence imply local melting of the material as will be discussed in Section 4.4.1. It seems that an internal crack was provoked during the first tensile cycle, due to a brittle fracture at the surroundings of dendritic defects. At the frontier of the internal cleavage crack, the failure surface convey the impression of the martensitic lath of the underlying microstructure (see Figs.4.4c and 4.16d). Seemingly, a

crystallographic fatigue crack propagation occurred corresponding to stage I-like fatigue crack propagation at low levels of stress intensity factor and small plastic zones sizes. This phenomena has been approached elsewhere (Abdesselam et al., 2018; Petit and Sarrazin-Baudoux, 2010). The final ductile rupture mechanisms are put in evidence by the dimples of Fig.4.16f. A better understanding about the origin of these dendritic defects and

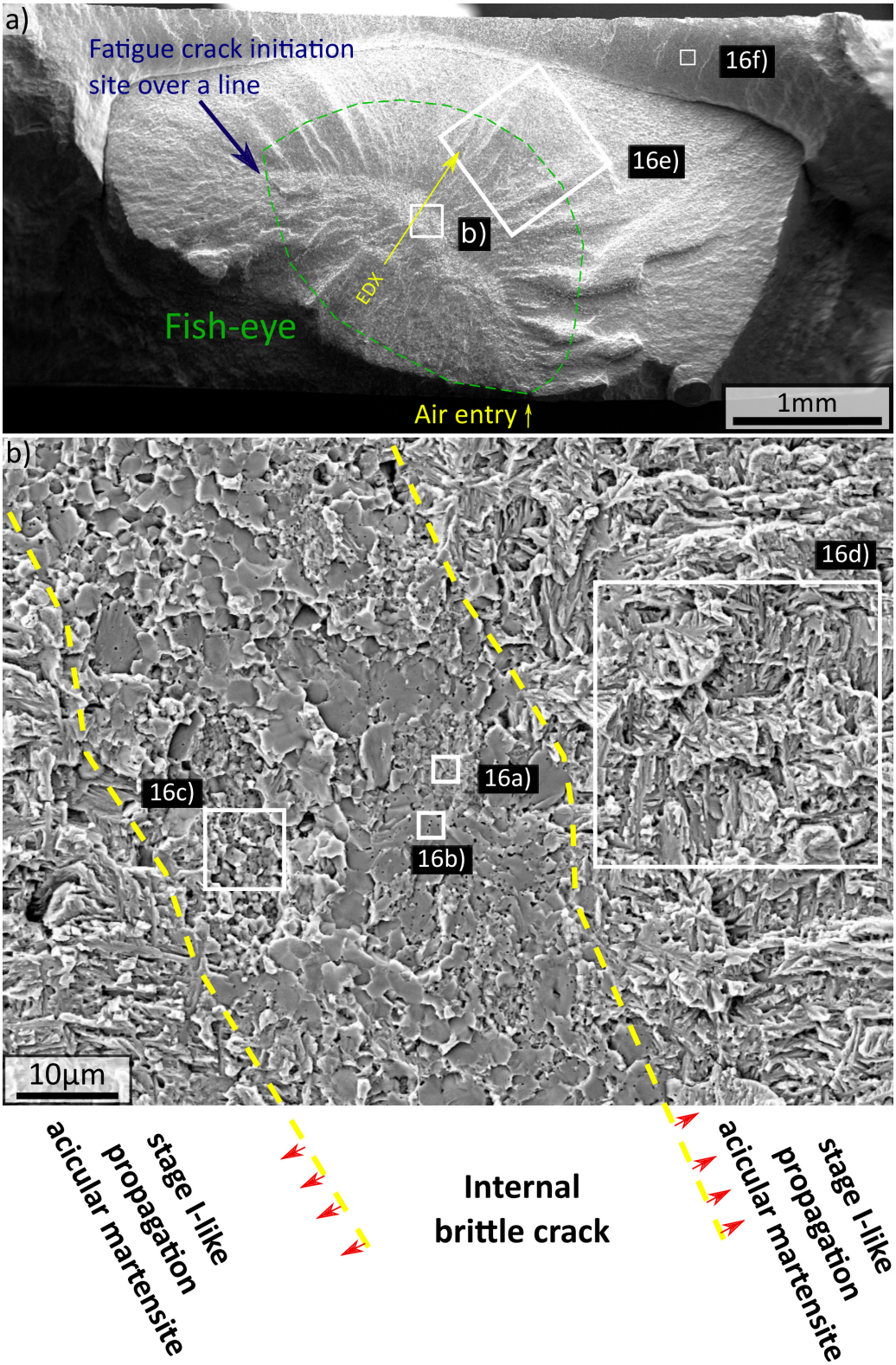

Figure 4.15: a) Fractograph of the LFW-1 fatigue specimen showing the internal crack; b) High magnification fractograph of the internal crack showing dendritic defects and first stages of the crystallographic stage I-like fatigue propagation. Region of interests (ROIs) of Fig.4.16 are indicated by white rectangles.

the internal cleavage crack is required.

4.3.8 Chemical Analysis

A chemical analysis was performed over the fracture surface of the LFW-1 fatigue specimen to get a better understanding on the origin of fatigue crack initiation site. A view of the internal fatigue crack initiation site is shown in Fig.4.17b. The red line shows the curvilinear path on which a EDX analysis has been performed. It should be noted that at the coordinate ∼400 µm of the analysed path, the dendritic defect shown of Fig.4.16a is located. In this analysis, all elements on Table 4.1 plus two extra elements not present in the PM composition have been indexed: Cu and Zn. These elements are present in the cutting tool as described in Section 4.2. Fig.4.17b shows the weight percentage of Cu and Zn over the red line of Fig.4.17a. A maximum of 5 % wt. Cu

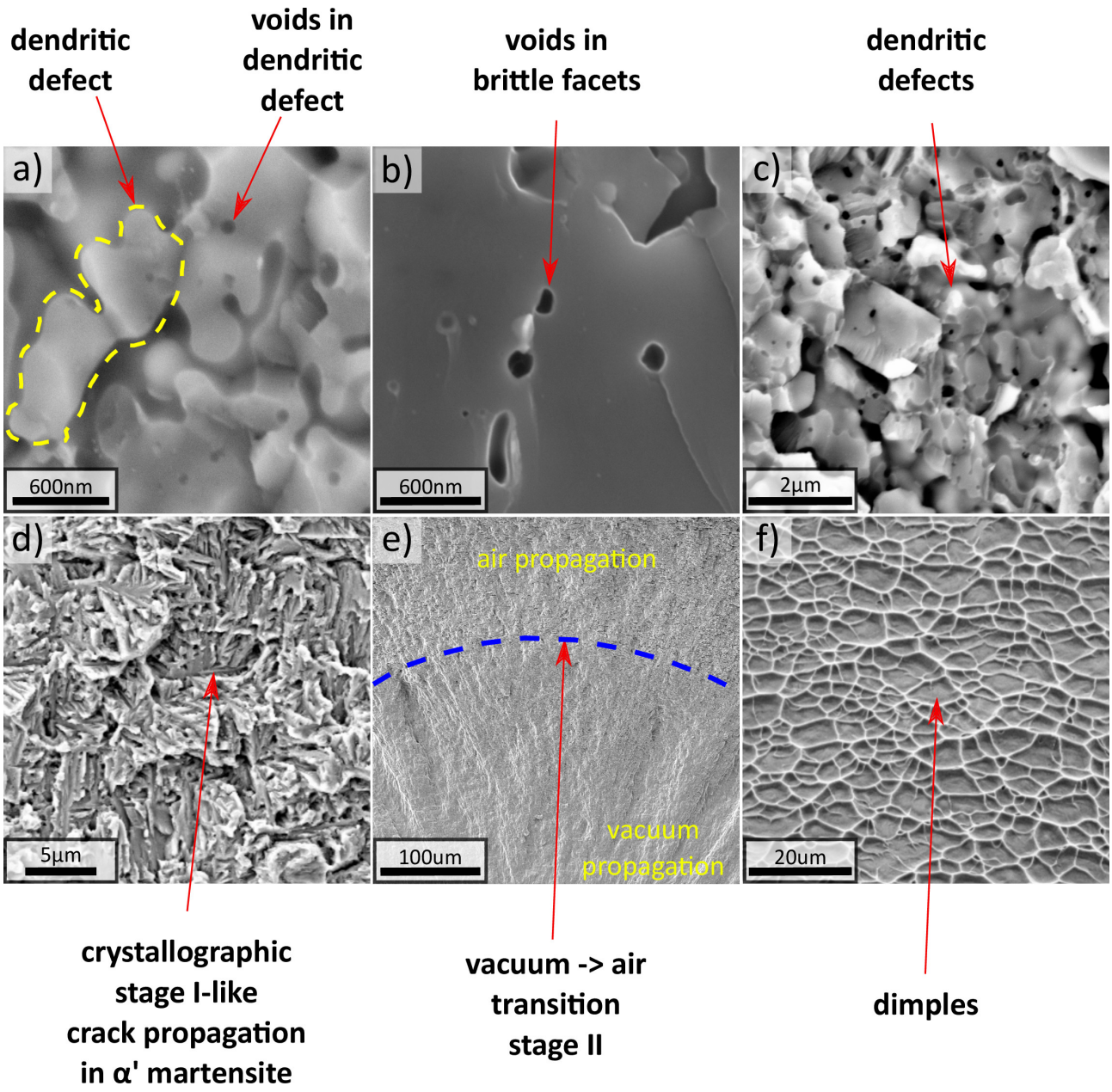

Figure 4.16: a) Fractographs of the LFW-1 fatigue specimen showing a) dendritic defect; b) brittle facets; c) dendritic defects; d) crystallographic stage I-like crack propagation in α' martensite; e) transition of crack propagation in vacuum/air; f) dimples showing the final ductile fracture.

is found for the coordinate 388 µm. A maximum of 3 %*wt*. Zn is find for the coordinate 913 µm.

4.4 Discussion

The microstructure observed at the WCZ and the monotonic mechanical properties of the studied joint have shown a strong agreement with available research in literature on similar LFW joints made of comparable Ti alloys (Dalgaard et al., 2012b; McAndrew et al., 2014). The quality of the studied weld in terms of UTS, ductility and burn-off is satisfactory. In terms of presence of defects and cyclic properties, it is more compromising.

4.4.1 Origin of defects.

In Section 4.3.8, the presence of Cu-Zn hot spots has been highlighted. From the present study the following scenario can be suggested. It is very likely that the observed brass contaminants were spread by the EDM cutting tool during the machining of the blocks prior to welding. Dalgaard et al. (2012a) registered local temperature measurements during LFW of similar joint made of IMI-834 titanium alloy which is material comparable to the Ti6242 used in this study. The registered temperatures overreached ∼1000 °C which is comparable to the melting point of a vast range of Cu-Zn alloys Predel (1994). These brass smeared hot spots may have melted and then further solidified favouring the apparition of dendrites and shrinkage voids (see Figs.4.16a-c). These kind of voids have already documented for casting alloys (Hayakawa et al., 1991a). It may reasonably be assumed that the power input was enough to produce overmatching strength but slightly insufficient to properly self-clean the smeared weld interface leaving contaminants as suggested by McAndrew et al. (2015). A less likely hypothesis for the apparition of these voids may be related to the vaporisation of low melting point elements present in the weld interface. The presence of a Cu-Zn hot spots leads to localized melting of the bulk. In such conditions, the welding technique is no longer a solid-state joining process. To the author's knowledge, this phenomena has not been studied yet.

Another possible explanation to this phenomenon is the so called strain induced porosity. Semiatin et al.

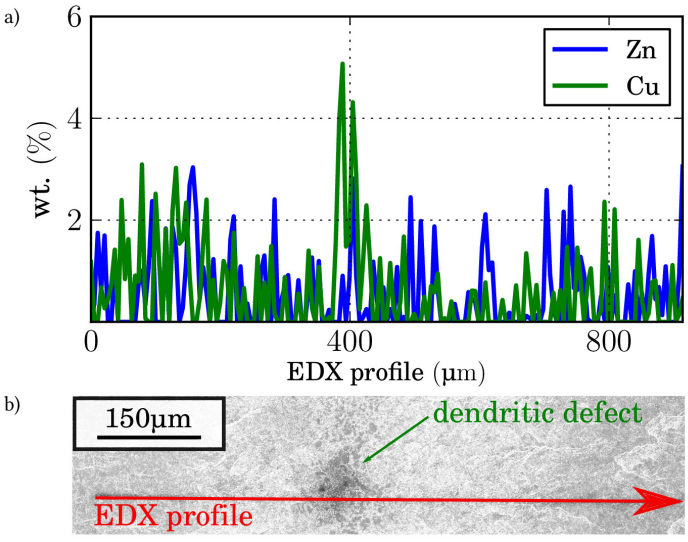

Figure 4.17: a) Zn and Cu profile indexation of an EDX analysis over the red path of Fig.4.17b and b) fractograph of the LFW-1 fatigue specimen showing the EDX profile of Figure Fig.4.17a (red line).

(1997) and Tamirisakandala et al. (2001) documented the apparition of void nucleation in microstructural phases boundary when loading two-phase titanium alloys under high temperature for certain levels of strain rates. The computation of the maximum strain rate using the weld parameters and the theoretical formula proposed by Vairis (1997) turned out to be $\dot{\varepsilon}_{max} = \frac{a\,f}{L} = 1.25\,\mathrm{s}^{-1}$. If this value, the temperature measured by Dalgaard et al. (2012a) and the grain-boundary micro-cracking map proposed by Semiatin et al. (1997) were taken into account, it appears that the strain induced porosity phenomenon might have occurred.

Two populations of nanometric and micrometric cavities have been observed in the non destructive observations and fractographs of Sections 4.3.2 and 4.3.6, respectively. Similar voids have already been observed elsewhere (Wanjara and Jahazi, 2005). Nonetheless, their origin remains unexplained.

4.4.2 Fatigue crack initiation site and early plastic activity

Microhardness profiles and tensile test revealed that the WCZ and its vicinity have higher strength than the PM. An early plastic activity was however observed in the vicinity of the WCZ. The origin of this activity is of particular interest since it allowed the fatigue crack initiation site location to be predicted (see Section 4.3.5). Several authors have reported high levels of tensile residual stresses following the P axis (Frankel et al., 2009; Romero et al., 2009; Kim et al., 1995), which are likely to have caused to the first states of plasticity in the vicinity of the WCZ. According to Romero et al. (2009), a maximum tensile residual stress peak is located a few millimetres away from the WCZ on the oscillating workpiece side of the weld. These results are consistent with the fact that localized plastic activity initiates on the oscillating workpiece side, as shown in Fig.4.10.

4.4.3 Defects and fatigue life scatter

The LFW-1 and LFW-3 fatigue specimens were tested at a maximum stress level of 500 MPa. Fatigue life for both specimens were 0.3 and 2×10^5 cycles, respectively. An important fatigue life scatter was found. If the graph of Fig.4.11 were used as a reference for the design of a workpiece under cycling loading, the fatigue life of the LFW-1 specimen would be very limiting. Hence, it is worthy to better understand the underlying cause of this fatigue life scatter. Both fatigue specimens were pre-polished to a mirror-like state. Thus, it could be stated that the surface roughness of both samples led to similar surface stress concentrations. In Section 4.3.7, a fish-eye crack and the creation of a ∼40 µm wide internal crack from a dendritic defect on the LFW-1 fatigue specimen during the first fatigue cycles is shown. Consequently, the fatigue crack propagation for the LFW-1 sample occurred with a significant initial stress intensity factor caused by the defect.

The threshold of the stage II for the fatigue crack propagation is known to take place when the plastic zone size at the crack tip is in the order of several grains. By considering the internal crack as crack in a infinite plate, an approximative and conservative estimation of the stress intensity factor can be made using $\Delta K = \Delta\sigma \times \sqrt{\pi\,a} \approx 5.16\mathrm{MPa}\sqrt{\mathrm{m}}$ (Murakami, 2002). Crack size, associated small plastic zone size and the vacuum environment (internal crack) seem to favour a stage I-like propagation (Abdesselam et al., 2018). The stress intensity factor continued to increase until reaching stage II. Crack propagation took place at first in vacuum and then in air for the LFW-1 fatigue specimen. Sarrazin-Baudoux et al. (1997) shown that fatigue crack propagation rate is lower in vacuum, in particular for stage I-like propagation. Therefore, compared to the LFW-3 fatigue specimen, more cycles should be needed in propagation. Despite the slower fatigue crack

propagation, the fatigue life was strongly reduced by the internal crack. The initial stress intensity factor was finally decisive in the trade-off between fatigue crack growth rate and number of cycles for fatigue crack initiation. The fatigue failure scenario for the internal defect is summarized in the schematic graph of Fig.4.18 and as following: during the first cycles of tensile cyclic loading an internal crack was created in the surroundings of brass contaminants hot spots due to a brittle fracture; the stress intensity factor induced by this internal crack favoured a stage I-like fatigue propagation revealing the underlying α' acicular martensite microstructure; the growth of the internal fatigue crack continued until the stress intensity factor was enough to favour a stage II fatigue propagation in vacuum; the internal crack reached the specimen surface enabling the air entry and changing the crack propagation environments conditions; oxides layers on the crack tip changed the roughness around the fatigue ridges and increased the fatigue propagation speed; finally, ductile mechanisms are found.

4.4.4 Weld self-cleaning

Certainly, brass contamination should receive special attention. However, It could be argued that EDM cutting is not a commonly used technique in the industry and that industrial cutting techniques could probably less contaminate the surface of the blocks prior to welding. In such case, joints of better quality in terms of defects and fatigue life scatter may have been produced. Furthermore, the choice of welding parameters could be questioned. Increasing power input could favour the extrusion of impurities but conversely increase temperature, promoting further melting in the weld interface. It is worthy to highlight that only the fatigue specimen coming from the centre of the welded joint was affected by this contamination and that the fatigue life scatter would be significantly lower, if this single internal crack initiation had not occurred.

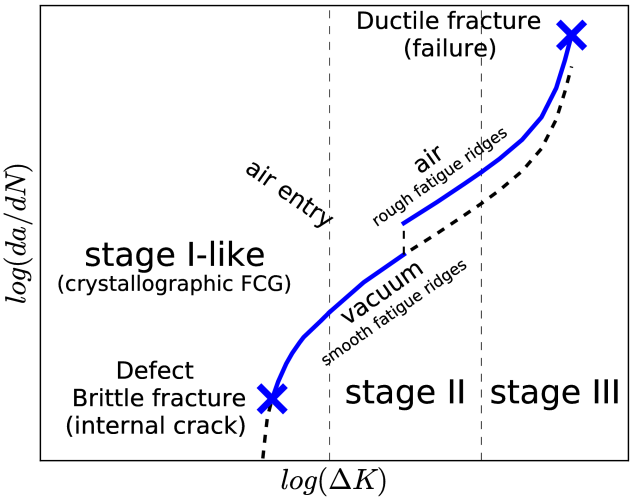

Figure 4.18: Schematic fatigue crack propagation describing the fatigue scenario of the LFW-1 fatigue specimen.

4.5 Conclusions

Similar Ti6242 LFW joints in the as welded state were investigated and compared to the PM. The following conclusions can be drawn:

- The PM microstructure, consisting in equiaxed α grains situated in a β matrix, was recrystallized into an entangled acicular α' martensite in the WCZ.
- Two populations of nanometric and micrometric voids were observed in the WCZ.
- Microhardness of the PM and the WCZ were $330HV_{0.5}$ and $420HV_{0.5}$, respectively. Microhardness showed an increase of 27 %. The zone exhibiting modified microhardness was less than 5 mm wide.
- The weld showed overmatching strength. LFW cross-weld samples have shown a strength of 960 MPa such as the PM and a total strain of 9.2 % measured over a 25 mm basis compared to 14.0 % for the PM.
- Under monotonic loading, failure occurred at the oscillating workpiece, 10 mm away from the WCZ in the PM.
- An original DIC measurement of the normalized strain rate fields showed an early strain activity close to the WCZ, despite the weld overmatching strength.
- The fatigue strength for 10^5 cycles of the PM and the LFW cross-weld sample was ~625 MPa and ~600 MPa, respectively. LFW fatigue strength was compromised by significant scatter. The fatigue crack initiation site for all samples was located in the vicinity of the TMAZ at a distance of 1.5 mm away from the WCZ consistent with the early strain activity measured by DIC and probably linked to residual stresses.
- An unexpected internal dendritic defect in the centre of the WCZ caused the reduced fatigue life for a welded joint and led to a fish-eye crack.
- A contamination of Cu and Zn was observed in the WCZ in the dendritic defect. It was attributed to EDM cutting of the blocks before welding and associated local melting/solidification of the brass contaminants during welding.

4.6 Acknowledgements

The authors wish to thank *UTC*, *CEMEF, Mines-ParisTech* and Airbus Central R&T for the valuable discussions. ACB is thanked for providing the welds for this study. Lukas Helfen at ESRF ID 19 line is gratefully acknowledged for his kind help in non destructive laminographic observations. Henry Proudhon at *Centre des Matériaux* is thanked for the provided training on the PyMicro library (http://github.com/heprom/pymicro) for the 3D image processing. Vladimir Esin at *Centre des Matériaux* insight in microstructure analysis is acknowledged. Anne-Françoise Gourgues-Lorenzon at *Centre des Matériaux* is kindly thanked for the discussions about rupture mechanisms. Steve Dodds at TWI is to be thanked for the discussions about the Strain Induced

Porosity phenomenon. The authors acknowledge the financial support from the French National Research Agency (ANR) and FRAE through OPTIMUM ANR-14-CE27-0017 project.

5

3D synchrotron tomography and microscopy *in situ* assessment of fracture mechanisms during micro notched tensile tests comparing similar Ti6242 linear friction welded joints to the parent material.

In the previous Chapter, the similar Ti6242 LFW joint exhibited overmatching strength and failed at the PM. During cyclic loadings, fatigue crack initiation far from the WCZ with the exception of one fatigue specimen. The reduced fatigue life of this specimen was related to a dendritic defect that was linked to prior to welding contamination. A study on the strength and damage mechanisms of the WCZ is required. Furthermore, a sound understanding of the influence of prior to welding contamination on the mechanical properties of LFW joints is required.

In this Chapter, the damage mechanisms and strength of the WCZ of similar Ti6242 LFW joints are assessed by synchrotron tomography and optical microscope *in situ* tensile tests of axisymmetric and flat notched micro-tensile specimens. The notch was placed centred with respect to the WCZ. Furthermore, the influence of prior to welding contamination is assessed by comparing the fracture mechanisms of two joints that were welded with different prior to welding surface preparations.

This work is presented in the form of article project: *3D synchrotron tomography and microscopy in situ assessment of fracture mechanisms during micro notched tensile tests comparing similar Ti6242 linear friction welded joints to the parent material. Juan–Manuel García, Andrew King and Thilo–Frank Morgeneyer.*

Résumé de chapitre

La déformabilité et les mécanismes de rupture du noyau de la soudure d'un joint monomatériau Ti6242 soudé par friction linéaire (LFW) ont été étudiés et comparés à ceux du matériau de base (MB) *via* des essais de traction avec entaille *in situ* au synchrotron et au microscope optique. Pour étudier l'effet de la contamination, un joint a été soudé à l'état brut d'usinage par électroérosion (LFW–AW) et un autre joint a été nettoyé avant soudage (LFW–AW–PC). Comparé à la microstructure du MB, la martensite aciculaire et enchevêtrée α' du noyau de la soudure a montré une résistance en traction supérieure et une ductilité mesoscopique réduite. La rupture a eu lieu au niveau du noyau de la soudure révélant un faciès du rupture plan avec des lèvres de cisaillement. Le MB a révélé des cupules microscopiques tandis que le noyau de la soudure a révélé de cupules nanométriques. Une étude quantitative de la morphologie et alignement des cavités du MB a été menée en utilisant des observations tomographiques. Aucun effet de la contamination n'a été observé en termes de mécanismes de rupture.

Chapter Abstract

The deformability and fracture mechanisms of the weld centre zone (WCZ) of similar Ti6242 linear friction welded (LFW) joints were studied and compared to the parent material (PM) *via* 3D synchrotron tomography and microscopy *in situ* notched micro-tensile tests. To study the effect of prior to welding contamination, one similar Ti6242 was welded in the as machined state after cutting by electrical discharge machining (LFW–AW) and the other was welded after grinding prior to welding (LFW–AW–PC). Compared to the α/β microstructure of the PM, the α' martensite of the WCZ exhibited higher notch tensile strength and lower mesoscopic ductility. The fracture surface was planar and occurred at the WCZ with shear lips at the TMAZ. The PM exhibited microscopic dimples whilst the WCZ exhibited nanometric dimples. A quantitative study of morphology and alignment of damage features of the PM was performed using the non destructive tomographic observations. No effect of prior to welding contamination was observed in terms of fracture mechanisms.

Contents

Figures

Keywords

Linear friction welding, notch micro-tensile test, Ti6242, synchrotron tomography, microscopy in situ

Nomenclature

α (h.c.p.), hexagonal closed packed titanium crystal lattice;

β (b.c.c.), body centred cubic titanium crystal lattice;

F, friction axis;

P, pressure axis;

T, thickness axis;

E, Young's modulus;

Y, yield strength;

UTS, Ultimate Tensile Strength.

5.1 Introduction

Titanium alloys are of great interest for several engineering applications such as aero-engine parts (Meetham, 1981), biomedical (Khorasani et al., 2015) and off-shore applications (Li et al., 2019). Their creep resistance, high strength/density ratio and their ability of working in high temperatures make of them one of the most used high performance materials. For instance, Ti−6Al−2Sn−4Zr−2Mo−0.1Si was invented in 1978 to answer to elevated-temperatures requirements in jet engines since it exhibits a stable strength up to 550 °C (Chen, 1982). The high strength/density ratio has recently been further exploited by their assembling though novel joining techniques such as Linear Friction Welding (LFW) (García, 2011).

LFW is a solid-state joining process in which a stationary workpiece is put in contact with a second workpiece describing an oscillatory motion of frequency f and amplitude a. After a fraction of a second of friction, a forging pressure P is applied to attain a target axial shortening Δh (burn-off). The plastic deformation and localized heat generated in the weld interface lead to considerable levels of residual stresses (Romero et al., 2009; Frankel et al., 2009), microstructural changes (Ballat-Durand et al., 2019; Wang et al., 2019) and, sometimes, enhanced mechanical strength (Dalgaard et al., 2012b). As a final consequence, all these features give birth to a strong heterogeneity distributed in four distinct zones : the weld centre zone (WCZ), the thermo-mechanically affected zone (TMAZ), the heat affected zone (HAZ) and the parent material (PM). This technique was first suggested by Ritcher (1929) and presents several advantages such as fast welding, reduced milling operations, the conception of dissimilar welds, and the quality of being a self-cleaning to some extent (see Section 4.4.4).

A certain wealth of literature is available concerning the mechanical properties of near-α titanium alloys welds. The formation of α' martensite observed in Section 4.3.1 leads to overmatching strength (Dalgaard et al., 2012b; Ballat-Durand et al., 2019; Chamanfar et al., 2016). The microhardness ratio between the WCZ and the PM was about 1.22 for a similar IMI834 LFW joint (Dalgaard et al., 2012b). During tensile testing of smooth cross-weld specimens, strain localization and failure occurred at the PM. The authors also documented a strong basal plane texture parallel to the P direction that may suggest some anisotropy. In Chapter 4, the similar Ti6242 LFW joint exhibited a microhardness peak at the WCZ with a WCZ/PM microhardness ratio of 1.27 (see Section 4.3.3). Subsequently, failure occurred at the PM during monotonic loading of smooth cross-weld specimens (see Section 4.3.4). In addition, normalized strain rate spatio-temporal graphs highlighted an early plastic activity in the vicinity of the WCZ through that was attributed to residual stresses which also led to fatigue crack initiation in this area (see Section 4.3.5). These informations are crucial and give a certain understanding of the mechanical behaviour of the welded structure. However, studies concerning local measurements of strain and strength of the WCZ and its fracture mechanisms are still missing in literature. Similarly, the influence of prior to welding contamination on the mechanical properties of similar LFW joints has little been studied.

In Section 4.3.6, fatigue crack initiation never occurred at the WCZ with exception of one fatigue specimen. Brass contaminants coming from EDM machining led to local melting at the WCZ. Subsequently, a dendritic defect was created that, during the first steps of cyclic elastic loading, induced an internal brittle crack of some tents of micrometres. An internal fish-eye fatigue crack propagation occurred from the crack at the WCZ that significantly reduced the fatigue life. In a similar manner, (Chamanfar et al., 2016) documented the mechanical properties of a similar Ti6242 laser welded joint exhibiting overmatching strength. The microhardness profiles

announced the overmatching strength that was confirmed by DIC strain field measurements showing strain localization at the PM. However, failure at the WCZ was observed. The authors attributed this to a transgranular microvoid coalescence of porosity at the WCZ that came from post-weld solidification. Therefore, even for joints exhibiting overmatching strength, understanding the WCZ damage and crack propagation mechanisms is of great importance since potential defects can induce failure at this location.

The typical size of the WCZ of similar near$-\alpha$ alloys LFW joints is about 150 µm (see Section 4.3.1). This implies several complications such as high precision machining of specimens and the need for miniaturized instrumentations. In the last 40 years, researchers have extended our knowledge on mechanics of materials to the microscopic scale through sophisticated experiments, such as synchrotron *in situ* and scanning electron microscope (SEM) *in situ* micro-tensile tests. A clear example of this is the statistical analysis that (Bridier et al., 2005) performed in the activation of slip systems of a Ti64 grade, during SEM *in situ* micro-tensile testing. In a similar experiment, (Barkia et al., 2015) studied the deformation mechanisms of titanium with different oxygen levels and found a scatter on the activation of the apparent critical resolved shear stress for prismatic glide. This was partly attributed to grain size scatter but mostly to intergranular compatibility stresses that may influence the critical resolved shear stress measurements. (Hémery et al., 2018) gainsaid this hypothesis arguing that the elastic interactions between crystallites were likely to lead to such stresses heterogeneities. SEM *in situ* micro-tensile testing of an aluminium grade have shown that grain boundary cracking occurs on boundaries normally oriented to the applied tensile stress (Pouillier et al., 2012).

The damage mechanisms of different materials has been approached through tomographic observations performed during synchrotron *in situ* micro-tensile tests. For instance, Madi et al. (2019) studied the strain and damage anisotropy of a cold rolled X100 pipeline steel grade by performing synchrotron *in situ* micro-tensile tests over axisymmetric micro-tensile specimens. Void nucleation, growth and coalescence were observed to be aligned over lines parallel to the rolling direction containing (CaS/TiN) particles. Buffière et al. (1999) identified the damage mechanisms of a AA6061 alloy grade reinforced with SiC particles *via* mechanical tests using high resolution *in situ* synchrotron X-ray tomography. The authors observed that, at the early stages of plastic activity, the rupture of the SiC particles occurred. Thereafter, some particle matrix decohesions and growth of extrusion–induced interfacial decohesions were observed. Concerning titanium alloys, Lecarme et al. (2014) developed an advanced algorithm that successfully tracked cavities during voids nucleation, growth and even coalescence of a Ti–6Al–4V grade using 3D tomographic observations. Dang et al. (2019) performed similar experiments on a Ti64 grade with lamellar microstructure and observed elongated micro-cracks that seemed to preferentially nucleate and propagate at the α colonies. Furthermore, the authors used the tomographic observations for measuring the lateral deformation of the axisymmetric micro-tensile specimen with an initial gage length of 1 mm. Being able to relate damage mechanisms to the underlying microstructure and performing measurements at the microscopic scale is a very interesting feature of *in situ* tomography.

In this work, the deformability, strength and fracture mechanisms of the WCZ of similar Ti6242 LFW joints were studied *via* 3D synchrotron tomography and microscopy *in situ* notch micro-tensile tests. First, the microstructures of the WCZ and PM are characterized through SEM observations. EBSD mappings of both PM and LFW flat micro-tensile specimens are presented. Second, the tensile test curves for both the flat and axisymmetric specimens are presented. Third, the location of failure in the welded structure is assessed using tomographic slices and back-scattered electron observations. Fourth, the fracture mechanisms are studied by

fractographic analysis and 3D tomographic and SEM observations. Fifth, a discussion concerning failure at the WCZ and contamination prior to welding is presented. Finally, a quantitative analysis of the morphology and alignment of damage for the PM is carried out.

5.2 Experimental and materials

5.2.1 Materials

Parent material (PM) Ti6242 titanium alloy was used as PM in this study. Ti6242 is a near-α alloy with a β matrix (b.c.c.) and α grains (h.c.p.). The nominal chemical composition is exhibited in Table 6.1. Billets having a diameter of 250 mm produced by Timet were forged in the $\alpha + \beta$ domain. Blocks with 80 mm × 70 mm × 15 mm dimensions have been machined using Electrical Discharge Machining (EDM) for LFW using as cutting tool, a brass wire composed of Zinc and Copper. The long and short direction coincided with the extrusion direction (RD) and transverse direction (TD) of the billet, respectively.

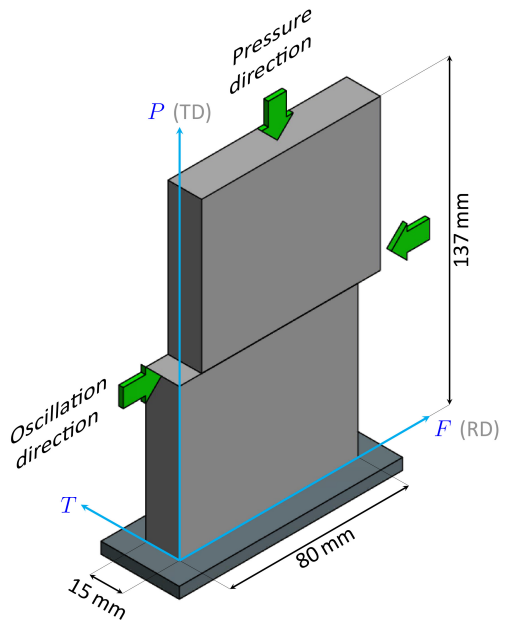

Figure 5.1: A schematic view of the welded joint showing the friction direction (F), the forging pressure direction (P) and the thickness direction (T).

Al	Sn	Zr	Mo	Si
6	2	4	2	0.1

Table 5.1: Nominal chemical composition (%*wt.*) of the Parent Material.

Linear Friction Welds Two similar Ti6242 LFW joints were produced by ACB to study the effect of prior to welding contamination on the mechanical properties of the joints. The first was welded in the EDM as machined state (LFW–AW) and the second was welded after grinding the surfaces to be welded for 2 min using a 1200 grit SiC paper followed by an acetone bath (LFW–AW–PC). During joining, friction occurred along the F axis and a forging pressure was applied along the P axis, as shown in Fig.5.1. F and P axes were parallel to the long and short directions of the blocks, respectively and the third direction corresponds to the thickness (T).

Material	Denomination	Specification
PM	Ti6242 parent material	forging at 950 °C+ air cooling 8 h ageing at 635 °C+ air cooling
LFW–AW	As welded similar Ti6242 LFW joint.	Welded in the EDM as machined state and self-cleaned
LFW–AW–PC		Surface pre-cleaned by grinding prior to welding.

Table 5.2: PM and similar Ti6242 LFW joints configurations.

5.2.2 Experimental

Synchrotron *in situ* micro-tensile testing

Axisymmetric micro-tensile specimens Two axisymmetric notched micro-tensile specimens were tested: one made of Ti6242 (PM-1) and one having the notch centred with respect to the WCZ of a simi-

lar Ti6242 LFW joint (LFW-1). The geometry of the specimens is shown in Fig.5.2a. The diameter of the minimal cross-section and the radius of the notch respectively were 1.28 mm and 0.46 mm. It should be noted that machining of a notch of 0.46 µm radius centred with respect to the WCZ of 150 µm thickness is quite difficult. To reveal the position of the WCZ, the surface of the specimens were carefully ground with a 1200 grit SiC paper and later attacked using Kroll's 2 reagent ($12\%HF + 18\%HNO_3 + 70\%H_2O$). Thereafter, the notches were carefully machined using a grinding wheel. A 3D SEM observation of the notch was performed to verify the positioning of the WCZ (see Fig.5.2b). The surface roughness after wheel-grinding prevented the WCZ to be observed. Although, the TMAZ just above and just below the notch can be seen in Figs.5.2d and 5.2e.The long direction of the grips was parallel to the F axis, as shown in Fig.5.2c.

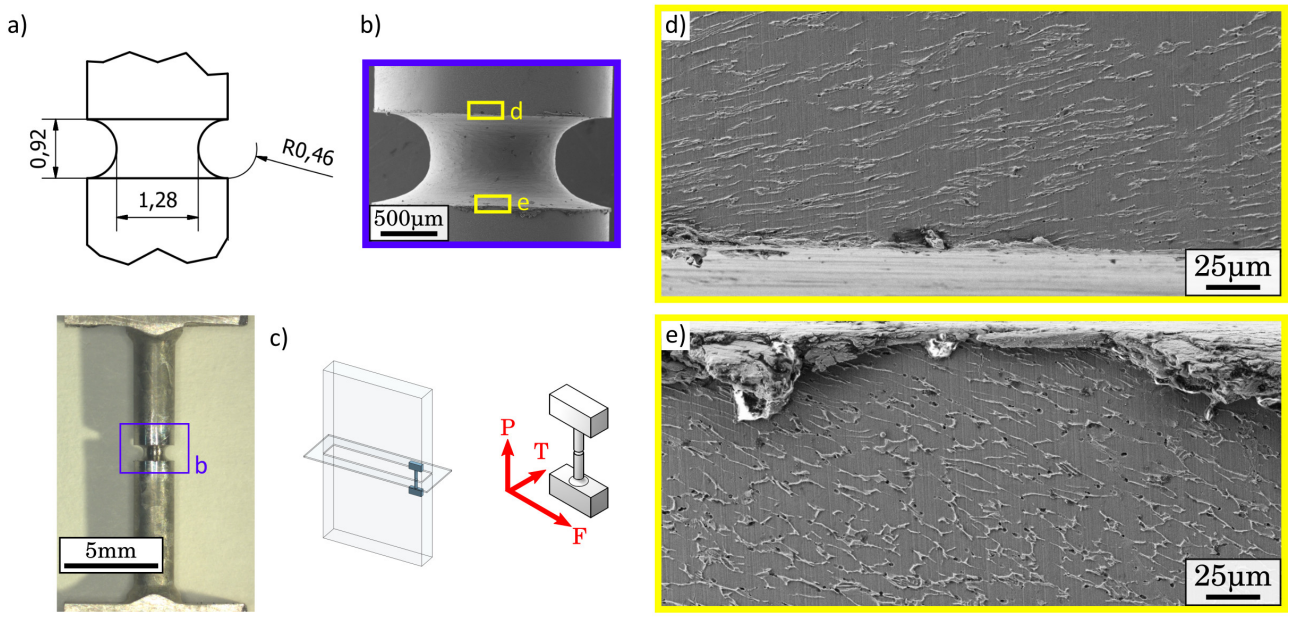

Figure 5.2: a) Tomographic axisymmetric micro-tensile specimen geometry; b) SEM observation of the notch; c) schematic view of the tomographic axisymmetric micro-tensile specimen on the similar Ti6242 joint and SEM/BSE observations of the TMAZ d) just above and e) just below the notch. All dimensions are in mm.

Tomographic observations and synchrotron *in situ* micro-tensile test Non destructive 3D observations were obtained through X-ray micro-tomography measurements achieved at the *Psyché* beamline at *Soleil* synchrotron (France). Each axisymmetric micro-tensile specimen was mounted on the mechanical stage described later in this Section. A total of 14 and 23 tomographic observations were performed for the PM–1 and LFW–1 axisymmetric micro-tensile specimens, respectively. A white beam having a peak energy of 65 keV was used to go through the notch region of the micro-tensile specimens. The transmitted photons were subsequently acquired by a 2D detector as shown in Fig.5.3a. Contrast is given by the sample absorption of coherent X-rays, according to Beer-Lambert's law of absorption (Kak et al., 2002). A total of 1500 projections of the sample were captured and were used to reconstruct 3D 8-bit grey scale images with a voxel size of 0.65 µm vx^{-1}. The exposure time per frame was 0.11 s. The size of the volume of interest was ($1330\times1330\times1330 µm^3$). Total scanning time per observation was 2.5 min. Objects with a higher mean atomic number lead to brighter gray levels and *vice versa*, after final reconstruction. The 3D images were processed and visualized using various python packages such as *pymicro* (http://github.com/heprom/pymicro), *particles* (http://github.com/garciajuanm/particles) and the VTK library.

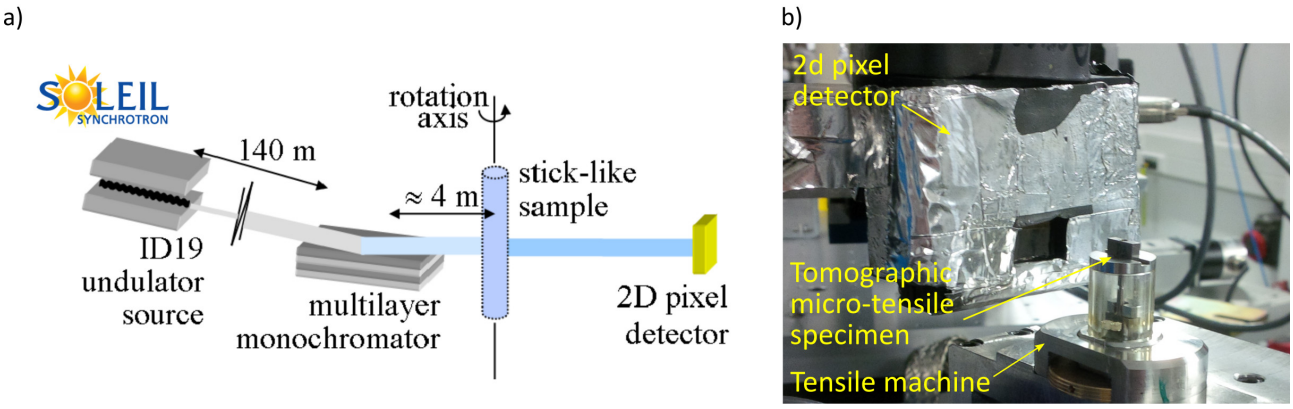

Figure 5.3: a) Schematic view of the tomographic observation principle (adapted from (Helfen et al., 2013)) and b) photograph of the 2D detector and the tomographic micro-tensile specimen mounted on the *in situ* tensile machine "*Bulky*" (Pelerin et al., 2019).

Micro-tensile testing Micro-tensile tests were performed applying a stepwise monotonic loading on the tensile machine nicknamed *Bulky* conceived to perform *in situ* 3D imaging using synchrotron X-ray tomography (Pelerin et al., 2019). The load frame can measure forces up to 5 kN and perform a mechanical stroke of 15 mm (see Fig.5.3b). Load was applied under displacement-control imposing a stepwise monotonic loading with a cross-head speed of $100\,\mu m\,s^{-1}$. The force was transmitted to the load cell though a transparent polymethyl methacrylate (PMMA) acrylic glass cylinder. Given the size of the specimens, no instrumentation for a continuous measurement of strain was possible. Instead, engineering lateral strains were computed using the tomographic 2D slices of reconstructed data of the minimum cross-section for two perpendicular axes through Python scripts, as explained in Section 5.2.2. A 3D tomographic acquisition was performed during each interruption of the micro-tensile tests.

Post-processing of tomographic observations

Various tools were developed for post-processing tomographic volumes using Python scripts and these are detailed in this Section. First, using tomographic observations, an extensometer was developed for lateral strain measurement of the axisymmetric micro-tensile specimens. Second, a simple morphological characterization of 3D particles and their alignment with respect to the frame of reference, was developed to perform a quantitative analysis on the damage features population observed by tomography, during the tensile test of the PM–1 axisymmetric micro-tensile specimen. The mathematical and computational details of all tools used here are detailed by the following. The required libraries are standard Python libraries (*numpy*, *matplotlib* and *scipy*), *pymicro* (https://github.com/heprom/pymicro) and *particles* (https://github.com/garciajuanm/particles).

3D Measurement of diametral strain in axisymmetric specimens The 3D 2048 px × 2048 px × 2048 px volumes are segmented into two levels: 1 for the specimens material and 0 for everything else (surrounding air and potential damage voids). The 3D images are projected on the yz and xz coordinate planes (see Fig.5.4). This is fulfilled by performing two row-wise sums along the coordinates x and y axis followed by an segmentation operations. Finally, two row-wise operations are performed to obtain the ϕ_x and ϕ_y diameters as a function of z (see the orange and blue curves in Fig.5.4). X-ray absorption during tomographic acquisition is dependent on the depth of the specimen parallel to the X-rays propagation direction. After a certain threshold

depth, absorption is excessive and the signal becomes weak. Notice that the quality of the images is decreased beyond a certain distance from the minimum cross-section. The z extent for which the signal is exploitable is contained within the local maximum of $\phi_i\,(z)$ (see Fig.5.4). The local minimum within these thresholds determines the position on the z axis of the minimal cross-section and its values give both diameters. For instance, the initial and final diameters following the x direction respectively were 1197.3 µm and 1166.1 µm, leading to a engineering strain of 0.026 (see Fig.5.4).

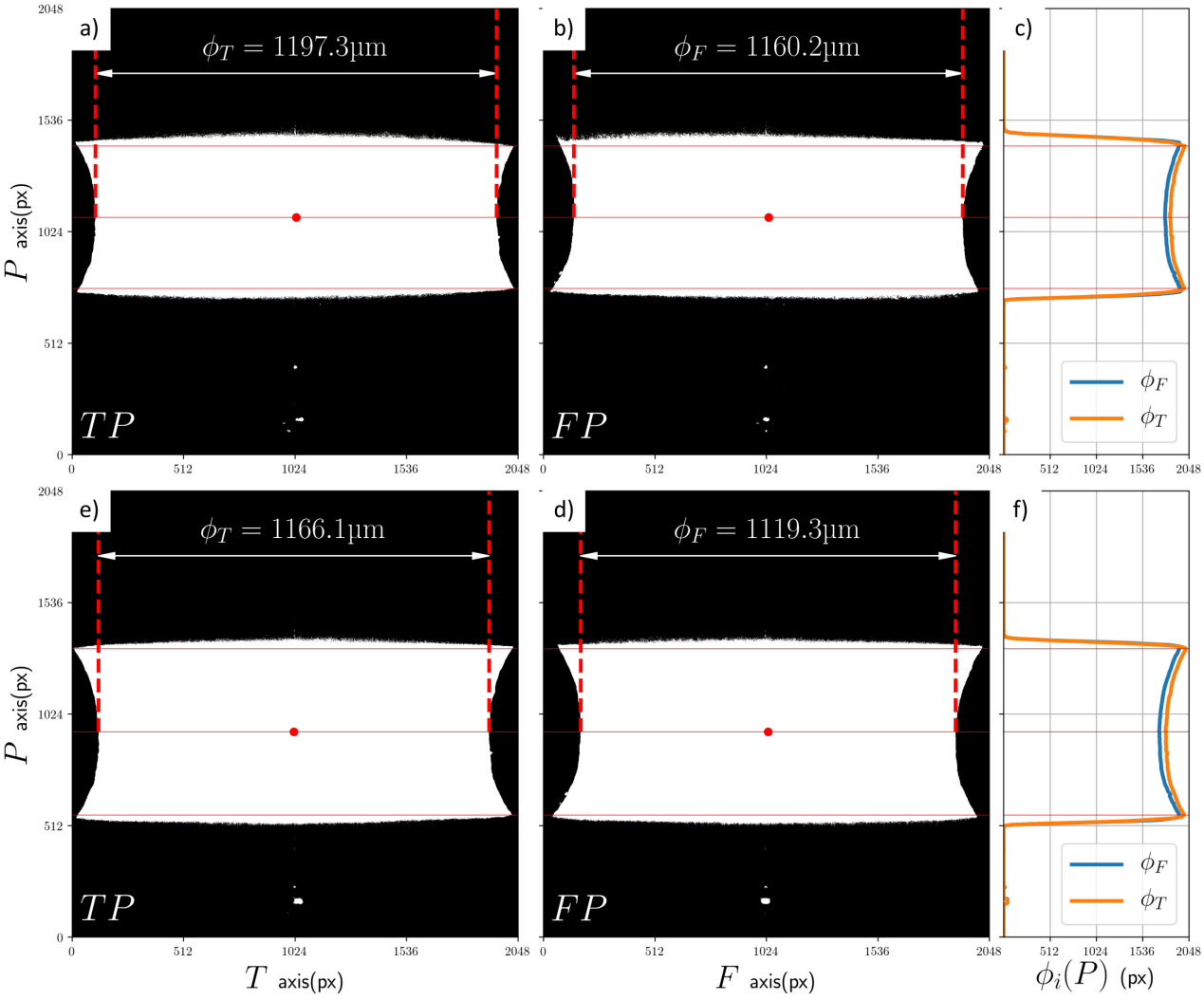

Figure 5.4: Diameter measurement of the minimum cross-section following the a,d) x and b,e) y directions for a-c) the first and d-f) the last tomographic acquisitions of the LFW–1 micro-tensile specimen.

Particle analysis The function *particle_analysis* is built-in the *particles* package (https://github.com/garciajuanm/particles). It is used for the computation of the barycentre, volume and the components of the tensor of inertia of each particle in a volume. The input is a segmented 2D o 3D array and the output is a plain text file containing in each line information about each particle in the input array. This information is used for the morphological characterization of particles explained later in this Section. To explain the procedure, a simple 2D case is explained here in detail. The analysis on 3D particles is analogous.

Let Fig.5.5a be the segmentation of a set of n particles in a 2D image. Pixels on the array take one of two values: 1 for pixels belonging to a particle and 0 elsewhere. The first operation is to label the segmented image. This operation is fulfilled with the *label* tool built-in in the *scipy.ndimage* package. It takes the segmented image as a single input and it return two outputs. The first is an array with the same dimensions as the input variable having the labelled array and the second is an integer containing the number of labelled particles. Every pixel in the labelled array holds the label of the particle to which it belongs, as it can be seen in Fig.5.5b. Notice that each particle matches its colour with every level on the colour bar.

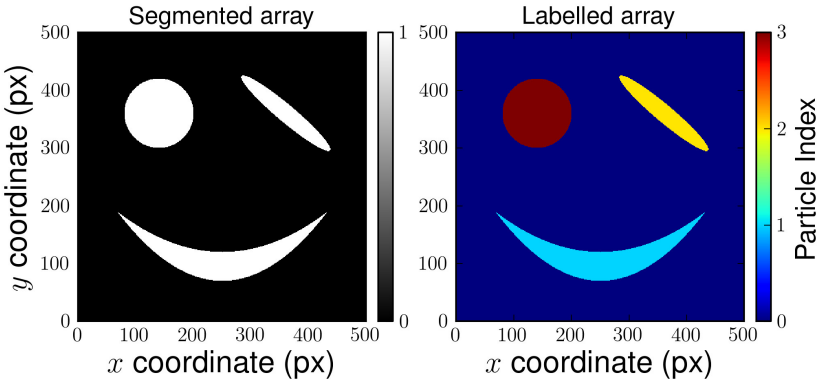

Figure 5.5: a) 2D example of segmented particles and b) particles labels.

The next operation is to compute the tensor of inertia of each particle. To do so, each particle is isolated and treated as a body of constant unitary density and each of its pixels is considered as an element of mass. In such case, the mass of the particle is equal to the area for 2D particles (or the volume for 3D particles). The isolation of each particle not only optimises computational time but also allows us to work in the local frame of reference for each particle.

First, each particle is isolated and its centre of mass is computed. The isolation of each particle is fulfilled by taking the smallest possible array that inscribes each particle. This is performed by using the *bounding_box* tool built-in in the *particles* package. The inputs are the labeled array and the index of the $i-$th particles. The output is stored in the `part` array (see first row of Fig.5.6). Thereafter, the barycentre on the local frame of reference $(x_{\mathrm{cm}}; y_{\mathrm{cm}})$ is computed using the *center_of_mass* function built-in in the *ndimage.measurements* package. The `part` for each particle and its centre of mass (red dot) are shown in the first row of Fig.5.6. Five arrays having the same dimensions as `part` array will be introduced: `x`, `y`, `i_xx`, `i_xy` and `i_yy` (see each row of Fig.5.6).

Second, two arrays `x` and `y` are created which contain the horizontal and vertical coordinates of the `part` array having the origin at the barycentre of the particle. For the 3D case, a third array `z` is created. This is fulfilled by creating a mesh grid using the *meshgrid* function built-in the *numpy* package. The origin is offset

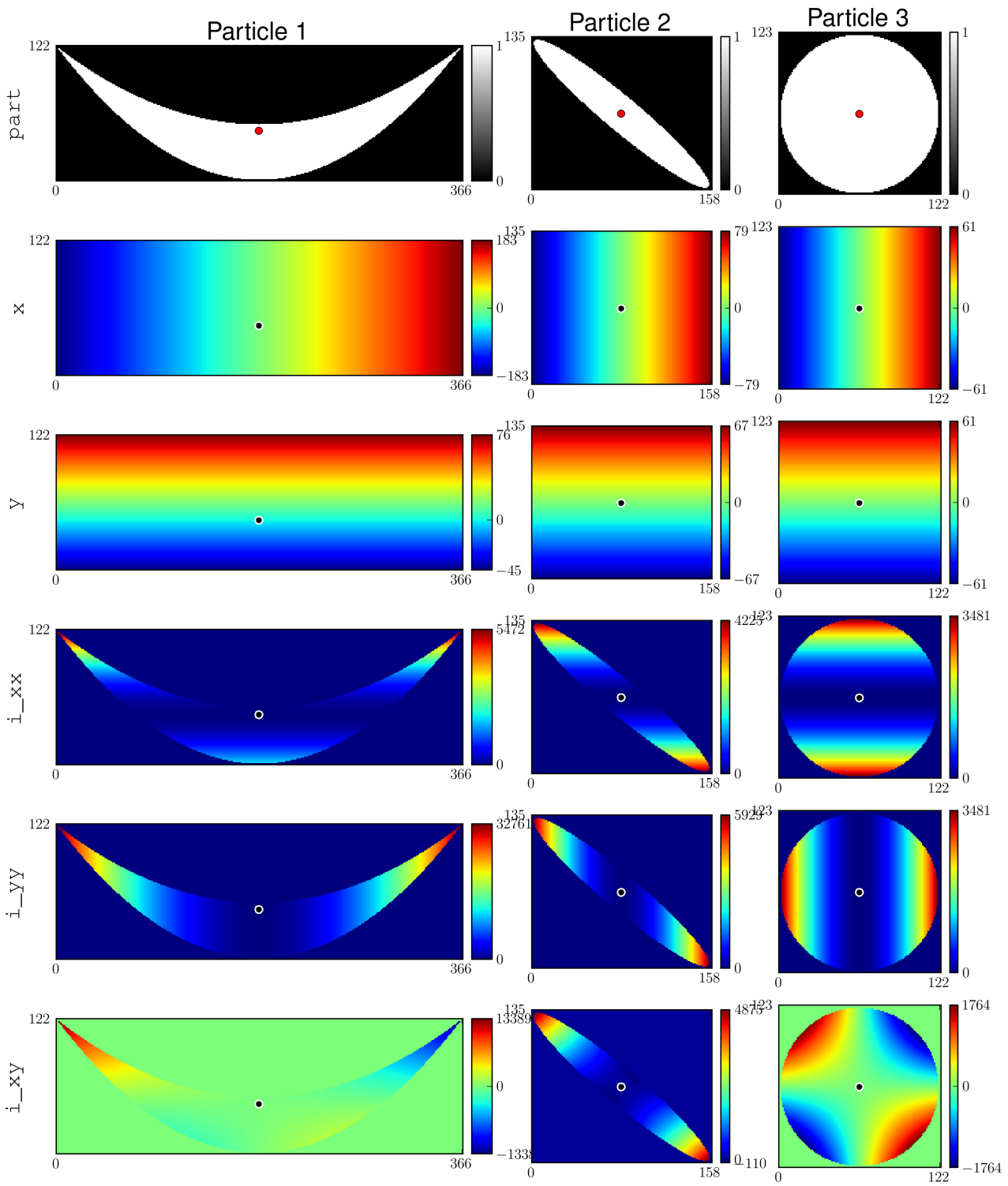

Figure 5.6: 2D visualization of the `part`, `x`, `y`, `i_xx`, `i_xy` and `i_yy` arrays for the computation of x, y, I_{xx}, I_{yy} and I_{xy} for the computation of the tensor of inertia of each particle of Fig.5.5.

to the barycentre of the particle by subtracting to each array of mesh grid the coordinates of the barycentre. The results of this operation are shown in the second and third rows of Fig.5.6. Notice that origin and the barycentre are coincident.

Third, the square of the `x` and `y` arrays are computed using the particle `part` array as a mask. This consists in the pixel-pixel multiplication between the particle and each coordinate array, raised to the second power (for

instance, `i_xx=(part*x)**2`). In other words, each pixel on the particle contains the squared of its distance to each barycentric axis. An approximation of the moments of inertia I_{xx}, I_{yy} and I_{xy} can be obtained by applying nested row-wise summations, as detailed in Eq.5.1. The results are shown in the third row `i_yy`, the forth row `i_yy` and fifth row `i_xy` of Fig.5.6.

$$\begin{aligned} I_{xx} &= \int_{\text{Area}} (x - x_{\text{cm}})^2 \, dx \, dy && \approx \sum\sum \texttt{i\_xx} \\ I_{yy} &= \int_{\text{Area}} (y - y_{\text{cm}})^2 \, dx \, dy && \approx \sum\sum \texttt{i\_yy} \\ I_{xy} &= \int_{\text{Area}} (x - x_{\text{cm}})\,(y - y_{\text{cm}}) \, dx \, dy && \approx \sum\sum \texttt{i\_yx} \end{aligned} \tag{5.1}$$

Then, the tensor of inertia for 2D and 3D objects is symmetric and can be written as in Eq.5.2.

$$\bar{\bar{I}} = \begin{bmatrix} I_{xx} & I_{xy} \\ I_{xy} & I_{yy} \end{bmatrix} \qquad \bar{\bar{I}} = \begin{bmatrix} I_{xx} & I_{xy} & I_{xz} \\ I_{xy} & I_{yy} & I_{yz} \\ I_{xz} & I_{yz} & I_{zz} \end{bmatrix} \tag{5.2}$$

The principal moments of inertia and the principal axis directions are respectively represented by the eigenvalues $I_i \, (i = \{1, 2, 3\}$ and $I_1 > I_2 > I_3)$ and eigenvectors $v_i \, (i = \{1, 2, 3\})$ of the tensor of inertia. This is fulfilled by using the *eig* function built-in in the package *numpy.linalg*. The computation of the barycentre, volume, the components of the tensor of inertia expressed in the global frame of reference, and the components of the principal moments of inertia are stored in a *particle_analysis.dat* plain text file that will be used for the morphological characterization.

Morphological characterization of particles This is fulfilled by the use of the *morphological_analysis* function built-in the *particles* package. The input is the *particle_analysis.dat* plain text file and the output is a scatter plot containing information about the morphology distribution of the particle population.

The characterization of a particle is performed by finding the ellipsis or ellipsoid that has a equivalent tensor of inertia. In such case, the semi axis can be computed using the eigenvalues as described in Eq.5.3 (see Figs.5.7 and 5.8).

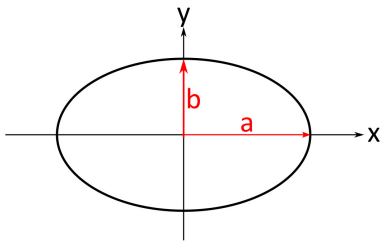

Figure 5.7: Ellipsis.

$$I_1 = \frac{\pi\, a\, b^3}{4} \qquad I_2 = \frac{\pi\, a^3\, b}{4} \qquad \Longrightarrow \qquad a = \sqrt[8]{\frac{4^2\, I_2^3}{\pi^2\, I_1}} \qquad b = \sqrt[8]{\frac{4^2\, I_1^3}{\pi^2\, I_2}} \tag{5.3}$$

Similarly, for a 3D ellipsoid of volume V:

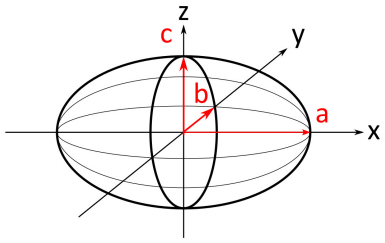

Figure 5.8: Ellipsis.

$$I_1 = \frac{\pi\left(b^2+c^2\right) V}{5} \qquad I_2 = \frac{\pi\left(a^2+c^2\right) V}{5} \qquad I_3 = \frac{\pi\left(a^2+b^2\right) V}{5} \qquad \Longrightarrow$$
$$a = \sqrt{\frac{5}{2V}\left(-I_1+I_2+I_3\right)} \qquad b = \sqrt{\frac{5}{2V}\left(I_1-I_2+I_3\right)} \qquad c = \sqrt{\frac{5}{2V}\left(I_1+I_2-I_3\right)} \tag{5.4}$$

The morphology of particles can be described by the use of the adimensional principal moments of inertia λ_1 and λ_2 (Denis et al., 2008; Delloro, 2015). It consists in normalizing the principal moments of inertia of the particle with respect to their summation, as described in Eq.5.5. In such manner, they become independent of the volume and are reduced to two independent parameters.

$$\lambda_1 = \frac{I_1}{I_1+I_2+I_3} \qquad \lambda_2 = \frac{I_2}{I_1+I_2+I_3} \tag{5.5}$$

By the use of the definition of adimensional principal moments of inertia λ_i and the principal moments of inertia I_i, three inequalities can be obtained, as detailed in Eq.5.6.

$$\lambda_1 > \lambda_2 \qquad \lambda_2 < 0.5\,(1-\lambda_1) \qquad \lambda_i < 0.5 \tag{5.6}$$

These parameters are useful since the distribution of shapes of an entire population of particles can be easily represented with a single 2D scatter plot. Each particle is represented with a dot in the grey region of Fig.5.9 which is defined by the inequalities of Eq.5.6. Depending on the values of λ_1 and λ_2, the shape of the particle is likely to resemble to one of the reference shapes in Fig.5.9. For instance, consider a single particle having the same value for all moments of inertia then $\lambda_1 = \lambda_2 = 0.33$ (red dot in Fig.5.9). In such case, the particle shape is close to a sphere. In the case of a particle having a predominant direction, its morphology is close to a needle shape (green dot in Fig.5.9). In a similar manner, particles close to the blue, red and green lines are respectively similar to prolate ellipsoids, flat-shaped particles and oblate ellipsoids. Flat and needle shape particle be close to the red an blue. The drawback is that the alignment of the particles can not be interpreted from of this representation.

This representation provides valuable information about the morphological trends of a population of particles but it does not inform about the alignment of the particle with respect to the frame of reference.

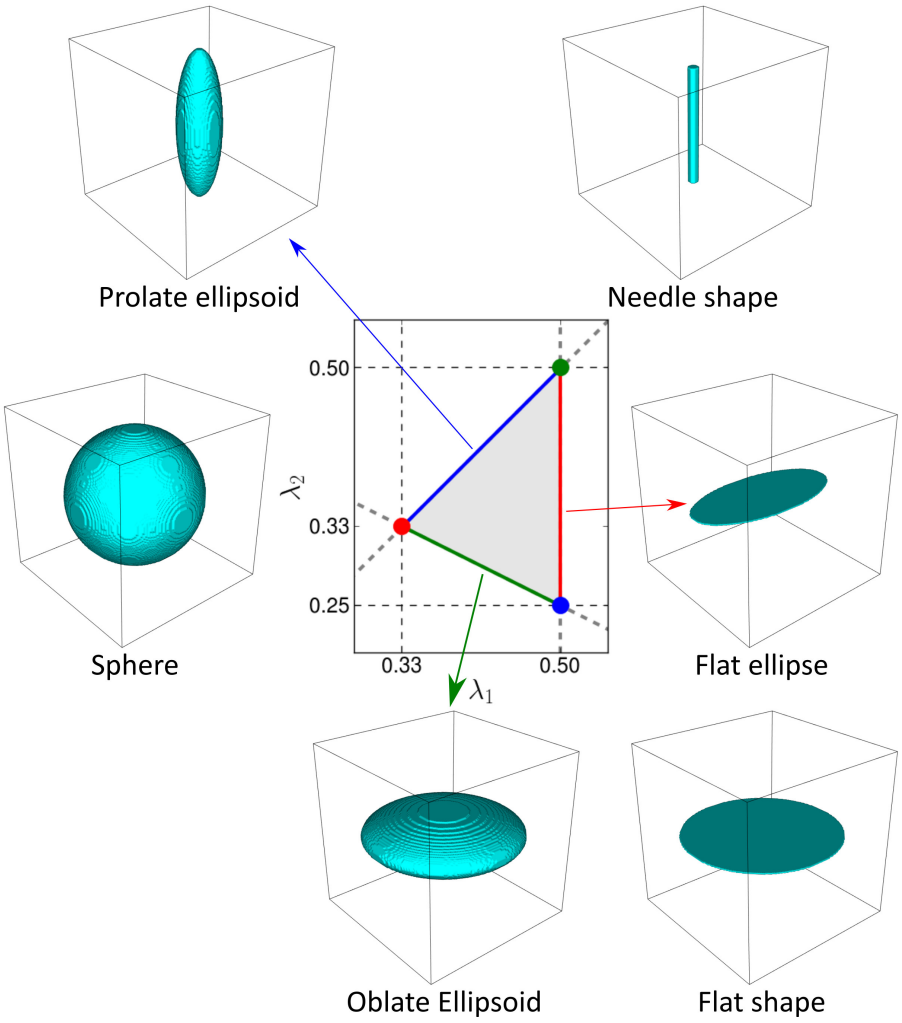

Figure 5.9: Schematic view of different particle shapes and the scatter analysis of adimensional principal moments of inertia.

Particle alignment characterization In Fig.5.10, a prolate and an oblate ellipsoid are shown. Notice that the eigenvectors have been rescaled to match the semi axis dimensions, using the expressions of Eq.5.4. The axis that better describes the alignment of a particle resembling a oblate ellipsoid is the axis parallel to v_1, the eigenvector associated with the highest eigenvalue. In the case of a particle resembling to a prolate ellipsoid, the axis that better describes the alignment is v_3, the eigenvector associated with the lowest eigenvalue. In other words, for an oblate ellipsoid, the alignment is better described by the axis for which the moment of inertia is maximum (I_3) and for a prolate ellipsoid, the axis for which the moment of inertia is minimum (I_1). Thus, the representation of the alignment by the eigenvectors requires a previous study of the morphology. Once the choice of the eigenvector for the alignment characterization has been set, the alignment of a particle can be represented by the α, β and γ: the angles formed between the eigenvector v_i and the positive semi axes of the frame of reference $(\hat{i}, \hat{j}, \hat{k})$ (see Eq.5.7). Each angle is comprised between $[0; \pi/2]$. For example, a prolate ellipsoid having $\alpha = \beta = \pi/2$ and $\gamma = 0$, its v_3 eigenvector is perpendicular to xy plane and parallel to z axis, as shown in Fig.5.10a. When analyzing a population of particles, the distribution of α, β and γ can easily be represented in polar scatter plots.

This analysis gives reliable information if the studied particles exhibit anisotropic morphology. In the case of spherical particles, any axis is a principal axis, therefore there is no alignment. With this analysis, each

a)

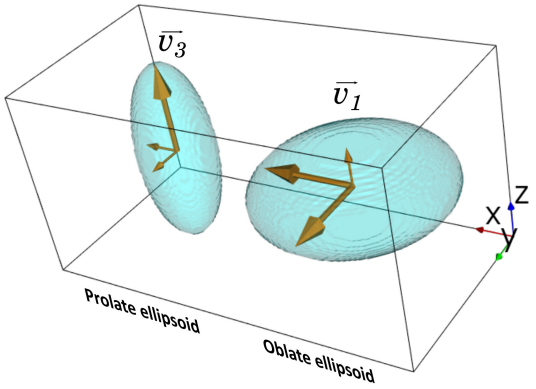

b)

$$\alpha = \arccos\left(\frac{v_{ix}}{\|\vec{v_i}\|}\right)$$

$$\beta = \arccos\left(\frac{v_{iy}}{\|\vec{v_i}\|}\right) \tag{5.7}$$

$$\gamma = \arccos\left(\frac{v_{iz}}{\|\vec{v_i}\|}\right)$$

Figure 5.10: a) Prolate and oblate ellipsoid with their associated eigenvectors and b) expressions for the computation of the angles formed between the eigenvectors and the global frame axes.

particle is isolated to study the alignment of its morphology with respect to a global frame of reference. No information is provided concerning the global alignment of a population, i. e., a single line formed by spherical particles. The *morphological* and *alignment* characterization give quantitative information about a population of particles that can be used for statistical analysis.

Optical microscope *in situ* micro-tensile testing

Flat notch micro-tensile specimens PM and cross-weld flat notched micro-tensile specimens were machined. The micro-tensile specimen geometry is displayed in Fig.5.11a. For the precise machining of the notches, the position of the WCZ for each cross-weld specimen was determined through measurements on SEM micrographs. The specifications of the specimen for the notch height and radius respectively were 0.92 µm and 1280 µm. As it can be seen in Fig. 5.15, the width machining precision is within 5 %. The centring on the notch with respect to the WCZ has been fulfilled with very good precision. For all specimens, mirror like quality was achieved by polishing using a SiC paper grit 1200 followed by 24 h of suspension polishing using a solution composed of 200 mm^3 Struers oxide and 200 mm^3 distilled in a Buehler VibroMet (see Fig.5.11b).

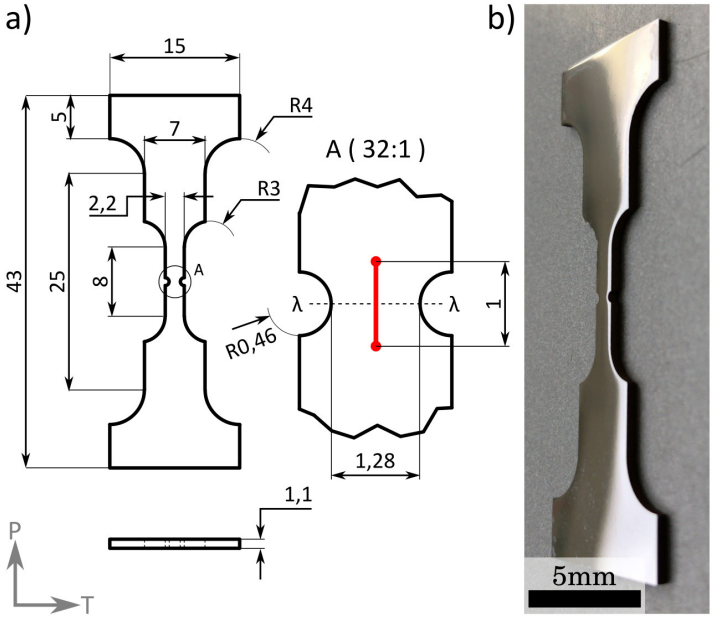

Figure 5.11: a) Flat notched micro-tensile specimen geometry. b) View of a typical flat micro-tensile specimen exhibiting the surface state for tensile testing.

Micro-tensile testing Flat notched micro-tensile specimens were mounted on a *FONDIS MT100* mini-tensile testing machine, originally designed for SEM *in situ* testing, but at that time the BSE detector of the laboratory SEM was out of service. The dimensions of the machine are 502 mm × 327 mm × 250 mm with a total screw travel of 150 mm, and a maximum load capacity of 5 kN. Boundary conditions of fixation and displacement are applied on the curved surfaces of the specimen having 4 mm radius (see Fig.5.11a). Loading was applied on a displacement control basis with a cross-head speed of 5 µm s^{-1}. Mesoscopic strain measurements were carried out with optical extensomenters with a typical gauge length of 1 mm, as shown with in red in Fig.5.11a.

Optical microscope *in situ* micro-tensile testing The load frame was mounted on the stage of a VHX-1000E Keyence optical microscope instrumented with a VH-Z50L zoom lens. The displacement field of the notch region was monitored through a 2D Incremental Digital Image Correlation using the microstructure as a speckle. The choice of performing incremental DIC instead of DIC is explained later in this Section. Microstructure was revealed using Kroll's 2 reagent (12%HF + 18%HNO_3 + 70%H_2O). During loading, the microscope was set to carry out a time-lapse image recording with a frequency of 1 Hz over a region of interest of a 1.4 mm × 1.8 mm around the notch. Incremental DIC was performed with Vic-2D™ from Correlated Solutions, Inc. (ver-

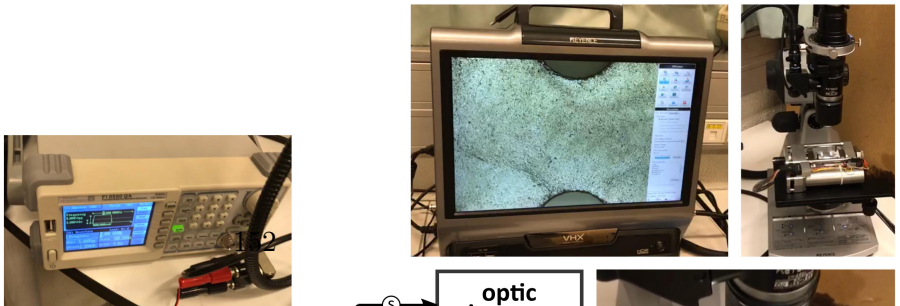

sion8.2.4, 2014). The size of the optical images was 1600 px × 1200 px. Subset size was 50 px ≈ 50 µm, step size was 13 px and filter size was 5 px.

The set up is schematically described in Fig.5.12. The load frame control sends the displacement signal to the load frame and measures the reaction force. These two signals are recorded by a Hioki Memory HiLOGGER 8430-20 data logger. A function/arbitrary waveform generator *FI 5500GA Serie* of *Française d'Instrumentation* sends a square signal to the microscope to trigger each image recording. In parallel, the square signal is recorded by the data logger. In such manner, the synchronized recording of time, displacement, force and optic images during testing is warranted.

EBSD mapping and fractographic observations

A single EBSD mapping was carried out on the notch zone of flat notched micro-tensile specimens made of PM. For a single flat micro-tensile cross-weld specimen, a multi-field EBSD mapping was carried out. Mappings were performed using a camera Nordif UF300 to cover an area of approximately 1 mm^2 with a step size of 1 µm. The dimensions of each EBSD pattern were 840 px × 840 px. The working distance was 24 mm. Indexation was carried out taking into account only the α phase. The fractographic observations were carried out at low and high magnification using secondary electron detector in a ZEISS DSM982 Gemini scanning electron micropscope (SEM) operated at an accelerating voltage of 20 keV.

5.3 Results

5.3.1 Microstructure characterization

Microstructure of parent material (PM) and weld centre zone (WCZ)

Fig.5.13a shows a micrograph obtained using BSE detector for the PM. One can see that the microstructure consists of equiaxed α grains and lamellar α situated in a β matrix. The Average Grain Intercept method was performed using SEM/BSE images of the PM microstructure (not shown here) to compute the average grain size of the α grains. The resulting average grain size was about 10.7 µm. Fig.5.13b shows the microstructure observed in the cross section of the welded joint on a PT plane. The presence of the WCZ is observed within the horizontal ∼100 µm thick band. Microstructure in the surroundings of the WCZ shows indications of strong levels of plastic deformation and the fragmentation of former α grains. The level of plastic deformation is higher close to the WCZ. Fig.5.13c shows a high magnification view of the WCZ. A very fine recrystallization is observed. Needle shape like grains of ∼150 nm thickness are observed. An acicular entangled α' martensite is formed within prior-β RX grains (Ballat-Durand et al., 2019). This microstructure is comparable to the one observed in Ti64 and IMI-834 similar LFW joints found in literature (McAndrew et al., 2014; Dalgaard et al., 2012b).

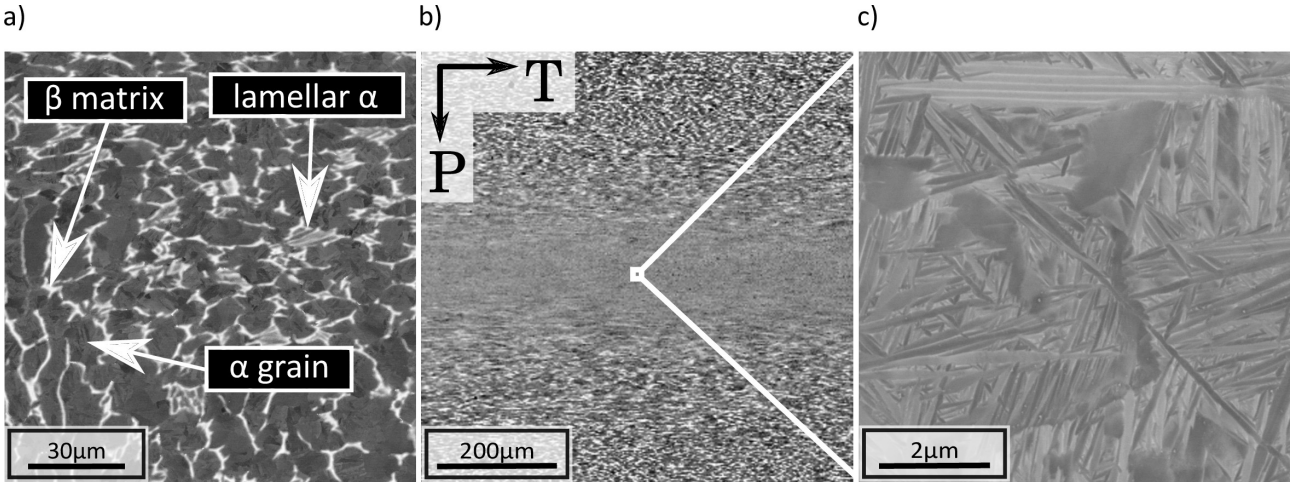

Figure 5.13: SEM/BSE observation of a) PM microstructure, b) the affected zone containing the WCZ and the TMAZ and c) the very fine entangled acicular α' martensite on the WCZ.

EBSD mapping of flat micro-tensile specimens

In this section, the EBSD mappings of the both sets of specimens are presented. These mappings were meant to be compared with the strain field maps obtained by DIC. Unfortunately, the reliability of the strain fields measured by incremental DIC using microstructure as speckle is still uncertain using the optical microscope. However, these mappings will be used to discuss the scatter on the measured tensile strength in Section 5.3.2.

PM flat micro-tensile specimen Fig.5.14 shows the EBSD mappings for three typical specimens made of PM. The extrusion direction of the billet is perpendicular to the screen. The pole figures show that the crystal

lattice distribution is heterogeneous from specimen to specimen. Microstructure shows zones with localized texture that are comparable to the notch size. It seems reasonable to state that response in terms of strain and stress of these specimens should show a certain scatter.

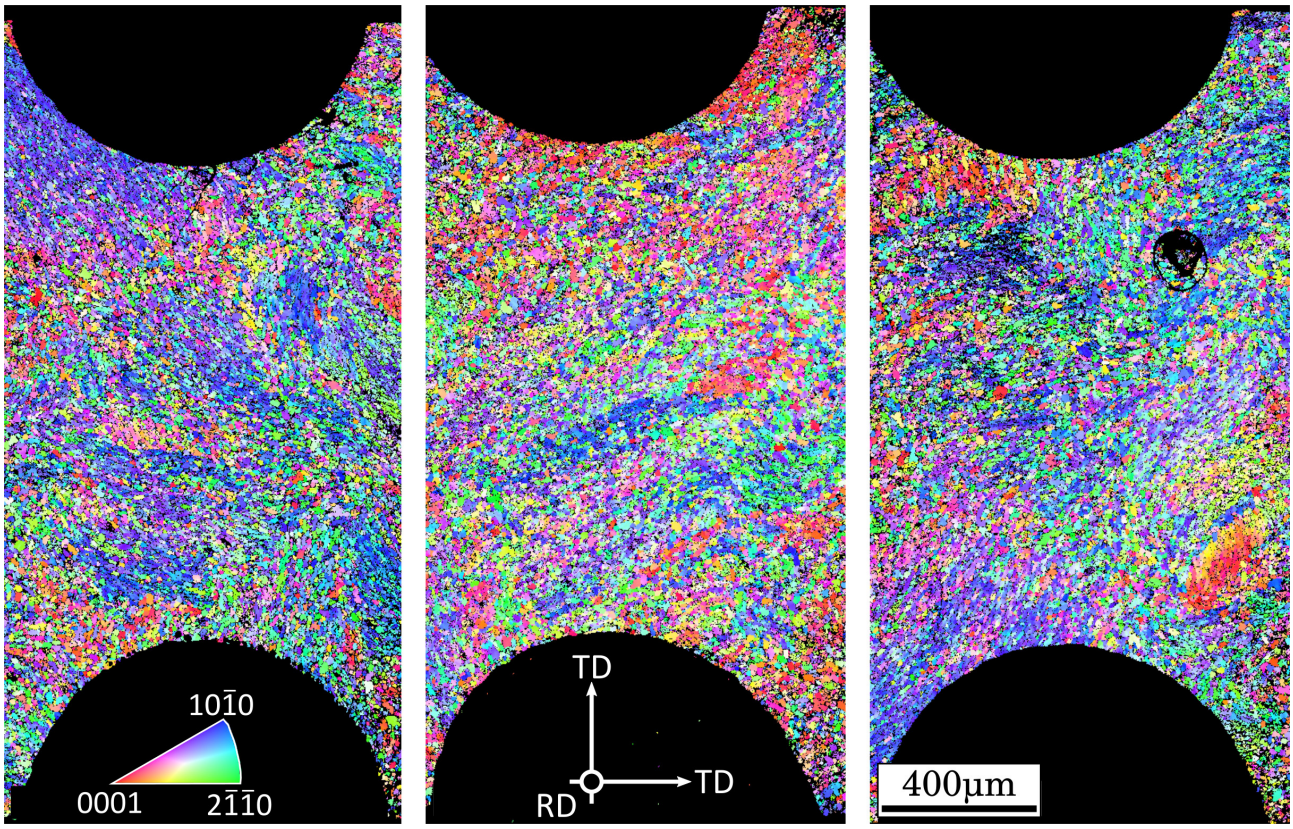

Figure 5.14: Inverse pole figures of three typical flat micro-tensile specimens made of PM.

LFW micro-tensile specimen The SEM observation of Fig.5.15a shows the notch centred with respect to the WCZ for a typical cross-weld specimen. A pole figure is shown in 5.15b. The frontier between each side of the weld can clearly be seen in the centre of the notch. It is worthwhile noticing that crystal lattice orientation appears to be different from each side of the WCZ. The microstructure affected by LFW reaches regions beyond the notch zone. Far from the affected zone, the macrozones documented by (Le Biavant et al., 2002; Echlin et al., 2016; Kasemer et al., 2017) are seen in the PM. Fig.5.15c shows a high magnification SEM/BSE observation of the acicular entangled α' martensite at the WCZ, already described in Section 5.3.1.

5.3.2 Micro-tensile tests

Synchrotron *In situ* micro-tensile tests

The vertical axis of Figs.5.16a, 5.16b and 5.16c is shared and it represents the mesoscopic engineering stress. The horizontal axis of Figs.5.16a, 5.16b and 5.16c respectively represent the time of the experiment, the cross-head displacement and the lateral strains. The white dots represent the tomographic observations for which damage was observed, this is further discussed in Section 5.3.4. The maximum measured strains for the x and y directions are summarized in Table 5.3. For the LFW–1 micro-tensile specimen, the x and y directions are respectively parallel to the T and F axis.

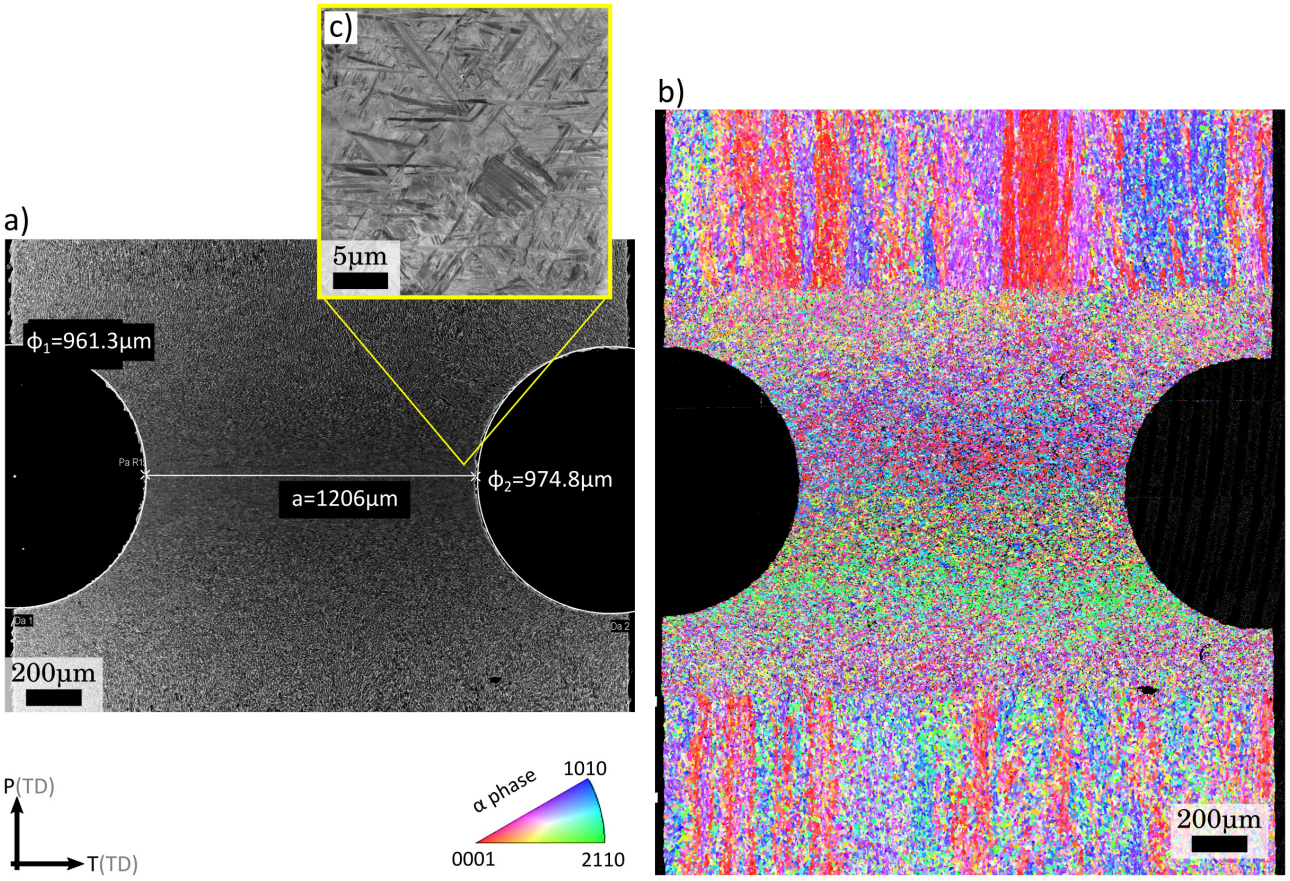

Figure 5.15: a) SEM observation of a typical flat micro-tensile specimen exhibiting the notch centred with respect to the WCZ. b) Inverse pole figure in the vicinity of the notch. c) SEM observation of the acicular entangled α' martensite at the WCZ. This specimen was not tested.

The PM–1 and LFW–1 axisymmetric micro-tensile specimens exhibited a maximum nominal engineering stress ((F/S_0)) of 1720 MPa and 2360 MPa, respectively. The cross-head displacement for the PM–1 and LFW–1 axisymmetric micro-tensile specimens respectively were 0.90 mm and 0.81 mm (see Fig.5.16b). Compared to the specimens made of PM, the strength of the cross-weld specimens is 37 % greater. Stress relaxation during

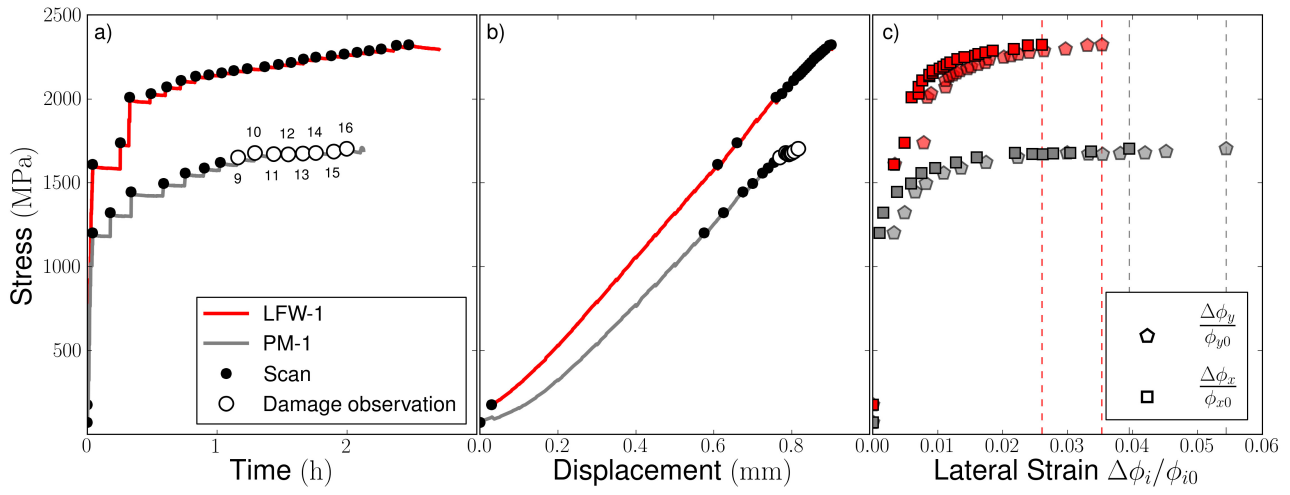

Figure 5.16: The curves for the PM–1 and LFW–1 axisymmetric micro-tensile specimens are respectively plotted in grey and red. Macroscopic engineering stress *versus* a) time, b) load frame cross-head displacement and c) lateral strains. The black dots represent tomographic acquisitions. The white dots represent scans for which damage was observed. For the LFW–1 axisymmetric micro-tensile specimen, the x and y directions are respectively parallel to the T and F axis.

Specimen	$\frac{\Delta\phi_x}{\phi_{x0}}$	$\frac{\Delta\phi_y}{\phi_{y0}}$	F/S_0 Max MPa
PM-1	0.054	0.039	1025
LFW-1	0.026	0.035	1307

Table 5.3: Maximum engineering lateral strain and mesoscopic engineering stress for the PM–1 and LFW–1 axisymmetric micro-tensile specimens. For the LFW–1 axisymmetric micro-tensile specimen, the x and y directions are respectively parallel to the T and F axis.

holding for tomographic acquisition is highlighted by a stress drop and a stress plateau after every black point in Fig.5.16a. Notice that failure occurred abruptly without exhibiting stress drop for any of both specimens. In particular, the LFW–1 axisymmetric tomographic specimen failed during relaxation. It is also interesting to note that, during the elastic domain, the slope of these curves is quite similar, which suggests that the WCZ and the PM have similar Young's modulus. The same observation has been previously pointed out based upon the homogeneity exhibited by the strain fields obtained by DIC during the macroscopic tensile specimens in Section 4.3.5.

The PM–1 axisymmetric micro-tensile specimen exhibited lateral strains parallel to the x and y directions of respectively $\varepsilon_{xx} = 0.054$ and $\varepsilon_{yy} = 0.039$ (see Fig.5.16c). This significant difference suggests some underlying texture. No EBSD observations were performed on the axisymmetric micro-tensile specimens to confirm this but, as for flat micro-tensile specimens of Section 5.3.1, the presence of macrozones may be at the origin of this anisotropy. As it would be expected, the notch favoured plastic deformation at the WCZ having lateral strains parallel to the T and F directions of respectively $\varepsilon_{\mathrm{TT}} = 0.026$ and $\varepsilon_{\mathrm{FF}} = 0.035$ (see Fig.5.16c). Compared to the PM–1 axisymmetric micro-tensile specimen, the maximum engineering stress for the LFW–1 axisymmetric micro-tensile specimen is ∼30 % greater. Indeed, the similar Ti6242 LFW joint exhibited overmatching strength. This is very interesting since, during macroscopic tensile tests of smooth specimens presented in Section 4.3.4, failure always occurred at the PM and the UTS was that of the PM.

Optical microscope *in situ* micro-tensile tests

Fig.5.17 shows the tensile curves for the flat micro-tensile specimens. Black and red lines respectively represent the flat micro-tensile specimens made of PM and the flat cross-weld micro-tensile specimens. The LFW–AW–PC and LFW–AW flat micro-tensile specimens are represented with thin and thick lines. Fig.5.17a shows the grip displacement-stress curve. The stress-strain curves are shown in Fig.5.17b.

The cross-weld specimens showed a mean maximum engineering stress of 1550 MPa whereas the LFW–AW-1 cross-weld maximum stress was 1601 MPa. The specimens made of PM exhibited a mean maximum engineering strength of 1230 MPa. Compared to the PM flat micro-tensile specimens, the strength of the cross-weld flat micro-tensile specimens is 26 % higher. A comparable ratio was observed for the axisymmetric specimens. The maximum displacement for both sets of specimens is quite similar. Conversely, the responses of the specimens in terms of strain are staggeringly different. It is worthy of being noticed that the overall plastic strain is larger for the PM than for the cross-weld specimens. This is in agreement with the tensile behaviour of the axisymmetric micro-tensile specimens of Section 5.3.2.

Both sets of specimens have shown a certain scatter in strength that was not observed for the macroscopic tensile tests in the macroscopic tensile tests of Section 4.3.4. A similar scatter in strength was observed on the Ti64 micro-tensile specimens performed by (Lunt et al., 2017). The authors observed that specimens containing

hard macrozones led to more heterogeneous strain fields and subsequently to higher levels of strength. As shown in Section 5.3.1, both the specimens made of PM and the cross-welds specimens exhibited zones of local texture. It is fairly reasonable to state that these macrozones are likely to be at the origin of the strength scatter observed in Fig.5.17. In this study, the complex stress field generated by the notch and the microstructural heterogeneity (in the case of cross-weld specimens) may have enhanced these effects.

The apparent elastic behaviour of all axisymmetric micro-tensile specimens is unexpected. In some cases, some compression is measured even if loading is monotonic and tensile. A possible explanation for this phenomenon is the strain measurement artefact induced by an out-of-plane displacement. For instance, when the grip starts to displace, an out-of-plane rotation around an axis containing the width of the flat micro-tensile specimen, namely the $\lambda\lambda$ axis in Fig.5.11, may occur. This would induce optic extensometer to become virtually smaller from the microscope perspective. After a certain level of load, the specimen describes a planar displacement in an oblique plane and tensile strain is measured with slight underestimation. A similar phenomenon has been observed during the micro-tensile tests conducted by (LaVan and Sharpe, 1999). The authors have explained that a slight misalignment between the grips could induce bending moments and hence some compression. The fact that this phenomenon is more pronounced for the cross-weld specimens is puzzling. The strain measurements performed in Section 5.3.2 seem more reliable that the ones presented here. Nonetheless, in this study, these values were used to develop a qualitative understanding of the overall behaviour.

5.3.3 Failure location

Axisymmetric micro-tensile specimens

Failure location Fig.5.18c and 5.18d respectively exhibit 2D slices of prior to loading and *post-mortem* tomographic observations for both specimens. The observations prior to loading for both specimens exhibit a slight contrast that reminds the microstructure of the PM (see Fig.5.13). Contrast is homogeneous on the LFW–1 micro-tensile specimen observation (see Fig.5.18b). This is consistent with the fact that microstructural features at the WCZ are smaller than the tomographic spatial resolution used here and hence can not be observed.

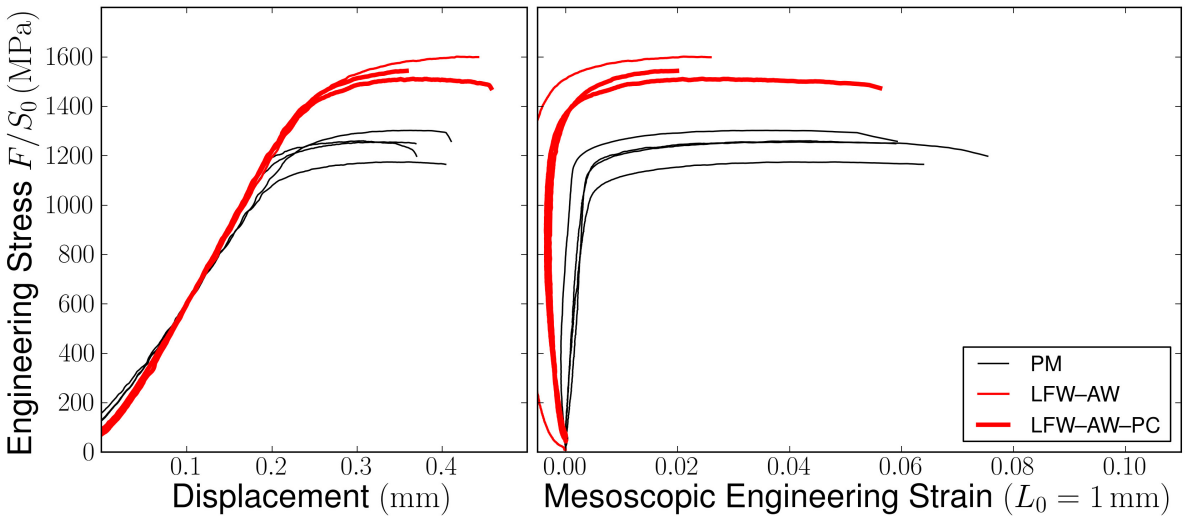

Figure 5.17: Stress-displacement and stress-strain curves for the PM (black lines) and LFW (red lines) flat micro-tensile specimens.

It seems that the WCZ is located about 50 µm below the minimum cross-section. Previous laminographic observations of a cross-welded sample allowed the microstructure of the PM far from the WCZ to be revealed and some porosity to be observed in Section 4.3.2. Conversely, no pores were observed for this sample.

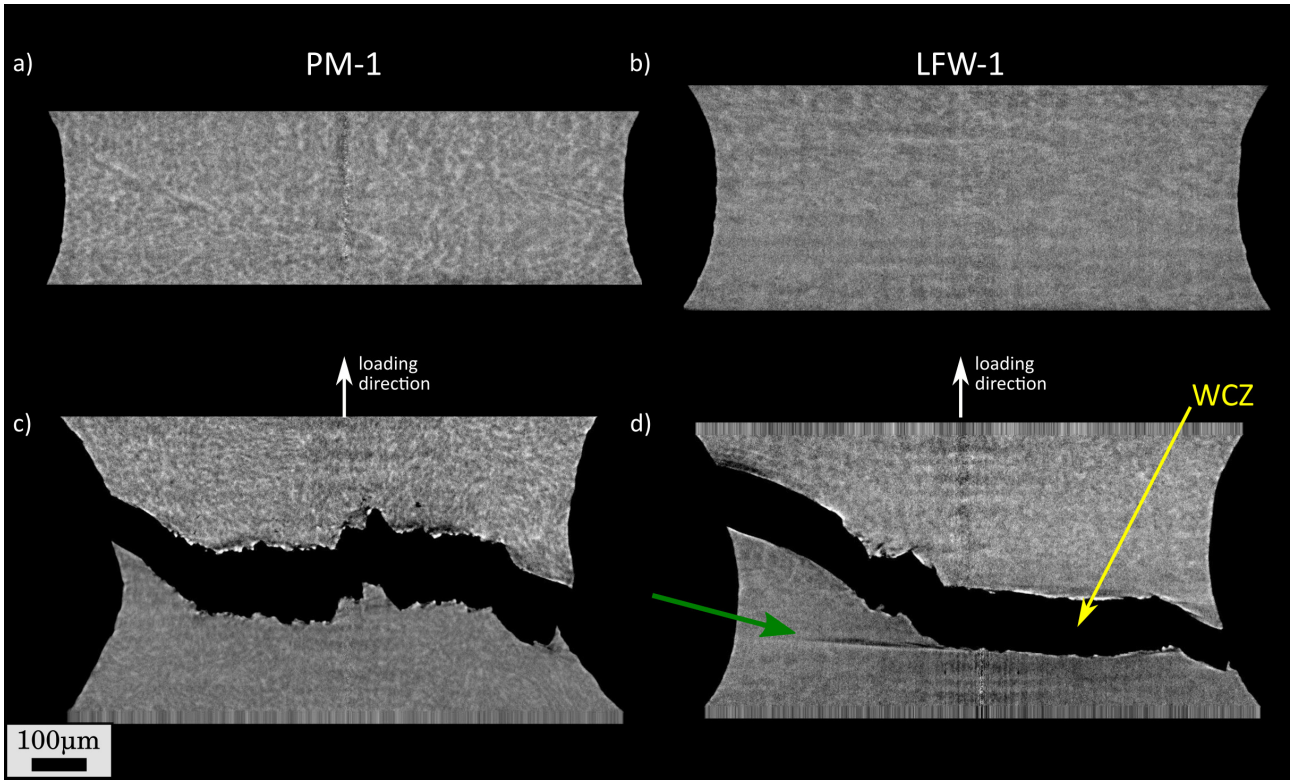

Figure 5.18: a,b) Prior to loading and c,d) *post-mortem* 2D slices of the reconstructed tomographic volume for the a,c) PM–1 and b,d) LFW–1 axisymmetric micro-tensile specimens. The loading direction was vertical.

The *post-mortem* observation of the PM–1 flat micro-tensile specimen (Fig.5.18c) revealed a cup-cone fracture with shear lips that suggests ductile fracture. The *post-mortem* observation of the LFW–1 flat micro-tensile specimen (Fig.5.18d) exhibited a flat surface contained on the zone that shows no contrast due to microstructure hinting to failure located at the WCZ (yellow arrow in Fig.5.18d). The linearly shaped features pointed by the green arrow in Fig.5.18d are artefacts inherent to the tomography technique and are related to the strong contrast between the flat surface and the surrounding air.

Flat micro-tensile specimens

Fig.5.19a shows a *post-mortem* SEM/BSE observations of the surface of a typical LFW–AW and LFW–AW–PC flat micro-tensile specimens. The chemical contrast of the SEM/BSE observations allows the WCZ and both TMAZ's to be seen (notice the yellow arrows in Fig.5.19a and 5.19b). The acicular entangled α' martensite described in Section 5.3.1 is clearly seen in the zoom of Fig.5.19c and 5.19d. Notice that the crack crossed the WCZ for both specimens. This is also reflected in the mid-plane cut shown in Fig.5.19e. It is interesting to note that the geometry of the flat micro-tensile specimens has successfully induced failure at the WCZ. It is also worthwhile noting that the crack path for both LFW–AW and LFW–AW–PC flat micro-tensile specimens is very similar. At this level of analysis, no influence of prior to welding contamination is observed.

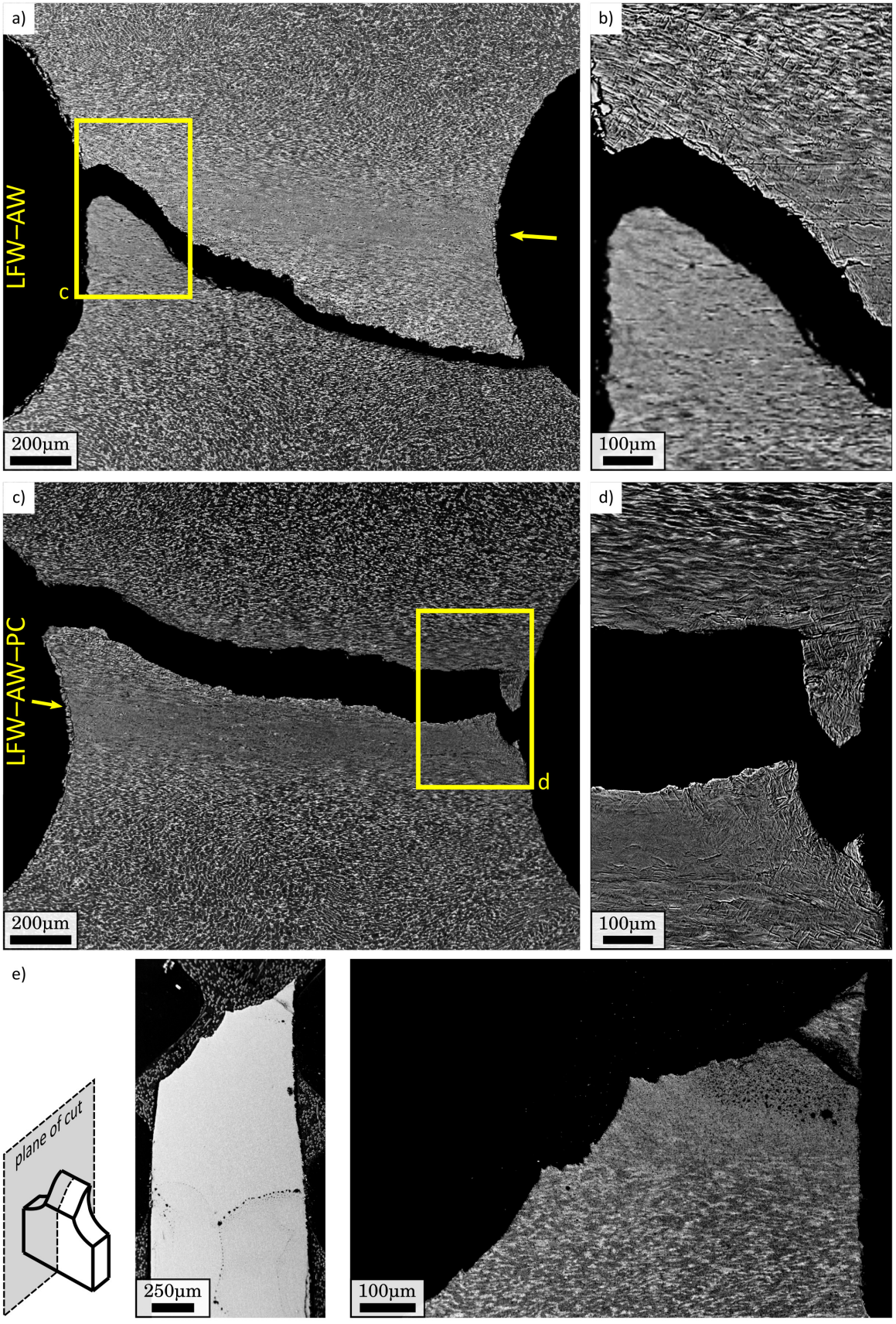

Figure 5.19: SEM/BSE observations of the surface of typical a,c) LFW–AW and b,d) LFW–AW–PC flat micro-tensile specimens. e) SEM/BSE observation of the mid-plane of a typical flat micro-tensile specimens showing microstructure in the vicinity of the fracture surface.

5.3.4 Fracture mechanisms

Damage mechanisms of the PM

In this Section, the damage mechanisms of the PM are studied. Fig.5.20a shows a 2D slice of the minimum cross-section of the PM–1 axisymmetric micro-tensile specimen taken from the last tomographic scan before failure (see scan 16 in Fig.5.16a). As for this 2D slice, some void nucleation and growth can be observed for the last 8 tomographic observations of the PM–1 axisymmetric micro-tensile specimen, after the onset of plastic mesoscopic strain (see white dots in Fig.5.16a). Using image processing through Python scripts, a colour was given to cavities and everything else has been set in absolute transparency. This allows the 3D visualization of damage in Fig.5.21 to be constructed. Despite the high triaxiality levels induced by the notch, diffuse damage occurred in the whole observed volume. It seems that void nucleation is driven by microstructural interactions, instead of triaxiality. Furthermore, it is worthy of being noticed that damage seems to be aligned with the RD direction of the billet and exhibits penny-shaped cracks. A quantitative study of the observed damage on the PM–1 micro-tensile specimen is presented in Section 5.3.4.

Fig.5.20b shows a 2D slice of the minimum cross-section of the LFW–1 axisymmetric micro-tensile specimen taken from the last tomographic scan before failure (see scan 24 in Fig.5.16a). Unlike the PM–1 axisymmetric micro-tensile specimen, no damage was observed for the LFW–1 axisymmetric micro-tensile specimen (see Fig.5.20b). Two possible explanations can be stated for the absence of damage. First, it could be related to damage occurring at lower scales than the tomographic spatial resolution, this will be discussed in Section 5.3.4. A second possibility, is that void nucleation, growth and coalescence occurred during the unstable failure mentioned in Section 5.3.2. This is further discussed in Section 7.4.

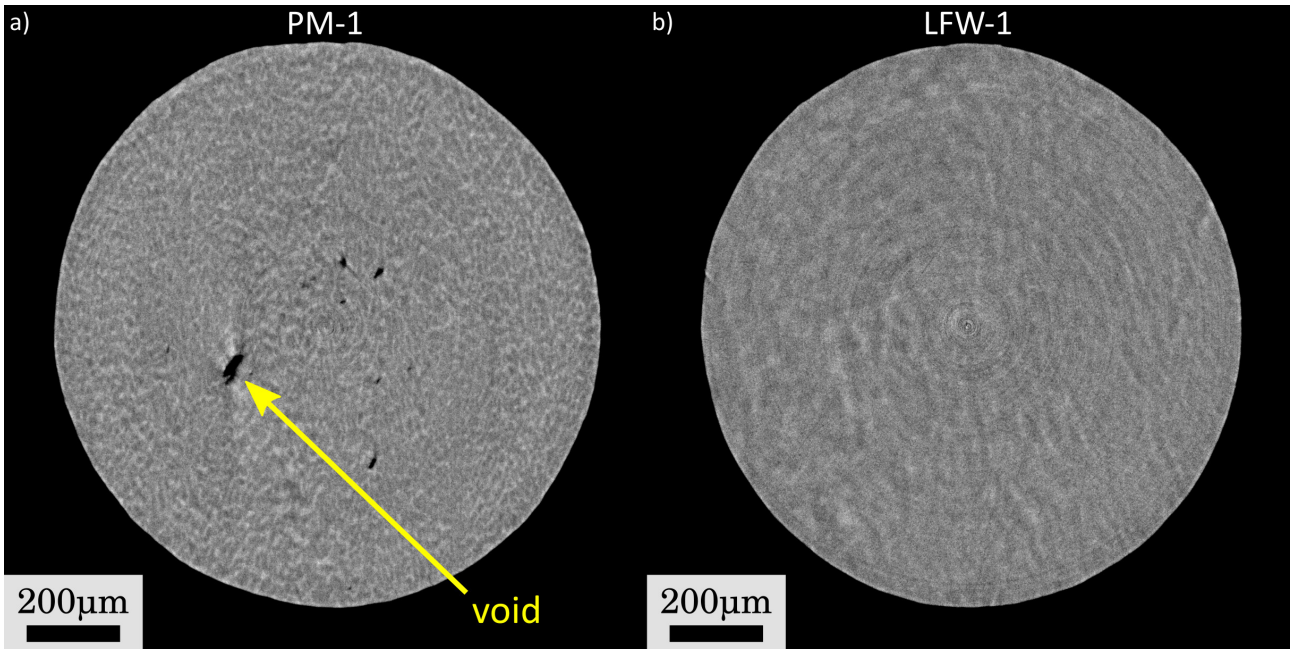

Figure 5.20: 2D slices normal to the loading direction of the reconstructed tomographic volume for the a) PM–1 (scan 16) and b) LFW–1 (scan 23) tomographic specimens in each respective last tomographic scan.

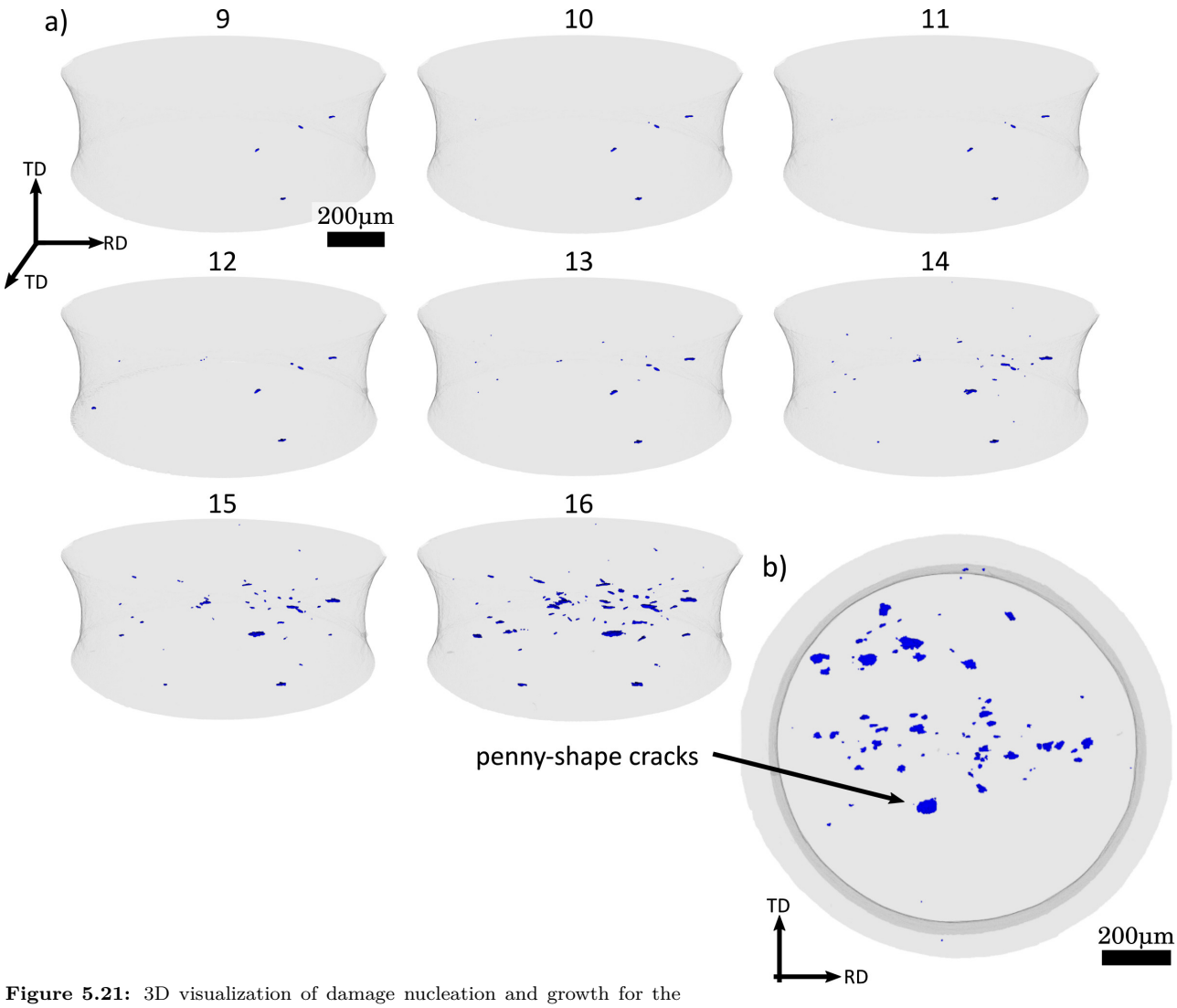

Figure 5.21: 3D visualization of damage nucleation and growth for the PM–1 tomographic micro-tensile specimen corresponding to the 8 latest tomographic scans (See Fig.5.16) and b) top view of damage for the latest tomographic scan. c) Initial and final 3D visualizations of the LFW–1 tomographic micro-tensile specimen.

Fractographic analysis of axisymmetric micro-tensile specimens

Axisymmetric micro-tensile specimens 3D *post-mortem* visualizations of the fracture surfaces for both specimens are shown in Fig.5.22a and5.22b. The PM–1 axisymmetric micro-tensile specimen exhibits a classic cup-cone fracture surface, whereas the flat surface of the WCZ is clearly distinguished for the LFW–1 axisymmetric micro-tensile specimen. The most remarkable fact is that the geometry of the specimen successfully led to failure at the WCZ with shear lips on the TMAZ. No void nucleation and growth were observed for the LFW–1 axisymmetric micro-tensile specimen but the fracture mechanisms of the WCZ can be studied through fractographic analysis.

Fractographs of the PM–1 and LFW–1 axisymmetric micro-tensile specimens are shown in Figs.5.23. The PM–1 axisymmetric micro-tensile specimen shows dimples that are rather classical for α/β (Wojtaszek et al., 2013) and near–α titanium alloys (see 5.23c). The dimples exhibit a diameter of about $\sim$10 µm that is comparable to the size of the α grains on the PM microstructure. In Fig.5.23d, a fractograph of the flat zone in the fracture surface of the LFW–1 axisymmetric micro-tensile specimen is shown. For the sake of comparison,

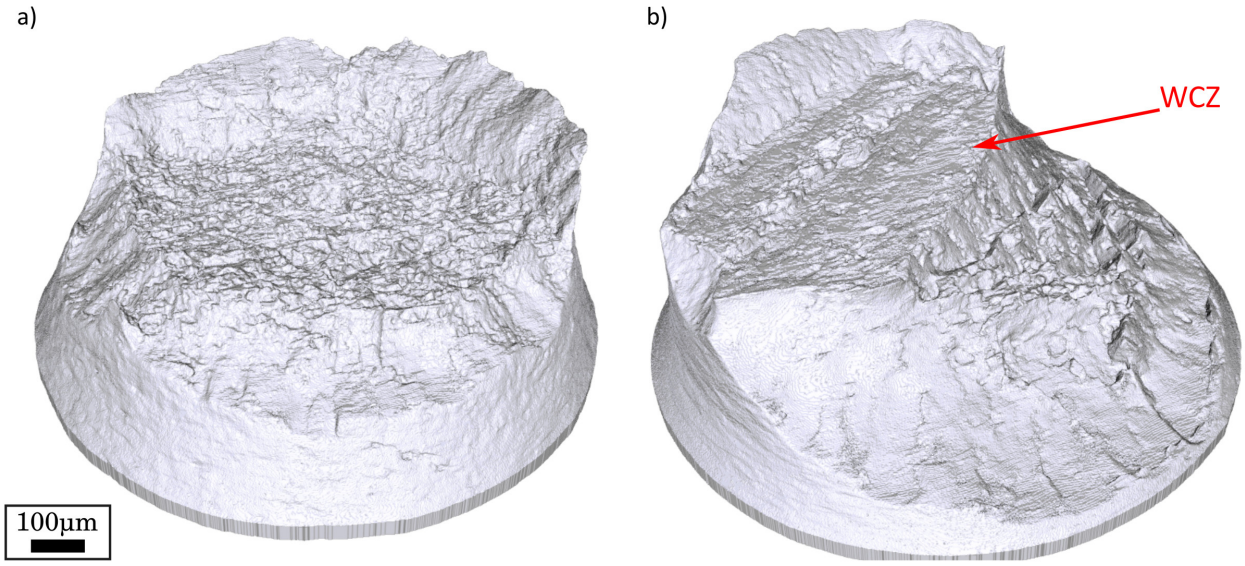

Figure 5.22: *Post-mortem* 3D visualizations of the (a) PM–1 and b) LFW–1 axisymmetric micro-tensile specimens.

the observations of Figs.5.23c and 5.23d were taken with the same level of magnification. The fracture features seen in the LFW–1 axisymmetric micro-tensile specimen are remarkably smaller than those seen in the PM–1 axisymmetric micro-tensile specimen. A high magnification fractograph of the WCZ is shown in Fig.5.23e. The observed nanometric equiaxed objects convey the shape of dimples and exhibit rough surfaces that suggest plastic deformation. These damage features could not have been observed using tomographic scans, since their size is smaller that the tomographic spatial resolution. It can be concluded that the LFW–1 axisymmetric micro-tensile specimen failed at the WCZ through the growth and coalescence of nanoscale cavities.

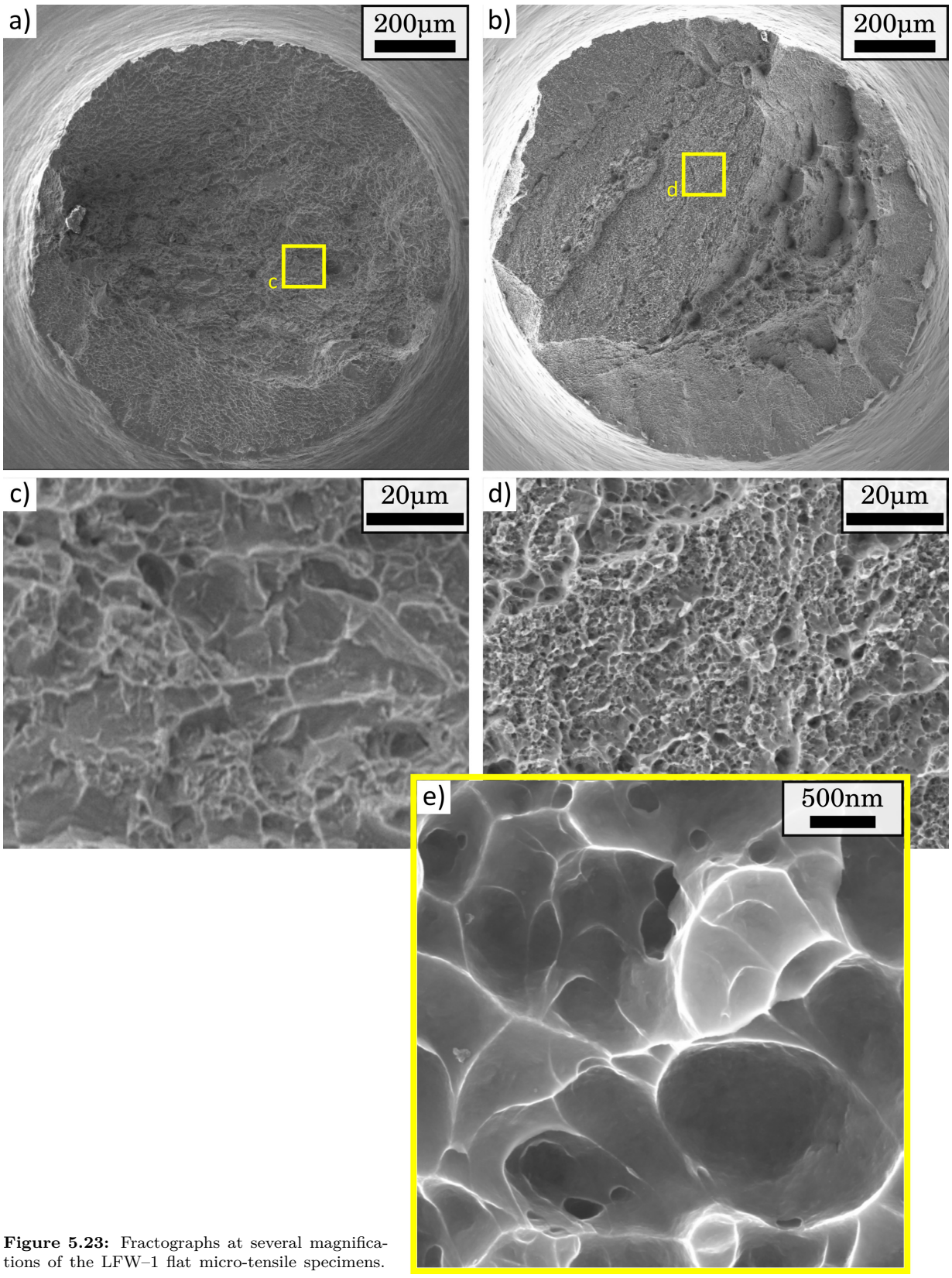

Figure 5.23: Fractographs at several magnifications of the LFW–1 flat micro-tensile specimens.

Flat micro-tensile specimens Fig.5.24 shows 3D SEM observations of the fracture surface of flat micro-tensile specimens. Figs.5.24a and 5.24c correspond to a typical LFW–AW flat micro-tensile specimen and Figs.5.24b and 5.24d correspond to a typical LFW–AW–PC flat micro-tensile specimen. For both specimens, yellow arrows point to white lines on the specimen surface (see Figs.5.24a and 5.24b.). This straight line is perpendicular to the specimen main axis. It resembles to the oxide layer at the WCZ documented for a similar Ti64 LFW joint by (Wanjara and Jahazi, 2005) and to the line observed in the 2D laminographic sections at the WCZ of similar Ti6242 LFW joint previously studied in Section 4.3.2. As for the axisymmetric micro-tensile specimens described in Section 5.3.3, it seems that failure occurred at the WCZ at the centre of the specimen with shear lips that went through the TMAZ of both sides. It is interesting to note that, on the fracture surface of both specimens, flat surfaces suggesting the WCZ can be seen (see Figs.5.24c and 5.24d).

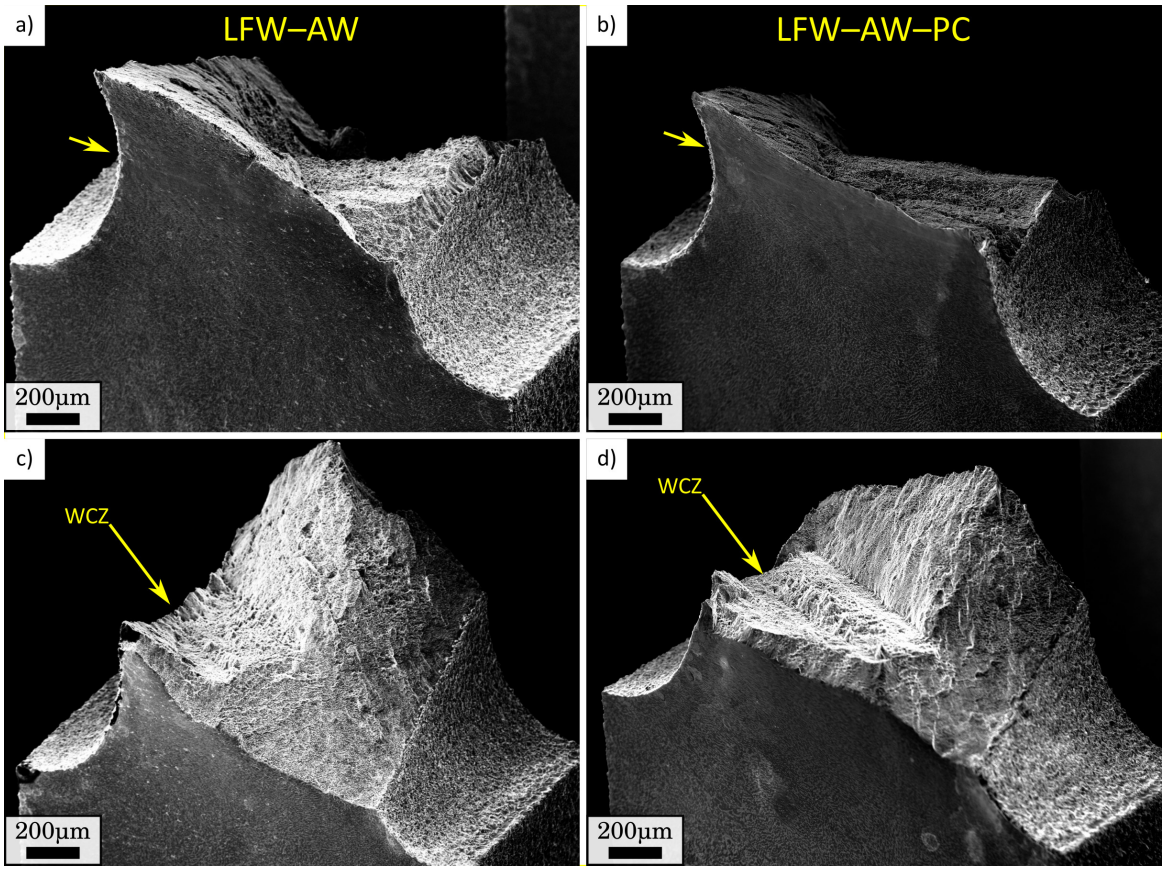

Figure 5.24: 3D SE observations of the fracture surface of typical (a-c) LFW–AW and (b-d) LFW–AW–PC flat micro-tensile specimens.

Fractographic analysis of PM Fig.5.25 shows fractographs of a typical PM flat micro-tensile specimen. As for the PM–1 axisymmetric micro-tensile specimen, classical near–α titanium alloys dimples are observed in the central region of the fracture surface. Some necking is observed. It is interesting to note that necking is stronger on the sides of the specimen (vertical sides on the image) than in the surface observed by the microscope (horizontal sides on the image).

Fractographic analysis of LFW–AW and LFW–AW–PC flat micro-tensile specimens

Figs.5.26a-d show the fractographs for a typical LFW–AW flat micro-tensile specimen. The roughness of the fracture surface exhibits a long out-of-plane extent. As seen in Fig.5.24, the fracture surface is very

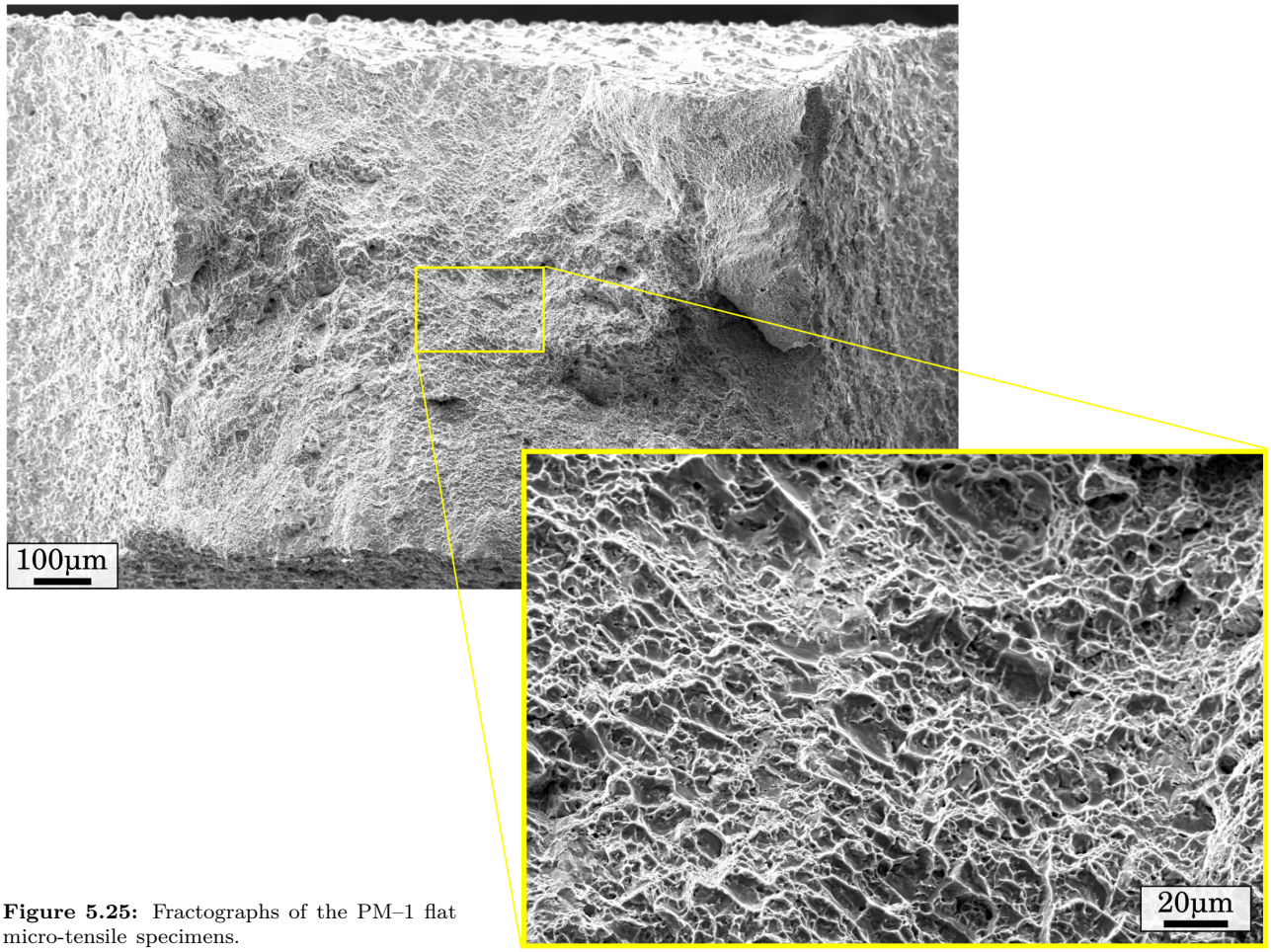

Figure 5.25: Fractographs of the PM–1 flat micro-tensile specimens.

three-dimensional and it exhibits a flat surface that is highlighted with a yellow rectangle and exhibited in Fig.5.26b. It is interesting to note that for the observation in Fig.5.26d, the acicular entangled α' martensite described in Section 5.3.1 is observed. In Fig.5.26c, the same observation can be made but the shape of the α' martensite is less blatant. It seems that the region shown in Fig.5.26d is within the WCZ, whilst 5.26c is at the beginning of the TMAZ.

Figs.5.26e-h show the fractographs for a typical LFW–AW–PC flat micro-tensile specimen. As for the LFW–AW flat micro-tensile specimen, the LFW–AW–PC flat micro-tensile specimen exhibits a fracture surface with a long out-of-plane extent (see Fig.5.26e), a flat specimen at the centre with shear lips on its sides (see Fig.5.26f), dimples and objects that convey the shape of the underlying acicular entangled α' martensite. Seen the flat surfaces, this martensite could have failed in a brittle manner. Other regions seem to contain very small dimples and could be coalescence regions between the broken martensite. It should be stated that no effect of prior to welding contamination is observed in terms of damage mechanisms.

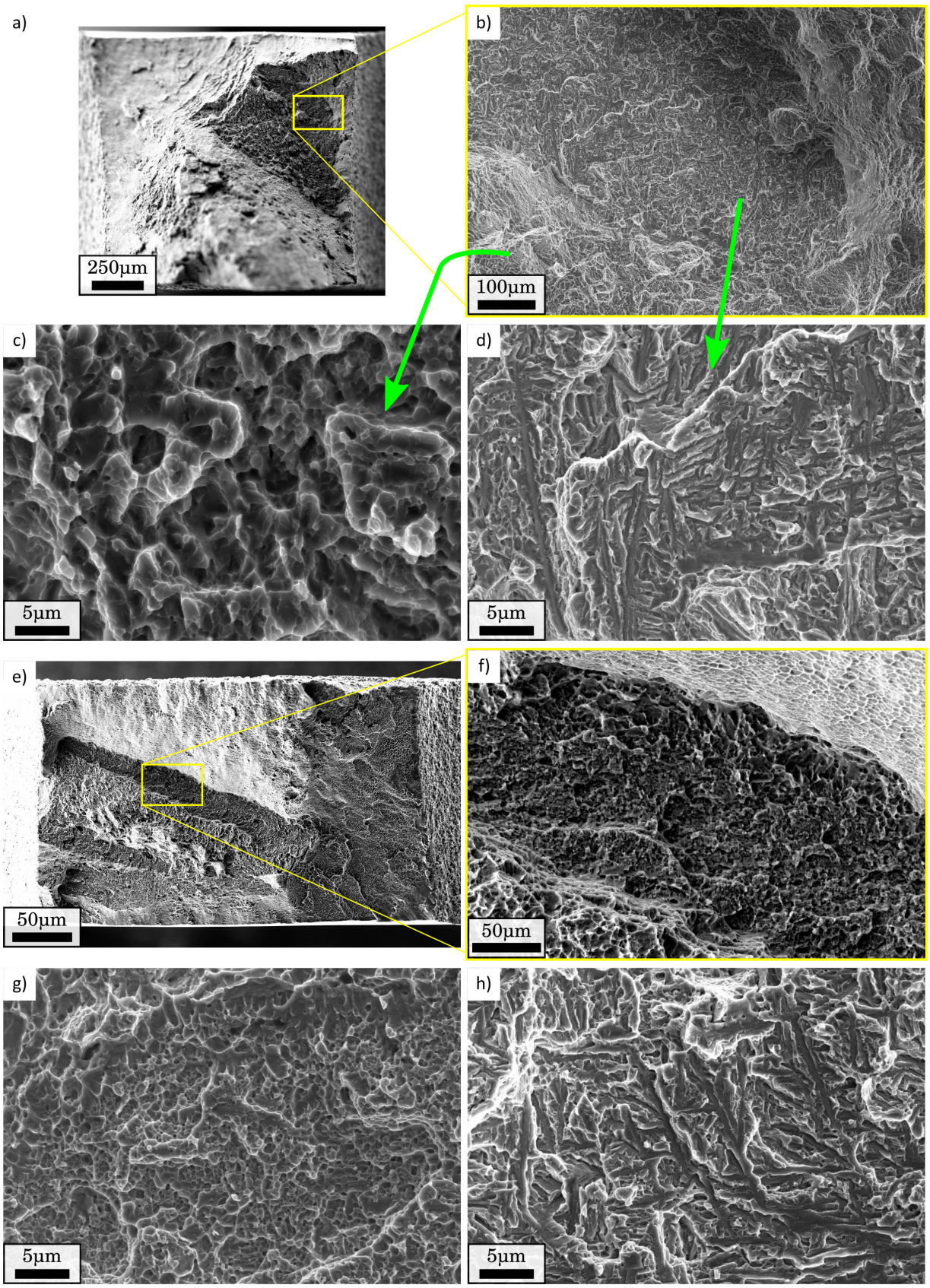

Figure 5.26: Fractographs to several magnifications of the a-d) LFW–AW and e-b) LFW–AW–PC flat micro-tensile specimens.

5.3.5 Quantitative analysis of morphology and alignment of PM damage

The quantitative data concerning the alignment and morphology of cavities for the PM–1 tomographic micro-tensile specimen is represented in Fig.5.27. Data has been extracted from the two tomographic observations 15 and 16 (see in Fig.5.16a and Fig.5.21).

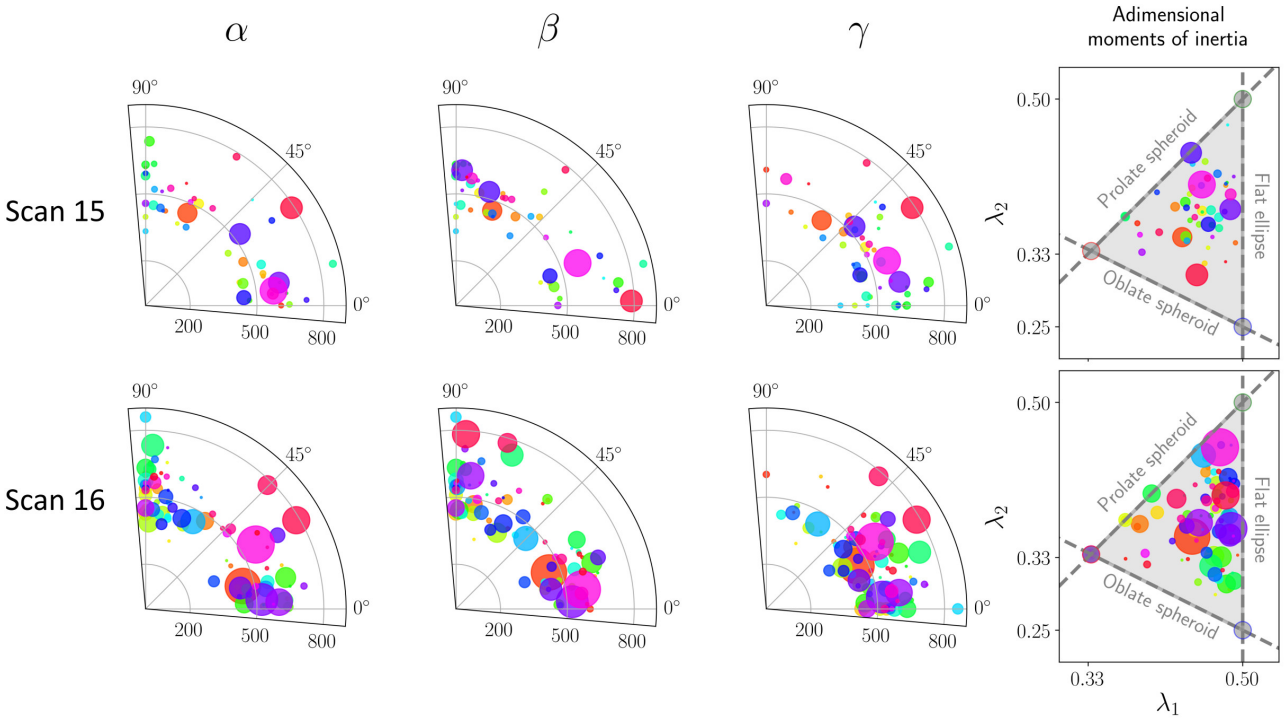

Figure 5.27: Scatters plots of the voids in scans 15 and 16 (see Figs.5.16a and 5.21) for the alignment and morphology distribution of the PM–1 tomographic micro-tensile specimen.

A total of 49 and 89 voids were examined in the scan 15 and the scan 16, respectively. Each void is represented by a circular marker and its colour corresponds to its index number on each scan. In this manner, a single void can easily be identified in the four scatters plots, for each scan. Particle tracking was not performed for this analysis hence, as the number of cavities increases with void nucleation, a given void is likely to have different index number (color) in each scan. The size of the marker is proportional to the volume of void. In the adimensional moments of inertia scatter plot, it can be seen that the morphology of the biggest voids is close to a flat ellipse. This morphology is commonly known as penny-shape. The alignment of this kind of voids is better represented with the principal axis parallel to v_3, the eigenvector associated with the smallest eigenvalue. The angle formed by v_3 and the positive semi axes x, y and z is denoted by α, β and γ and is represented by the angular coordinate in three polar scatter plots. The radial coordinate represents the distance to the specimen barycentre.

The driving forces of damage growth are triaxiality and strain. Notched specimens induce high levels of triaxiality at the centre of the notch. It is interesting to notice that, despite the triaxiality induced by the notch, most voids nucleated far from the centre of the net section. This suggests that damage is driven by microstructural interactions. In Fig.5.21b, damage seems to appear in lines parallel to the RD direction of the billet. No particular trend is observed with respect to the alignment in terms of morphology.

Fig.5.28a shows the void volumetric fraction (VVF) in the primary vertical axis, the macroscopic engineering

stress in the secondary axis and the lateral strain in the horizontal axis for the PM–1 axisymmetric micro-tensile specimen. The lateral strain was measured parallel to the x axis (see Section 5.3.2). The region of interest in which the VVF measurement was performed was the volume of the notch contained in height h centred with respect to the minimum section (see Fig.5.28b). For each measurement, the height of the ROI was varied to keep the volume of the ROI constant. Some measurable porosity is observed when the strain reaches ~ 0.021, which corresponds to VVF $= 1.94 \times 10^{-6}$ for scan 9 (see Fig.5.16c). Notice that this measurement corresponds to the maximum engineering stress that remains constant up to failure, with a maximum value of VVF of 4.22×10^{-4}.

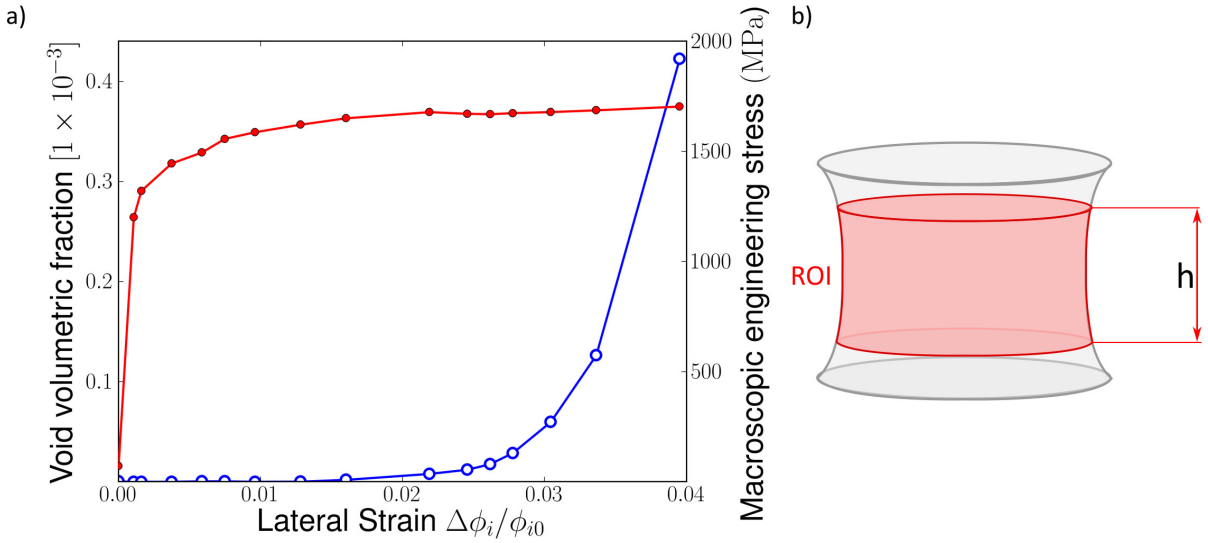

Figure 5.28: a) Void volumetric fraction (blue line with white dots) and macroscopic engineering stress (red line with red dots) evolution with lateral strain parallel to the x axis for the PM–1 axisymmetric micro-tensile specimen. b) Schematic view of the ROI with variable height h to maintain constant volume.

5.4 Discussion

Contamination prior to welding and surface preparation The self-cleaning mechanism of LFW is one of its most well-known advantages. Researchers studied this mechanism through numerical approaches that provided a wealth of understanding (Effertz et al., 2017; Ji et al., 2016a; McAndrew et al., 2015; Turner et al., 2011). For instance, McAndrew et al. (2015) has shown numerically and confirmed experimentally that contaminants at the centre of the joint are susceptible of not being extruded if the axial shortening is insufficient. Brass contaminants coming from EDM machining led to local melting at the WCZ of similar Ti6242 LFW joint (see Section 4.4.4). As a consequence, a fatigue specimen coming from the centre of the joint contained a dendritic defect that, during the first steps of cyclic elastic loading, induced an internal brittle crack of some tenths of micrometres. This internal crack induced a a stress concentration that led to an internal fish-eye fatigue crack propagation at the WCZ and implied a significantly reduced fatigue life. Interestingly, the fatigue specimen studied in Section 4.4.3 came from the centre of the joint.

In the report presented herein, no effect of prior to welding contamination in terms of mechanical properties or fracture mechanisms was observed. Notwithstanding, none of the specimens studied here were machined at the centre of the LFW joint. It may reasonable be stated that for the furtherance of the analysis, it would had been better to perform notch micro-tensile tests over specimens machined at the centre of the WCZ. Although, if contaminants were found at the centre of the LFW joint and considering that no traces of prior to welding contamination were found here, it would be reasonable to claim that insufficient extrusion due to insufficient axial shortening has a very localized effect as it is confined to the centre of LFW joints. In any case, grinding the surfaces to be weld prior to LFW is a rather simple operation that could enhance the self-cleaning mechanisms of LFW and subsequently, the mechanical properties of LFW joints.

Ultimate tensile strength of the WCZ The strength of the WCZ is higher than that of the PM. Therefore, failure occurs at the PM for smooth cross-weld samples. In this Chapter, the strength of the WCZ was measured by tensile tests in notched flat and axisymmetric micro-tensile specimens. The notches in the micro-tensile specimens induces complex stress fields that increase triaxiality. Hence, the measured strength using notched micro-tensile specimens is higher that that of a smooth tensile specimen. It also should be considered that the microstructure of the cross-weld micro-tensile specimens is heterogeneous. Not only is this heterogeneity observed in the P axis of a joint, but can also be observed in the F and T axes Rotundo et al. (2010). Thus, comparing two specimens machined from the same joint can also be contentious. Nonetheless, it is interesting to see that the ratio between the strength of the PM and cross-weld micro-tensile specimens is about ~ 1.27 (see Sections 5.3.2 and 5.3.2). These findings are consistent with microhardness measurements. The microhardness ratio between the α' martensite of the WCZ and the α/β microstructure of the PM is about 30 % (Ballat-Durand et al., 2019; Dalgaard et al., 2012b). The same ratio was observed in Section 4.3.3 for a similar Ti6242 LFW joint. It seems reasonably to state that strength of the WCZ is roughly 1.3 times higher that that of the PM. Finally, it is also very interesting to see the WCZ undergoes an important plastic deformation (see Figs.5.16 and 5.17). It was shown hat the WCZ exhibits some plastic deformation before failure, which is a positive feature.

Unstable failure of axisymmetric micro-tensile specimens Both the flat and axisymmetric micro-tensile specimens exhibited ductile fracture mechanisms, as explained in Section 5.3.4. Unlike the flat micro-tensile specimens, neither of the axisymmetric micro-tensile specimens exhibited stress drop after UTS (see Figs.5.16 and Fig.5.17). This may be interpreted as a structural effect, as the flat specimens cause a less severe mechanical state on the flat surfaces and allow plasticity to deviate to the softer zone outside the WCZ. Seemingly, unstable fracture occurred for the axisymmetric micro-tensile specimens. In this conditions, void nucleation, growth and coalescence occurred too quickly to be observed. This is undesirable since one of the aims of synchrotron *in situ* tensile testing is to observe the damage mechanisms of the WCZ and the PM. However, some damage was observed for the PM axisymmetric micro-tensile specimens (see Section 5.3.4). Given the available information, it is difficult to establish the origin of such unstable failure.

First, as it can be seen in the force-time curves of Fig.5.16a, failure occurred during relaxation. Furthermore, both parts of the broken specimen and the load frame were ejected by the springback of the system after failure (see Fig.5.29). This suggests that failure was driven by the stored elastic energy on the load frame-specimen system. Probably, at high level of stress, the low stiffness of both the PMMA tube and the titanium alloys specimens stored significant amounts of elastic energy. A similar unstable crack propagation so called "pop-in" was observed during toughness tests over aluminium alloys compact tensions specimens (Petit et al., 2018). The authors have shown that the apparition of "pop-in" propagation could be activated by decreasing the stiffness of the load frame. An additional *ex situ* test not shown here was performed using a load frame made of a steel grade with a higher Young's modulus. Nonetheless, no necking and a similar unstable failure were observed.

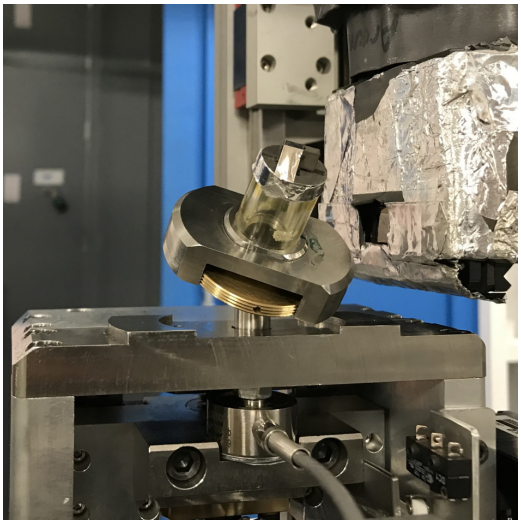

Figure 5.29: Load frame ejected by springback of the load frame-specimen system after failure of a specimen.

It seems reasonable to state, that a less severe notch may have led to a more stable void nucleation and growth. Case of point, (Dang et al., 2019) have studied the damage mechanisms of a Ti64 grade and have shown that the preferential site for nucleation and propagation of tiny micro-cracks was at the α colonies. Similarly, (Lecarme et al., 2014) proposed an algorithm for tracking voids in the volume of a Ti64 grade. These studies were based on damage observations during synchrotron *in situ* micro-tensile tests over notched axisymmetric samples but, compared with axisymmetric micro-tensile specimens used here, the ratio between the notch radius and the minimum section radius was higher. Machining specimens with smoother notches may have led to a more stable fracture but this is still contentious, since the strength of the WCZ is greater than the rest of the welded structure. Smoother notches may also have led to failure at the TMAZ. In such case, the fracture mechanisms of the WCZ (detailed in Section 5.3.4) would have not been able to be observed.

In a previous work, the anisotropic damage mechanisms of a modern X100 steel grade were associated with elongated and aligned (CaS/TiN) particles parallel to the rolling direction (Madi et al., 2019). Unlike the titanium alloys studied here, the (CaS/TiN) particles of the X100 steel grade and its stable post-necking behaviour allowed significant damage to be observed. This is also reflected by the reduced necking exhibited by the macroscopic specimens in Section 4.3.4 and the flatness of the dimples observed in the PM fractures surfaces

(see Fig.5.25). A different feasible approach may have been to perform synchrotron *in situ* micro-tensile tests using laminography and flat specimens, instead of tomography and axisymmetric specimens. Nevertheless, the spatial resolution used here was too low to capture the nanometric dimples of the WCZ.

5.5 Conclusions

In this work, the deformability, strength and fracture mechanisms of the WCZ of similar Ti6242 LFW joints have been studied *via* 3D synchrotron tomography and microscopy *in situ* notch micro-tensile tests and they were compared to the behaviour of the parent material. Also, the effect of prior to welding contaminants on the mechanical properties has been assessed by comparing the LFW–AW and the LFW–AW–PC joints through tensile tests using flat micro-tensile specimens. The following conclusions can be drawn:

Synchrotron tomography *in situ* tensile testing of axisymmetric micro-tensile specimens:

- The notch tensile strength for the axisymmetric specimens made of PM was 1720 MPa and a fracture strain of 0.06 was found. A ductile but unstable rupture was observed showing classical titanium dimples with moderate necking a shear lips.
- The notch tensile strength for the cross-weld specimens centred on the WCZ was 2360 MPa and a lateral strain of 0.035. Failure occurred at the WCZ showing nanometric dimples and shear lips in the TMAZ of both sides of the LFW joint.
- No defects were observed for the LFW–1 micro-tensile specimen.
- *In situ* tomography of the PM–1 showed limited diffuse damage nucleation and growth with penny-shape voids aligned to the RD direction of the billet. The void volume fraction before unstable fracture was in the order of 1×10^{-4}. No damage was observed for the LFW–1 micro-tensile specimen prior to failure.

Optical microscope *in situ* tensile testing of flat micro-tensile specimens:

- The notch tensile strength for the PM micro-tensile specimens was 1230 MPa and the mean strain to failure was 0.065.
- The notch tensile strength for the cross-weld flat micro-tensile specimens was 1601 MPa and the mean strain to failure was 0.03. As for the axisymmetric samples, failure occurred partially at the WCZ along flat regions at the acicular entangled α' martensite with nanometric dimples and resembled to a mixture of brittle and ductile mechanisms.
- No effect of prior to welding contamination was observed in the WCZ.

6

Effect of defects and weak zones on strength, fatigue resistance and toughness of dissimilar Ti17-Ti64 LFW joints.

In the previous Chapter, the strength and damage mechanisms of the similar Ti6242 LFW joints and the influence of prior to welding contamination were studied. Prior to welding contamination was at the origin of the reduction in fatigue life for a specimen in Chapter 4, yet, in Chapter 5, no influence was observed. A better understanding of prior to welding contamination is required.

In this Chapter, the influence of prior to welding contamination is assessed for a dissimilar Ti17-Ti64 LFW joint by studying the mechanical properties in terms of monotonic, cyclic and fracture toughness behaviours of three joints with different surface preparations and heat treatments. In addition, this weld procedure is highly application relevant as so called 'blisks' are produced using this material combination. However, the literature review showed that despite its usage, there is very few fatigue data for this weld type.

This work will be submitted as following: *Effect of defects and weak zones on strength, fatigue resistance and toughness of dissimilar Ti17-Ti64 LFW joints. Juan–Manuel García and Thilo–Frank Morgeneyer. Material Science & and Engineering:A.*

Résumé de chapitre

L'effet des défauts et des zones faibles sur les propriétés mécaniques en termes de comportement monotone, résistance en fatigue et ténacité pour différents joints bi-matériaux Ti17-TA6V soudés par friction linéaire a été étudié. Ainsi trois joints soudés ont été fabriqués : le premier a été nettoyé avant soudage, le deuxième a été soudé à l'état brut d'usinage et le dernier a été soudé à l'état brut d'usinage et traité thermiquement. Les joints testés à l'état brut de soudage ont révélé une morphologie α Widmanstätten du côté du TA6V et des grains β equiaxes du côté Ti17. La zone thermo-mécaniquement affectée a souffert d'un épuisement de la phase α et a été identifiée comme une zone faible. Pour la configuration étudiée ici, le mécanisme auto-nettoyant du LFW n'a pas réussi à extruder les contaminants présents dans l'interface et a induit une rupture pseudo-fragile au niveau du noyau pendant les essais de traction, fatigue et ténacité. Le joint nettoyé avant soudage a montré une rupture ductile tantôt au niveau du MB TA6V tantôt au niveau de la zone thermo-mécaniquement affectée côté Ti17. L'amorçage des fissures de fatigue a eu lieu avec une résistance réduite par rapport au MB. La ténacité a également été dégradée et le faciès de rupture au niveau de la TMAZ a dévoilé des amas de cavités allongées et parallèles.

Chapter Abstract

The effect of defects and weak zones on the mechanical properties in terms of tensile behaviour, fatigue strength and toughness for three dissimilar Ti17-TI64 linear friction welded (LFW) joints are studied. Three joints were produced: one with cleaned surfaces prior to welding (LFW–AW–PC), one not cleaned prior to welding (LFW–AW) and one not clean and post weld heat treated (LFW–PWHT). The microstructure of the weld centre zone (WCZ) was formed by a Widmanstätten acicular entangled α martensite on the Ti64 side and fine equiaxed distorted β grains on the Ti17 side. The thermo-mechanically affected zone on the Ti17 side (Ti17 TMAZ) was formed by α depleted β grains and was identified as a weak zone. For the studied welding parameters, the LFW self-cleaning mechanism failed to extrude the contaminants at the weld interface of the LFW–AW joint and formed a defect layer that led to a pseudo-brittle fracture in at the WCZ during tensile testing, cyclic loading and fracture toughness testing. During tensile testing of the pre-cleaned LFW–AW–PC joint, failure occurred sometimes at the Ti64 PM and sometimes at the Ti17 TMAZ, previously identified as a weak zone. Fatigue crack initiated at this weak zone with a reduced fatigue strength. Compared to the PM, fracture toughness was substantially reduced for the LFW–AW–PC even for samples without fatigue pre-crack. Failure at the weak zone highlighted unexpected colonies of elongated dimples of voids that nucleated on transgranular deformation bands on a grain boundaries.

Contents

Figures

Keywords

Linear friction welding, Mechanical properties, Ti−5Al−2Sn−2Zr−4Cr−4Mo, Ti−6Al−4V, Ti17, Ti64

Nomenclature

α (h.c.p.), hexagonal closed packed titanium crystal lattice;

β (b.c.c.), body centred cubic titanium crystal lattice;

F, friction axis;

P, pressure axis;

T, thickness axis;

E, Young's modulus;

Y, yield strength;

UTS, Ultimate Tensile Strength;

$\varepsilon_{\mathrm{macro}}$, macroscopic engineering strain;

$\varepsilon_{\mathrm{PP}}$, local strain following the P axis;

$\dot{\varepsilon}_{\mathrm{PP}}$, local strain rate following the P axis;

σ_{max}, maximum fatigue stress;

R, fatigue stress ratio; N_f, fatigue life;

ΔK, stress intensity factor;

a, crack size;

da/dN crack growth rate.

6.1 Introduction

The utilisation of titanium alloys is widespread in the aerospace industry. Their corrosion resistance, strength/density ratio and their ability of working in high temperatures make them one of the most used high performance materials. Aircraft components with intricate geometries are exposed to strong and complex loadings in very aggressive environments. In aero-engines for instance, compressors are required to have disks with high resistance in both tensile strength and low cycle fatigue and blades with good resistance to high cycle fatigue and creep. This mixed requirement is commonly addressed by the assembly of different materials using innovative joining techniques, such as the fabrication of the so-called "Blisks": A blade made of Ti−6Al−4V (Ti64) assembled to a disk made of Ti−5Al−2Sn−2Zr−4Mo−4Cr (Ti17) by the use of Linear Friction Welding (LFW) (García, 2011; Nunn, 2005).

Ti–6Al–4V is un α/β alloy commonly known as Ti64. For the study presented herein, its microstructure contained 10 µm diameter α grains and $\alpha+\beta$ colonies with big macrozones sharing crystallographic orientations to a extent of roughly 100 times the apparent grain size (Le Biavant et al., 2002; Echlin et al., 2016; Kasemer et al., 2017). This feature enhances its creep resistance up to a temperature of about 400 °C (Boyer, 1996) at the expense of a low resistance to crack propagation during the stage I of the fatigue life (Le Biavant et al., 2002; Bantounas et al., 2007). Ti64 was patented by (Stanley, 1959) at the end of the 1950s and it still accounts for about 50% of the titanium tonnage of the world and up to 80% of the aerospace industry applications (Welsch et al., 1993).

Ti−5Al−2Sn−2Zr−4Cr−4Mo, also known as Ti17, is β−metastable titanium alloy known for its deep hardenability, fracture toughness and fatigue crack growth rates (Lütjering and Williams, 2003; Banerjee and Mukhopadhyay, 2010). Its microstructural features consisted in large β grains namely 500 µm diameter containing different kinds of α precipitates: grain boundary α (α_{GB}), Widmanstätten lath colonies growing from the grain boundary (α_{WGB}) and two kinds of intergranular Widmanstätten laths (primary α^{p}_{WI} and secondary α^{s}_{WI}). It was invented in 1973 by General Electric for its utilization in fans and compressor discs (Meetham, 1981; Welsch et al., 1993).

LFW is a solid-state joining process in which a stationary workpiece, namely the disk, is put in contact with a second workpiece, i.e. the blades, describing an oscillatory motion of frequency f and amplitude a. After a fraction of a second of friction, a forging pressure P is applied to attain a target axial shortening Δh (burn-off). The plastic deformation and localized heat generated in the weld interface lead to considerable levels of residual stresses (Romero et al., 2009; Frankel et al., 2009), microstructural changes (Ballat-Durand et al., 2018; Wang et al., 2019; Baeslack et al., 1994) and, sometimes, enhanced mechanical properties (Dalgaard et al., 2012b). As a final consequence, all these features give birth to a strong heterogeneity distinguished in four distinct zones : the weld centre zone (WCZ), the thermomechanically affected zone (TMAZ), the heat affected zone (HAZ) and the parent material (PM). This technique was first patented by (Ritcher, 1929) and presents several advantages such as fast welding, reduced milling operations, the conception of dissimilar welds and, particularly, the quality of being a self-cleaning to some extent (see Section 4.4.4).

A certain wealth of literature concerning the tensile behaviour of dissimilar Ti17-Ti64 LFW joint is available. For the documented LFW configurations, failure under monotonic loading occurs in the Ti64 PM meaning that both Ti17 and the WCZ have a higher strength after welding (García, 2011; Nunn, 2005; Ji et al., 2016b, 2012).

This fact is in agreement with the specifications of Blisks design. Nonetheless, during the hot deformation of LFW, Ti17 undergoes a depletion of the α phase at the vicinity of the WCZ that induces some softening (Ballat-Durand et al., 2018). A similar depletion was observed for the Ti17 (Li et al., 2010) and Ti5553 (Dalgaard et al., 2012a) LFW joints documented in literature, in which failure occurred at the TMAZ, suggesting that this location is a potential weak zone. The effect of these potential weak zones on tensile properties, fatigue and toughness as well as the cyclic behaviour of dissimilar Ti17-Ti64 LFW joints has not yet been studied.

LFW is a solid state joining process (Ritcher, 1929; Vill, 1962; Maurya and Kauzlarich, 1969; Vairis and Frost, 1998) known to be self-cleaning (Bhamji et al., 2011; Li et al., 2016). Yet, several authors clean the workpieces prior to welding (Li et al., 2014; Wanjara and Jahazi, 2005; Amegadzie et al., 2012; Ji et al., 2016b) and nevertheless, the presence of impurities and welding defects have previously been registered (Wanjara and Jahazi, 2005; Li et al., 2014). The effective extrusion of contaminants outside the weld interface into the flash is dependent of the welding parameters. Several authors have studied this issue by the use of numerical tools (Effertz et al., 2017; Ji et al., 2016a; McAndrew et al., 2015; Turner et al., 2011). Tracking points in the weld interface are followed during simulations of the welding process to determine the efficiency of the welding parameters in terms of contaminants removal. These approaches gave valuable insight about the self-cleaning mechanism of LFW. For instance, increasing the burn-off enhances the proper extrusion of the weld interface contaminants (McAndrew et al., 2015). However, their limitation seems to be that the PM tracking points do not necessarily model the physics of impurities, *i.e.* oxides or intermetallics. Such contaminants are present in the surfaces to be welded and can have severe detrimental consequences on the mechanical properties of LFW joints, namely ductility reduction (Rotundo et al., 2013) or severe shortening in fatigue life (see Section 4.4.3). A better understanding of the consequences of the surface state prior to LFW and its resulting mechanical properties is required.

Ti17 undergoes softening during LFW. The depletion of the α phase favours the formation of microstructures consisting in fine equiaxed distorted β grains and deformed β grains at the WCZ and TMAZ, respectively (Ballat-Durand et al., 2018). Microhardness profiles across the WCZ of similar LFW joints made of these alloys revealed their undermatching strength (Ji and Wu, 2014; Ballat-Durand et al., 2018; Li et al., 2010). Li et al. (2010) carried out a study on the tensile properties of a similar Ti17 LFW joint and found out that, for one specimen, failure occurred at the TMAZ exhibiting reduced macroscopic strain and UTS compared to the PM. The authors observed elongated fracture features in the fractographs that attributed to a brittle fracture at the TMAZ. The same α phase depletion was observed in LFW joints made of Ti5553, a comparable alloy (Dalgaard et al., 2012a; Wanjara et al., 2014) that led to poor mechanical properties. It seems clear that the depletion of the α phase at the WCZ and TMAZ represents a structural weakness for similar Ti17 and Ti5553 LFW joints. Nevertheless, a sound explanation about the mechanisms leading to failure at these weak zones and its underlying mechanisms are still missing in literature.

In this work, the mechanical properties in terms of microhardness, tensile strength, fatigue strength and fracture toughness of three dissimilar Ti17-Ti64 LFW joints were studied. The first one was welded after EDM workpiece cutting without additional surface preparation; the second one was welded in the EDM as as machined condition and post-weld heat treated and the third one was ground prior to welding. First, a microstructural characterization of the joints is carried out using EDX and EBSD analyses. Second, the tensile behaviour of all joints is compared. An assessment of the strain and strain rate obtained by DIC instrumentation of the tensile

tests is performed to identify the fracture location on the welded structure.

Third, the fatigue strength, the fatigue crack initiation and propagation of the cross-welded specimens are studied. Fourth, toughness testing with non standard specimens is performed. Finally, the consequences of contaminants in the weld interface prior to welding and the potential threat to the welded structure integrity given by weak zones are discussed.

6.2 Experimental & Materials

Parent materials Ti64 and Ti17 titanium alloys were used as parent materials (PM) in this study. The PM nominal chemical compositions are exhibited in Table 6.1. Ti64 presents a bimodal α/β microstructure containing α (h.c.p) grains of about $10-20\,\mu m$ in diameter with a colony-type lamellar matrix of alternating α and β (b.c.c) plates. The microstructure of Ti17 consists in $550\,\mu m$ diameter prior-β grains (b.c.c.) containing α laths (h.c.p.) in four forms: grain boundary α (α_{GB}), Widmanstätten lath colonies growing from the grain boundary (α_{WGB}) and two kinds of intergranular Widmanstätten laths (primary α^p_{WI} and secondary α^s_{WI}). The entangled intergranular α^p_{WI} had length and width of respectively $4.4\,\mu m$ and $1.6\,\mu m$ (Ballat-Durand et al., 2018).

The material was provided in the form of 250 mm diameter billets by Timet. Blocks with 80 mm × 70 mm × 15 mm dimensions have been machined using Electrical Discharge Machine (EDM). The long direction of the blocks coincided with the extrusion axis of the billet. The EDM cutting tool was a brass wire composed of Zinc and Copper.

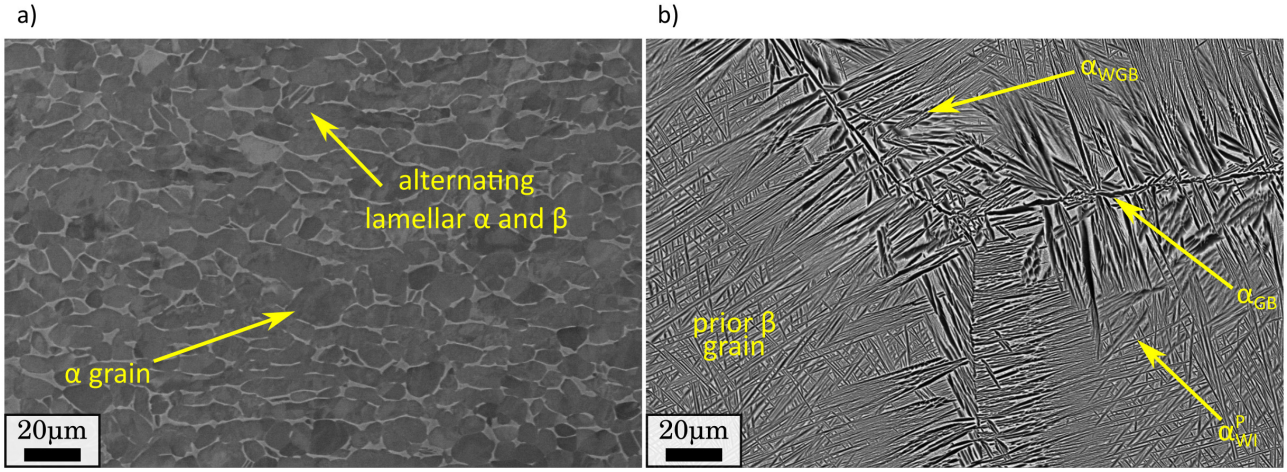

Figure 6.1: SEM/BSE observations of the microsctructure of the a) Ti64 and b) Ti17 PM's.

Linear Friction Welds Dissimilar Ti17-Ti64 LFW joints were provided by ACB. The Ti17 and Ti64 blocks were used as the stationary and oscillatory workpieces, respectively. During welding, friction occurred parallel to the F axes and the forging pressure was applied along the P axes, as shown in Fig.6.2. The third direction corresponds to the thickness (T). The F and P axes were parallel to the long and short directions of the PM blocks, respectively. Welding was performed with the following parameters : friction and forging pressure $P = 90\,MPa$, frequency of oscillation $f = 50\,Hz$, amplitude of oscillation $a = 2\,mm$ and burn-off

	Al	Zr	Sn	Mo	Cr	V
Ti17	5	2	2	4	4	–
Ti64	6	–	–	–	–	4

Table 6.1: Parent materials' nominal chemical composition (%*wt.*).

$\Delta h = 5\,\text{mm}$. The average welding time was about $\Delta t = 3.075\,\text{s}$. The blocks were degreased using an acetone bath prior to welding. Three joints dissimilar Ti17-Ti64 LFW joints were produced:

1. LFW–AW: PM blocks welded having the surfaces to be weld in the EDM as machined state.
2. LFW–PWHT: PM blocks welded in the EDM as machined state and post weld heat treated.
3. LFW–AW–PC: PM blocks welded after grinding the surfaces to be weld for 2 min using a 1200 grit SiC paper followed by an acetone bath.

The post weld heat treatment consisted in an isothermal hold at 910 °C for 3 h in vacuum followed by cooling to 635 °C in 2 h and finally, aged for 8 h and air cooled.

Microscopic observations and fractographic analysis Standard procedures were performed for the metallographic sample preparation consisting in mounting, grinding and polishing to a mirror like quality. Microstructural observations were carried out in a ZEISS DSM982 Gemini Scanning Electron Microscope (SEM) operated at 15 keV using backscattered electrons (BSE) detector. The fractographic analysis was accomplished at low and high magnification using secondary electron (SE) detector in both ZEISS DSM982 Gemini SEM.

Energy-dispersive X-ray spectroscopy (EDX) Metallographic specimens were machined from the PM blocks and the welds. Samples were plated in nickel strike baths at room temperature for 3 min. Electron dispersive X-ray analysis (EDX) analysis were performed in a ZEISS DSM982 Gemini Scanning Electron Microscope (SEM) operated at 20 keV. Chemical analysis were carried out indexing for all the alloying elements of both parent materials (see Table 6.1) plus copper.

Electron Backscattered Diffraction EBSD mappings were carried out using a camera Nordif UF300 of 840 px × 840 px with a step size of 0.5 µm. Samples were ground using an Leco PX500 automatic polisher. After grinding, the mirror like quality was fulfilled by polishing using a solution composed of 200 mm^3 Struers oxide polish suspension and 200 mm^3 distilled water for 24 h on a Buehler VibroMet. No etching was performed. The working distance was 24 mm. The tension was set to 20 kV. A grain size filter of 5 px and a minimal confidence coefficient of 0.2 filter were previously applied.

Microhardness Vickers microhardness profiles were carried out across the weld with a step size of 200 µm, a load of 500 g and a dwell period of 15 s. Test were conducted following the ASTM E384-17 (2017) standard.

Tensile test Tensile tests were conducted following the ASTM E8/E8M-16a (2016) standard. Three sets of cross-weld tensile specimens were machined from the LFW–AW, LFW–AW–PC and LFW–PWHT joints described in Section 6.2. The geometry of the tensile specimens is shown in Fig.6.2a. The tensile test specimens

were machined parallel to a PT plane and were tested having their principal axis parallel to the P direction. Load was applied with a MTS 250 kN load frame at room temperature. Typical gage length and cross section respectively were 25 mm and 3 mm × 6 mm. Elongation was measured with optical extensometers as described later in this Section. Load frame cross-head speed was 0.032 mm s^{-1}.

Stereo Digital Image Correlation (SDIC) During tensile testing, the local strain over the tensile specimens surface was monitored using a standard system of SDIC. A system of two 2048 px × 2048 px Manta G-419B cameras was placed to follow the displacement of an artificial random black and white speckle applied on the specimen surface. The distance between the cameras was $a = 26$ cm and the camera-object distance was $b = 31$ cm, leading to a field of view of 40 mm × 40 mm. Images were exploited with Vic-3D™ from Correlated Solutions, Inc. (version 7.2.4, 2014). Acquisition was carried out taking 2 frames per second. Subset size was 35 px ≈ 175 µm, step size was 9 px and filter size was 15 px. Before tensile testing, the displacement and the Hencky $\varepsilon_{\mathrm{PP}}$ measurements uncertainty were determined by correlating two consecutive images of the static specimen. Uncertainty in displacement measurements turned out to be 0.1 µm. This corresponds to a Hencky strain uncertainty of $\Delta\varepsilon_{\mathrm{PP}} = 0.0002$ with a standard deviation of $\sigma_{\varepsilon_{\mathrm{PP}}} = 9.56 \times 10^{-5}\%$. The load line, the specimen and the cameras frame were aligned using a laser level as a reference. Both cameras were aligned to gravity using a water level.

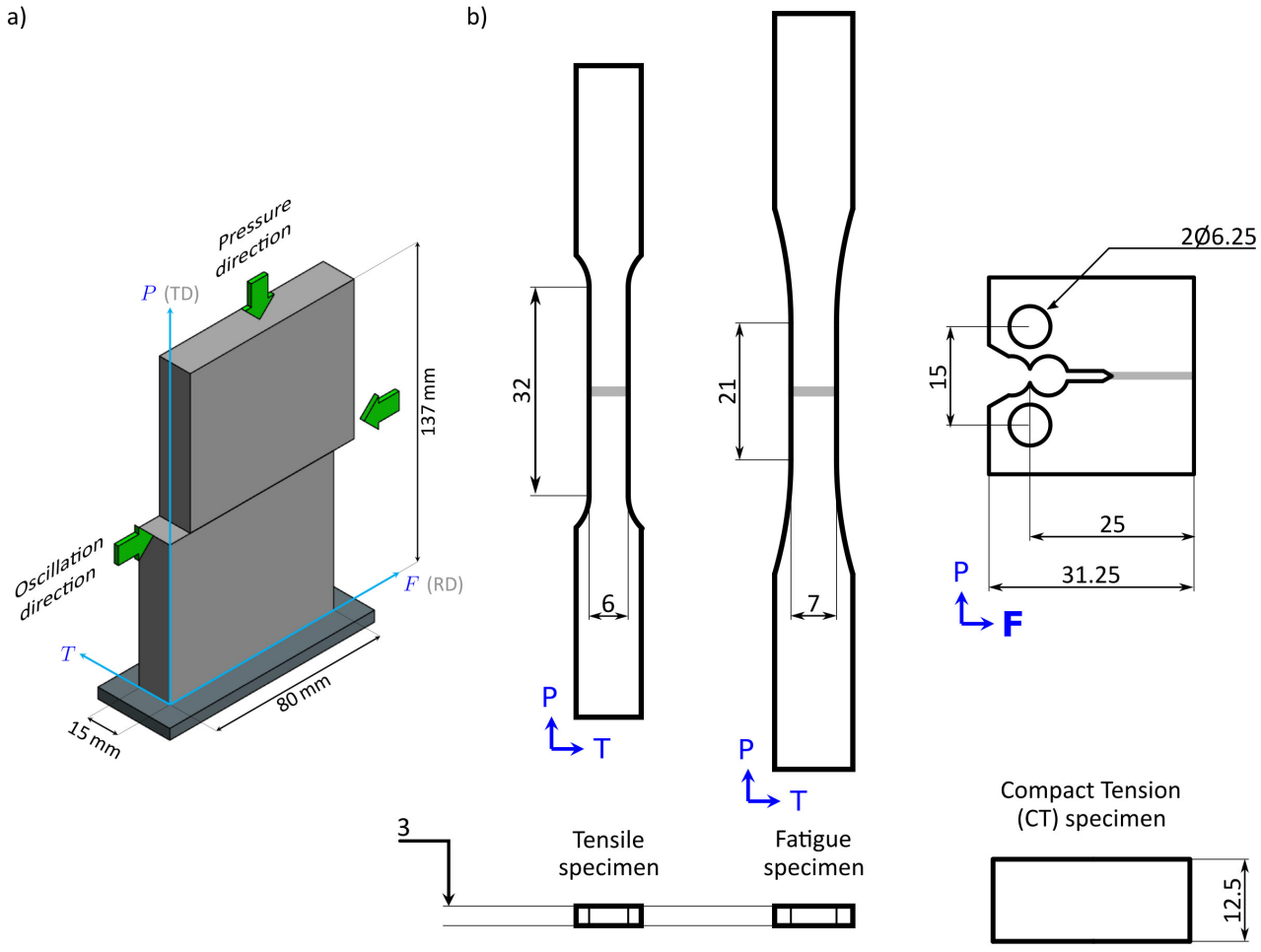

Figure 6.2: a) A schematic view of the welded joint showing the friction direction (F), the forging pressure direction (P) and the thickness direction (T) and b) geometry of the tensile, fatigue and fracture toughness specimens. All dimensions are given in mm.

Fatigue test Standard fatigue test were carried out following the ASTM E 466-07 (2007) standard. The load frame was aligned following the procedure described in Chapter 3. Smooth cross-weld specimens were machined parallel to a PT plane of the joint, having its principal axis parallel to the P direction, as shown in Fig.6.2. Specimens' corners were rounded with a lime and their surface were polished to a mirror-like state. The uniaxial tension zone had a length of 21 mm and a constant gage section of 3 mm × 7 mm. A sinusoidal waveform was imposed using a MTS 250 kN servo-hydraulic load frame. The test frequency was 20 Hz. The target fatigue life was $N_f = 10^5$ cycles with a stress ratio of $R = 0.1$.

Fracture toughness Compact Tension (CT) specimens were machined according to ASTM E1820-08 standard. The specimen geometry is shown in Fig.6.2. All specimens were machined with thickness of $B = 12.5$ mm to assure a crack propagation under plane strain and notch of $h = 11.0$ mm. The CT cross-weld specimens were machined parallel to a FT plane having crack propagation parallel to the F direction. The crack of the cross-weld CT specimens was precisely centred with respect to the WCZ. The target pre-crack extension was $f = 1.5$ mm and it was performed under force-controlled fatigue. The pre-crack extension was monitored on both sides of the specimen. The pre-crack extension of each CT specimens is indicated on each graph of Fig.6.15. The pre-crack that respected the standard requirement are written in green and the pre-crack for the invalid tests is written in red. Detailed information concerning the validity of each trial is detailed in Section 6.3.5. Fracture toughness tests were performed using three PM17 CT specimens (pre-cracked), one LFW–AW CT specimens (without pre-crack) and two LFW–AW–PC specimens (one with a pre-crack and one without a pre-crack). Trials were carried out applying a displacement-controlled loading on an Instron 8500 load frame with a load ratio of $\dot{K}_{Ic} < 2.75\,\mathrm{MPa}\sqrt{\mathrm{m}}/\mathrm{s}$, as recommended by the standard. Force and crack mouth opening displacement (CMOD) were simultaneously recorded during the test for the evaluation of the stress intensity factor as a measure of the fracture toughness. CMOD was measured with an MTS 632,02F-21 extensometer. A pre-load of 0.2 kN was applied to every specimen prior to testing.

6.3 Results

6.3.1 Microstructural characterization

Flash morphology and weld microstructure for the LFW–AW–PC joint

A cross-weld optical observation for an LFW–AW–PC sample along a PT plane is shown in Fig.6.3a. Ti17 and Ti64 are respectively seen on the upper and lower parts of the weld. The flash for the Ti17 and Ti64 sides respectively show a length of about 10 mm and 25 mm. No ripples are observed for either material. The optical observation of the out-of-plane flash, while not conclusive, suggests that the power input used here led to sufficient softening of both materials and enhanced the continuous extrusion of impurities in the weld interface.

The strong contrast in the SEM/BSE observation of Fig.6.3b is provided by the chemical content of each material and it highlights very clearly the frontier between both materials at the WCZ and their microstructures. The localized diffusion of Ti17 into the Ti64 side seen in Fig.6.3c suggests that the transformation of both materials is mostly a consequence of the hot deformation during friction welding rather than diffusion. In other words, the extent of diffusion and its subsequent effect seem to be very localized. In such case, the trans-

formation of each material can be compared to the transformations in similar Ti17 LFW joints and similar Ti64 LFW joints, already available in literature. For instance, in the Ti64 side, an acicular entangled microstructure can be seen that is very similar to the Widmanstätten morphology already seen in the WCZ of similar Ti64 LFW joints (Wanjara and Jahazi, 2005) and in the hot deformation of α/β titanium alloys (Semiatin et al., 1997). This microstructure suggests that the temperature developed during welding locally overreached the $\beta-$transus temperature. It seems that, during rapid cooling after the oscillations stopped, a displacive diffusionless transformation led to the formation of α' plates that conserved the chemical composition of the parent

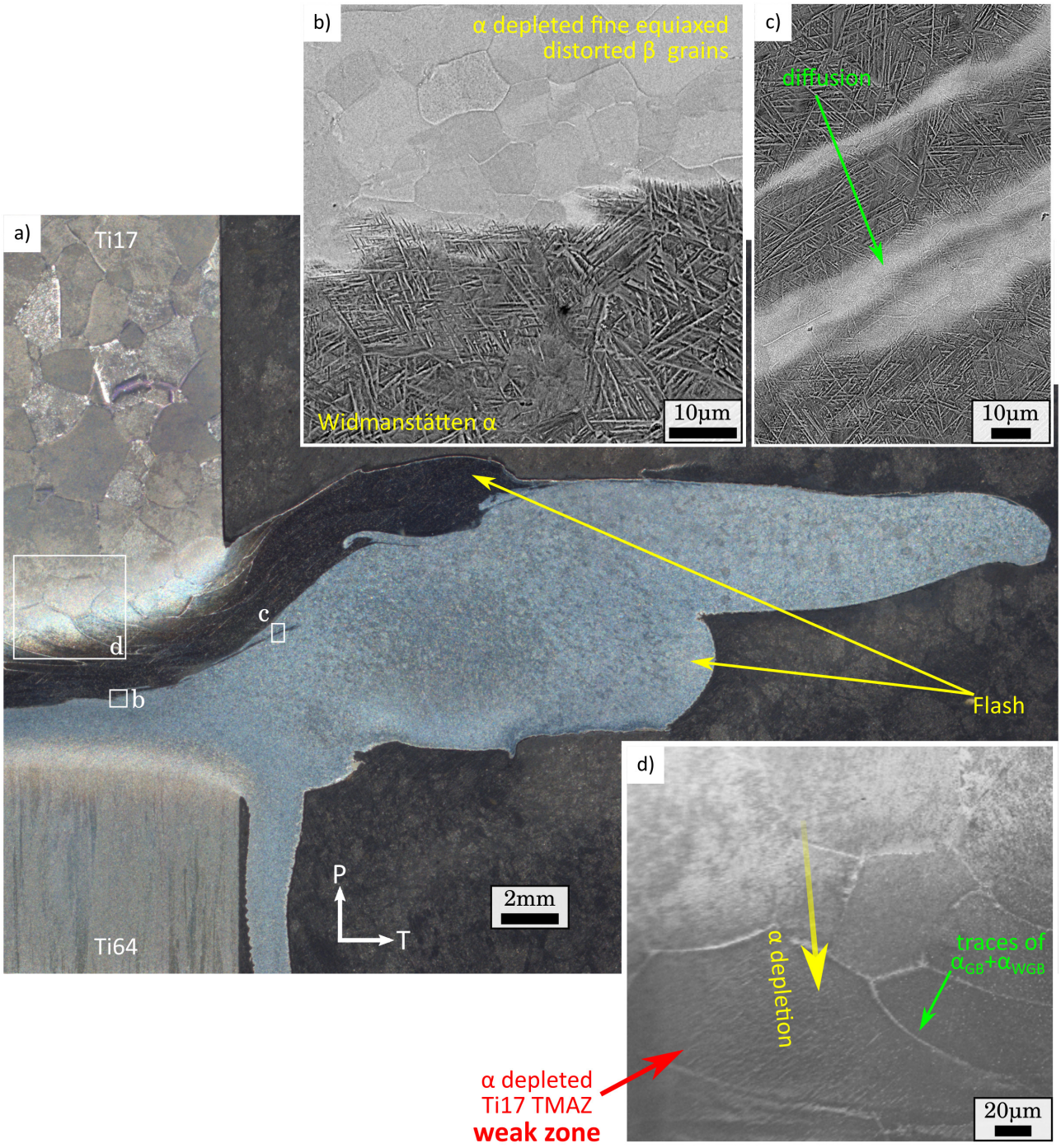

Figure 6.3: a) Cross-weld optical observation of a LFW–AW–PC joint sample showing the microstructure of PM, TMAZ and the WCZ for both materials. The upper and lower parts of the weld respectively correspond to Ti17 and Ti64 PM's; b) Observation of the WCZ showing α depleted fine equiaxed distorted β grains and the Widmanstätten α martensite of Ti64; c) diffusion of Ti17 into the Ti64 side of the WCZ and d) α depleted deformed β grains in the weak zone (Ti17 TMAZ).

material. In addition, the 10 µm diameter features observed in the Ti17 side of the WCZ are very similar to the α depleted β distorted grains seen in the WCZ of the similar Ti17 LFW joints characterized by Ballat-Durand et al. (2018).

A SEM/BSE observation of the Ti17 TMAZ is shown in Fig.6.3d. The arrow with a yellow transparency gradient shows the gradual depletion of the α phase that increases with decreasing distance to the WCZ. The green arrow in Fig.6.3d points to the former α_{GB} layer at the grain boundary of β grain at the Ti17 TMAZ that were previously denominated as "traces of $\alpha_{GB} + \alpha_{WGB}$" (Ballat-Durand et al., 2018). The region with a darker shade of grey represents the Ti17 TMAZ. This region reminds the TMAZ of the similar Ti5553 LFW joint studied by Dalgaard et al. (2012a), which was the location for failure during monotonic loading.

Analysis of the Defect Layer (DL) at the WCZ of the LFW–AW joint

Chemical analysis During the microstructural characterization of the LFW–AW joint, an unexpected defect layer (DL) was observed at the Ti17-Ti64 frontier in the centre of the WCZ (see the SEM/BSE observation of Fig.6.4a). The DL was about 11 µm thick and exhibited a length of 1.8 mm over an observed surface of 3 mm length (not shown here). It exhibited round cornered objects and voids that resembled to the solidification shrinkage voids previously registered for a titanium casting alloy (Hayakawa et al., 1991b). These features do not convey the shape of microstructures commonly seen in the WCZ of LFW joints for either similar or dissimilar Ti17-Ti64 LFW joints. Similar voids were observed in Section 4.3.2 and in the reports documented by (Wanjara and Jahazi, 2005; Ballat-Durand et al., 2019).

To better characterize the DL, a chemical composition profile obtained by EDX analysis over the transparency white arrow of Fig.6.4a is shown in Fig.6.4b. The alloying elements of both PM's plus Cu, Zn and O were included in the analysis. V is found on the nominal composition of Ti64 however some concentration of V is observed in the Ti17 side of the DL. Similarly, low concentrations of Sn, Zr, Mo and Cr are observed on the Ti64 side of the DL, given that they belong to the nominal composition of Ti17. Whilst Ti64 and Ti17 respectively contain 6 %wt and 5 %wt of Al in their nominal compositions, the DL exhibited a concentration of about 3.8 %wt. Furthermore, about 6.25 %wt of O was observed at the DL. These trends are also observed on the chemical composition mappings of Fig.6.4c. The O concentration observed at the entire region can be explained by the fact that titanium alloys develop an oxide layer almost instantaneously when put in contact with the atmosphere. Nevertheless, it is very interesting to note that the concentration of O is higher at the DL (see Fig.6.4b). The DL contains significant amounts of Ti, Al and O and it is surrounded by Cu and Zn gradients that decrease with increasing distance to the DL.

In Section 4.4.4, it was suggested that, during the EDM machining of the PM blocks prior to welding, the brass wire may have smeared the surfaces of the blocks with significant amounts of Cu or Zn. To confirm this, the chemical content of PM blocks prior to welding has been studied through EDX mappings. SEM/BSE observations of the surface of two PM blocks are shown in Figs.6.4e and Fig.6.4f (read Section 6.2). An EDX mapping showing the %wt content of Cu is overlaid in red transparency. The microstructure of both PM's is easily recognized. Astonishingly, an undesired layer containing a maximum of 8 %wt of Cu is observed in the surfaces to be welded. It seems that, during EDM machining, the EDM brass wire smeared Cu at the surfaces to be welded. These findings highlight that the LFW–AW joint was produced with contaminated surfaces.

EBSD mapping analysis An EBSD orientation mapping and a phase map of both α (hcp) and β (bcc) phases are respectively shown in Fig.6.5a and Fig.6.5b. This maps corresponds to region highlighted by the white rectangle in Fig.6.4a. For both mappings, the indexation confidence index has been overlaid in transparency. Both the DL and the Ti64 side of the WCZ exhibit an hexagonal crystal lattice. The Ti17 side of the WCZ show ~10 mm diameter β grains.

The transparency level highlights that the indexation confidence index varies in each region. It is minimum for the Ti17 side of the WCZ and maximum for the DL. The lower confidence index on the β phase is attributed to the fact that the microstructure at the Ti17 WCZ consists in α depleted distorted β grains that exhibit slightly different crystal lattice parameters than the standard titanium β (Ballat-Durand et al., 2018). On the Ti64 side, the Widmanstätten morphology already mentioned in Section 6.3.1 can be seen. It is interesting to

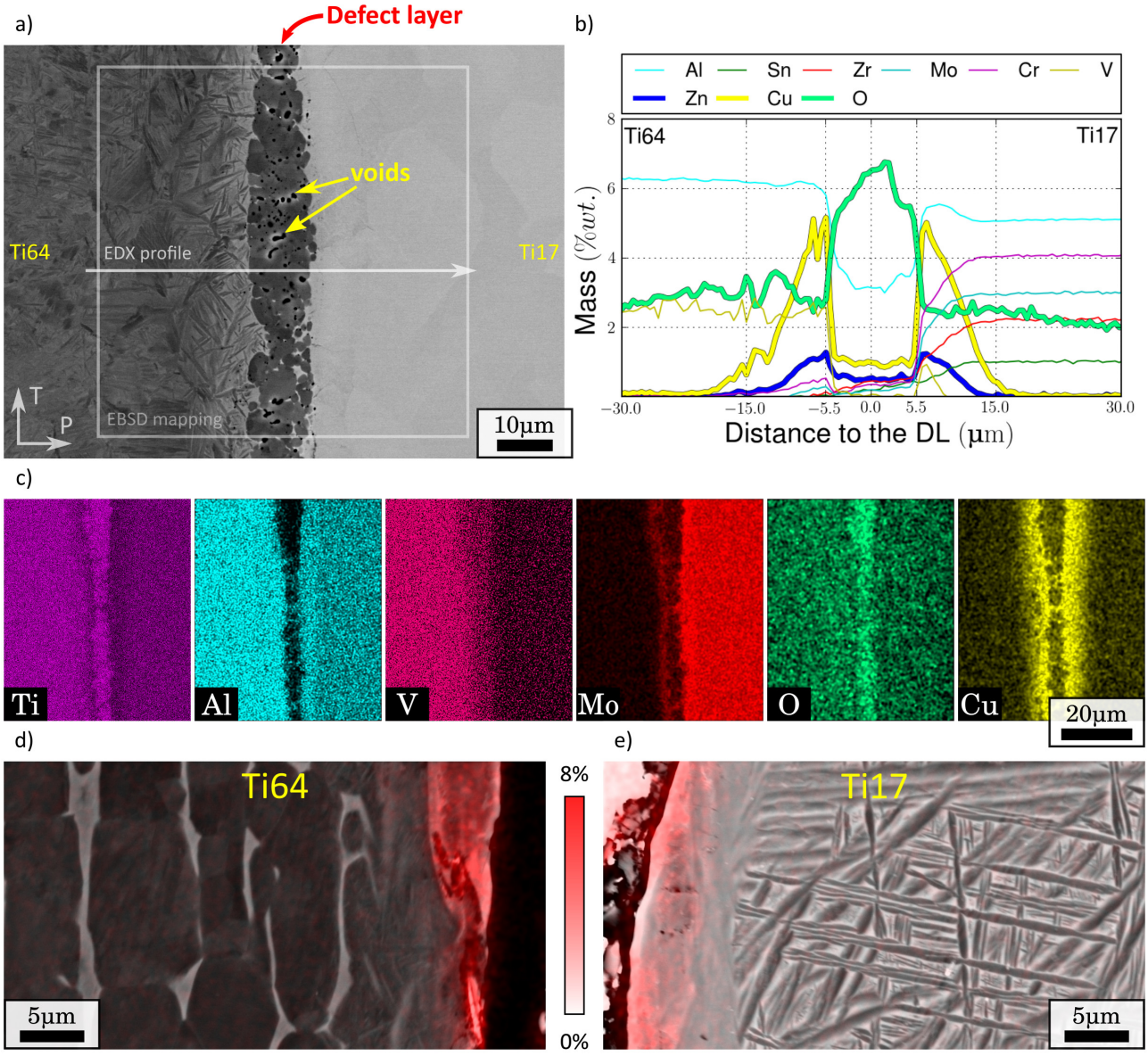

Figure 6.4: a) SEM/BSE observation of the LFW–AW joint showing the defect layer (DL) containing round objects and voids; b) chemical composition profile across the DL obtained by EDX analysis over the white transparency line on Fig.6.4a; c) chemical composition mappings of different chemical elements obtained by EDX analysis and prior to welding BSE observations with mappings of Cu content expressed in %wt overlaid in red transparency of the PM's blocks: e) Ti64 and d) Ti17.

note that the recrystallization undergone by both PM seems to be as the same as for the LFW–AW–PC joint, regardless of the presence of DL. The EDX analysis of Section 6.3.1 have shown that the DL is mostly composed of Ti, Al and O and it contains some Cu and Zn. The EBSD analysis have shown that the crystal lattice of the defect layer is hexagonal closed packed. Identifying the microstructure of the DL with data shown here is rather difficult. A better precision concerning the crystallography of the DL could be obtained by X-Ray Diffraction but considering the 11 µm thickness of the DL, this could not be fulfilled with a standard laboratory SEM. Instead, synchrotron X-Ray diffraction would be needed which would expensive, cumbersome and time consuming.

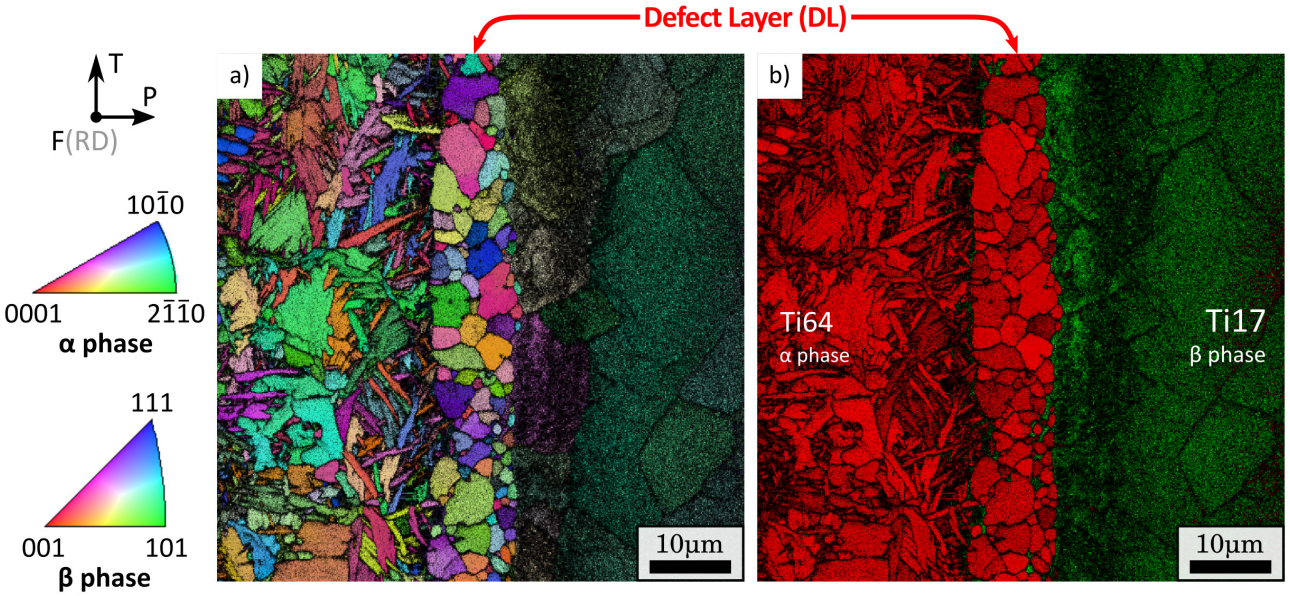

Figure 6.5: a) EBSD inverse pole figure of both α and β phases on the region highlighted by a white transparency rectangle in Fig.6.4a showing the the weld and the DL, and b) phase map respectively showing titanium α and β phases in red and in green. The indexation confidence index is overlaid for both maps.

This DL exhibited an hcp crystal lattice and was observed to be rich in Ti, Al and O and it is surrounded by Cu and Zn gradients that decrease with increasing distance to the DL. The high content in O may have favoured the diffusion of the others elements (Deshmukh et al., 2017) and have induced the formation of a brittle phase known as α–case (Huang et al., 2015). In further Sections, it will be shown that the DL is very detrimental for the mechanical properties and that can be easily avoided by a proper surface preparation. Hence, a deeper investigation on the nature of this DL seems unjustified.

Microstructure of the LFW–PWHT joint

Fig.6.6e shows the microstructure of the Ti17 TMAZ for the LFW–PWHT joint. The former α depleted regions seem to have precipitated the α phase at the expend of the grain size as observed by Ballat-Durand et al. (2018). Similarly, the recrystallization of the Ti64 is similar to the one observed elsewhere for the similar Ti6242 LFW joint characterized by Ballat-Durand et al. (2019). The application of STA heat treatments in titanium alloys is well known. For instance, Dalgaard et al. (2012a) showed that failure during monotonic loading of a similar Ti5553 LFW joint occurred ad the α Ti17 TMAZ but later, Wanjara et al. (2014) showed that the application of a standard STA treatment led to failure far from the former Ti17 TMAZ.

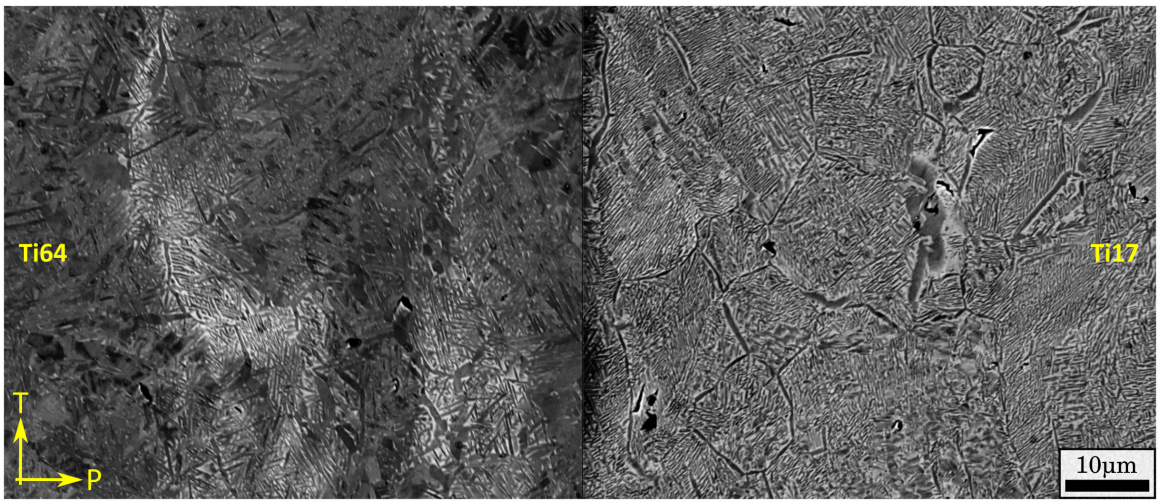

Figure 6.6: SEM/BSE observation of the WCZ of the LFW–PWHT joint on the a) Ti64 and b) Ti17 sides.

6.3.2 Microhardness

Fig.6.7 shows microhardness profiles across the weld for the three configurations. Profiles are parallel to the P direction. The microhardness profiles are plotted in green for the LFW–AW joint, in red for the LFW–AW–PC joint and in black for the joint LFW–PWHT. Microhardness exhibited a local maximum of 380 HV at $P = 0$ mm and a gradual decrease to the Ti64 PM for all configurations. The LFW–AW and LFW–AW–PC joints exhibited local minima at the TMAZ of the Ti17 material. These findings are in agreement with the results already registered in literature (Ji et al., 2016b; chen ZHANG et al., 2013). Furthermore, the local decrease of microhardness at the TMAZ on the Ti17 side is consistent with the α depleted β grains in the TMAZ of similar Ti17 LFW joints documented elsewhere for similar Ti17 LFW joints (Ji and Wu, 2014; Dalgaard et al., 2012a; Ballat-Durand et al., 2018; Li et al., 2010). After PWHT, microhardness of the Ti17 stabilized around PM's microhardness. The microhardness gradient on the Ti17 side was drastically sharper compared to the Ti64 side. The width of the affected zone was about 1 mm for the Ti64 side and 3 mm for the Ti17 side. One may state that the monotonic and cyclic failure locations should take place at the TMAZ on the Ti17 side or far on the Ti64 PM given that these zones are softer. Moreover, it is interesting to note that the microhardness evolution of the LFW–AW joint is fairly the same than the one of the LFW–AW–PC joint which suggests that the defect layer described in Section 6.3.1 does not affect the microstructural evolution during the hot deformation of the material in the vicinity of the WCZ. In other words, the defect layer remains unseen in terms of microhardness.

6.3.3 Monotonic tensile behaviour

The macroscopic engineering stress-strain curves for the LFW–AW, LFW–AW–PC and LFW–PWHT tensile specimens are respectively plotted in green, red and black in the graph of Fig.6.8. The blue crosses depict failure for each curve. The LFW–AW and LFW–PWHT tensile specimens failed in the elastic domain with very low deformation and a maximum engineering stress of about 560 MPa. This purely elastic deformation is not desirable for engineering applications. The LFW–AW–PC specimens showed some plastic deformation with significant scatter on the strain to failure. The tensile specimens LFW–AW–PC–1 and LFW–AW–PC–3

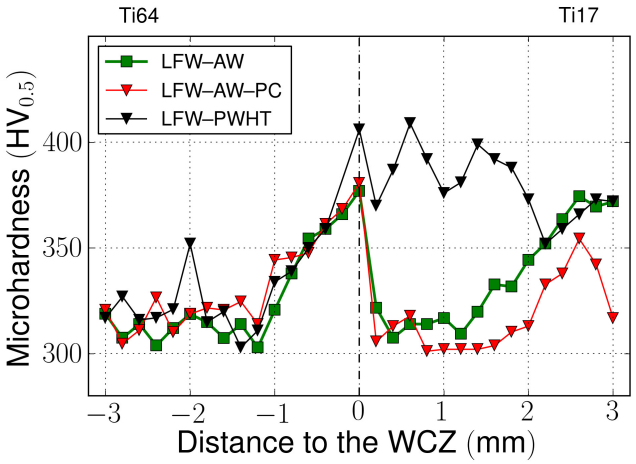

Figure 6.7: Microhardness profiles across the WCZ for the three configurations: the LFW–AW (green), LFW–AW–PC (red) and LFW–PWHT (black) joints.

exhibited a mean UTS of 1050 MPa and failed after significant deformation and some necking far from the WCZ at the Ti64 PM. The tensile specimens LFW–AW–PC–2 and LFW–AW–PC–4 failed with no necking at the UTS in the vicinity of the WCZ. Given that the tensile specimens are cross-welded structures, it would be interesting to track the location of the first stages of plastic activity and failure. Furthermore, it seems of primary interest to understand the origin of the scatter in strain to failure exhibited by the LFW–AW–PC tensile specimens. These questions are approached in Sections 6.3.3 and 6.3.3. The most outstanding fact is how detrimental the defect layer described in Section 6.3.1 can be for the tensile strength and plastic behaviour of cross-weld tensile specimens. It also should be noticed that the the problem of contamination prior to welding can not be solved by means of the thermal treatment. These findings suggest that the LFW–AW and LFW–PWHT joints may exhibit a very poor behaviour in terms of fatigue and fracture toughness. To grind the surfaces machined by EDM prior to welding seems critical to obtain desirable mechanical properties.

First stages of plastic activity and failure location

The aim of this Section is to better understand the scatter in macroscopic strain to failure exhibited by the LFW–AW–PC tensile specimens of Section 6.3.3 and to measure the local strains in the different weld zones. To do this, the location on the welded structure of both the first stages of plastic activity and failure are studied by comparing the SDIC results of the specimen that failed at the Ti64 PM and the specimen that failed at the Ti17 WCZ. See the graphs of the LFW–AW–PC–1 tensile specimen in Figs.6.9a-e and those of the LFW–AW–PC–2 tensile specimen in Figs.6.9f-h. The macroscopic tensile curves are plotted in the graphs of Figs.6.9b, 6.9e, 6.9g and 6.9j having the macroscopic engineering strain in the horizontal axis and the macroscopic engineering stress in the secondary vertical axis. The overlaid numbers on the tensile curves correspond to the eight maps of cumulated strain $\varepsilon_{\mathrm{PP}}$ (see Figs.6.9a and 6.9f) and normalized strain rate $\dot{\varepsilon}_{\mathrm{PP}}^{\mathrm{norm}}$ fields (see Figs.6.9d and 6.9i). The $\dot{\varepsilon}_{\mathrm{PP}}^{\mathrm{norm}}$ computation is performed as shown in Eq.6.1. Notice that $\dot{\varepsilon}_{\mathrm{PP}}^{\mathrm{norm}}$ is computed by normalizing the entire strain rate field with respect to the maximum strain rate found on the field, unlike the computation introduced in Section 4.3.5, in which the normalization was performed with respect to the maximum strain rate

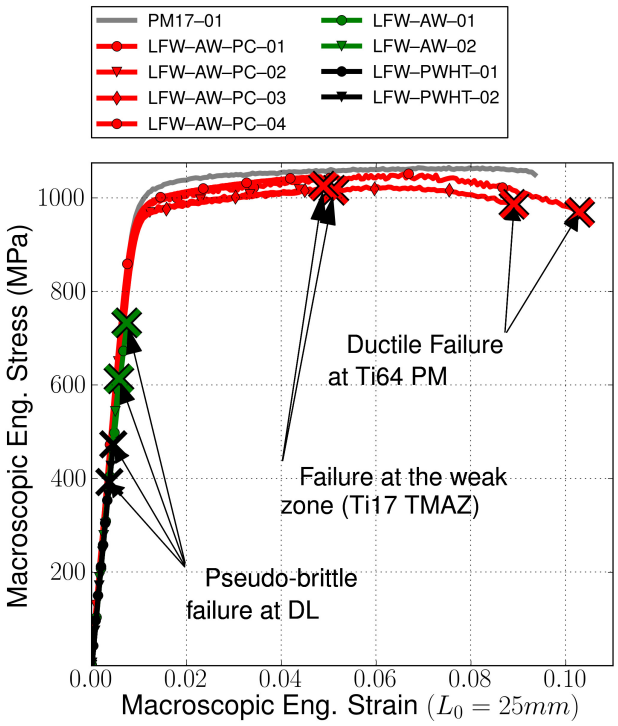

Figure 6.8: Macroscopic engineering stress-strain curves for the three configurations: the LFW–AW (green), LFW–AW–PC (red) and LFW–PWHT (black) joints.

found on the generatrix line.

$$\dot{\varepsilon}_{\mathrm{PP}}^{\mathrm{norm}}\left(\varepsilon_{\mathrm{macro}_i}; P\right) = \frac{\dot{\varepsilon}_{\mathrm{PP}}\left(\varepsilon_{\mathrm{macro}_i}; P\right)}{\max\left\{\dot{\varepsilon}_{\mathrm{PP}}\left(P\,; T\,; \varepsilon_{\mathrm{macro}_i}\right)\right\}} \tag{6.1}$$

Each first map corresponds to the domain of macroscopic elastic deformation and each second map has been taken after the onset of macroscopic plastic activity. The $\varepsilon_{\mathrm{PP}}$ and $\dot{\varepsilon}_{\mathrm{norm}}$ spatio temporal graphs (see Figs.6.9b, 6.9e, 6.9g and 6.9j) were constructed using the generatrix lines indicated in Figs.6.9d and 6.9i. The P coordinate along the generatrix lines has been set to match the location of the WCZ (see the white horizontal dashed lines on the maps and spatio temporal graphs). The $\dot{\varepsilon}_{\mathrm{norm}}$ spatio-temporal graphs for the LFW–AW–PC–1 and LFW–AW–PC–2 tensile specimens are respectively plotted in Figs.6.9g and 6.9j. Each set of maps share the colour bar with their corresponding spatio-temporal graphs. *Post-mortem* views of the tensile specimens are exhibited in Figs.6.9c and 6.9h. The overlaid green rectangles show the region of interest (ROI). Both specimens have the Ti17 side on top and the Ti64 side at the bottom. To compare the strain evolution of LFW–AW–PC–1 and LFW–AW–PC–2 tensile specimens, the maximum macroscopic engineering strain on the horizontal axes of the spatio temporal graphs (Figs.6.9b, 6.9e, 6.9g and 6.9j) and the maximum local $\varepsilon_{\mathrm{PP}}$ strain on the colour bar of Figs.6.9a and 6.9f have been set to the match the maximum values reached by the LFW–AW–PC–1 tensile specimen.

Failure at Ti64 PM The LFW–AW–PC–1 tensile specimen showed a maximum macroscopic engineering strain of 0.10 and a maximum local $\varepsilon_{\mathrm{PP}}$ strain of 0.34 exhibiting a slight stress drop and necking. Conversely, the LFW–AW–PC–2 tensile specimen showed a maximum macroscopic engineering strain of 0.05, a maximum local $\varepsilon_{\mathrm{PP}}$ strain of 0.11 and failed at the UTS (see Section 6.3.3). The heterogeneity of the $\varepsilon_{\mathrm{PP}}$ maps increases

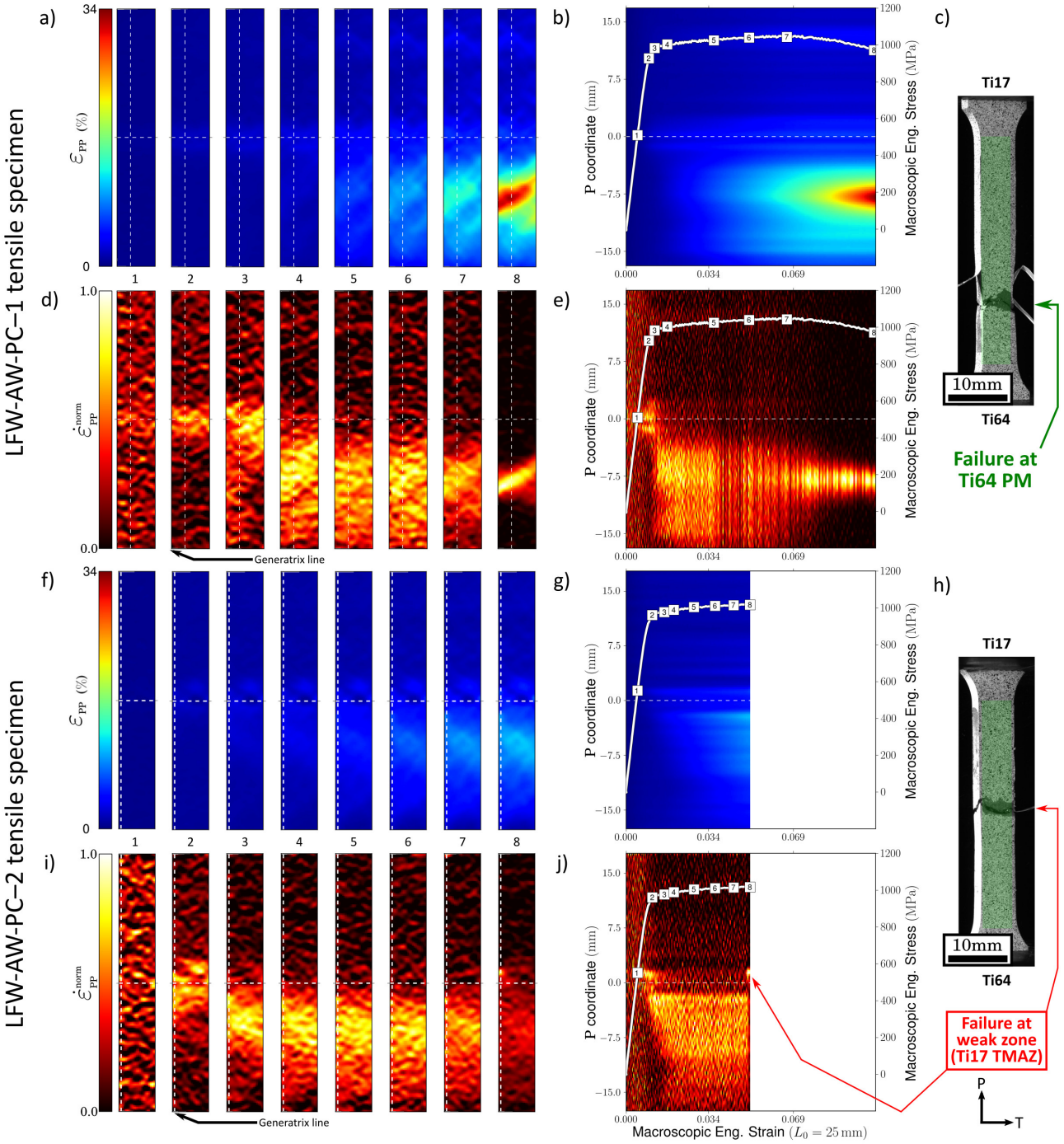

Figure 6.9: a,f) Cumulated strain maps; b,g) cumulated strain spatio-temporal graphs; d,i) normalized strain rate maps; e,j) normalized strain rate spatio-temporal graphs and c,h) *post-mortem* views of the tensile specimens in the load frame showing failure location for the a-e) LFW–AW–PC–1 and f-j) LFW–AW–PC–2 tensile specimens.

with increasing macroscopic strain for both specimens. Localization is observed at approximately $P = -7.5\,\text{mm}$. Local strain was slightly greater over a region extending from the Ti64 PM to the Ti17 TMAZ (see Figs.6.9a 6.9f). The spatio-temporal graph of $\dot{\varepsilon}_{\text{norm}}$ for the LFW–AW–PC–1 tensile specimen highlights an early plastic activity in the vicinity of the WCZ at both TMAZs that gradually shifts to the Ti64 PM, leading to final rupture (see Fig.6.9c). This early plastic in the vicinity of the WCZ has already been observed for a similar Ti6242 LFW joints and was attributed to the presence of residual stresses in Section 4.3.5.

Identification of weak zone: Failure at Ti17 TMAZ The evolution of ε_{PP} and $\dot{\varepsilon}_{\text{norm}}$ for both tensile specimens is similar until map 7 and a macroscopic engineering strain of 0.05. It is interesting to note that, at the latest stages of deformation, the ε_{PP} and $\dot{\varepsilon}_{\text{norm}}$ maps of the LFW–AW–PC–1 tensile specimen exhibit similar gradients. This means that the maximum $\dot{\varepsilon}_{\text{norm}}$ occurs at the location of the maximum ε_{PP}, highlighting a continuous and steady evolution of strain, which is consistent with the smooth drop of macroscopic stress and necking. The behaviour of the LFW–AW–PC–2 tensile specimen at the final stages of deformation is strikingly different. Failure occurred at the Ti17 TMAZ and it was preceded by an abrupt jump of the $\dot{\varepsilon}_{\text{norm}}$ maximum from the Ti64 PM in map 7 to the Ti17 TMAZ in map 8 (see Figs.6.9h and 6.9i). Failure at Ti17 TMAZ is startling, since ε_{PP} reaches a maximum value of 0.11 at the Ti64 PM, which is substantially higher than the 0.06 reached at the Ti17 TMAZ. This suggests that the underlying α depleted β grains of the Ti17 TMAZ require low levels of plastic deformation to reach failure, which may also explain both the sudden failure at UTS and the absence of necking for the LFW–AW–PC–2 tensile specimen. Given this abrupt failure, the Ti17 TMAZ is identified as a weak zone.

The $\dot{\varepsilon}_{\text{norm}}$ spatio temporal graphs have clearly evidenced that some of the LFW–AW–PC tensile specimens failed at the Ti17 TMAZ and some at the Ti64 PM. It seems that there is a competition between the soft macro-zones of the Ti64 PM and the well-oriented α depleted β grains of the Ti17 TMAZ. The most remarkable fact is that failure never occurred at the WCZ, as it was seen for the LFW–AW tensile specimens. The same set of welding parameters that failed to extrude the contaminants at the weld interface of the LFW–AW joint, favoured the LFW–AW–PC joint to develop overmatching strength.

Fracture mechanisms of the DL during tensile testing

The fracture surface on the Ti17 side of the LFW–AW–1 tensile specimen is remarkably planar which is consistent with the fact that they failed in the elastic domain (see Fig.6.10a). Small equiaxed dimples surrounding the aforementioned elongated fracture features are observed in Fig.6.10b. This ductile rupture can be seen to a very limited extent. The fracture surface is mostly covered by features that suggest a pseudo brittle fracture, as seen in Fig.6.10c. These fracture mechanisms are unexpected for titanium alloys. A SEM/BSE observation of the fracture surface is shown in Fig.6.10d. Some grey contrast is observed. A light shade of grey predominates with some spots of a darker grey (see the spot surrounded by a white dashed line in Fig.6.10d). This contrast suggests that the chemical composition of the fracture surface is not homogeneous. To confirm this, EDX analyses have been performed on the fracture surface integrating the alloying elements of both PM's and copper. The chemical content in %wt over objects highlighting different grey levels are exhibited in the tables of Fig.6.10d. The blue and green points over the light and dark grey levels highlight chemical compositions that are comparable to Ti17 and Ti64, respectively. Contrary to expectations, substantial amounts of copper

were measured even if this element is not contained in the nominal chemical composition of either of the parent materials. It should also be remembered that this specimen failed abruptly in the elastic domain. Self evidently, bonding was fulfilled only in isolated spots and during monotonic loading, the weld interface was separated at the defect layer leading to a pseudo brittle fracture.

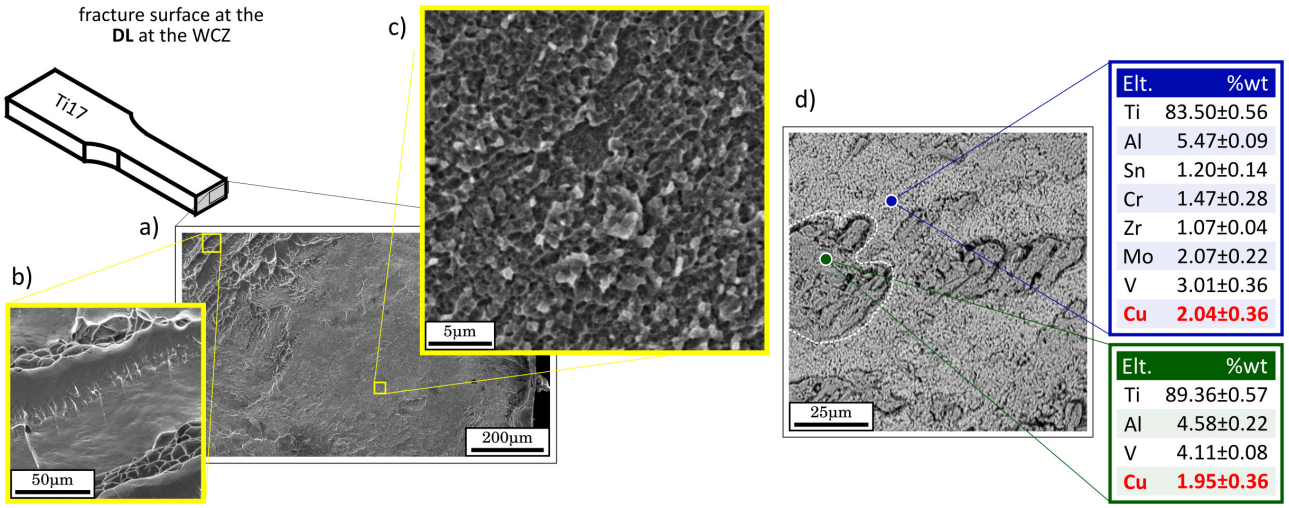

Figure 6.10: a) Fractographic observation of the the LFW–AW–1 tensile specimen showing mostly b) pseudo brittle fracture and some c) elongated dimples of "unstable" ductile rupture at the Ti17 TMAZ next to the DL. d) EDX point analysis of the fracture surface showing an approximation of the %wt. content of the PM alloying elements and Cu. Notice that some Cu is found despite the fact that this element does not belong to either PM nominal chemical composition.

Fracture mechanisms under monotonic loading: LFW–AW–PC tensile specimens

Failure at the Ti64 PM The LFW–AW–PC–1 tensile specimen failed at Ti64 PM and its fracture surface is exhibited in Fig.6.11. The observed dimples highlight ductile rupture and are comparable to the dimples of Ti64 registered elsewhere (Wojtaszek et al., 2013). The red arrows Fig.6.11a and 6.11b point to mesoscopic lines parallel to the RD direction of the PM billet. The presence of localized texture over bands parallel to the RD direction is well documented for Ti64 (Le Biavant et al., 2002; Kasemer et al., 2017; Echlin et al., 2016). These so called macro-zones have shown to be at the origin of the strain heterogeneity during micro tensile testing (Lunt et al., 2017; Echlin et al., 2016) and to have an effect on impact toughness and the fracture behaviour (Buirette et al., 2014). It seems reasonable to state that the alignments observed in the fracture surface are a consequence of potential underlying PM macro-zones.

Failure at the Ti17 TMAZ The LFW–AW–PC–2 tensile specimen abruptly failed at the Ti17 TMAZ (see Sections 6.3.3) and its fracture surface is exhibited in Fig.6.12. At first sight, it can be seen that clusters of elongated fracture features (see Fig.6.12c) cover a substantial proportion of the fracture surface and are surrounded by classical titanium alloys dimples (see Fig.6.12b). These clusters of elongated fracture features (see Fig.6.12) were already seen in the fracture surface of another similar Ti17 LFW joints that also failed at the TMAZ (Li et al., 2010). The authors reported a macroscopic deformation of 2 % on cross-weld tensile specimens for which failure occurred at the TMAZ. This suggests that local deformation at the TMAZ was greater. Moreover, Dalgaard et al. (2012a) measured a local deformation to failure of 9.28 % for a similar Ti5553 LFW that also failed at the TMAZ. Considering these facts, it seems unlikely that the clusters of

elongated fracture features might be at the origin of a brittle fracture, as suggested by Li et al. (2010). These elongated fracture features are further discussed in Section 6.3.5.

6.3.4 Fatigue test

The S–N curve for the LFW–AW–PC fatigue specimens is shown in the graph of Fig.6.13. For the sake of comparison, the S–N curve of the Ti17 PM are taken. The LFW–AW and the LFW–PWHT where not included in this graph since failure occurred at a very low number cycles in some cases and at the first fatigue cycle for others. Closed and open symbols respectively represent the fatigue trials for which fracture occurred and those

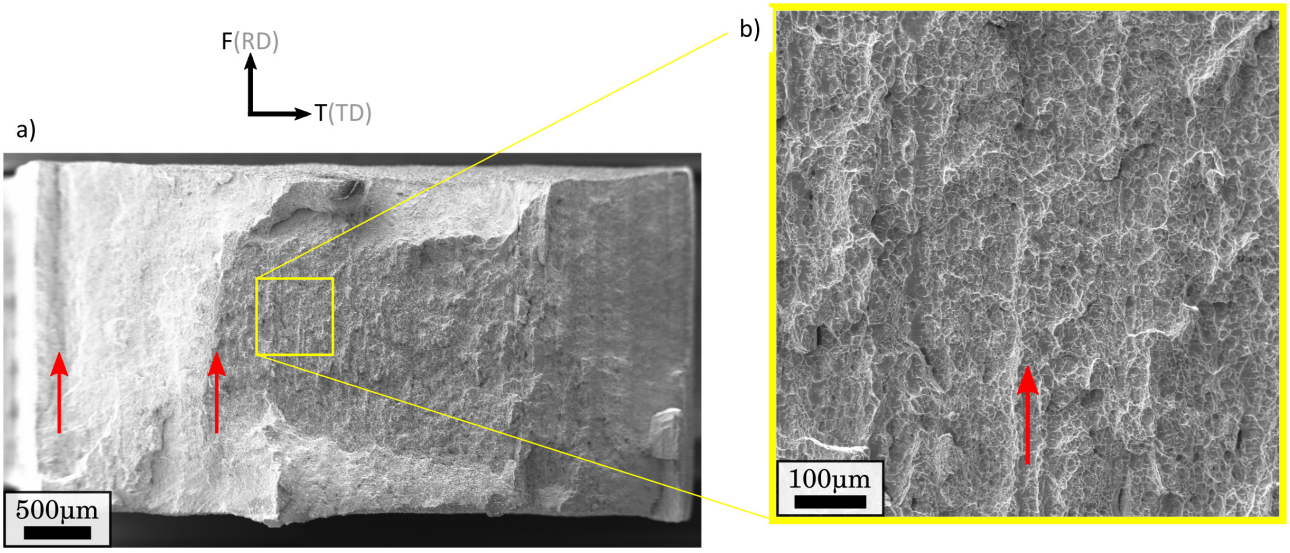

Figure 6.11: Fractographic observations showing ductile rupture at the Ti64 PM (at P = −7.5 mm) of the LFW–AW–PC–1 tensile specimen.

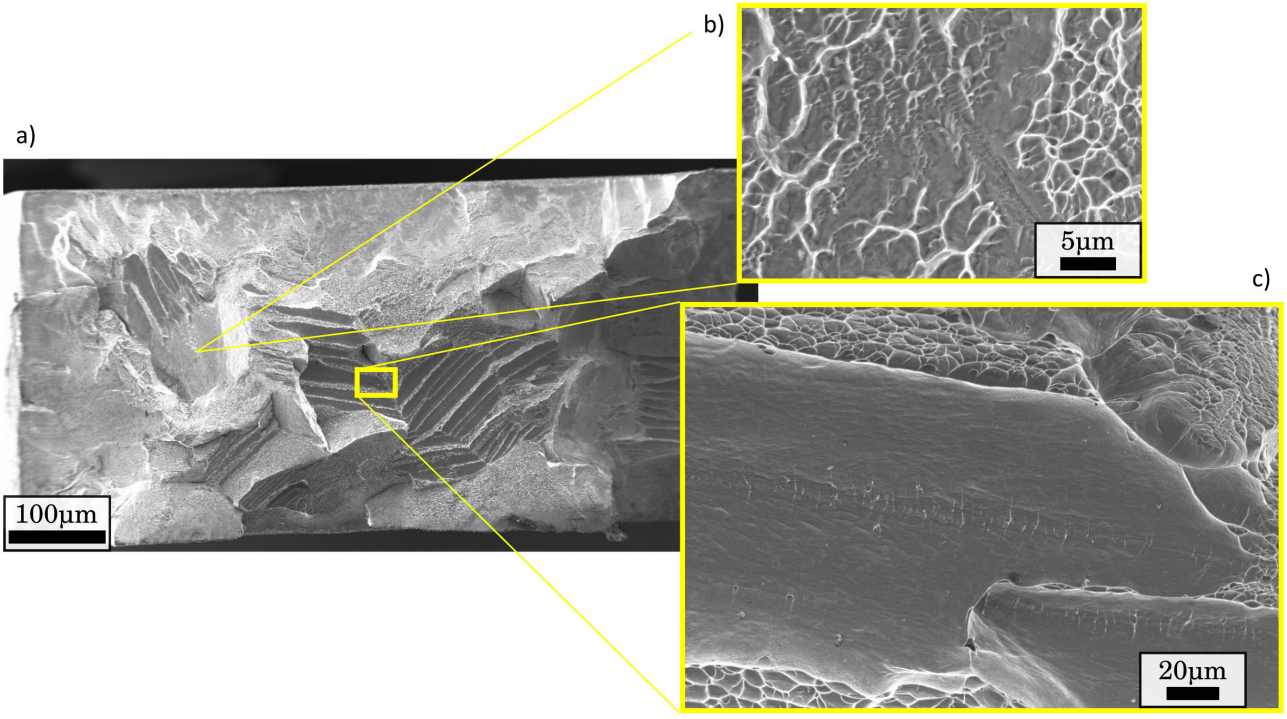

Figure 6.12: Fractographic observations showing ductile rupture at the Ti17 TMAZ of the of the LFW–AW–PC–2 tensile specimen.

for which it did not (run out). For the target life of $N_f = 10^5$ cycles the fatigue strength turned out to be 450 MPa.

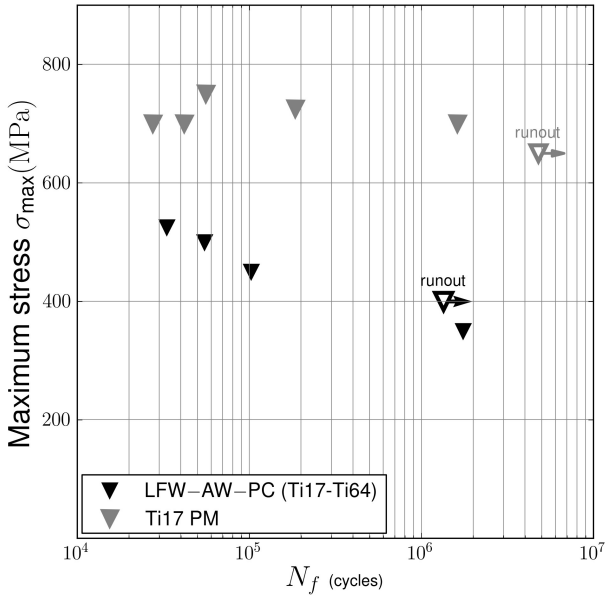

Figure 6.13: S–N curves for the LFW–AW–PC fatigue specimens (black triangles) and the Ti17 PM (grey triangles) (R = 0.1).

Fatigue crack initiation and propagation

Considering the results presented in previous Sections, it is possible to word about the potential location of the fatigue crack initiation on the welded structure of the LFW–AW–PC fatigue specimens. First, it seems reasonable to postulate the Ti17 TMAZ and the Ti64 PM as candidates for fatigue crack initiation sites since they exhibited local minimums on the microhardness profiles (see Section 6.3.2). Second, an early plastic activity in the vicinity of the WCZ was evidenced by the $\dot{\varepsilon}_{\text{norm}}$ spatio-temporal graphs and was attributed to the presence of residual stresses (see Section 6.3.3). This location should be considered as a potential fatigue crack initiation site since this was the scenario described for a LFW joint of a comparable titanium alloy previously studied in Section 4.4.2. The fatigue strength for both the Ti6242 PM and the similar Ti6242 LFW joint turned to be 650 MPa and 625 MPa, respectively (see Section 4.3.6).

Finally, in Section 6.3.3, the Ti17 TMAZ was identified as a weak zone since, during monotonic loading, localization abruptly shifted to this location and led to failure. Therefore, the Ti17 TMAZ weak zone is a potential fatigue crack initiation site and might exhibit a lower fatigue strength.

Fig.6.14a shows a fractograph of a typical LFW–AW–PC fatigue specimen. Fatigue crack initiation occurred at the weak zone (Ti17 TMAZ). Figs.6.14c and 6.14d show respectively the primary and secondary fatigue crack initiation sites (see red arrows). It seems that fatigue crack initiated at the corner of the specimen potentially at the α_{GB} layer of a β grain on the specimen surface and propagated parallel to the green arrows in Fig.6.12a. A secondary fatigue crack also probably initiated at the α_{GB} layer of a β grain at the specimen border and propagated parallel to the cyan arrows in Fig.6.12d. Final rupture exhibited elongated fracture features (see Fig.6.14b) comparable to the ones seen in the fracture surface of the LFW–AW–PC–2 tensile specimen (see Fig.6.12).

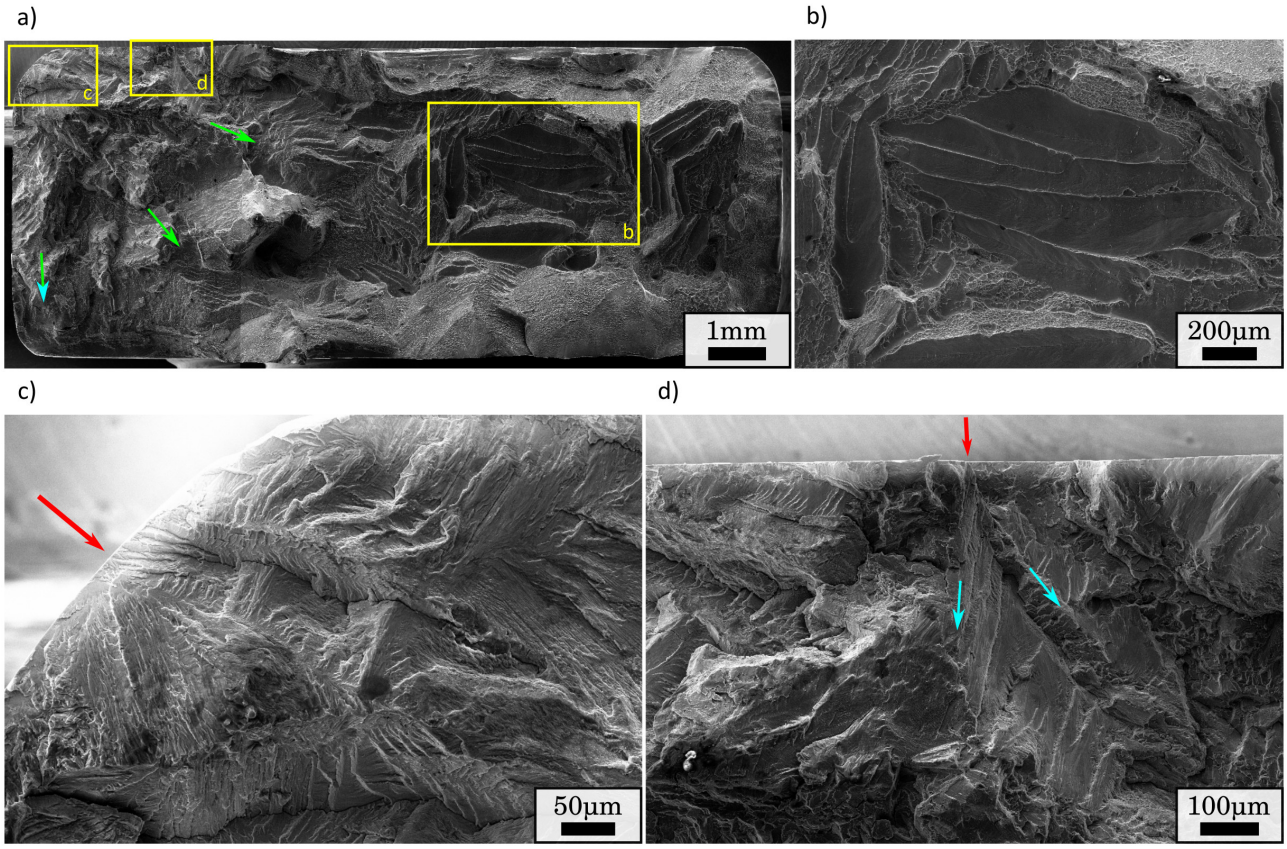

Figure 6.14: a) Fractograph of a typical LFW–AW–PC fatigue specimen showing b) elongated dimples; c) primary and d) secondary fatigue crack initiation sites.

6.3.5 Fracture toughness

According to the *Blisks* specification, the disk made of Ti17 is meant to exhibit a high fracture toughness (García, 2011). The aim of the fracture toughness experiments presented in this Section is threefold. First, to highlight the poor fracture toughness of the defect layer at the WCZ of the LFW–AW CT specimens. Second, to qualitatively compare the fracture toughness and fracture mechanisms of the PM17, LFW–AW and LFW–AW–PC CT specimens. Finally, to study the aforementioned potential cracking bifurcation from the WCZ to the Ti17 TMAZ of the LFW–AW–PC joint and its fracture mechanisms.

Fracture toughness results

Fig.6.15 shows the force - CMOD curves corresponding to the fracture toughness trials for the PM17, LFW–AW and LFW–AW–PC CT specimens. The PM17 CT specimens showed a type-I force-displacement curve with some plastic macroscopic deformation (see Fig.6.15a) whereas the cross-weld showed an type-III force-displacement curve with a purely elastic macroscopic deformation (see Fig.6.15b-c). Fracture toughness for the PM17 CT specimens was computed using the K_{Q} by P_5. For the cross-weld specimens, fracture toughness was computed using $K_Q = K_{\mathrm{IC}}$. Results are summarized in Table 6.2.

The mean stress intensity factor computed using the PM17-1 and PM17-2 CT specimens trials turned out to be $K_{\mathrm{Q}} = 99.02\,\mathrm{MPa}\sqrt{\mathrm{m}}$. The defect layer at WCZ of the LFW–AW-1 CT specimen led a to pseudo brittle fracture during pre-cracking (not shown here). Considering the poor fracture toughness of the LFW–AW joint

due to the presence of the defect layer, the LFW–AW-2 and the LFW–AW–PC-2 CT specimens were tested without pre-cracking to compute measurements of fracture toughness under comparable conditions. A total of 1.5×10^6 cycles were necessary to achieve a pre-crack extension of 0.9 mm on the sides of the LFW–AW–PC-1 CT specimen but *post-mortem* observations revealed that pre-crack extension at the centre was 2.9 mm. Thus, the test for the cross-weld specimens are not in according to the standard requirements. Nevertheless, their resulting fracture toughness computations are used here to perform a qualitative comparison. Fracture toughness computations turned out to be $K_Q = 42.7\,\text{MPa}\sqrt{\text{m}}$ for the non pre-cracked LFW–AW-2 CT specimen, $K_Q = 62.62\,\text{MPa}\sqrt{\text{m}}$ for the non pre-cracked LFW–AW–PC-1 CT specimen and $K_Q = 88.74\,\text{MPa}\sqrt{\text{m}}$ for the pre-cracked LFW–AW–PC-2 CT specimen.

Damage mechanisms of fracture toughness specimens

Fig.6.16a shows a fractograph of the no pre-cracked LFW–AW–PC–2 CT specimen. The fracture surface is completely populated of elongated and flat dimples. These fracture features were not observed in the parent material. Dimples appeared in clusters contained in regions that convey the shape prior β grains.

Failure occurred at the weak zone (Ti17 TMAZ) during monotonic loading, cyclic loading and fracture toughness testing (see Sections 6.3.3, 6.3.4 and 6.3.5). In all fracture surfaces, clusters of elongated fracture features were observed. In this Section, a *post-mortem* analysis of the microstructure next to the fracture surface of the LFW–AW–PC–2 CT specimen is presented to better understand the origin of these clusters of elongated

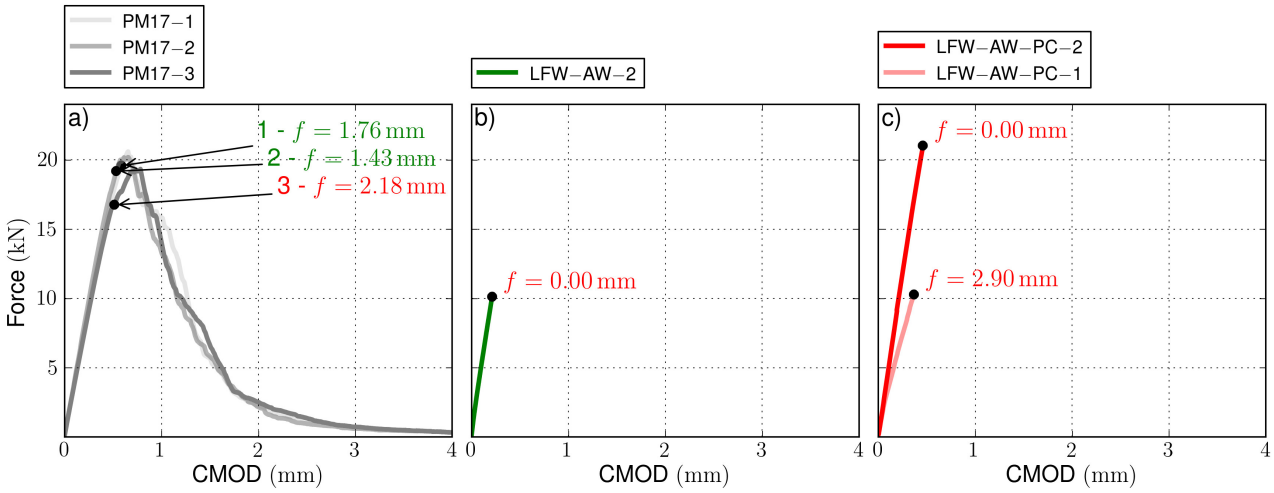

Figure 6.15: Force-CMOD curves for a) PM; b) LFW–AW and c) LFW–AW–PC CT specimens.

Specimen	K_i	(MPa$\sqrt{\text{m}}$)	Pre-crack (mm)	Observations
PM17–1	K_{IC}	102.1	1.76	Valid test
PM17–2	K_{IC}	95.94	1.43	Valid test
PM17–3	K_Q	92.30	2.18	Excessive pre-crack.
LFW–AW–1	K_Q	–	–	Failure at defect layer during pre-cracking.
LFW–AW–2	K_Q	45.75	0.00	No pre-crack.
LFW–AW-PC–1	K_Q	62.62	2.90	Excessive pre-crack.
LFW–AW–PC–2	K_Q	88.74	0.00	No pre-crack.

Table 6.2: Summarization of fracture toughness experiments results for the PM17, LFW–AW and LFW–AW–PC CT specimens.

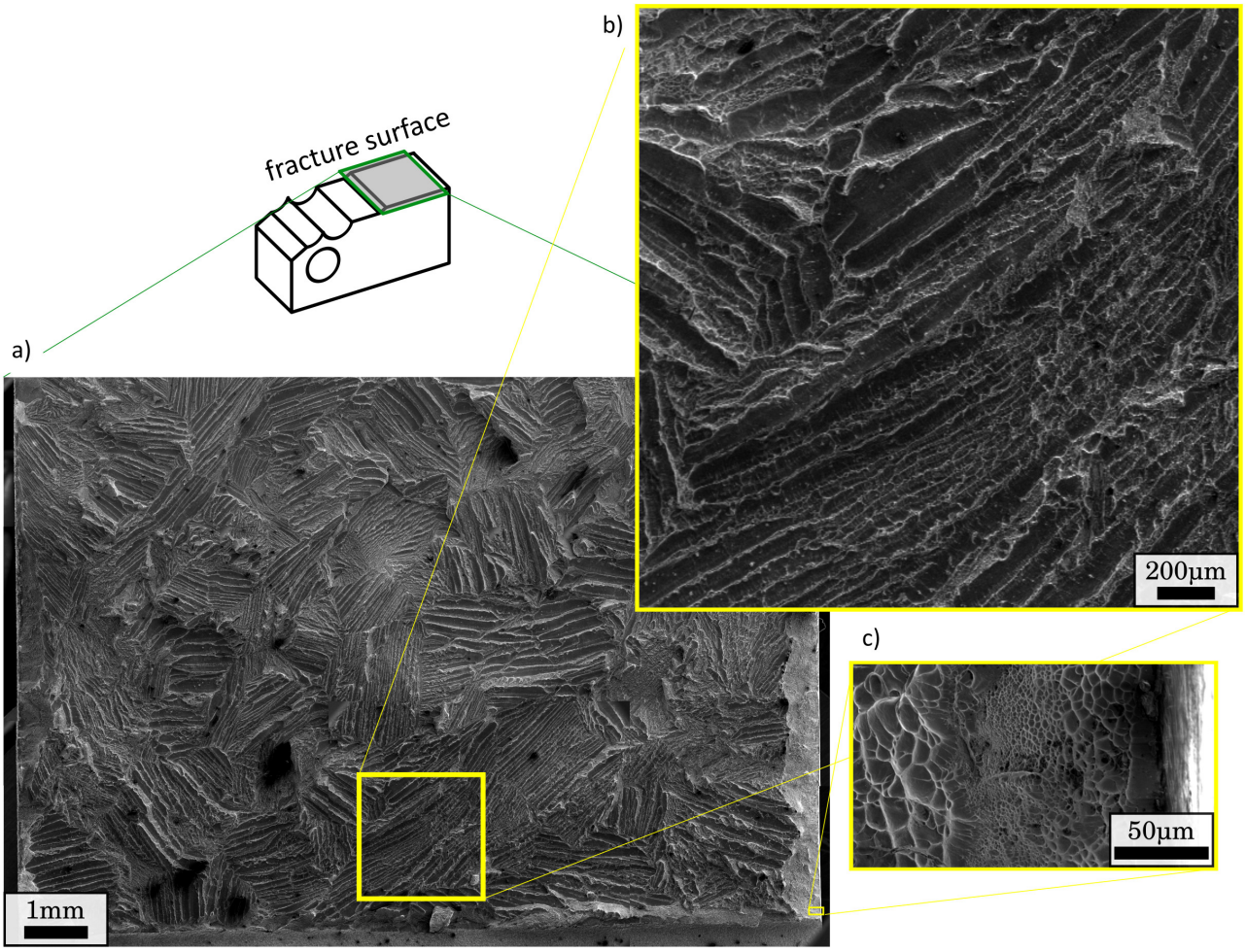

Figure 6.16: Fractograph of the no pre-cracked LFW–AW–PC–2 CT specimen exhibiting clusters of elongated fracture features.

fracture surfaces.

After performing the fractographic analysis, the Ti17 side of the LFW–AW–PC–2 CT specimen was cut in halves parallel to a FP plane, as shown in the schematic view of Fig.6.17a. As a reminder, this specimen failed at the weak zone (Ti17 TMAZ), in which the microstructure consisted in α depleted β grains. Furthermore, the fracture surface exhibited showed exclusively clusters of elongated fractures features. This two points can easily be recognized in Fig.6.17b, since the chemical contrast observed in the SEM/BSE observation hints to the α depletion of the weak zone and the toughness of the fracture surface reminds the morphology of the elongated fracture features. For instance, in Fig.6.17c, a yellow dashed line highlights an object on the fracture surface that seems to be a cut on a plane perpendicular to the main axis of the elongated fracture surfaces seen in Fig.6.16.

In the CMOD-F curve of this specimen (see 6.15), it was observed that the crack propagated abruptly at a maximum stress during elastic loading. One could suspect that these fracture features are at the origin of a brittle fracture, as suggested by Li et al. (2010). To verify this, the entire weak zone was inspected to identify potential nucleation of the elongated fracture features. Indeed, in Figs.6.17c, 6.17d, 6.17f and 6.17g, rhombus-shaped voids were observed. This suggests that the elongated features are produced as a result of nucleation and growth process as a ductile mechanism. Although, it should be noted that the nucleation and growth of these elongated features require very low levels of plastic energy, as observed in the CMOD-F curve

for this specimen.

The question about the underlying microstructural features at the origin of these elongated fracture features may arise. After performing the SEM/BSE observation of Fig.6.17c, the specimen was attacked with a Kroll's 2 reagent ($12\%HF + 18\%HNO_3 + 70\%H_2O$). Thereafter, a SEM observation was performed in the surroundings of the elongated fracture features nucleation. It should be reminded that the microstructure at this location is

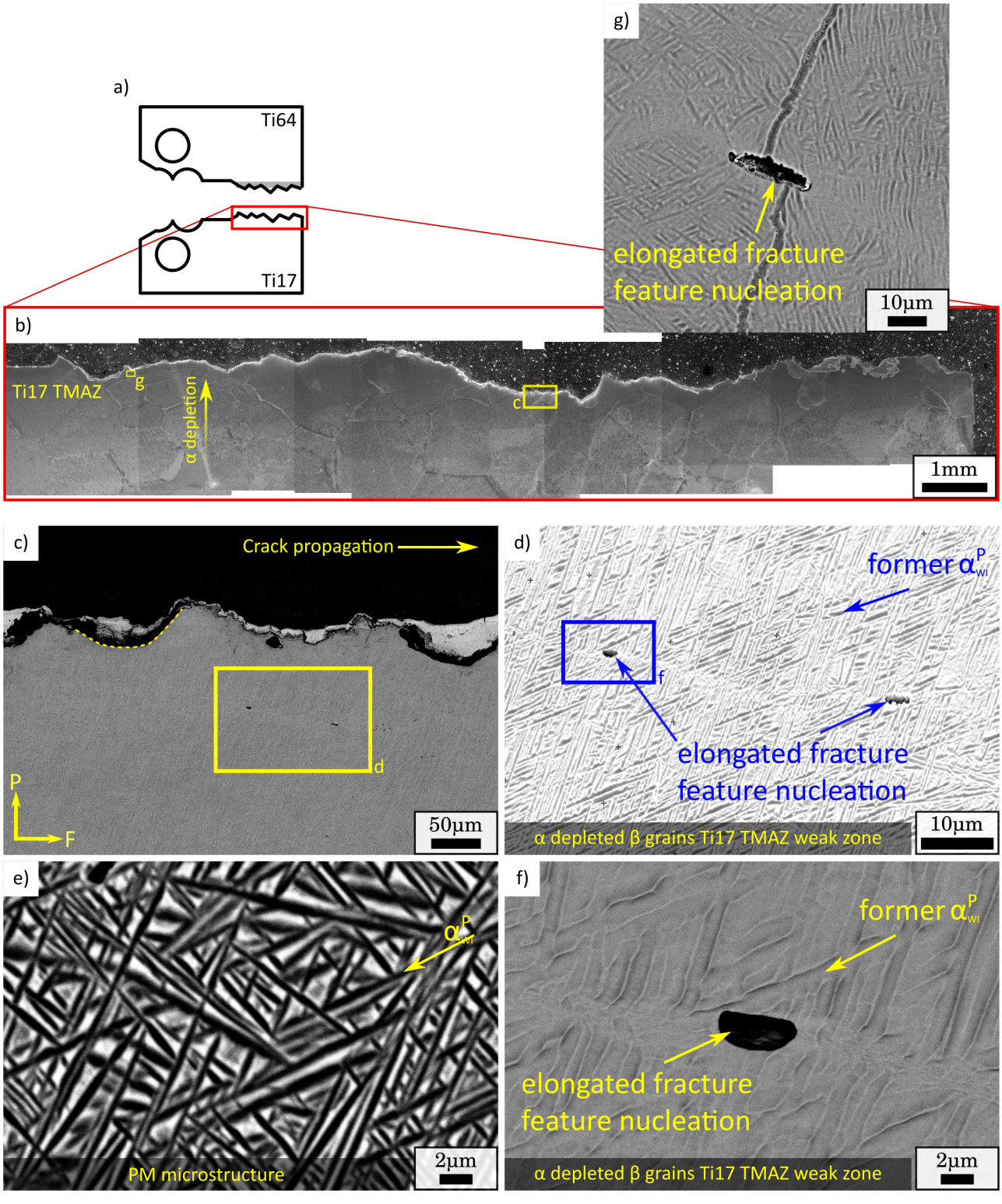

Figure 6.17: Fractographic analysis of the LFW–AW–PC–2 CT specimen.

α depleted β grains of the Ti17 TMAZ. Nevertheless, the roughness of the specimen after the attack recalls the former α^{p}_{GB} plates in the core of the β grain of the PM. This suggests that, despite the α depletion, the attack interacted with the chemical composition of former α^{p}_{GB} plates and generated the specimen roughness. To confirm this, a SEM/BSE observation of the Ti17 PM at the same level of magnification is shown in Fig.6.17e. The characteristic angles between the α^{p}_{GB} plates at the core of the β grain seen in Fig.6.17e are recognized in the relief patterns of Fig.6.17f. This is very interesting since it highlights that the elongated fracture features nucleated in a former α^{p}_{GB} plate. Similarly, in Fig.6.17g, the elongated fracture features seems to have nucleated in a former $\alpha^{p}_{\mathrm{WGB}}$ colony. It seems pretty clear that nucleation is strongly related to the presence of the former α phases in the α depleted β grains of the weak zone (Ti17 TMAZ).

6.4 Discussion

Oxide layer, welding parameters and surface preparation In this work, three joints were produced using the same set of welding parameters. The first was joined in the as machined state after EDM machining (LFW–AW), the second was welded after EDM machining and was post-weld heat treated (LFW–PWHT), and the third was ground prior to welding using a 1200 grit SiC paper for 2 min (LFW–AW–PC). Welding in the EDM as machined state produced a defect layer probably formed by intermetallics or oxides that was not observed in the joint that was ground prior to welding. The defect layer exhibited an undesirable pseudo brittle fracture in the elastic domain during monotonic loading, cyclic loading and fracture toughness tests. The analysis of the fracture surface of the LFW–AW tensile specimen clearly evidenced the separation of the WCZ as a consequence of a very poor bonding (see Section 6.3.3). Conversely, failure never occurred at the WCZ for the LFW–AW–PC specimens. It could be argued that the power input was enough to favour the LFW–AW–PC to develop overmatching strength but not enough to extrude the EDM brass contaminants at the weld interface of the LFW–AW joint. It however should be considered that brass contaminants coming from the EDM wire have a relatively low melting point and hence, local melting is likely to occur. A very drastic reduction on the fatigue life due to the presence of dendritic defects related to local melting has already been observed for the similar Ti6242 LFW joint (see 4.4.3).

It could be argued that EDM brass contaminants would not be an issue for broadcast industrial machining techniques, such as water jet machining. However, the presence and effective extrusion of contaminants in general has already been largely discussed in literature. For instance, some very interesting numerical approaches have been proposed for the optimization of welding parameters. They consist in verifying if a certain set of welding parameters accomplishes the effective extrusion of tracking points at the weld interface by the end numerical simulations of the welding process (Effertz et al., 2017; Ji et al., 2016a; McAndrew et al., 2015; Turner et al., 2011). Their limitations seem nonetheless to be that the tracking points bear the physical properties of the PM, instead of bearing those of the contaminants. Performing numerical simulations taking into account the nature of contaminants seems cumbersome since the nature of contaminants and subsequently their behaviour are *a priori* unknown. Furthermore, considering the 5 µm thickness of the defect layer, the optimization of welding parameters through a numerical approach by considering the nature of contaminants seems rather infeasible.

The surface preparation prior to LFW has been approached differently by researchers in scientific literature. A literature review concerning the surface preparation techniques is shown in the chart of Fig.6.18. Four classes have been set: welding after alcohol/acetone bath, welding after grounding, welding in the as machined state and welding without specifying the surface preparation. About 44 % of the population has adopted a surface preparation technique and only 8.3 % of them have specified welding in the as machined state. This is rather puzzling since LFW is reputed to be a self-cleaning process. In the mechanical characterization of the dissimilar linear friction welding between a SiC particle reinforced aluminium composite and a monolithic aluminium conducted by (Rotundo et al., 2013), the authors have claimed :

"*Since the surface oxide layer originating from the EDM wire cutting was expected to be expelled during the LFW, the specimens were not submitted to any further machining prior to welding* [...]." Yet, the fractographs for both tensile and fatigue specimens in their study exhibited pseudo-brittle features very similar to the ones shown in Fig.6.10 with the difference that some plastic macroscopic deformation was observed. Interestingly,

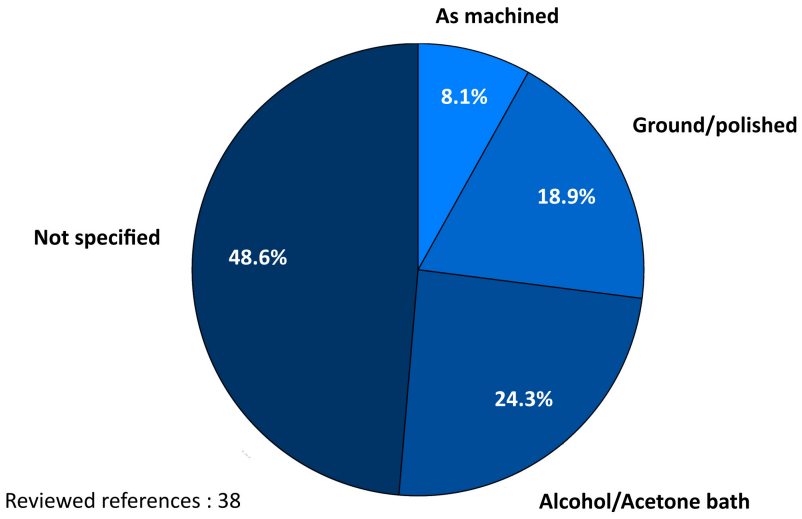

Figure 6.18: Literature review concerning the surface preparation for linear friction welding.

fatigue crack seems to have initiated at the TMAZ but at final rupture, a de-cohesion of the WCZ appears to have occurred due to the presence of a potential oxide layer.

Only 20 % of the researchers have ground the surfaces to be welded prior to LFW. The addition of a 2 min grinding operation prior to welding is a rather simple and economical practise. Its implementation should seriously be considered since not only seems it to bolster the self-cleaning property of LFW but also leads to LFW joints with dramatically enhanced mechanical properties (see Fig.6.8). Finally, about a half of the researchers did not specify the surface preparation technique. This, in junction with the diversity of the adopted surface preparation techniques, could be interpreted as a symptom of one issue among others, that has prevented LFW of becoming a more trending technique: The lack of a standard. The creation of a standard for LFW should definitely include a paragraph concerning the surface preparation. Despite more experimental research should be carried out to sustain this, it is advised to perform a 2 min grinding operation with a 1200 grit SiC paper followed by an acetone bath, a few minutes before LFW.

Failure at the Ti17 TMAZ The specification for the fabrication of Blisks states that the disk should exhibit high tensile strength and resistance under low cycle fatigue crack, whilst the blades should highlight creep resistance and high cycle fatigue (García, 2011). Thus, disks can be made of Ti17 (or Ti6246) and the blades of Ti64 (or Ti6242). Some of LFW–AW–PC cross-weld specimens failed far from the WCZ at the Ti64 side (see Section 6.3.3). This is desirable since it implies that both Ti17 and the WCZ have a higher strength. Although, some of the LFW–AW–PC cross-weld specimens failed at the TMAZ of Ti17 with a significant reduction in ductility and abrupt failure without necking.

For a similar Ti6242 LFW joint, an early plastic in the vicinity of the WCZ that later shifted to the PM was highlighted using normalized strain rates spatio-temporal graphs (see Section 4.4.2). This phenomenon was attributed to the presence of residual stresses at this location and was at the origin of fatigue crack initiation. As for the cross-weld tensile specimens studied here, regardless of the location of the final failure on the welded structure, the same early plastic activity at the Ti64 TMAZ and the same shift to the Ti64 PM were observed (see Fig.6.9). This hints to the presence of residual stresses at this location. Interestingly, for the cross-weld fatigue specimens studied here, fatigue crack always initiated at the Ti17 TMAZ. This is particularly astonishing

because it seems that, in terms of cyclic behaviour, the microstructure at the Ti17 TMAZ is a bigger threat to the integrity of the welded structure than the residual stresses at the Ti64 TMAZ.

The blades of the disk are meant to resist in high cycle fatigue. Therefore, for a fatigue life of 10^5 cycles, it may reasonably be stated that fatigue crack initiation occurring at the Ti17 TMAZ is acceptable. In spite of that, the fatigue strength of the cross-weld fatigue specimens is 450 MPa, which is much lower than the fatigue strength of both PM's. Moreover, for the fracture toughness tests of Section 6.3.5, the values of fracture toughness were particularly low and exhibited a pseudo-brittle fracture at the Ti17 TMAZ. Considering the behaviour of cross-weld specimens during fracture toughness tests and monotonic and cyclic loadings, it seems pretty clear that the Ti17 TMAZ is an important threat to the integrity of the welded structure.

Thermal treatments are largely used after friction welding (Chamanfar et al., 2012b). For instance, the similar Ti5553 LFW joint studied by Dalgaard et al. (2012a) exhibited failure at the Ti17 TMAZ but after the application of a STA thermal treatment, Wanjara et al. (2014) showed that failure no longer occurred at the former Ti17 TMAZ. Similarly, Ballat-Durand et al. (2018) proposed a standard STA heat treatment that seems to restore the PM microstructure of a similar Ti17 LFW joint. This recrystallization of the α phase at the WCZ and TMAZ was also observed in the here studied LFW–PWHT joint, as observed in Fig.6.6. Hence, the post-weld STA heat treatment proposed by Ballat-Durand et al. (2018) seems promising for restoring the mechanical properties of the weak zones.

6.5 Conclusions

The mechanical behaviour in terms of tensile strength, fatigue strength and fracture toughness of three dissimilar Ti17-Ti64 LFW joints have been studied. The first was joined in the as machined state after EDM machining (LFW–AW), the second was welded after EDM machining and was post-weld heat treated (LFW–PWHT), and the third was ground prior to welding using a 1200 grit SiC paper for 2 min (LFW–AW–PC). Results led to the following conclusions:

- The microstructure of the WCZ showed 10 µm diameter α depleted β grains in the Ti17 side and a Widmanstätten acicular α martensite in the Ti64 side. The β microstructure of Ti17 PM suffered a depletion of the α phase in the vicinity of the WCZ that led to the creation of weak zones at the Ti17 TMAZ.
- The LFW–AW joint presented a defect layer rich in Ti, Al and O of possibly oxides or intermetallics that led to an undesirable pseudo-brittle rupture in the elastic domain during tensile testing, fatigue testing and fracture toughness testing. This defect layer was linked to Cu and Zn contamination caused by the brass wire during the machining of the PM's blocks prior to welding.
- The LFW–AW–PC tensile joints presented a mean UTS of 1050 MPa and considerable scatter in macroscopic strain to failure since two failure scenarios were observed. Some tensile specimens failed at the Ti64 PM presenting a macroscopic strain to failure of 0.10 and ductile rupture. Whilst some tensile specimens failed at the Ti17 TMAZ exhibiting a macroscopic strain to failure of 0.05 and a failure at elongated dimples at the weak zone (Ti17 TMAZ).
- Normalized strain rate spatio-temporal graphs have shown an early plastic activity at the vicinity of the WCZ that later shifted to the Ti64 PM for LFW–AW–PC tensile specimens. Some cross-weld specimens failed at Ti17 TMAZ.
- For the target fatigue life of 10^5 cycles, the fatigue strength of the LFW–AW–PC fatigue specimens turned out to be 450 MPa. During cyclic loading, fatigue crack initiated at the former α_{GB} precipitates at the β grains of the the Ti17 TMAZ).
- The LFW–AW CT specimens showed very low fracture toughness failing at the maximum load exhibiting a pseudo-brittle damage features at the DL. The LFW–AW–PC specimens showed higher fracture toughness but still lower than the PM CT specimens highlighting a fracture surface completely populated by elongated dimples that occurred in slip planes of the α depleted β grains of the Ti17 TMAZ.

- The Ti17 TMAZ was identified as a weak zone since failure occurred during monotonic loading, cyclic loading and fracture toughness testing. Clusters of elongated fracture features were observed to be at the origin of very low energy ductile rupture that nucleated at the former α_{GB^P} plates in the core of the α depleted β grains and at the α_{WGB} colonies at the grain boundary of the α depleted β grains.
- The threat to the integrity of the welded structure given by the DL was not solved by the application of the PWHT. Conversely, the applied surface preparation for LFW led to more desirable mechanical properties in terms of tensile strength, fatigue strength and fracture toughness. The self-cleaning mechanism of LFW is reliable to some extent.

6.6 Acknowledgements

The authors wish to thank *UTC*, *CEMEF, Mines-ParisTech* and Airbus Central R&T for the valuable discussions. ACB is thanked for providing the welds for this study. Yvon Millet at Timet is acknowledged insight in microstructure analysis. Anne-Françoise Gourgues-Lorenzon at *Centre des Matériaux* is kindly thanked for the discussions about rupture mechanisms. Achilles Vairis (Technological Education Institute of Crete), Anthony McAndrews (TWI, UK) and Bertrand Flipo (TWI, UK) are gratefully acknowledged for the kind discussions on the self-cleaning mechanism of LFW. The authors acknowledge the financial support from the French National Research Agency (ANR) and FRAE through OPTIMUM ANR-14-CE27-0017 project.

7

On the effect of a thermal treatment on the tensile and fatigue properties of weak zones of similar Ti17 linear friction welds and parent material

In the previous Chapter, it was shown that prior to welding contamination may have very detrimental consequences in terms of mechanical properties for dissimilar Ti17-Ti64 LFW joints. Furthermore, for the joint that was cleaned prior to welding, the mechanical properties were improved, yet, the Ti17 TMAZ was identified as a weak zone since failure occurred at this location during monotonic loading, cyclic loading and fracture toughness tests. During joining, the Ti17 TMAZ suffered a depletion of the strengthening α precipitates that were observed to re-precipitate through the application of post weld heat treatment proposed in the work-package 1 of the OPTIMUM project. The effect of this thermal treatment on the mechanical properties of both the parent material and weak zones are unknown.

In this Chapter, the effect of a thermal treatment on the tensile and fatigue properties of weak zones and parent material of similar Ti17 linear friction welded joints are studied. Tensile tests instrumented with Stereo Digital Image Correlation. The damage mechanisms are assessed and related to the underlying microstructure through fractographic analysis.

This work will be submitted as following: *On the effect of a thermal treatment on the tensile and fatigue properties of weak zones of similar Ti17 linear friction welds and parent material. Juan–Manuel García, Fabrice Gaslain and Thilo–Frank Morgeneyer. Materials characterization.*

Résumé de chapitre

Les propriétés mécaniques en traction, en fatigue et en termes de mécanismes de rupture ont été étudiées en lien avec la microstructure pour des joints soudés mono-matériaux Ti17 testés d'une part à l'état brut de soudage (LFW–AW) et d'autre part après avoir subi un traitement thermique (LFW–PWHT), et comparées au matériau de base (MB). Le joint LFW–AW a souffert d'un épuisement de la phase α au niveau du noyau de la soudure (WCZ) et de la zone thermo-mécaniquement affectée (TMAZ), qui auparavant avait été identifiée comme zone faible. Une analyse des champs de déformation obtenus par stéréo-corrélation d'images (SDIC) sous chargement monotone a souligné que l'hétérogénéité de déformation est reliée au facteur de Schmid des gros grains β du MB. Comparés au MB, le joint LFW–AW a montré une réduction de la résistance mécanique et une forte réduction de la ductilité macroscopique. Les cartographies de déformation et de vitesse de déformation normalisée obtenues par SDIC ont clairement souligné une localisation au niveau des zones faibles. Pour la durée de vie visée de 10^5 cycles, la résistance en fatigue du joint LFW–AW a été réduite de moitié révélant les zones faibles comme sites d'amorçage de fissures de fatigue. De façon remarquable, le traitement thermique a permis de retrouver avec succès des propriétés proches de celles du MB. Les anciennes zones faibles ont été recristallisées en grains β comparables à ceux du MB. Les résistances en traction et en fatigue ont été presque rétablies. Sous chargements monotone et cyclique, la rupture a eu lieu loin des anciennes zones faibles.

Chapter Abstract

The tensile and fatigue properties and the damage mechanisms of as welded (LFW–AW) and post-weld head treated (PWHT) similar Ti17 LFW joints as well as Ti17 parent material (PM) were studied in link with the underlying microstructure. The LFW–AW joints exhibited a depletion of the α phases in the weld centre zone (WCZ) and in the thermo-mechanically affected zone (TMAZ), which was previously qualified as a weak zone. Stereo Digital Image Correlation (SDIC) analysis of the strain field for monotonic loading of the PM showed strain heterogeneity that was linked by EBSD and Schmid's factor analysis to the large β grains containing α precipitates. Compared to the PM tensile specimens, the LFW–AW joint highlighted lower UTS and a strongly reduced and scattered macroscopic ductility. Maps and spatio-temporal graphs of normalized strain rate fields obtained by SDIC clearly highlighted localization at the weak zone. For the target fatigue life of 10^5 cycles, the fatigue strength of the AW joint was about half of that of the PM with fatigue crack initiation at the β grain boundary in the weak zones. Remarkably, the PWHT made the AW joints comparable to the PM in terms of microstructure and mechanical properties. The former weak zones recrystallized into β grains, the UTS and fatigue strength were almost recovered, macroscopic and local ductility were enhanced, failure during monotonic and cyclic loadings occurred far from the former weak zones.

Contents

Figures

Keywords

Linear friction welding, Mechanical properties, Ti17, Ti−5Al−2Sn−2Zr−4Cr−4Mo

Nomenclature

α (h.c.p.), hexagonal closed packed titanium crystal lattice;

β (b.c.c.), body centred cubic titanium crystal lattice;

F, friction axis;

P, pressure axis;

T, thickness axis;

E, Young's modulus;

Y, yield strength;

UTS, Ultimate Tensile Strength;

ε_{macro}, macroscopic engineering strain;

ε_{PP}, local strain following the P axis;

$\dot{\varepsilon}_{PP}$, local strain rate following the P axis;

$\dot{\varepsilon}_{norm}$, normalized strain rate with respect to the instantaneous maximum; σ_{max}, maximum fatigue stress;

R, fatigue stress ratio;

N_f, fatigue life;

ΔK, stress intensity factor;

a, crack size;

da/dN crack growth rate.

7.1 Introduction

Titanium alloys are used in multiple engineering fields such as the aerospace (Boyer, 1996) and the biomedical industries (Rack and Qazi, 2006; Long and Rack, 1998). Despite their high cost, they highlight several advantages such as high resistance to corrosion, high strength/density ratio, creep resistance, fatigue crack propagation resistance, high compatibility of forming composites and Weldability (Leyens and Peters, 2003; Flipo et al., 2016). At room temperature, pure titanium exhibits a high resistance hexagonal close-packed crystal lattice (α phase), beyond a so called $\beta-$transus temperature it undergoes an allotropic transformation to a ductile body cubic centred crystal lattice (β phase). The addition of alloying content and the application of thermo-mechanical processes allows the β phase to be stabilized at room temperature and consequently, complex microstructures are developed having both α and β phases. Since the titanium manufacturing process was developed in 1939 (Kroll, 1940), a very vast amount of alloys have been developed and they can be classified in α alloys, near$-\alpha$ alloys, α/β alloys and β alloys (Leyens and Peters, 2003).

The β alloys, first categorized by Jaffee (1955), can also be classified in stable and metastable β alloys. For the second kind, the β phase is said to be metastable because despite it is capable of retaining 100% of the β phase after quenching, it is susceptible of precipitating a secondary phase which is usually but not only α (Bania, 1994). The processing of $\beta-$metastable alloys during manufacturing determine the resulting microstructure and consequently, their mechanical properties. Solution treatment consists in heating the bulk beyond the $\beta-$transus temperature and, eventually, applying hot deformation. Decreasing temperature from the β domain provokes the precipitation of α_{GB} on the β grain boundary and the formation of α_{WGB} colonies. Increasing cooling rates implies decreasing length and width of the α_{GB} and increasing length, width and extension the α_{WGB} colonies (Lütjering, 1998). During ageing, the primary α^{p}_{WI} and secondary α^{s}_{WI} intergranular are formed. The macroscopic mechanical behaviour of $\beta-$metastable alloys is dependent on these microstructural features.

Under monotonic loading, ductility increases with increasing β grain size (Lütjering and Williams, 2003; Banerjee and Mukhopadhyay, 2010). The α precipitates are key in the strength of $\beta-$metastable alloys. Increasing volumetric fraction of intergranular α_{WI} increases strength (Aeby-Gautier et al., 2011). Increasing mean width of the α precipitates decreases tensile strength (Aeby-Gautier et al., 2013; Zhang et al., 2018), increases strain to failure and provokes intergranular fracture (Ivasishin et al., 2005). $\beta-$metastable alloys are known for their high specific strength, low elastic modulus, excellent fatigue/crack-propagation behaviour and excellent corrosion resistance (Boyer, 1996; Bania, 1994). Nonetheless, their application have found some limitations because of their high formulations and machining costs, complex processing (Eylon et al., 1994), low production volumes, and property scatter (Cotton et al., 2015). $\beta-$metastable alloys are often but not only used in structural applications such as the airframes (Banerjee and Williams, 2013). For instance, in 1973, General Electric patented the invention of Ti$-$5Al$-$2Sn$-$2Zr$-$4Cr$-$4Mo for its utilization in fans and compressor discs due to its deep hardenability, fracture toughness and fatigue crack growth rates (Welsch et al., 1993; Meetham, 1981). This alloy has several denominations such as UNS R58650 for the American Unified Numbering System of alloys, TA5CD4 for the French denomination, TC17 for the Chinese standards and it is commonly known as Ti17.

In the aerospace industry, the increasing need of improving the buy-to-fly ratio led to the development of novel joining techniques (Boyer, 2010). A clear example of this is the invention of solid-state joining processes

such as Linear Friction Welding (Ritcher, 1929). In this process, a so called friction force is applied to a stationary workpiece towards an oscillating workpiece describing a linear oscillatory motion. Parent material and contaminants in the weld interface are extruded to form the so called flash. Once pure contact between the two materials has been fulfilled, a forging pressure is applied to achieve a target axial shortening also known as burn-off (Vairis and Frost, 1998). The high levels of plastic deformation and localized heat generated around the weld interface provoke microstructural changes, unknown mechanical properties and considerable levels of residual stresses that are comprised in four distinct welding zones (Vairis and Frost, 1998): the weld centre zone (WCZ), the thermo-mechanically affected zone (TMAZ), the heat affected zone (HAZ) and the parent material (PM). LFW exhibits some advantages such as very short welding times, typically in the order of some seconds; the reduction of bulk milling operations and the possibility of performing dissimilar welds (García, 2011). Conversely, LFW requires some important investment and in some cases, compared to the PM, the weld can have inferior mechanical properties.

It is well known that aerospace structures work under cyclic loading. A trivial example of this is the taking off and landing of air-planes. The large wealth of available literature concerning the cyclic behaviour of titanium alloys, in particular for $\beta-$metastable alloys, substantially supports this assertion. For instance, internal fatigue crack initiation at the α phase at a β grain boundary has been observed for a Ti-8823 grade (Chait and DeSisto, 1977). Increasing the aspect ratio of the α phase of Ti$-$4.5Al$-$5Mo$-$1.5Cr grade enhances the fatigue crack growth resistance (Gilmore et al., 1985). Compared to the bimodal microstructure, the lamellar microstructure of Ti17 titanium exhibits superior properties in both threshold stress intensity factor and fatigue crack growth resistance (Liang et al., 2016). For low cycle fatigue, it has been shown that fatigue cracks initiation occurs at the α-plate interface (Funkenbusch and Coffin, 1978). As far as the authors are concerned, no investigation has hitherto been carried out concerning the fatigue strength nor the fatigue crack propagation mechanisms of similar Ti17 linear friction welds.

The microstructural characterization and tensile properties of the Ti17 LFW joints have previously been assessed. The microstructure of a dissimilar Ti17(lamellar)-Ti17(equiaxed) LFW joint exhibited a fine re-crystallized zone at the WCZ with significant reduced microhardness (Ji and Wu, 2014). A depletion of the hardening α phase was observed at the WCZ and TMAZ of a similar Ti553 LFW joint that led to failure at the TMAZ during monotonic loading (Dalgaard et al., 2012a; Wanjara et al., 2014). Similarly, it has been recently explained that microstructures consisting in α depleted deformed β grains and fine equiaxed distorted β grains were respectively developed at the WCZ and TMAZ of a similar Ti17 LFW joint that locally reduced microhardness (Ballat-Durand et al., 2018). The same microstructures were observed in the WCZ and Ti17 TMAZ of a dissimilar Ti17-Ti64 LFW joint in Section 6.3.3. The authors have denominated the Ti17 TMAZ as a "weak zone" since it was the location for failure under monotonic loading, fatigue crack initiation and crack propagation during fracture toughness testing. The common factor among the aforementioned welds is the α depletion of the WCZ and TMAZ and their subsequent reduced mechanical properties. It seems clear that developing a thermal treatment that could favour the precipitation of the α phase for enhancing the mechanical properties of the weak zones in similar Ti17 LFW joints, is highly necessary.

The application of thermal treatments to LFW joints and their subsequent mechanical properties have already been assessed in literature. For instance, Tao et al. (2015) carried out impact fracture toughness tests over specimens having notches centred at characteristics weld zones of dissimilar Ti17-Ti64 LFW joints, in

the AW conditions and after two annealing thermal treatments. It has been shown that the reduced impact fracture toughness of the TMAZ and WCZ on the Ti17 side was increasingly improved with increasing annealing temperature. The standard thermal treatment for $\beta-$metastable alloys is solution treating followed by ageing (STA). The poor mechanical properties of the similar Ti5553 LFW joint studied by Dalgaard et al. (2012a) were significantly improved by a PWHT applied by Wanjara et al. (2014). The thermal treatment consisted in a solutionizing at 816 °C for 45 min in vacuum followed by argon quench and ageing at 621 °C for 8 h in argon followed by argon quench. Precipitation of the α phase was fulfilled at the α depleted WCZ and TMAZ. As a consequence, not only were the tensile properties improved but also, the PWHT tensile specimen never failed at the former weak zone (Ti17 TMAZ). Recently, Ballat-Durand et al. (2018) proposed a STA thermal treatment for similar Ti17 LFW joints, in which the transition from the solution treatment to ageing phase is carried out through a slow temperature reduction. This thermal treatment is promising since the precipitation of the α was successfully fulfilled at the α depleted WCZ and TMAZ, and, with respect to the PM, microhardness was recovered up to 97 %. A study concerning the tensile and fatigue properties, and damage mechanisms of similar Ti17 LFW joints having followed this thermal treatment is missing in literature.

The present work is subscribed on the framework of a project focusing on several key aspects of LFW such as the microstructural characterization (Ballat-Durand et al., 2018), the numerical simulation of the welding process (Potet et al., 2017), and the mechanical characterization reported herein. The aim of the present scientific paper is to identify the deformation behaviour, strength and fatigue life of similar Ti17 LFW joints in the as welded and post welded heat treated conditions and compare them to the behaviour of the parent material. Special interest is laid on the relationship between the macroscopic properties and the underlying microstructures previously characterized by Ballat-Durand et al. (2018). First, texture on the PM is studied through multi-field electron backscatter diffraction (EBSD) mappings on the surface of PM and cross-weld tensile specimens. Second, the tensile properties and strain fields obtained by SDIC of all joints and parent material are presented and compared to the underlying β grains crystal lattice orientation through their Schmid's factor. The fracture mechanisms during monotonic loading are interpreted and related to the phases present in every microstructure. Third, the cyclic behaviour is assessed by a S-N approach and its associated fatigue crack propagation mechanisms are analysed. Finally, the contamination prior to welding, the benefits and effects of the post-heat weld treatment, as well as a potential optimization are discussed.

7.2 Experimental and materials

7.2.1 Parent Material

The PM used in this work was a Ti17 grade in the STA state provided by Timet. The solution treatment consisted in forging at 950 °C followed by air cooling. Then, the bulk was aged through an isothermal hold at 635 °C in a preheat furnace for 8 h and finally air cooled. The material was provided in the form of billets of 250 mm diameter. Blocks with 80 mm × 70 mm × 15 mm dimensions were machined by electrical discharge machining using a brass wire. The long direction of the blocks coincided with the extrusion axis of the billet. The relationship between the two others directions of the blocks and the billet directions was unknown.

The microstructure of the PM billet used in this study was previously characterized by Ballat-Durand

et al. (2018) and is shown in Fig.7.1a. It consisted in 550 µm diameter prior-β grains (b.c.c.) containing α phases (h.c.p.) in four forms: grain boundary α (α_{GB}), colonies of Widmanstätten laths growing from the grain boundary (α_{WGB}) and two kinds of intergranular Widmanstätten laths (primary α^p_{WI} and secondary α^s_{WI}). The entangled intergranular α^p_{WI} had length and width of respectively 4.4 µm and 1.6 µm .

7.2.2 Linear friction welds

Three similar Ti17 LFW joints were produced by ACB. During joining, frequency was $f = 50$ Hz, the amplitude was $a = 2$ mm, the friction and forging pressure were $P = 90$ MPa, and the target burn-off was 3 mm. Friction occurred parallel to the F axis, the friction and forging pressures were applied along the P axis, as shown in Fig.7.2. The third direction corresponded to the thickness T. The F axis was parallel to the long direction of the blocks and coincided with the RD direction of the billet. The first joint was welded in the as machined state after cutting by electrical discharge machining (EDM) using a brass wire (LFW–AW), the second joint was ground prior to welding using a SiC paper P1200 for 2 min (LFW–AW–PC) and the third block was welded in the as machined state after cutting by EDM and post-weld heat treated (PWHT). The aim of producing the LFW–AW and LFW–AW–PC joints was to study the effect of prior to welding contamination on the mechanical properties of these joints. All configurations are summarized in Table 7.1. The PWHT is described in Section 7.2.3.

Material	Denomination	Specification
PM	Ti17 parent material	forging at 950 °C+ air cooling 8 h ageing at 635 °C+ air cooling
LFW–AW LFW–AW–PC	As welded similar Ti17 LFW joint.	Welded as machined (EDM) Surface ground prior to welding
LFW–PWHT	Post weld heat treated similar Ti17 LFW joint.	annealing at 910 °C + 2 h cooling to 635 °C 8 h ageing at 635 °C+ air cooling

Table 7.1: PM and similar Ti17 LFW joints configurations.

As a consequence of LFW, a depletion of the α phase occurred at the WCZ and TMAZ. The TMAZ exhibited a width of about 1.2 mm and its microstructure was formed by α depleted deformed β grains (see Fig.7.1b). The Ti17 TMAZ is also known as a "weak zone" due to its proclivity to failure under various type of loadings in Section 6.3.3. At the β grain boundary in the TMAZ, Ballat-Durand et al. (2018) observed a chemical contrast having a β crystal lattice that they denominated "traces of $\alpha_{GB} + \alpha_{WGB}$" (see Fig.7.1b). The WCZ is shown in Fig.7.1c, its width was about 400 µm and it was formed by α depleted fine equiaxed distorted β grains having a diameter of about 10 µm (Ballat-Durand et al., 2018).

7.2.3 Post-weld Heat treatment

The post-weld heat treatment applied to the LFW–PWHT joint in this study was performed by Ballat-Durand et al. (2018) and it consisted in an annealing at 910 °C for 2 h followed by furnace cooling to 635 °C in 2 h. The cooling rate was about 2.3 °C/min. Then ageing was performed at 635 °C for 8 h followed by air cooling.

After PWHT, the microstructure at the WCZ and TMAZ recrystallized into grains comparable to those of the PM. The grains at the former WCZ exhibited a diameter of a about 230 µm and microhardness of 390 HV.

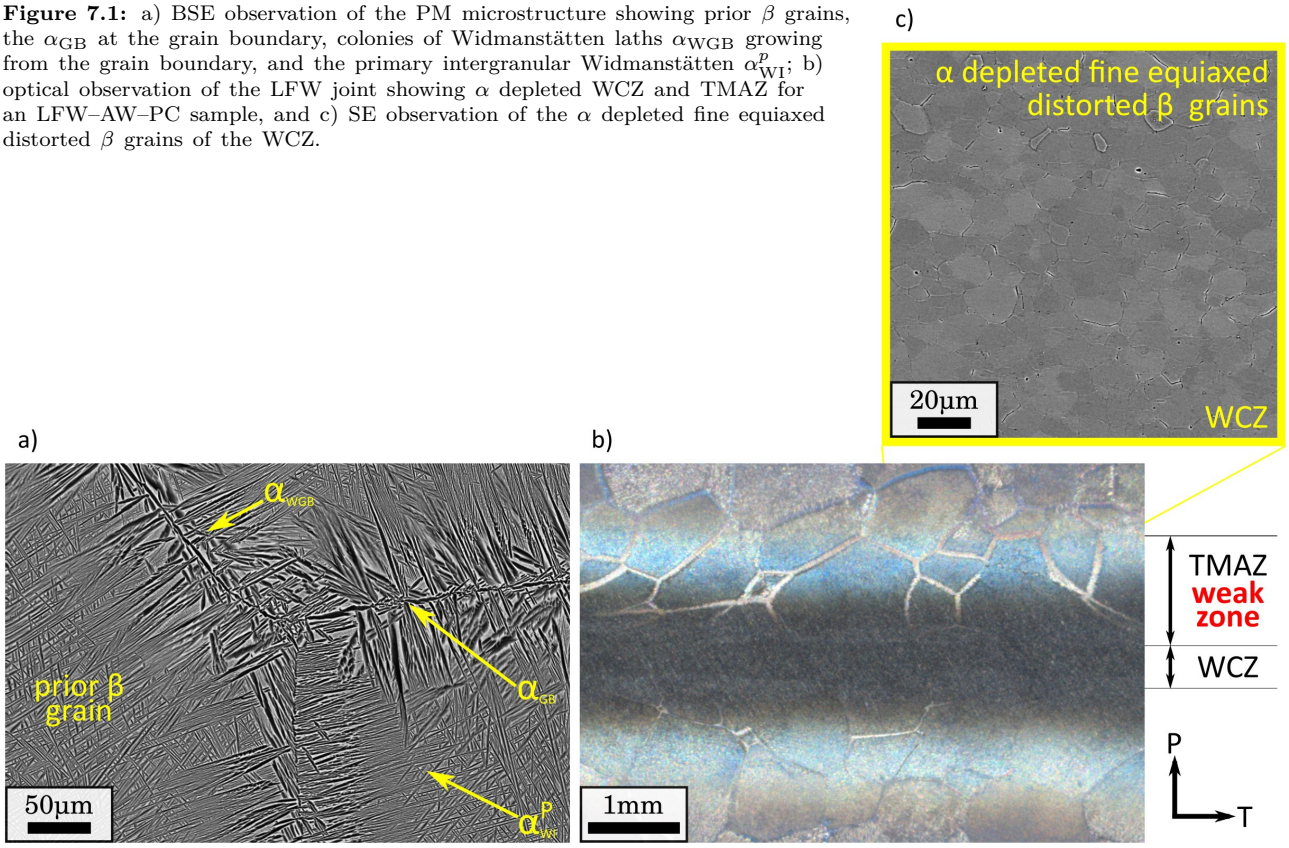

Figure 7.1: a) BSE observation of the PM microstructure showing prior β grains, the α_{GB} at the grain boundary, colonies of Widmanstätten laths α_{WGB} growing from the grain boundary, and the primary intergranular Widmanstätten α^{p}_{WI}; b) optical observation of the LFW joint showing α depleted WCZ and TMAZ for an LFW–AW–PC sample, and c) SE observation of the α depleted fine equiaxed distorted β grains of the WCZ.

Compared to the PM, the grains at the former WCZ exhibited significant smaller diameter and a microhardness reduction of about 3% (Ballat-Durand et al., 2018).

7.2.4 Microscopic observations

The samples were prepared by standard metallographic procedures consisting in mounting, grinding and polishing to a mirror like quality. The parent material and welded joints were observed in a LEICA DMI 5000 optical microscope and in a ZEISS DSM982 Gemini Scanning Electron Microscope (SEM) operated at 15 keV using secondary electrons detector (SE) and backscattered electrons detector (BSE). The fractographic analysis was carried out using secondary SE detector in a ZEISS DSM982 Gemini SEM.

7.2.5 EBSD mapping and fractographic observations

EBSD characterization was performed over very large areas, *i. e.*, the gage length of the tensile specimens described in Section 7.2.6. The aims of the EBSD characterization are detailed in Section 7.3.1.

The tensile specimens were mounted in pairs in sample-holders customized for their geometry and were ground to a mirror like quality using an Leco PX500 automatic polisher. The pressure force was set to 5 kN. The rotation frequency of the polisher head and tray were respectively 25 Hz and 200 Hz. By increasing the difference between the rotation speeds of the polisher tray and the polisher head, long grinding periods are induced for which grinding marks continuously change their direction. In such manner, the mirror like quality is almost achieved by using only a SiC paper grit 1200 for 2 min. After grinding, the mirror like quality was

fulfilled by polishing using a solution composed of 200 mm^3 Struers oxide polish suspension and 200 mm^3 distilled water for 24 h on a Buehler VibroMet.

Multi-field EBSD mappings were carried out on a ZEISS DSM982 Gemini Scanning Electron Microscope (SEM) operated at 20 keV instrumented with a Nordif UF300 camera. The region of interest was the gage length of three tensile specimens: one made of PM, one coming from the LFW–AW–PC joint and one coming from the LFW–PWHT joint. The specimen geometry is described in Section 7.2.6. For each tensile specimen, about 450 fields of 840 px × 840 px were performed to cover an area of typically 32 mm × 6 mm with a step size of 10 µm. The working distance was 24 mm. Indexation was carried out taking into account only the β phase. No filter was applied for the visualization of the EBSD mappings of Fig.7.3. To perform the texture analysis (see Section 7.3.1) and the Schmid's computation (see Section 7.3.3), a grain size filter of 5 px and a minimal confidence coefficient of 0.2 filter were previously applied.

A study on the PM β grains texture over surfaces perpendicular to the extrusion axis of the billet was performed using the gage length of the aforementioned tensile specimens as metallographic samples. Texture in the plane normal to the billet extrusion axis is studied since this was the only direction able to be tracked during machining. To get a representative sample for the determination of texture, at least 2000 crystal orientations should be observed (Kocks and Kallend, 1991). Considering the large size of PM grains of Ti17 (∼600 µm), large surfaces are required to properly carry out a study on texture.

As shown in Fig.7.2, the surface of the PM tensile specimen was perpendicular to the billet extrusion direction. Given that friction was parallel to the extrusion axis of the billet during welding, the PM far from the WCZ of a cross-weld tensile specimen is also contained in a plane perpendicular to the extrusion axis of the billet (see Fig.7.2). In this report, the texture analysis was carried out over a total of 2074 crystal orientations (1136 and 938 coming from the PM and cross-weld tensile specimens, respectively).

Schmid's factor mappings of the tensile specimens gages length were performed for three slip systems: {110}⟨111⟩, {112}⟨111⟩ and {123}⟨111⟩. Considering that three slip systems were taken into account in the computation of the Schmid's factor, it is not possible to determine which one is more likely to be activated. On the contrary, given that Schmid's factor maps show the maximum computed factor among all slips systems, grains with lower Schmid's factors are likely to undergo relatively low a plastic deformation, which could possibly be linked to low levels of local strain. To highlight this, the Schmid's factor colour bar in Fig.7.5 are inverted.

7.2.6 Tensile test

Four sets of tensile specimens were machined: 6 tensile specimens made of PM, 10 tensile specimens of the LFW–AW joint, 6 tensile specimens of the LFW–AW–PC joint and 6 tensile specimens of the LFW–PWHT joint. The denomination of every set of specimens is further explained in Table 7.1. The PM tensile specimens were machined having their main surface perpendicular to the extrusion axis of the billet. All cross-weld specimens were machined parallel to a PT plane of the joint. The principal axis of the cross-weld specimens was parallel to the P direction. Gage length was 25 mm and cross section was 3 mm × 6 mm. Fig.7.2a shows the geometry of the tensile specimens. Tensile tests were conducted following the ASTM-E8 standard with a MTS 250 kN load frame at room temperature. Load frame cross-head speed was 0.032 $mm\,s^{-1}$. Elongation was measured with optical extensometers as described in Section 7.2.7.

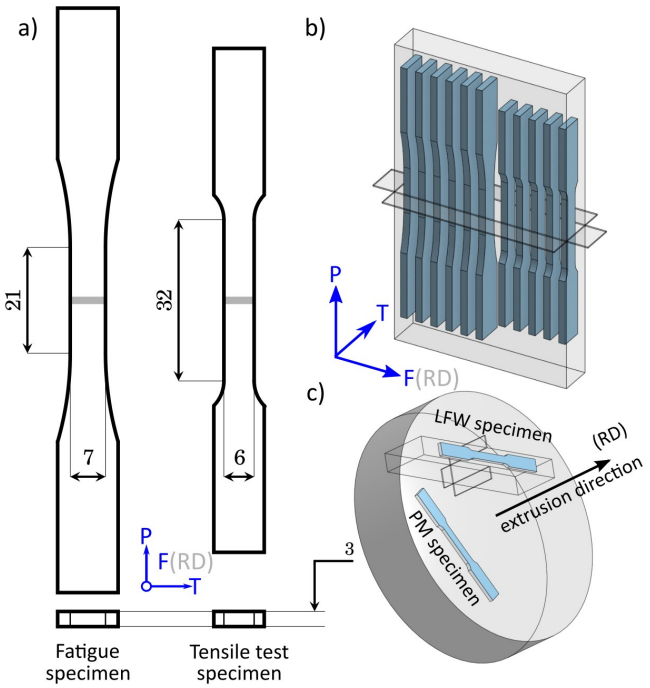

Figure 7.2: a) Specimen geometries for the tensile and fatigue specimens; schematic view of the machining of the specimens b) on the welded joint and c) the billet. All specimens were machined parallel to a perpendicular plane to the extrusion axis of the billet and a PT plane for the weld.

7.2.7 Stereo Digital Image Correlation (SDIC)

During tensile testing, the local strain over the tensile specimens surface was monitored using a standard system of SDIC. A system of two 2048 px × 2048 px Manta G-419B cameras was set to follow the displacement of an artificial random black and white speckle applied with an airbrush over the gage length of the tensile specimens. The distance between the cameras was $a = 26$ cm and the camera-object distance was $b = 31$ cm, leading to a field of view of 40 mm × 40 mm. Images were exploited with Vic-3D™ from Correlated Solutions, Inc. (version 7.2.4, 2014). Acquisition was carried out taking 2 frames per second. Subset size was 35 px ≈ 175 µm, step size was 9 px and filter size was 15 px. Before tensile testing, the displacement and the Hencky $\varepsilon_{\mathrm{PP}}$ measurements uncertainty were determined by correlating two consecutive images of the static specimen. Uncertainty in displacement measurements turned out to be 0.1 µm. This corresponds to a Hencky strain uncertainty of $\Delta\varepsilon_{\mathrm{PP}} = 0.0002$ with a standard deviation of $\sigma_{\varepsilon_{\mathrm{PP}}} = 9.56 \times 10^{-5}\%$. The load line, the specimen and the cameras frame were aligned using a laser level as a reference. Both cameras were aligned to gravity using a water level.

7.2.8 Fatigue test

Standard fatigue tests over smooth specimens were carried following the ASTM 466-07 standard. Fatigue specimens made of PM and the three cross-weld joints described Table 7.1 were machined. PM samples were machined in a perpendicular plane to the extrusion axis of the billet. Tests were performed using 6 specimens made of PM, 5 LFW–AW cross-weld specimens and 7 PWTHed cross-welded specimens. Cross-weld specimens were machined parallel to a PT plane of the joint, having its principal axis parallel to the P direction, as shown in Fig.7.2. The uniaxial tension zone had a length of 21 mm and a constant gage section of 3 mm × 7 mm. A

sinusoidal waveform was imposed using a MTS 250 kN servo-hydraulic load frame. The stress ratio was $R = 0.1$ and the test frequency was 20 Hz. Specimens corners were rounded with a lime and their surface were polished to a mirror like quality. The target fatigue life was $N_f = 10^5$ cycles.

7.3 Results

7.3.1 Microstructure: EBSD analysis for location of the WCZ, β crystal lattice orientation and PM texture analysis

Crystal lattice orientation mappings over the gage length surface of three tensile specimens were performed (see the schematic view of Fig.7.3d). The aim of these mappings is threefold. First and most importantly, to locate the WCZ on the cross-welded tensile specimens. This is particularly important for the PWHT tensile specimens since the only marker of the former WCZ is the grain size. Second, to acquire information about the underlying crystal lattice orientation to relate it to the local strain measured by SDIC of large β grains (see Section 7.3.3). Finally, to study potential textures on the PM parallel to the billet extrusion axis.

The inverse pole figures for the PM, LFW–AW–PC and PWHT tensile specimens are respectively shown in Figs.7.3a, 7.3b and 7.3c. All inverse pole figures are referred to the frame of reference and pole figure in Fig.7.3d. The PM grain size was measured using the Average Grain Intercept method over the black generatrix line in Fig.7.3a. Every black dot represents a grain boundary intercept. With a total of 57 intercepts through a distance of 34.2 mm, the grain size turned out to be ∼600 µm. Considering the grain diameter and the 6 mm × 3 mm surface of the tensile specimens gage length, it can be estimated that roughly 10 × 5 grains can respectively be found on the gage length of tensile specimen, which is a very low number of grains compared to the tensile specimens made of other engineering materials. This could be at the origin of the property scatter evoked by (Cotton et al., 2015). Considering the tensile specimen and grain sizes, the question about the representative elementary volume arises.

WCZ location on the cross-weld LFW–AW, LFW–AW–PC and PWHT tensile specimens

Fig.7.3b shows the inverse pole figure of the LFW–AW–PC tensile specimen. The WCZ is highlighted with a yellow rectangle, elsewhere the PM β grains can be recognized. The inverse pole figure of the PWHT tensile specimen is shown in Fig.7.3c. Compared to the inverse pole figures of the PM and LFW–AW–PC tensile specimens (see Figs.7.3a-b), the β indexation of the PWHT tensile specimen exhibits a lower quality (see Fig.7.3c). It is noteworthy that the indexation quality is particularly lower at the β grain boundary for all specimens. This can be explained by the presence of α_{GB} and α_{WGB} at these locations. This is clearly highlighted for the PWHT tensile specimen (see blue arrows Fig.7.3e) but notice that this effect was subtler for the PM nor LFW–AW–PC tensile specimens. It seems that the PHWT has coarsened the α phases at the grain boundary, which may imply that the LFW–PWHT joint may have slight differences in the monotonic and cyclic behaviour with respect to the PM. Conversely, this effect is not observed in the Ti17 TMAZ (see the higher magnification view of Fig.7.1). This highlights the depletion of the α phase at the weak zones.

Whilst the PWHT tensile specimen mapping is compromised with some noise, it is interesting to note that the former WCZ can easily be located even if it is not as clear as for the LFW–AW–PC tensile specimen (see

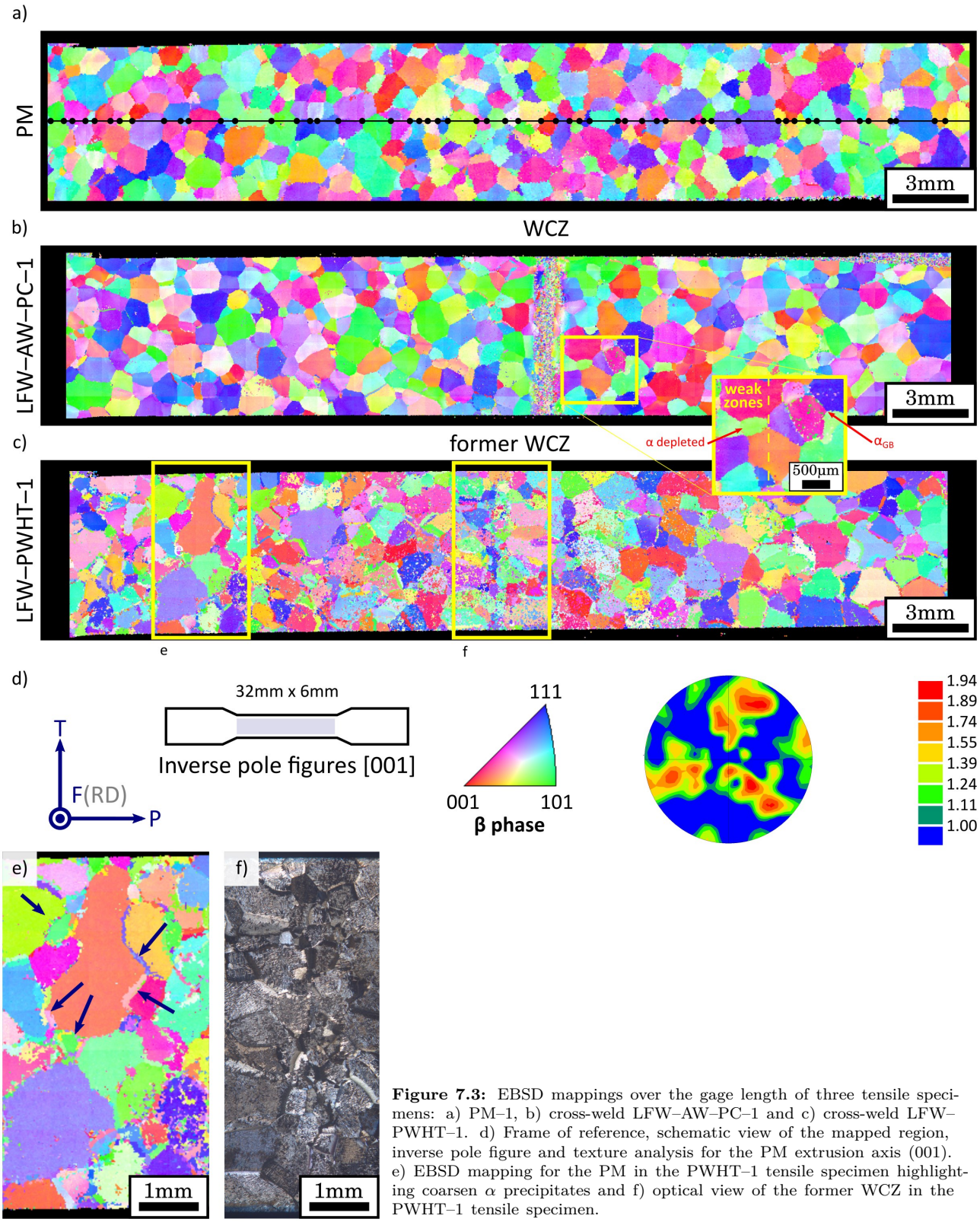

Figure 7.3: EBSD mappings over the gage length of three tensile specimens: a) PM–1, b) cross-weld LFW–AW–PC–1 and c) cross-weld LFW–PWHT–1. d) Frame of reference, schematic view of the mapped region, inverse pole figure and texture analysis for the PM extrusion axis (001). e) EBSD mapping for the PM in the PWHT–1 tensile specimen highlighting coarsen α precipitates and f) optical view of the former WCZ in the PWHT–1 tensile specimen.

the yellow rectangle at the centre of Fig.7.3c). To confirm this, an optical microscopic observation of this region is shown in Fig.7.3f. The relatively smaller recrystallized β grains at the former WCZ can be seen. This is remarkable since it shows that the PWHT has effectively achieved the recrystallization of the WCZ into PM β grains, as explained by Ballat-Durand et al. (2018). It is also interesting to notice that the β grains of the PM and the α depleted deformed β grains of the former TMAZ, previously denominated as a weak zone in Section

6.3.3, are no longer distinguishable.

Finally, having determined the locations of the WCZ (LFW–AW–PC) and former WCZ (PWHT), to compare them with failure location during monotonic and cyclic loading is of critical importance for judging the quality of the PWHT in terms of mechanical properties.

PM microstructure texture analysis The pole figure in Fig.7.3d accounts for 2074 β crystal orientations in both PM and LFW–AW–PC tensile specimens (see Section 7.2.5). No pattern is observed. The maximum intensity value is 1.94. These findings indicate that no significant texture is observed parallel to the extrusion direction of the billet. The EBSD mappings presented herein do not have a sufficient resolution for the study of texture in the WCZ. A study on texture of the WCZ of the similar Ti17 LFW joint studied here was carried out by Ballat-Durand et al. (2018) and, as for the similar Ti5553 LFW joint studied by Dalgaard et al. (2012a), a strong texture on $\{110\}\langle 111\rangle$ parallel to the friction direction was revealed.

7.3.2 Tensile behaviour

The aim of this Section is to study the tensile properties of the PM, LFW–AW, LFW–AW–PC and PWHT tensile specimens. Special interest is drawn on the tensile properties of the weld zones for the cross-weld tensile specimens (LFW–AW and LFW–AW–PC) and the tensile specimens coming from the LFW–PWHT joint. The tensile curves for each set of specimens are shown in Fig.7.4b. A comparison of the macroscopic plastic behaviour of all tensile specimens is shown in Fig.7.4a. The tensile curves are plotted in grey for the PM, in blue for LFW–AW joint, in green for the LFW–AW–PC joint and in red for the LFW–PWHT joint. The vertical dashed lines on each graph of Fig.7.4b indicate the strain to failure of each tensile specimen.

The PM tensile specimens showed an UTS of 1066 MPa and minimum, a mean and a maximum macroscopic engineering strains of 0.059, 0.074 and 0.093, respectively. The PWHT tensile specimens showed a mean UTS of 1030 MPa and minimum, a mean and a maximum macroscopic engineering strains to failure of 0.058, 0.047 and 0.101, respectively.

The LFW–AW tensile specimens showed a mean UTS of 1011 MPa and minimum, mean and maximum macroscopic engineering strains to failure of 0.020, 0.028 and 0.042, respectively. The LFW–AW–PC tensile specimens showed a mean UTS of 1061 MPa and minimum, mean and maximum macroscopic engineering strains to failure of 0.021, 0.038 and 0.066, respectively. Notice that, compared to the PM, not only is the UTS lower but also, the macroscopic ductility is highly reduced. These properties are undesirable for engineering applications. Furthermore, no significant difference is observed between the behaviours of the LFW–AW and EMD-GD tensile specimens.

The PM tensile specimens showed a weak hardening, low macroscopic stress drop during necking and significant ductility. The strong scatter in macroscopic strain to failure is consistent with the property scatter previously described for this alloy (Cotton et al., 2015). Compared to the PM tensile specimens, the UTS is slightly reduced and the strain to failure is higher but it exhibits a comparable scatter. The slight UTS reduction and the coarsening of the α phases explained in Section 7.3.1 are in according with the relationship between the UTS and mean width of the α phases explained by Aeby-Gautier et al. (2013); Zhang et al. (2018). Nevertheless, its should be noted that the tensile properties of the PWHT tensile specimens are astoundingly better that those of the cross-weld specimens.

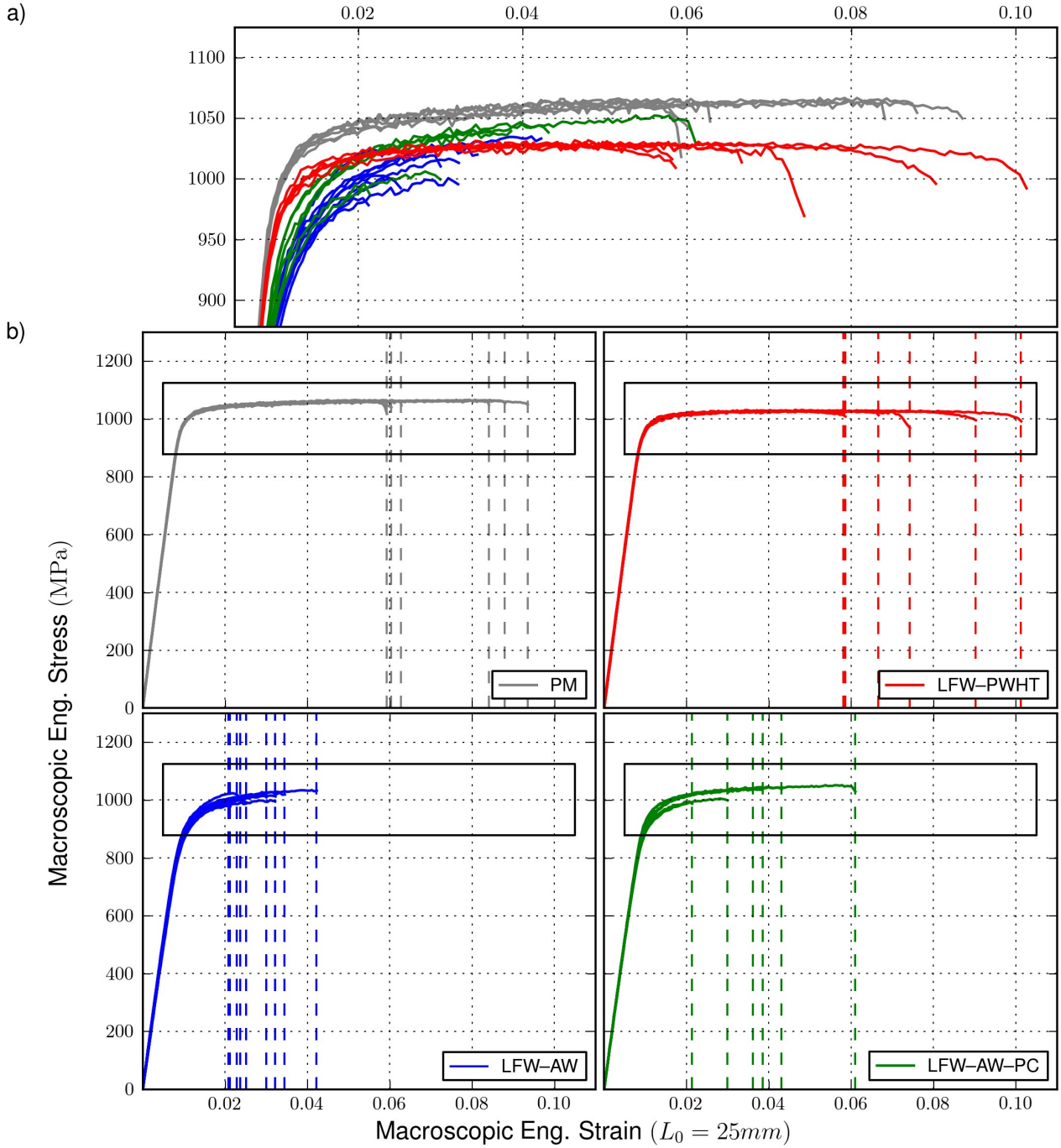

Figure 7.4: a) Tensile test curves comparison and b) tensile test curves for the PM tensile specimens (gray lines), LFW–AW tensile specimens (blue lines), LFW–AW–PC tensile specimens (green lines) and PWHT (red specimens). The vertical dashed lines in each subplot of Fig.7.4b indicate the strain to failure for each tensile specimen.

Unlike the PM, the cross-weld specimens (LFW–AW and LFW–AW–PC) failed at the UTS with a reduced macroscopic ductility confirming the weld undermatching strength anticipated by the microhardness profiles previously registered (Ji and Wu, 2014; Ballat-Durand et al., 2018; Li et al., 2010). The values of strain to failure and UTS registered for the cross-weld specimens are in good agreement with the results reported by (Li et al., 2010). Furthermore, failure occurred without a drop on the macroscopic stress exhibiting no substantial necking. These findings clearly suggest that, for the welding configuration studied here, the α depleted WCZ and TMAZ are a threat for the integrity of the cross-welded structure in terms of monotonic behaviour. To

properly assess the tensile behaviour of both the TMAZ and the WCZ, local strain measurements are required.

7.3.3 DIC strain field measurement and localization

The main objective of this Section is to study the relationship between the strain fields obtained by SDIC and the underlying microstructure of three tensile specimens:

- the β grains containing α precipitates of a PM tensile specimen;
- the large α depleted β grains of the TMAZ and fine equiaxed distorted β grains of the WCZ of a LFW–AW–PC tensile specimen and

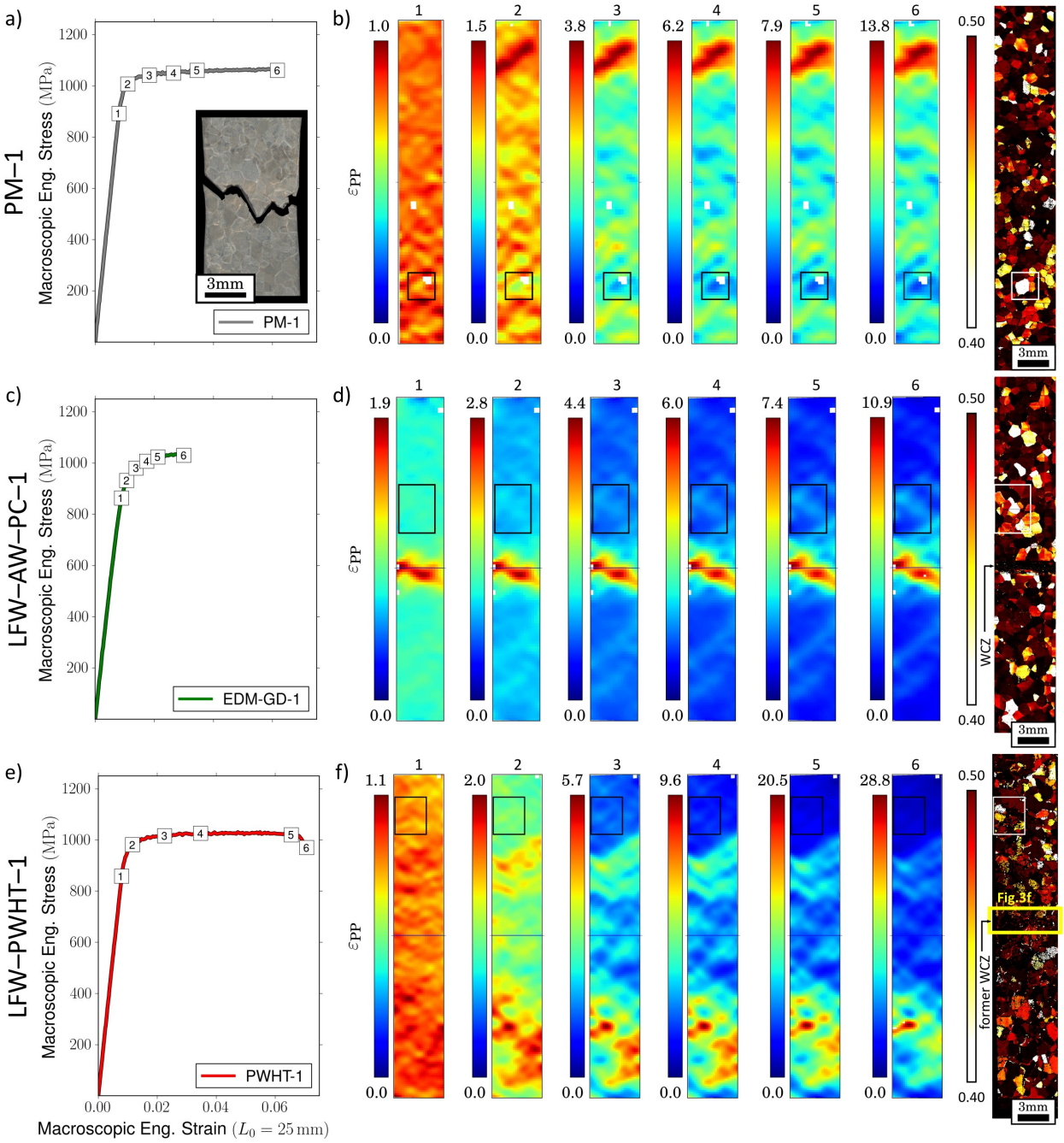

Figure 7.5: a-c-e) Tensile tests, b-d-f) ε_{PP} cumulated strain fields and Schmid's factor mappings for the tensile specimens: a-b) PM–1, c-d) LFW–AW–PC–1 and e-f) PWHT–1.

- the recrystallized former WCZ and TMAZ of a PWHT tensile specimen.

The tensile test curve for the PM–1, LFW–AW–PC–1 and PWHT–1 tensile specimens are respectively seen in Figs.7.5a, 7.5c and 7.5e. For each specimen, the cumulated local strain parallel to the P axis (ε_{PP}) fields are seen in the subplots of Figs.7.5b, 7.5d and 7.5f. Each subplot corresponds to the instants indicated with numbers on each tensile test curve. Each ε_{PP} map holds its corresponding colour bar at its left. The minimal value has been set to zero for all maps. The white dashed lines on each map of Figs.7.5d and 7.5f respectively show the position of WCZ and the former WCZ.

PM tensile specimens The ε_{PP} field for the PM–1 tensile specimen is rather homogeneous during elastic loading (see Fig.7.5b, map 1). After the onset of macroscopic plasticity on map 2, the ratio between the maximum and minimum ε_{PP} is increasing and superior to 3. The ε_{PP} localizes in diagonal bands such as the localization band at the top of the ROI. The maximum ε_{PP} was 13.8 % having failure close to the upper grip. As for most engineering materials, the ε_{PP} field for a tensile specimen made of Ti17 would be expected to be rather homogeneous but interestingly, this is not the case.

Using the crystal orientations obtained by EBSD shown in Section 7.3.1, a Schmid's factor mapping for three slipping systems has been plotted in Fig.7.5b. Three slip systems of the β phase are mapped: $\{110\}\,[111]$, $\{112\}\,[111]$ and $\{123\}\,[111]$. Two facts are worthwhile of being noticed. First, strain bands in the ε_{PP} fields go through several grains. It seems that, in every band, the observed mesoscopic deformation is the result of the contribution of about ten grains. A similar phenomenon has been observed on the micro DIC strain fields over Zirconium grade 702 and titanium aluminide registered by Héripré et al. (2007). Second, the strain bands measured by SDIC apparently avoid the low Schmid's factor grains (regions highlighted by rectangles in Figs.7.5b, 7.5d and 7.5f). Despite this information does not take into account the contribution of the α phases nor the complex stress field generated by the three-dimensional distribution of grain orientations, it is fairly reasonable to conclude that the observed ε_{PP} field heterogeneity is highly influenced by the β grains crystal orientation distribution.

LFW–AW–PC tensile specimens During elastic loading, the ε_{PP} field was somewhat greater at the WCZ and TMAZ (see map 1 in Fig.7.5d). Far from the WCZ, strain bands similar to the those observed in the PM–1 tensile specimen are seen (see Fig.7.5b). During elastic loading, the ε_{PP} at the WCZ and TMAZ was higher than at the PM in the cross-welded structure. This suggests that the depletion of the α phase at these locations entails a significant reduction of the local Young's modulus with respect to the microstructure of the PM containing β grains with α precipitates. The WCZ and TMAZ exhibited higher ε_{PP} up to final rupture. This phenomenon is consistent with the typical drop in microhardness at the WCZ and TMAZ exhibited by similar Ti17 LFW joints (Ji and Wu, 2014; Ballat-Durand et al., 2018; Li et al., 2010) and it explains the reduced macroscopic ductility exhibited by the LFW–AW–PC tensile specimens in Fig.7.4. This information is very interesting because it further highlights that the WCZ and TMAZ are threats for the integrity of the welded structure. Although, precisely locating both the first stages of plastic activity or failure on the welded structure is not possible by observing the ε_{PP} fields. This question is further analysed in Sections 7.3.4 and 7.3.5.

PWHT tensile specimens Unlike the LFW–AW–PC–1 tensile specimen, the ε_{PP} map corresponding to the elastic domain is homogeneous (map 1 in Fig.7.5f). This suggests that the PWHT has successfully homogenized Young's modulus at the former WCZ and TMAZ. The second ε_{PP} map corresponds to the onset of the macroscopic plastic activity. The ε_{PP} field becomes increasingly heterogeneous over the loading history. Both the heterogeneity on the elastic domain and the strain bands on the plastic domain remind of the strain field of the PM–1 tensile specimen. Moreover, no traces of the former WCZ can be detected in terms of strain. On the contrary, strain seems to be lower in the former WCZ, which may be due to the smaller grain size.

7.3.4 Normalized strain rate field and plastic activity tracking for the LFW–AW–PC tensile specimen

In this section, the chronological sequence of plastic activity on the welded structure is studied by the use of normalized strain rate ($\dot{\varepsilon}^{norm}_{PP}$) maps. The $\dot{\varepsilon}^{norm}_{PP}$ is computed by normalizing the instantaneous strain rate ($\dot{\varepsilon}_{PP}$) on a generatrix line with respect to the maximum $\dot{\varepsilon}_{PP}$ found on the entire $\dot{\varepsilon}_{PP}$ field, for a each value of the macroscopic engineering strain. The expression for the computation of the normalized strain rate is written in Eq.7.1. A similar computation of the normalized strain rate has previously been introduced and explained by the authors of the present work in Section 4.3.5.

$$\dot{\varepsilon}^{norm}_{PP}\left(\varepsilon_{macro_i}; P\right) = \frac{\dot{\varepsilon}_{PP}\left(\varepsilon_{macro_i}; P\right)}{\max\left\{\dot{\varepsilon}_{PP}\left(P\,; T\,;\, \varepsilon_{macro_i}\right)\right\}} \tag{7.1}$$

The $\dot{\varepsilon}^{norm}_{PP}$ fields of nine typical instants for the LFW–AW–PC–2 tensile specimen are shown in Figs.7.6a. The frame of reference has been set so that the position of the WCZ is at the 0 coordinate of the P axis. A spatio-temporal graph of the $\dot{\varepsilon}^{norm}_{PP}$ is shown in Fig.7.6b. The nine $\dot{\varepsilon}^{norm}_{PP}$ fields of Fig.7.6a and the $\dot{\varepsilon}^{norm}_{PP}$ spatio-temporal graph of Fig.7.6b share the colour bar exhibited in Fig.7.6a.

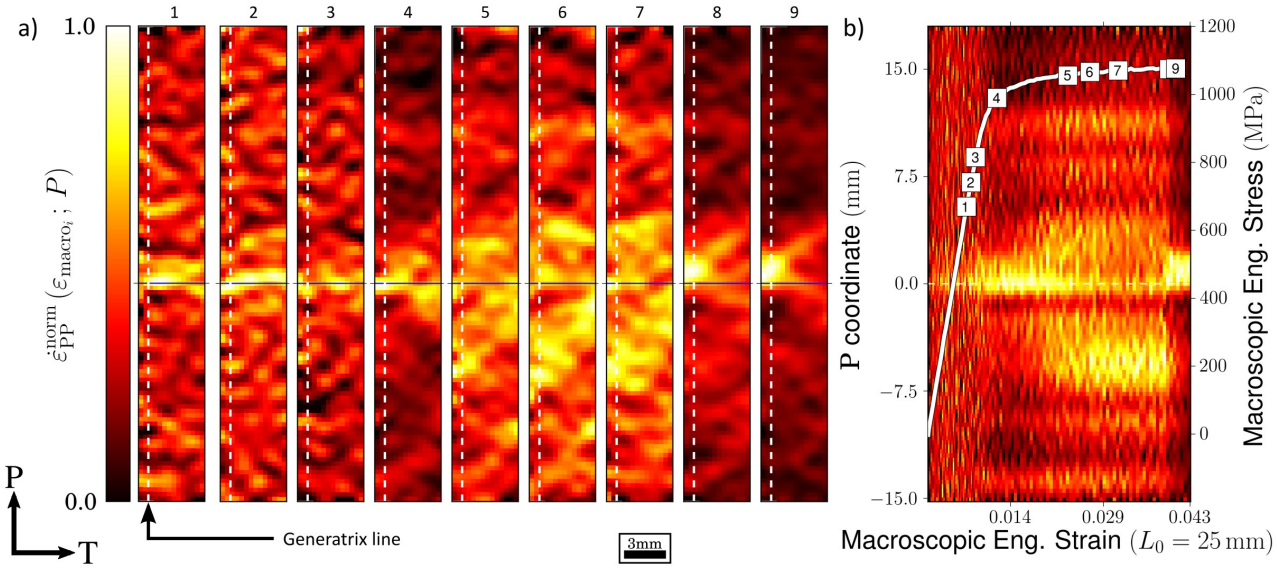

Figure 7.6: a) Surface normalized strain rate field for nine instants on the tensile test curve for the LFW–AW–PC-2 tensile specimen. and b) spatio-temporal graphs of the normalized strain rate over the generatrix line indicated in Fig.7.6a with the overlaid tensile test curve indicating the nine instants of Figs.7.6a-c. The expression for the computation of the normalized strain rate is detailed in Eq.7.1.

The first three $\dot{\varepsilon}^{norm}_{PP}$ maps correspond to the macroscopic elastic domain. The ε_{PP} and $\dot{\varepsilon}^{norm}_{PP}$ fields are

maximum in the vicinity of the WCZ (see Figs.7.6 and 7.5d). The $\dot{\varepsilon}_{PP}^{norm}$ map number 4 correspond to the first map after the onset of macroscopic plastic activity. It should be noticed that, not only is the $\dot{\varepsilon}_{PP}^{norm}$ maximum at the WCZ but also, the ratio between the $\dot{\varepsilon}_{PP}^{norm}$ at the WCZ and the $\dot{\varepsilon}_{PP}^{norm}$ far from it has increased. It seems that the first stage of plastic loading takes place at the WCZ. At the $\dot{\varepsilon}_{PP}^{norm}$ map number 5, the $\dot{\varepsilon}_{PP}^{norm}$ becomes heterogeneous suggesting that the WCZ underwent some hardening inducing a strain increase on the entire gage length. At the UTS (map number 8), localization is observed at the upper TMAZ. It is interesting to see that, despite the initial stages of plastic deformation occur at the WCZ, failure is located at the TMAZ. The failure location is in agreement with the weld undermatching strength previously announced by the local lower microhardness (Ji and Wu, 2014; Dalgaard et al., 2012a; Ballat-Durand et al., 2018; Li et al., 2010) and with the failure location of a dissimilar Ti17-Ti64 LFW joint studied in Chapter 6 and of a similar Ti5553 LFW joint identified elsewhere Dalgaard et al. (2012a).

7.3.5 Strain to failure and failure location

To illustrate further the effectiveness of the PWHT in terms of monotonic behaviour, the failure location and maximum ε_{PP} of all specimens are studied through the strain profiles of Fig.7.7. The horizontal axis of each subplot represents the P coordinate of a generatrix line of the tensile specimens. The frame of reference has been set so that the position of the WCZ is at the 0 coordinate of the P axis. The vertical axis represents the ε_{PP} strain level to failure. The strain profile is depicted in blue for the LFW–AW tensile specimens (Fig.7.7a), in green for the LFW–AW–PC tensile specimens (Fig.7.7b), in gray for PM tensile specimens (Fig.7.7c) and in red for the PWHT tensile specimens (Fig.7.7d). Each specimen is represented with a different level of opacity in every subplot. For each specimen, failure location is indicated with triangles. The grey rectangle in the background of Figs.7.7a-b-d schematically shows the position of the WCZ and the former WCZ.

The maximum ε_{PP} respectively was 18 % and 28 % for the PM and PWHT tensile specimens. The strong scatter in maximum ε_{PP} shown by the PWHT tensile specimens is in agreement with the macroscopic ductility scatter seen in Fig.7.4. The LFW–AW and LFW–AW–PC tensile specimens exhibited maximum ε_{PP} of about 12 %. Failure was located at the weak zone (Ti17 TMAZ). This in agreement with the failure location of several similar $\beta-$metastable titanium alloys LFW joints studied previously (Ji and Wu, 2014; Dalgaard et al., 2012a; Ballat-Durand et al., 2018; Li et al., 2010; García et al., 2019). The most remarkable fact is that, unlike as for the cross-weld tensile specimens, the PWHT tensile specimens never exhibited failure at the former WCZ.

7.3.6 Monotonic loading fracture mechanisms

Fracture mechanisms of PM tensile specimen

A typical fractograph of a PM tensile specimen is shown in Fig.7.8a. The yellow dashed line in Fig.7.8a and the observation of Fig.7.8b highlights a feature with size and morphology similar to the β grains of the PM. Yellow arrows point to secondary cracks that are also observed. The size of flat fracture zones and their orientation resemble grain surfaces. The failure mechanisms seem to be partly intergranular. It seems that intergranular rupture occurred on prior β grains. This phenomenon is also observed and further studied on the fractographic analysis of the cross-weld specimens, later on this Section. Equiaxed and elongated fracture

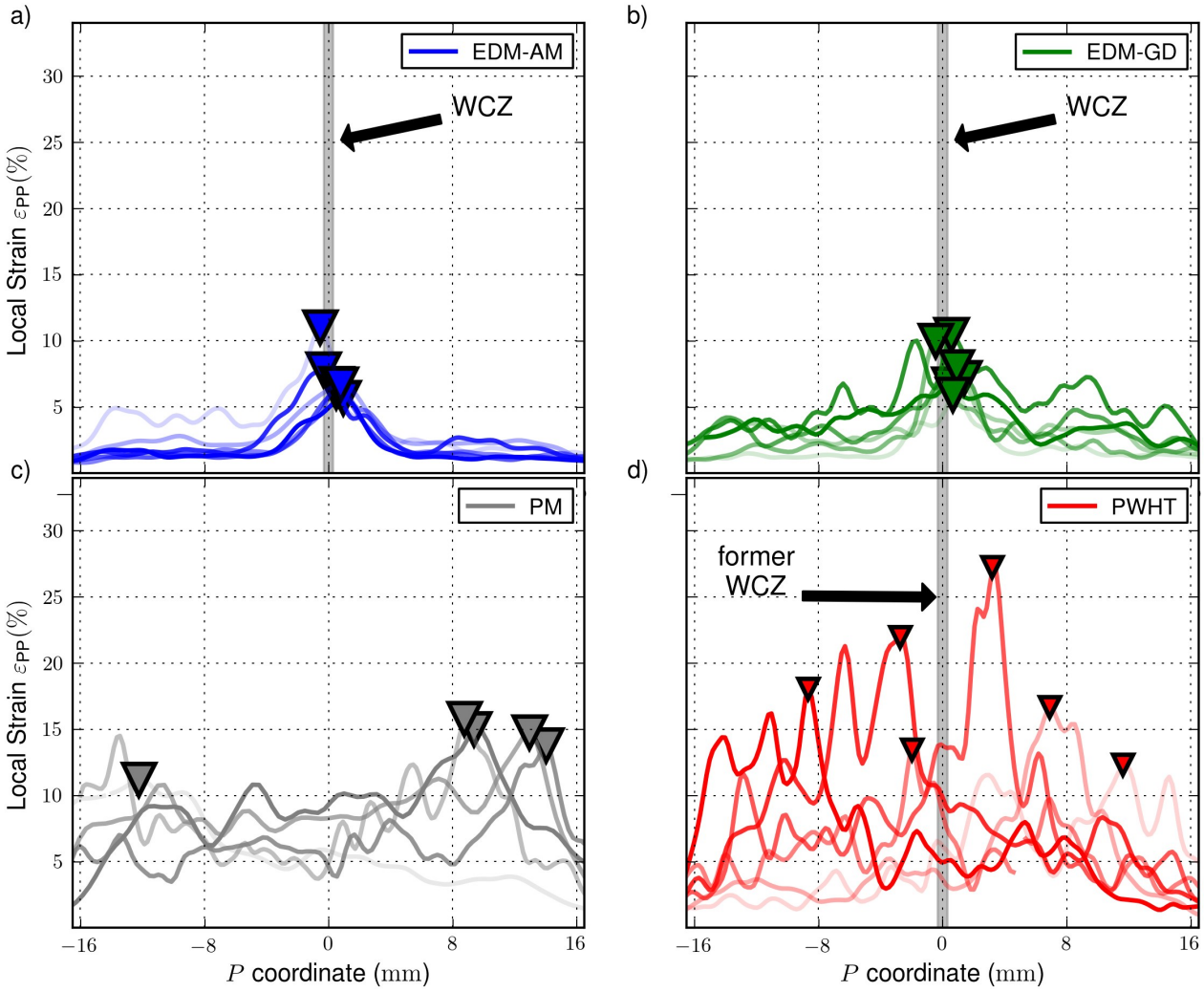

Figure 7.7: Strain profiles to failure over a generatrix line for the a) LFW–AW; b) LFW–AW–PC; c) PM and d) PWHT tensile specimens.

features can be seen. It appears that failure occurred first through intergranular fracture followed by coalescence through transgranular fracture. In Figs.7.8d-e, objects at the β grain boundary that may be linked to the α_{GB} are seen. The topography of the rupture surface is composed of two grain boundary planes forming an acute angle which also suggests a relationship with the underlying grain boundary.

Fracture mechanisms of the LFW–AW–PC tensile specimen

To identify the failure location on the as welded structure in a more accurate manner, *post mortem* observations were performed on the specimen surface. Failure location and both parts of the tensile specimen can be seen in Fig.7.9a. The upper and lower parts of the tensile specimen were observed using respectively BSE and SE detectors. Observations were carried out in the region highlighted in blue as depicted in the schematic drawing of the tensile specimen overlaid in Fig.7.9a.

The yellow arrow on the lower part indicates parallel curvilinear lines that convey the shape of slip bands (see Fig.7.9a). A horizontal region of about 400 µm height is revealed for which the surface roughness resembles the fine equiaxed distorted β grains of the WCZ. At both sides, the α depleted deformed β grains of the TMAZ can be seen. The chemical contrast at the TMAZ-HAZ transition is pointed with a yellow arrow that

highlights the depletion of the α phase from the HAZ to TMAZ with a transparency gradient (see Fig.7.9a). The most remarkable fact is that rupture occurs at the TMAZ close to the frontier with the WCZ. Similar failure locations were found for comparable LFW joints in Section 6.3.3 and elsewhere (Dalgaard et al., 2012a; Wanjara et al., 2014; Li et al., 2010). The green arrow in Fig.7.9a indicates two cracks that have an intersection at a grain boundary. The longer crack seems to be transgranular and parallel to slip bands on the TMAZ β grains suggesting that transgranular rupture mechanisms should be observed on the fracture surface.

The zone depicted by the white rectangle of Fig.7.9a is observed using BSE detector in Fig.7.9b. The red arrow points to the boundary between the WCZ and TMAZ. At the WCZ, the distorted β grains can be seen. In some regions, slip lines cross several grains which is consistent with the existence of microtextured zones that may allow for the deformation along similarly oriented planes, as documented by (Ballat-Durand et al., 2018). In particular, the thicker yellow arrow of Fig.7.9b shows a crack in the WCZ that is parallel to mesoscopic localization bands. Nonetheless, it can be seen that the slip bands are locally oriented for many grains. An example of a WCZ fine equiaxed distorted β grains with locally oriented slip bands is shown in Fig.7.9c. This local orientation phenomenon is not seen on the TMAZ since grains are much bigger at this location. The WCZ-TMAZ boundary effect is highlighted by the fact that slip bands change their direction at this frontier (yellow and blue arrows). There is a high probability to find orientations of small grains that make the slip transfer from the big TMAZ grain to the small WCZ grain difficult and thereby these small grains could increase local dislocation pile-up due to the strong size gradient and the quality of the grain boundary at WCZ-TMAZ frontier.

The fracture mechanisms of the microstructures of both the WCZ and TMAZ can be observed on the

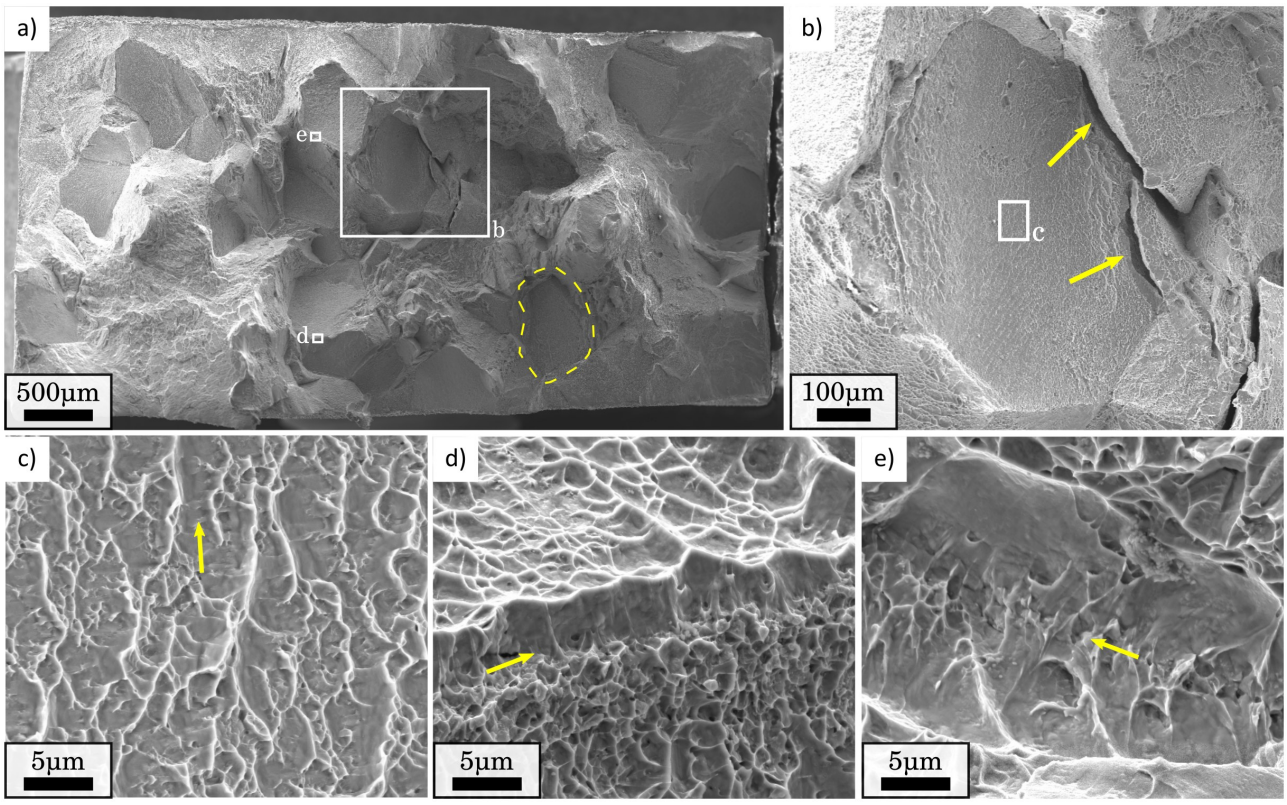

Figure 7.8: Fractograph of a typical PM tensile specimen showing a) the entire surface; b) the intergranular fracture surface of β grain; c) dimples at the the intergranular fracture surface of β grain; d-e) fracture mechanisms at the β grain boundary.

fracture surface of the LFW–AW–PC tensile specimen in Fig.7.10a. The dimples observed in Fig.7.10b exhibit a size of about 10 µm diameter and convey the shape of the WCZ fine equiaxed distorted β grains. As for the PM tensile specimen fracture surface studied earlier on this Section, some features resembling to the prior β grains can be seen (see the yellow dashed lines in Fig.7.10a). In Fig.7.10c, a cluster of elongated fracture features that were also observed on the fracture surface of the tensile, fatigue and fracture toughness specimens that failed at the weak zone (Ti17 TMAZ) of a dissimilar Ti17-Ti64 LFW joint in Section 6.3. Other clusters of elongated fracture features are pointed at by yellow arrows in Fig.7.10a. These clusters were related to the former α phases in the α depleted β grains of the weak zone (Ti17 TMAZ) in Section 6.3. It is worthwhile of being noticed that, in Fig.7.10d, another cluster of elongated fracture features is observed but here, the elongated fracture features are much smaller. This may suggest that, in this observation, the elongated fracture features associated to the former α_{WGB} colonies of β grain. This interpretation seems very likely since the cluster is located close to the border of a feature that conveys the shape of β grain (see yellow dashed line in Fig.7.10a).

In Fig.7.10e and 7.10f, 3D SEM observations of the clusters of elongated fracture features are shown. This observation is very interesting since the elongated fracture features exhibit a very similar morphology to the rhombus-shape voids in Fig.6.17, which may confirm that these elongated feaures are indeed voids at the origin

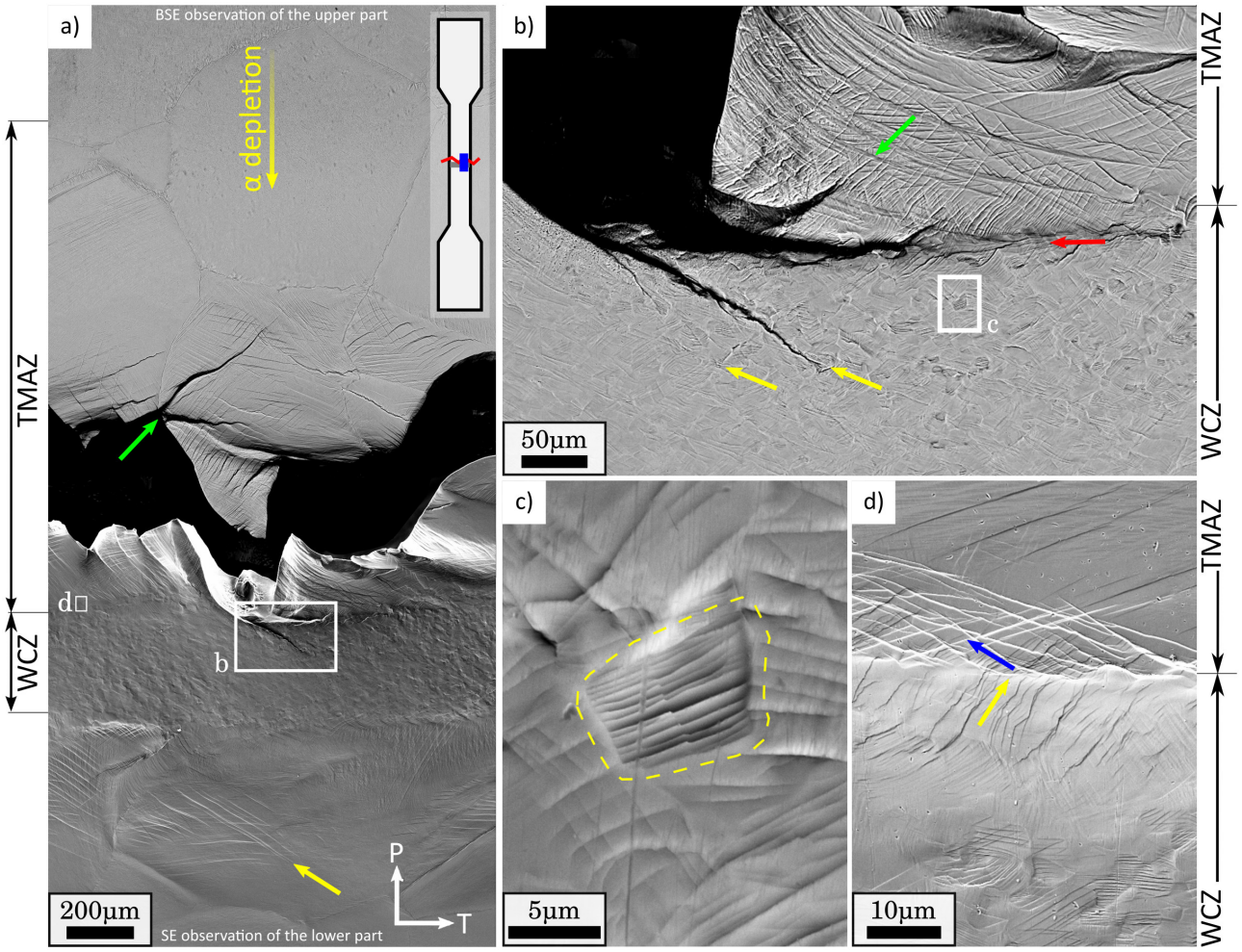

Figure 7.9: *Post-mortem* observations of the LFW–AW–PC tensile specimen surface showing a) the upper and lower parts of the tensile specimen using respectively using BSE and SE detectors; b) WCZ-TMAZ boundary showing slips bands and secondary cracks ; c) a WCZ fine equiaxed distorted β grains showing the locally oriented slip bands, and d) Slip bands at the WCZ-TMAZ boundary.

of a ductile rupture.

Fracture mechanisms of PWHT tensile specimens

Fig.7.11a shows the fractograph of the PWHT–2 tensile specimen. In Fig.7.11b, an elongated feature very similar to the α^{p}_{WI} in the core of β grains is seen. Typical fracture features found on the fracture surface of PWHT–2 tensile specimens are shown in Fig.7.11c-d. For the sake of comparison, features revealed on polished sections of the PM of PWHT samples, having strong similarities with features found on the SEM fractographs, were chosen and observed using BSE detector. For instance, in the observations of Figs.7.11e and 7.11f, the α_{GB} and colonies of α_{WGB} can be seen at a grain boundary. In Figs.7.11c and 7.11d, linearly shaped objects are indicated with yellow arrows that show remarkable similarity with the α_{GB} at the grain boundary (see Figs.7.11a and 7.11c), in terms of morphology, width and length. It seems plausible that these linearly shaped objects are indeed α_{GB} layers at the grain boundary. Furthermore, finer linearly shaped objects are indicated with a green arrow in Fig.7.11b, which convey the shape of α_{WGB} colonies. In Fig.7.11d, a flat surface is indicated with a green arrow, it seems that fracture occurred at the interface of the β matrix and a α_{WGB} platelet having the normal to its surface very close to the normal of the observation plane. The presence of the different kinds of α phases is seen in every fracture mechanism. These findings are in agreement with the coarsening of the α_{GB} layer and the α_{WGB} colonies explained in Section 7.3.1 and the intergranular rupture mechanisms due to coarsening of the α precipitates explained by (Ivasishin et al., 2005).

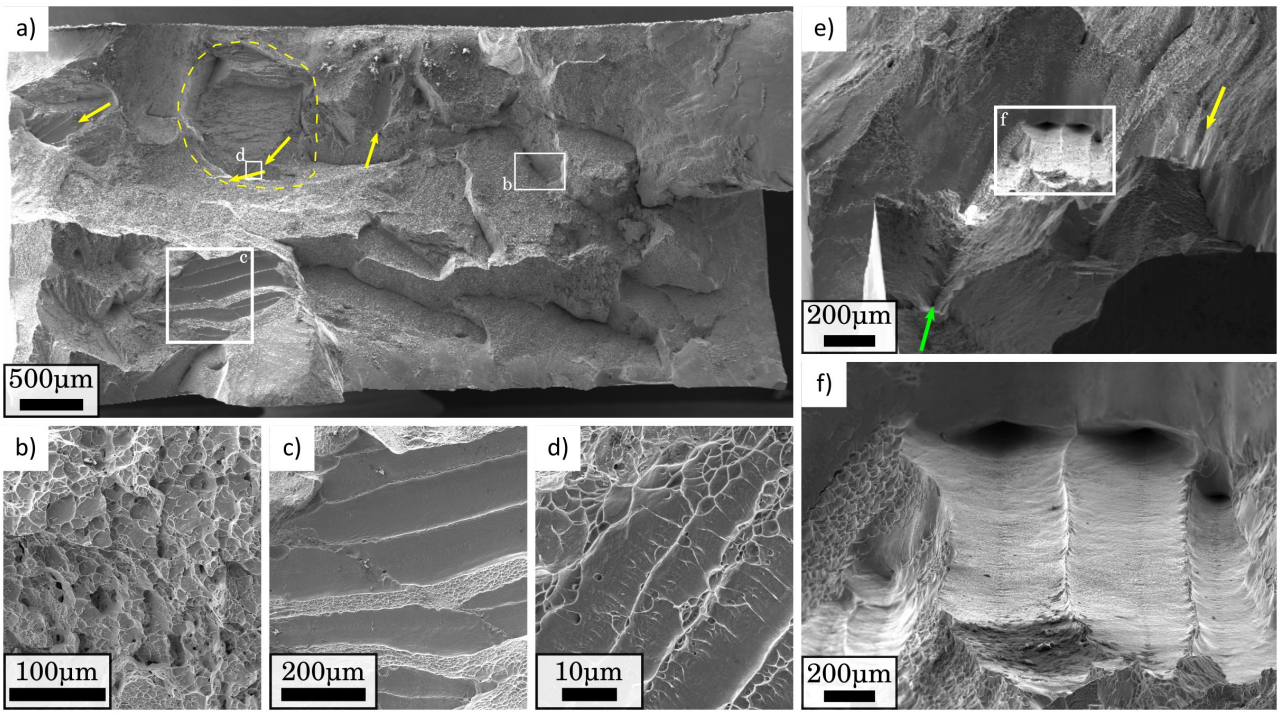

Figure 7.10: Fractographs of a LFW–AW–PC cross-weld tensile specimen showing a) the entire fracture surface; b) equiaxed objects with comparable size to the distorted β grains at the WCZ; elongated dimples with comparable morphology to c) the α_{WI} in the core of β grains and to d) the α_{WGB} colonies at the PM grain boundary –notice the difference in scale between c and d–; e and f) ED fractograph showing elongated dimples.

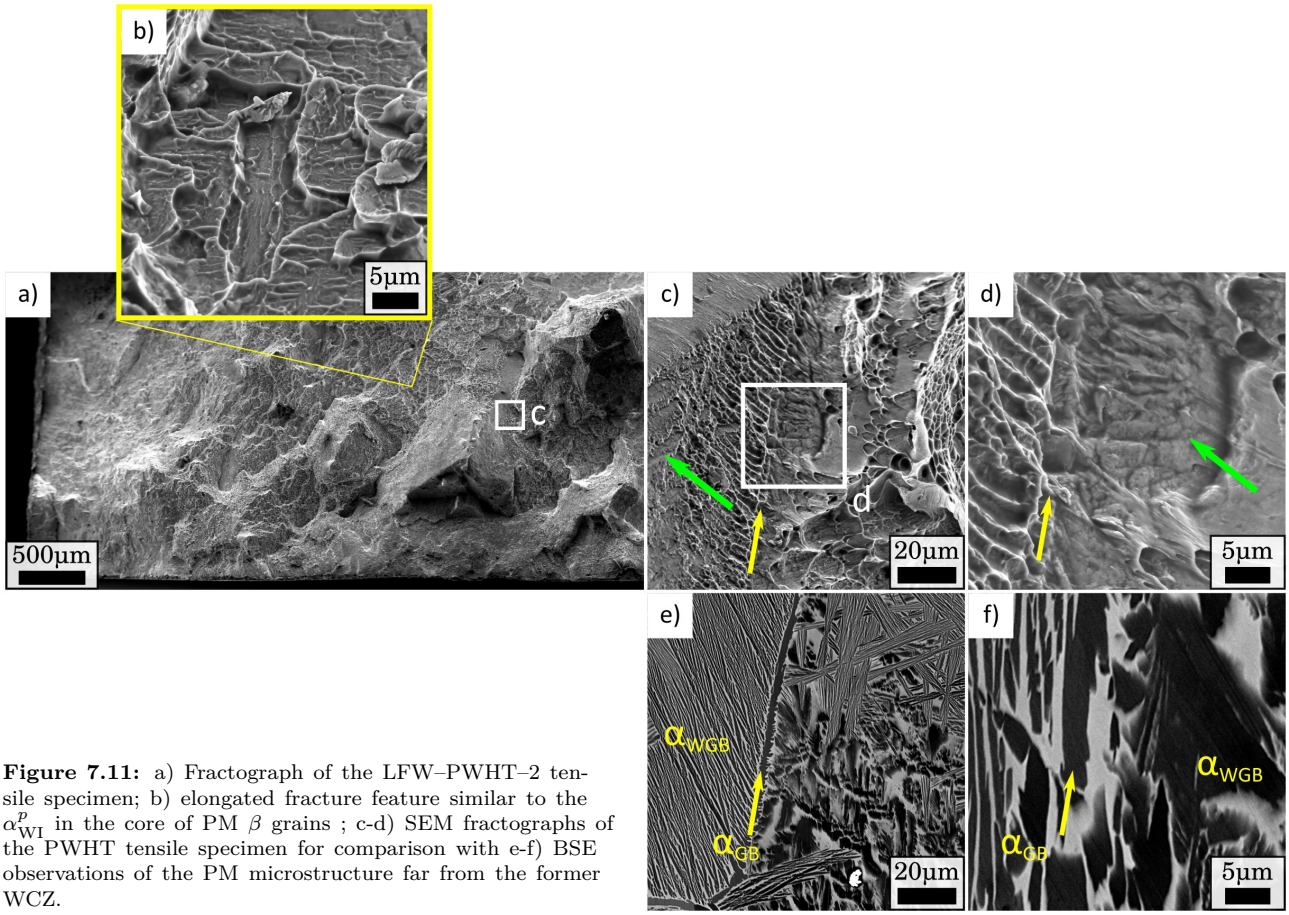

Figure 7.11: a) Fractograph of the LFW–PWHT–2 tensile specimen; b) elongated fracture feature similar to the α^{p}_{WI} in the core of PM β grains ; c-d) SEM fractographs of the PWHT tensile specimen for comparison with e-f) BSE observations of the PM microstructure far from the former WCZ.

7.3.7 Fatigue

Cyclic behaviour

Fig.7.12 shows the the Wöhler curves for the PM fatigue specimens (grey triangles), the LFW–AW fatigue specimens (blue triangles) and the PWHT fatigue specimens (red triangles). For the target life of 10^5 cycles, the fatigue strength was 450 MPa for the LFW–AW fatigue specimens and 720 MPa for both the PM and PWHT fatigue specimens. The Wöhler curves for the PM and LFW–PWHT fatigue specimens are almost the same, having the LFW–PWHT curve a slightly lower slope. This is very desirable and can be explained by the similarity of the LFW–PWHT joint and PM microstructures. The LFW–AW fatigue specimens curve is far from this first two which is consistent with a different microstructure since, as it will be shown in Section 7.3.7, failure took place at the TMAZ. The fatigue crack initiation site for the PWHT fatigue specimens was never on the former WCZ. Given the β grain size, only a few grains are contained on the fatigue specimens thickness as explained in Section 7.2.5. This puts into question the representativity of the fatigue specimen and may explain the observed scatter in fatigue life, since fatigue crack initiation takes place in crystallographic planes and preferential orientations.

PM fatigue specimens fracture mechanisms

A representative fracture surface for PM fatigue specimens is shown in Fig.7.13a. Long fatigue ridges converge to a point on the specimen surface indicated by yellow arrows. Crack initiation occurred in a corner

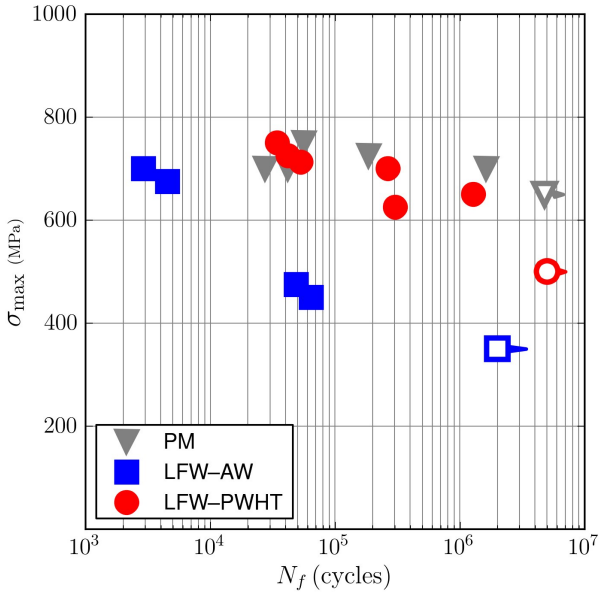

Figure 7.12: Wöhler curves for the PM (gray), LFW–AW (blue) and PWHT (red) fatigue specimens. (R=0.1)

on the α_{GB} layer at a β grain boundary (see Fig.7.13b) which is in accordance with the fractographs registered by (Sauer and Lütjering, 2001; Foltz et al., 2011). Far from the crack initiation site, intergranular rupture on prior β grains highlighted by a yellow dashed line can be observed.

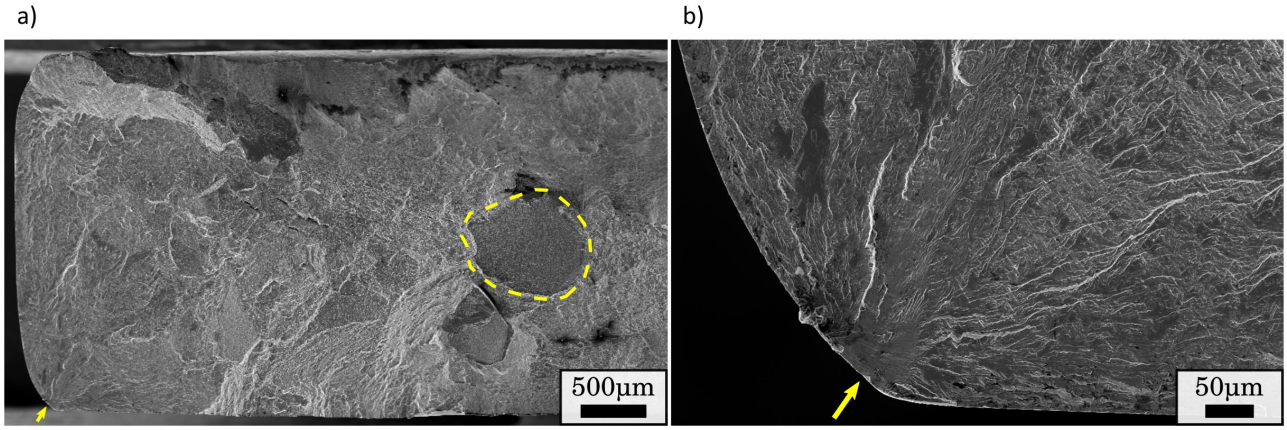

Figure 7.13: Fractograph of a typical PM fatigue specimen showing a) the entire fracture surface and b) the fatigue crack initiation site on a α_{GB} at the grain boundary.

LFW–AW fatigue specimens fracture mechanisms

Two typical fracture surfaces for LFW–AW fatigue specimens are shown in Figs.7.14a-c. Yellow arrows over fatigue ridges point at the fatigue crack initiation sites (see Figs.7.14a, 7.14d and 7.14e). For the fatigue specimen of Fig.7.14c, it seems that fatigue crack initiation took place in two different locations. The primary fatigue crack initiation site could not be identified. The yellow lines in Figs.7.14a, 7.14d and 7.14e points at bands with brighter colours in which the roughness of the fracture surface is slightly different. It seems that fatigue crack initiated at regions formerly covered by α_{GB} at β grain boundaries, for both fatigue specimens. It is worthy of being noticed that, for both specimens, the fatigue ridges exhibit a topology similar to the elongated dimples seen in Fig.7.10c after monotonic loading. The morphology of the fatigue ridges hints to

the *"traces of"* α_{WGB} colonies growing from the grain boundary of β grain at the TMAZ. The green arrows in Figs.7.14a and 7.14c point at planar macroscopic surfaces perpendicular to the loading direction with objects that convey the shape of the fine equiaxed distorted β grains were respectively developed at the WCZ that were also observed in the tensile fractograph of Fig.7.10. Furthermore, the red arrows in Figs.7.10a and 7.10c point to clusters of elongated parallel voids that have already been seen in the tensile fractograph of Fig.7.10c and in the fractographs explained in Sections 6.3.3, 6.3.4 and 6.3.5.

These observations suggest that fatigue crack initiated at a former α_{GB} layer at an α depleted deformed β grains at the TMAZ and propagated through the α_{WGB} colonies into the core of β grains. Propagation occurred

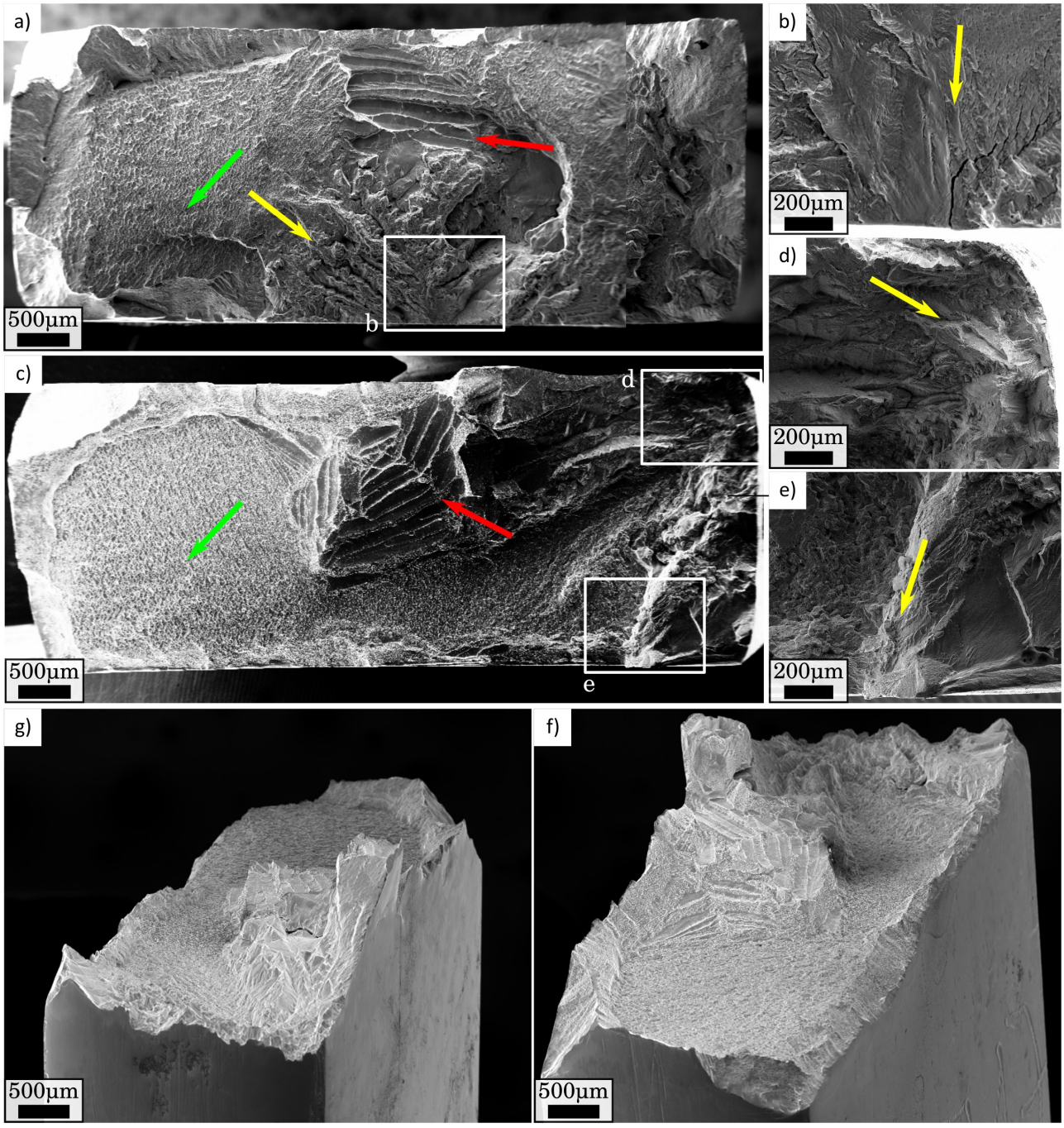

Figure 7.14: Fractographs of a-b) the LFW–AW-1 and c-d-e-f-g) the LFW–AW-2 fatigue specimens. Fatigue specimens life respectively were 0.48×10^5 and 0.64×10^5 cycles. Fatigue crack initiation sites at the specimens surface for b) the LFW–AW-1 and d-e) the LFW–AW-2 fatigue specimens. f-g) 3D SEM fractographs of the LFW–AW fatigue specimen of Fig.7.14c-d-e.

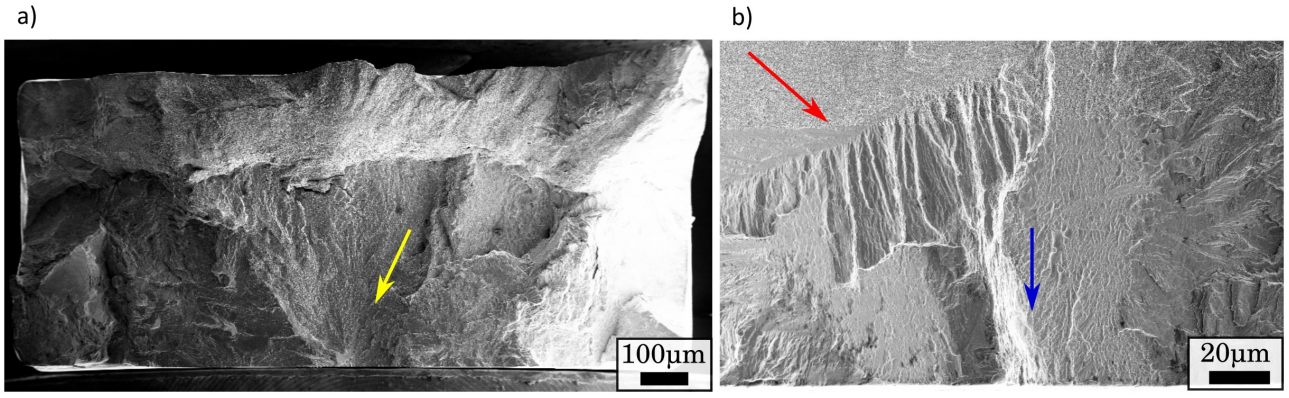

Figure 7.15: Fractographs of a typical PWHT fatigue specimen showing a) the entire fracture surface and b) the fatigue crack initiation site at the specimen surface, notice initiation occurs on a α_{GB} at the grain boundary.

up to the point the stress intensity factor was high enough to lead to a ductile fracture partly at the α depleted deformed β grains at the TMAZ and partly at the fine equiaxed distorted β grains of the WCZ. It is commonly accepted that, during the stage I of fatigue crack propagation, more or less three microstructural entities are involved (Suresh, 1998; Petit and Sarrazin-Baudoux, 2010; Abdesselam et al., 2018). Crystallographic micro-propagation is air has also been found by Herbig et al. (2011). The particularity of these materials is the significant size of the β grains. Thus, it could be imagined that a stage I fatigue crack propagation occurred over the lines highlighted by yellow arrows in Figs.7.14b, 7.14d and 7.14e.

PWHT fatigue specimens fracture mechanisms

The fracture surface of a typical PWHT fatigue specimen is shown in Fig.7.15a. The fatigue ridges converge to a point at the specimen surface indicated with a yellow arrow. In the high magnification observation of Fig.7.15b, the fatigue crack initiation site can be seen. The underlying microstructure at the fatigue crack initiation site may be the α_{GB} layer at a grain boundary (see blue arrow in Fig.7.15b). This would be in accordance with the fatigue crack initiation previously registered for other $\beta-$metastable alloys (Sauer and Lütjering, 2001; Foltz et al., 2011). Damage feature that have strong similarities with the coarsened α_{WGB} colonies can also be seen (red arrow in Fig.7.15b).

7.4 Discussion

Absence of the α phase and weld undermatching strength for welds in the as welded state In the aerospace industry, $\beta-$metastable alloys are often chosen because of their high strength. The key microstructural feature to fulfil this is the presence of the α precipitation, in particular the intergranular α_{WI} (Aeby-Gautier et al., 2011). The LFW–AW and LFW–AW–PC joints studied here exhibited a depletion of the α phase at the WCZ and TMAZ. These microstructures have shown very poor mechanical properties such as lower microhardness (Ji and Wu, 2014; Dalgaard et al., 2012a; Ballat-Durand et al., 2018; Li et al., 2010), lower UTS, an early strain localization at the WCZ and TMAZ during monotonic loading (see Fig.7.5 and Section 6.3.3), failure at the weak zones during monotonic loading (see Fig.7.4a, Section 6.3.3 and (Li et al., 2010; Dalgaard et al., 2012a)), fatigue crack initiation at the weak zones with reduced fatigue strength (see Sections 7.3.7 and 6.3.4), and very poor fracture toughness properties with crack propagating at the weak zones (see Section 6.3.5). These findings provide ample evidence to claim that the depletion of the α phase is undesirable. Thus, it seems logical to state that the similar Ti17 LFW joint is not well suited for high strength applications. Notwithstanding, it should be stated that, despite being a threat for the integrity of the welded structure, the WCZ and TMAZ exhibit some strength, ductility and fatigue strength. Some designers may still advocate the use of LFW for similar Ti17 joints by applying some over-dimensioning. However, this is particularly arguable, since one of the most interesting advantages of LFW is the weight loss.

PWHT Homogenization The PWHT recrystallized the WCZ and TMAZ microstructures into similar but smaller PM grains and favoured the precipitation of the α phase. The cross-weld microhardness profiles became constant and were enhanced up to 97 % with respect to the PM (Ballat-Durand et al., 2018). Unlike the LFW–AW and LFW–AW–PC tensile specimens, the PWHT tensile specimens never failed at the former WCZ or weak zones (see Section 7.3.3). Slight differences were observed in terms of mechanical properties and were attributed to a coarsening of the α phases during PWHT. Despite of this, compared to the PM tensile specimens, the PWHT tensile specimens exhibited a slightly lower UTS, slightly higher ductility, very similar fatigue strength, and similar slope on the S–N curve. By the application of the PWHT, not only were the mechanical properties comparable to the PM (see Sections 7.3.2 and 7.3.7) but also, they were staggeringly better than those of joints in the as welded state.

Improvement of the heat treatment As a general rule, the application of thermal treatments is advisable after machining workpieces made of $\beta-$metastable titanium alloys. In the particular case of similar 17 LFW joints, it is highly required since the depletion of the α phase is a considerable threat. The mechanical properties of the LFW–PWHT joint studied here were clearly superior than those of the as welded LFW joint yet, slightly lower than the PM. Thus, this thermal treatment could be further improved.

A brief qualitative analysis on the effect of the PWHT on the PM has been performed judging that the PWHT PM microstructure was similar to the as received PM microstructure (Ballat-Durand et al., 2018). As it can be seen on the EBSD map of Fig.7.5, the indexation of the β phase is less successful than the others (see Figs.7.5 and 7.5). It could be argued that the surface preparation for this specimen was not adequate. Nevertheless, it should be noticed that the indexation seems to have been successful to a large extent and

that it has allowed the β grains and the former WCZ to be identified. Contrarily, indexation seems to have been unsuccessful particularly there where both the α_{GB} and the α_{WGB} colonies are located, namely the grain boundaries. This is extensively explained in Section 7.3.1.

The heat treatments applied to the PM and the as welded LFW joint differ in one key aspect: The cooling rate after solution treating (see Sections 7.2.1 and 7.2.3). The PM was water quenched after solution treating whilst for the LFW–PWHT joint, temperature was gradually decreased from the solution treating to the ageing temperature in a total time of 2 h. The cooling rate applied to the PM was much higher than the one imposed to the LFW–PWHT joint. Lütjering (1998) have shown that the α_{GB} and the α_{WGB} colonies are developed during cooling after solution treating and that the thickness of the α precipitates increases with decreasing cooling rates. Two conclusions can be drawn from this. First, this reinforces the supposed coarsening of the α_{GB} and α_{WGB} colonies of the LFW–PWHT joint explained in Section 7.3.1 and could also explain the microhardness reduction, the poorer β EBSD indexation, the intergranular rupture during monotonic loading, and the lower UTS that the LFW–PWHT joint showed with respect to the PM. Second, despite the mechanical properties of the LFW–PWHT joint were better that those of the AW joints, the PWHT could still be optimized by increasing the cooling rate after solution treating, namely by air or water quenching. This is specially advised for workpieces having a thickness higher than 20 mm.

Contribution of residual stress to fatigue crack initiation There is a certain agreement in literature about the presence of tensile residual stresses parallel to the P axis at the TMAZ of titanium alloys LFW joints (Frankel et al., 2009; Romero et al., 2009; Xie et al., 2016). The authors of the present work have previously documented an early plastic activity in the vicinity of the WCZ of similar Ti6242 LFW joints that led to fatigue crack initiation during cyclic loading (see Section 4.3.6). Based on the results documented by (Frankel et al., 2009), this early localization was attributed to residual stresses parallel to loading direction. The presence of residual stresses and their relief by PWHT has been previously evidenced through displacement profiles obtained by SDIC over cross-weld samples after EDM machining (Frankel et al., 2009). In a similar manner, (Xie et al., 2016) measured the residual stresses of a dissimilar Ti17(β)-Ti17($\alpha+\beta$) LFW joint by the contour method. They claimed that X-ray diffraction exhibits a low spatial resolution for LFW joints but nevertheless, it served well for comparison and validation of the contour method measurements. It should be pointed out that, for the FEA computation of the welded structure residual stresses, the Young's modulus of the PM was used for the entire cross-welded structure (Xie et al., 2016). This is particularly arguable since, compared to the PM, the WCZ exhibits a significant lower Young's modulus and this may hence have led to an overestimation of the residual stresses. Thus, despite being relatively low, residual stresses surely contributed to the fatigue crack initiation at the TMAZ but unhappily they can not be captured by the normalized strain rate spatio-temporal graph as performed in Section 4.3.5, since the early localizations observed at the WCZ and TMAZ (see Fig.7.6) are also a consequence of their less resistant β microstructure.

Self-cleaning and brass contamination In previous work, the authors have studied the strength and fatigue strength of a similar Ti6242 LFW joint. Despite the overmatching strength, a dendritic defect related to prior to welding brass contamination was at the origin of a shortened fatigue life for a fatigue specimen and implied a strong fatigue life scatter (see Section 4.3.6). In the investigation reported herein, three joints were

performed to study the consequences of prior to welding brass contamination. Two of them were welded in the EDM as machined state (joints LFW–AW and PWHT) and one was ground prior to welding (LFW–AW–PC). During monotonic loading, failure was attributed to pile up dislocations at the TMAZ-WCZ boundary and localization at the TMAZ. During cyclic loading, fatigue crack initiation occurred at the TMAZ, at the coarsen ex α_{GB} layers at the grain boundary. For both monotonic and cyclic loading, the Ti17 TMAZ were the weak zones of the welded structure. No consequences of the potential brass contaminants at the weld interface were observed. The chosen welding parameters may have been accurate to properly self-clean the weld interface. Nevertheless, it could be stated that Ti17 and Ti6242 have different microstructures and physical properties, the interaction between the PM and the brass contaminants on the weld interface during welding may differ. Furthermore, the LFW–PWHT joint was welded in the EDM as machined state and, even after PWHT, the probable brass contaminants at the weld interface may have been a threat and yet, it was not the case.

7.5 Conclusions

In this investigation, the mechanical properties in terms of tensile and fatigue behaviour of as welded and post weld heat treated similar Ti17 LFW joints were studied and compared to the Ti17 parent material. Special interest was drawn on the relationship between the macroscopic properties and the underlying microstructure. In addition, two welds were performed to study the effect of prior to weld contamination on the mechanical properties of as welded similar Ti17 LFW joints. The foremost conclusions with regards to the present findings are:

- In terms of monotonic loading, the PM contained 600 µm diameter β grains and α precipitates and exhibited an UTS of 1066 MPa. Ductile inter and transgranular rupture at the α_{WGB} and along slip planes of the β grains was observed. The strain to failure was of about 0.074 compromised with a significant scatter. The macroscopic strain maps obtained by SDIC highlighted an early localization over a few grains of the coarse microstructure identified by SDIC. For the fatigue life of 10^5 cycles, the fatigue strength was of 720 MPa exhibiting a fatigue crack initiation on the specimen surface.
- The as welded LFW–AW and LFW–AW–PC similar Ti17 joints, containing α depleted β grains at the TMAZ and 10 µm distorted β grains at the WCZ, showed undermatching strength. The UTS was 1044 MPa and the macroscopic engineering strain at fracture measured over a 25 mm basis was reduced to 0.04 and showed considerable scatter. The strain field was heterogeneous and localized at the TMAZ and the WCZ. Normalized strain rate fields showed an early strain activity at the WCZ that later shifted to the TMAZ where failure took place. Local strain to fracture measured by SDIC was also lower than for the PM. Cracking probably initiated at the TMAZ-WCZ frontier. Colonies of elongated dimples were observed at the grain boundary of the α depleted β grains of the TMAZ. For the fatigue life of 10^5 cycles, the fatigue strength was of 450 MPa with a fatigue crack initiation probably located at the former $\alpha_{\mathrm{GB}} + \alpha_{\mathrm{WGB}}$ precipitates at the β grains of the TMAZ on the specimen surface.

- The LFW–PWHT joint recovered a microstructure close to the PM and failed far from the former WCZ. It showed an UTS of 1030 MPa which was attributed to slightly coarser α_{GB} and α_{WGB} colonies with respect to the PM. The ductility was even increased compared to PM and also showed significant scatter in macroscopic engineering strain. As for PM, the strain showed an early heterogeneity and the increased macroscopic strain to fracture was attributed to an increase local strain to fracture as measured by SDIC. In terms of cyclic loading, an excellent fatigue strength of 720 MPa for the fatigue life of 10^5 cycles was found. Compared to the PM, the slope of the SN curve was a slightly lower which was attributed to the slight difference in the microstructure. Fatigue crack initiated far from the former WCZ. Fatigue crack initiation is likely to have occurred at the α_{GB} phases of the β grain boundary. In summary, the proposed heat treatment revealed to be successful to recover mechanical properties that are almost identical to those of the PM.

Acknowledgments

The authors wish to thank *UTC*, *CEMEF, Mines-ParisTech* and Airbus Central R&T for the valuable discussions. ACB is thanked for providing the welds for this study. Anne-Françoise Gourgues-Lorenzon and Henry Proudhon at *Centre des Matériaux* are kindly thanked for the discussions about rupture mechanisms and EBSD analysis. The authors acknowledge the financial support from the French National Research Agency (ANR) and FRAE through OPTIMUM ANR-14-CE27-0017 project.

8

Conclusions

In this Section, instead of reporting the conclusions that have been drawn in each chapter, a conclusion about the major findings of this PhD thesis are presented. The reader is referred to the end of each chapter for detailed conclusions.

Résumé de chapitre

Une discussion des résultats les plus importants de cette thèse, des conclusions et les perspectives de cette thèse sont présentées dans ce chapitre.

Chapter Abstract

A discussion concerning the major findings of this PhD thesis, conclusions and prospects are presented in this Chapter.

Contents

Figures

8.1 Conclusions and prospects

Several welding configurations in terms of materials to be welded, surface preparation and post-weld heat treatment were studied. The capability of the welded structures to withstand high levels of monotonic and cyclic loads as well as their tolerance towards defects was the main interest of this PhD thesis. In a synthetic manner, the S–N curves and the fatigue strength for each configuration and parent material –which have poorly been documented in literature (see Chapter 2)– may give a good overview. Fig.8.2 shows the S–N data of all tests carried out during this PhD work that were in accordance with the ASTM E 466-07 (2007) standard. All weld configurations can be compared by means of the fatigue strength for the fatigue life of 10^5 cycles. Based on this, the weld integrity of each configuration was qualitatively classified between weld comparable to the PM and weak weld (see colour bar in Fig.8.2).

The most critical result is that the dissimilar Ti17-Ti64 weld failed during elastic loading of the first cycle (red squares in Fig.8.2). This result is related to the **self-cleaning mechanism** of LFW, which, for this particular configuration, failed to extrude **contaminants at the weld interface**. As explained in Chapter 6, the creation of a defect layer related to prior to welding contamination led to very poor mechanical properties. This joint was not cleaned prior to welding and, considering its null fatigue life, it is a very weak joint. Similarly, one fatigue specimen of the similar TI6242 LFW joint failed with a very short fatigue life (blue square highlighted in orange in Fig.8.2). It could be argued that this occurred only for one fatigue specimen and that this is not as critical as for the dissimilar Ti17-Ti64 LFW joint. Nevertheless, this specimen introduced showed short fatigue life that would need to be taken into account by designers.

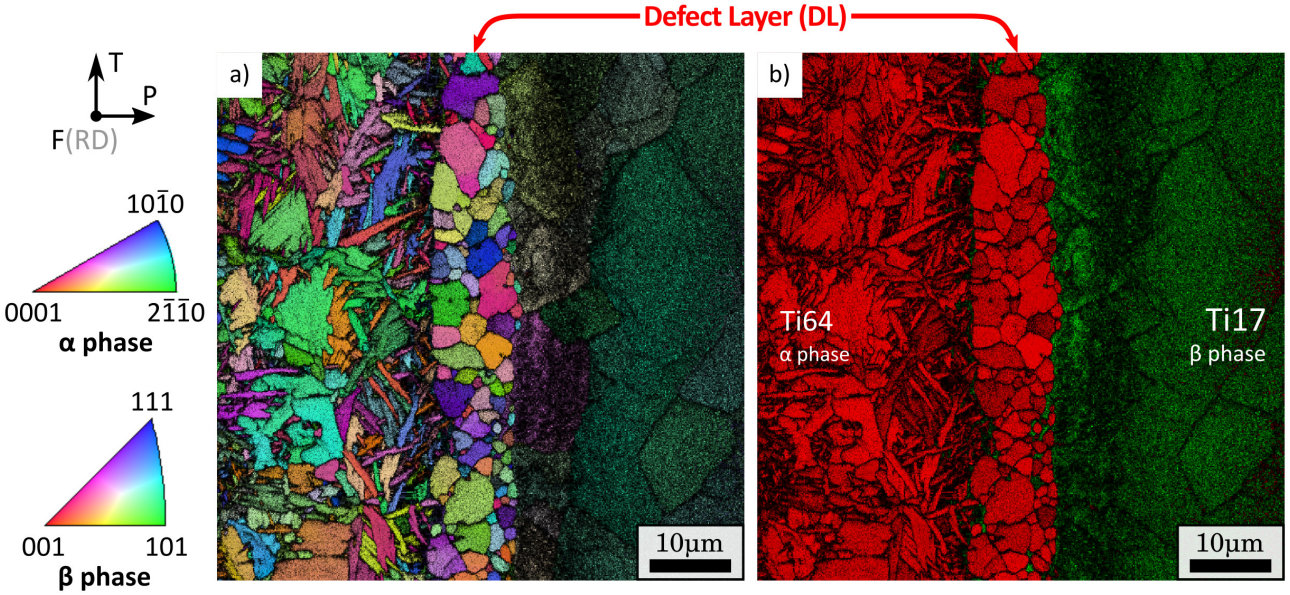

Figure 8.1: a) EBSD inverse pole figure of both α and β phases on the region highlighted by a white transparency rectangle in Fig.6.4a showing the the weld and the DL, and b) phase map respectively showing titanium α and β phases in red and in green. The indexation confidence index is overlaid for both maps.

All contaminated fatigue specimens of the dissimilar Ti17-Ti64 LFW joint failed at one cycle at the defect layer related to prior to welding contamination (see 8.1). Only one fatigue specimen of the similar Ti6242 LFW joint and none fatigue specimen coming from the similar Ti17 LFW joint exhibited problems related to prior to welding contamination (see blue rhombus in Fig.8.2). The self-cleaning mechanism of LFW seems to work

better for similar LFW joints. However, considering these facts, it seems clear that the self-cleaning mechanism is very complex. Nevertheless, it is worthy of being noticed that the fatigue specimens that came from the dissimilar Ti17-Ti64 LFW joint that was pre-cleaned prior to welding exhibited a much better behaviour than the ones that came from the dissimilar Ti17-Ti64 LFW joint that was not pre-cleaned prior to welding. As stated in the Discussion of Chapter 6, the addition of a grinding operation prior to welding in order to clean the surface to be welded and enhancing the self-cleaning mechanism of LFW seems to be a very reasonable and inexpensive practice that increases the reliability of the joint in terms of weld integrity. Likewise, the creation of a standard for LFW for addressing issues such as practices for surface preparation, standardization of tooling, workpieces geometries, among others seems necessary.

The behaviour of the dissimilar Ti17-Ti64 pre-cleaned prior to welding is staggeringly better than the weld with defect layer, although its fatigue strength is still much lower than that of the Ti17 PM. This highlights the second major potential weakness of the weld integrity of LFW joints: **the α depletion at the Ti17 TMAZ**. This weld zone was qualified as a weak zone in Chapter 6 since it led to failure during monotonic loading, cyclic loading and fracture toughness testing. During monotonic loading, for instance, failure at this location occurred abruptly and was associated to a ductile mechanism that exhibited clusters of parallel elongated voids on the fracture surface, as shown in Fig.8.3. Due to the localized nature of this failure event the macroscopically absorbed energy was very limited and thereby was a problem for the structural integrity.

Both macroscopic ductility (see Fig.8.3) and fatigue strength (see Fig.8.2) represent about half of those of the PM specimens. Despite this, one may still advocate the utilization of these welds in the as welded state, by the application of greater security factors. For these reasons, the similar Ti17 and the dissimilar Ti17-Ti64 LFW joints are placed half way the colour bar of Fig.8.2. Similarly, the fatigue specimens of the similar Ti6242 LFW joint failed at the Ti6242 TMAZ but exhibited a slightly reduced fatigue strength.

There is however a major difference between the behaviour of the Ti6242 PM and the similar Ti6242 LFW joint: **the presence of residual stresses**. The normalized strain rate spatio temporal graphs in Chapters 4, 6 and 7 were used to track the location on the welded structure of the instantaneous plastic activity. Fig.8.4 shows the normalized strain rate maps and spatio temporal graph of a similar Ti6242 LFW joint. This joint exhibited an early plastic activity at the TMAZ that later shifted to the PM, far from the WCZ (see Chapter 6), which is consistent with the fatigue crack initiation at this location.

Residual stress relief can be achieved by means of **post weld heat treatments** such as annealing (Xie et al., 2016; Frankel et al., 2009) or solution treatment plus ageing (Ballat-Durand et al., 2018). However, most importantly, the PWHT similar Ti17 LFW joint showed a microstructure and an associated fatigue strength comparable to those of the PM (see Fig.8.2). This highlights that LFW joints may show an excellent fatigue behaviour if no contamination problems are encountered and if the microstructure is recovered by a heat treatment. It is thus highly advisable to perform post weld heat treatments before putting in service linear friction welded structures.

As a global observation, it is quite interesting how cyclic loading always led to fatigue crack initiation at the weakest point of the cross-welded structure, even for the joints that exhibited a weld-overmatch. It is then reasonable to conclude that the study of the integrity of linear friction welded structures imperatively requires the study of the cyclic behaviour.

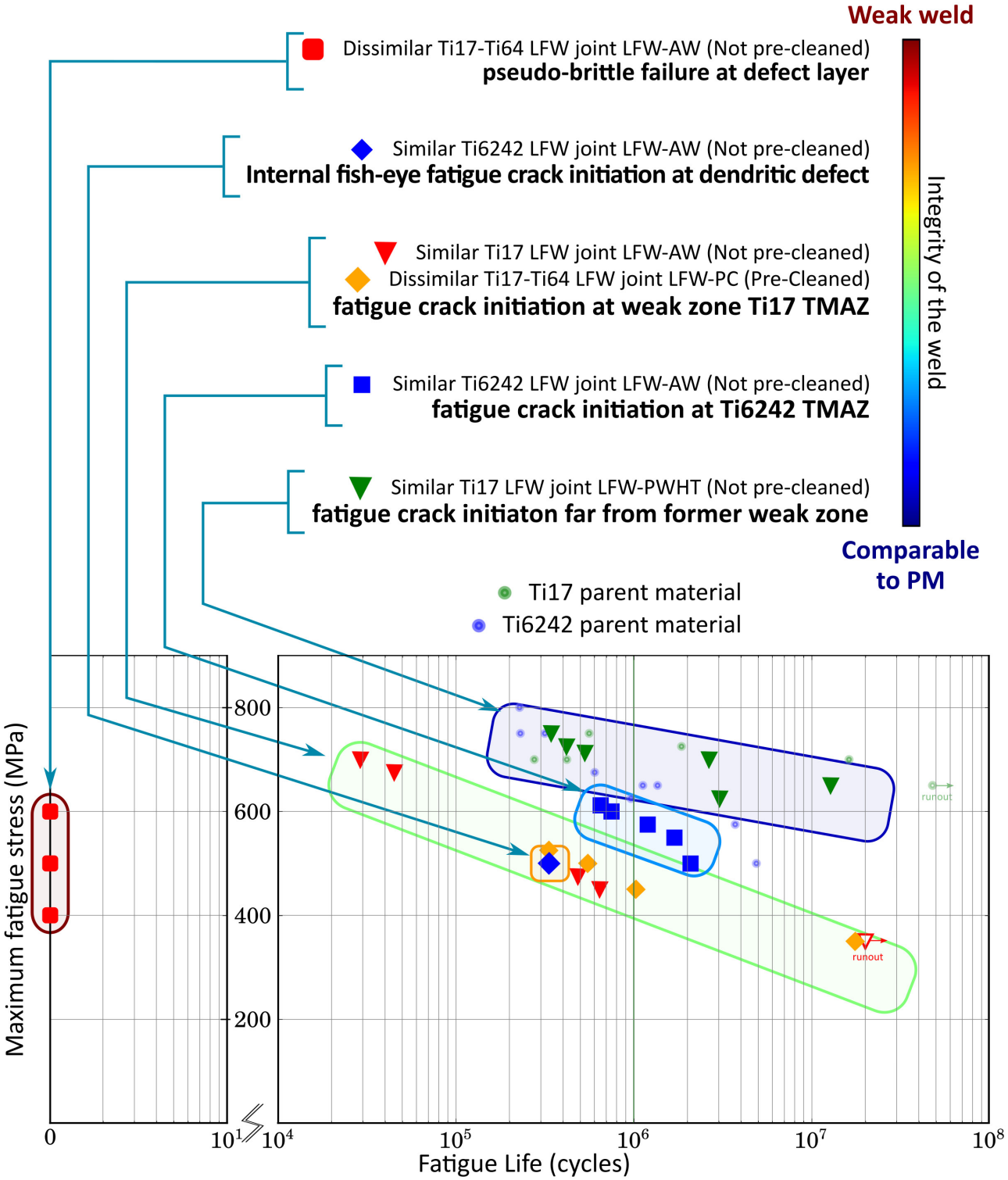

Figure 8.2: S–N curves for smooth specimens for all studied configurations. R= 0.1.

8.2 Prospects

8.2.1 Mechanical characterization

Comparable studies of LFW joints made of Ti17-Ti6242 or Nickel-based superalloys seem necessary. Concerning the damage mechanisms, a tomography damage study of the Ti17 and Ti6242 PM's using less severe

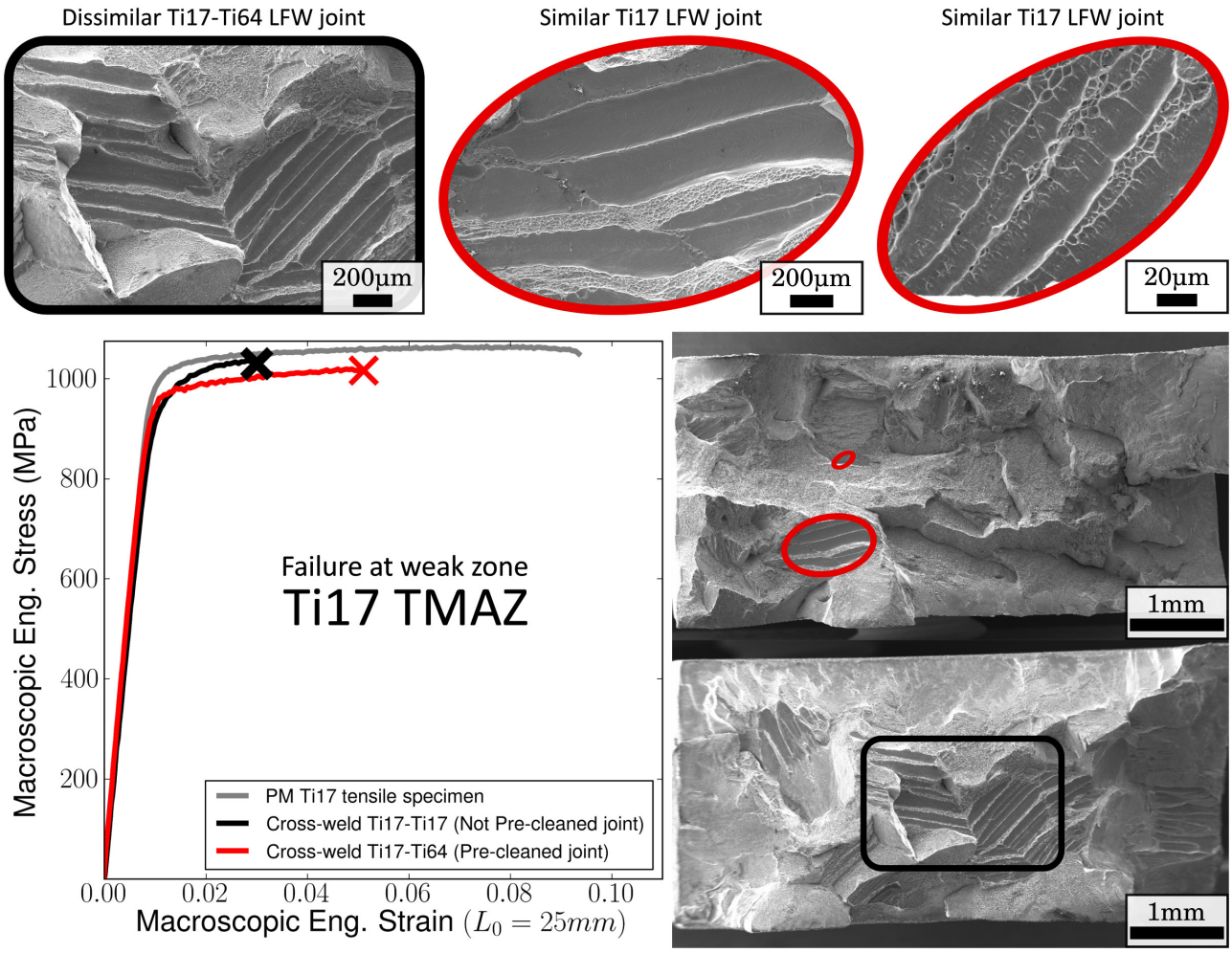

Figure 8.3: Tensile test for a Ti17 PM (gray line), a cross-weld tensile specimen of a similar Ti17 LFW joint (black line) and a cross-weld tensile specimen of a dissimilar Ti17-Ti64 LFW joint (red line). Fracture surfaces for both cross-weld tensile specimens highlighting clusters of parallel elongated fracture dimples.

notches should be interesting. In the case of LFW joints, a more detailed study on the origin and nucleation of the clusters of parallel voids in the Ti17 TMAZ seems relevant.

A sound study of the residual stresses seems necessary as well as a better understanding of their role in fatigue crack initiation. Concerning the cyclic behaviour, it would be interesting to obtain more detailed information in terms of microstructure for the fatigue crack initiation of the similar Ti17 TMAZ LFW joint in the as welded condition. There are still several other unexplored domains concerning the cyclic behaviour of linear friction welded structures. For instance, the behaviour under dwell fatigue or fatigue crack propagation rates as a function of the initial positioning of the notch in the welded structure. Similarly, it would also be interesting to study the fracture toughness of each weld zone.

Titanium alloys such as Ti64 and Ti6242 are known for their tensile strength at **high temperature**. LFW is used mostly for "blisks", in which the blades work under creep loading. No studies were found to this matter that seems primary for the mechanical characterization of LFW structures.

In Chapter 5, a first measurement of the local strain for the WCZ was achieved through tomographic and optical observations. A better characterization of the local strain could be achieved by performing SEM *in situ* micro-tensile tests and using SEM/BSE observations for digital image correlation.

In this PhD thesis, it has been advised to apply post weld heat treatments to enhance the development of

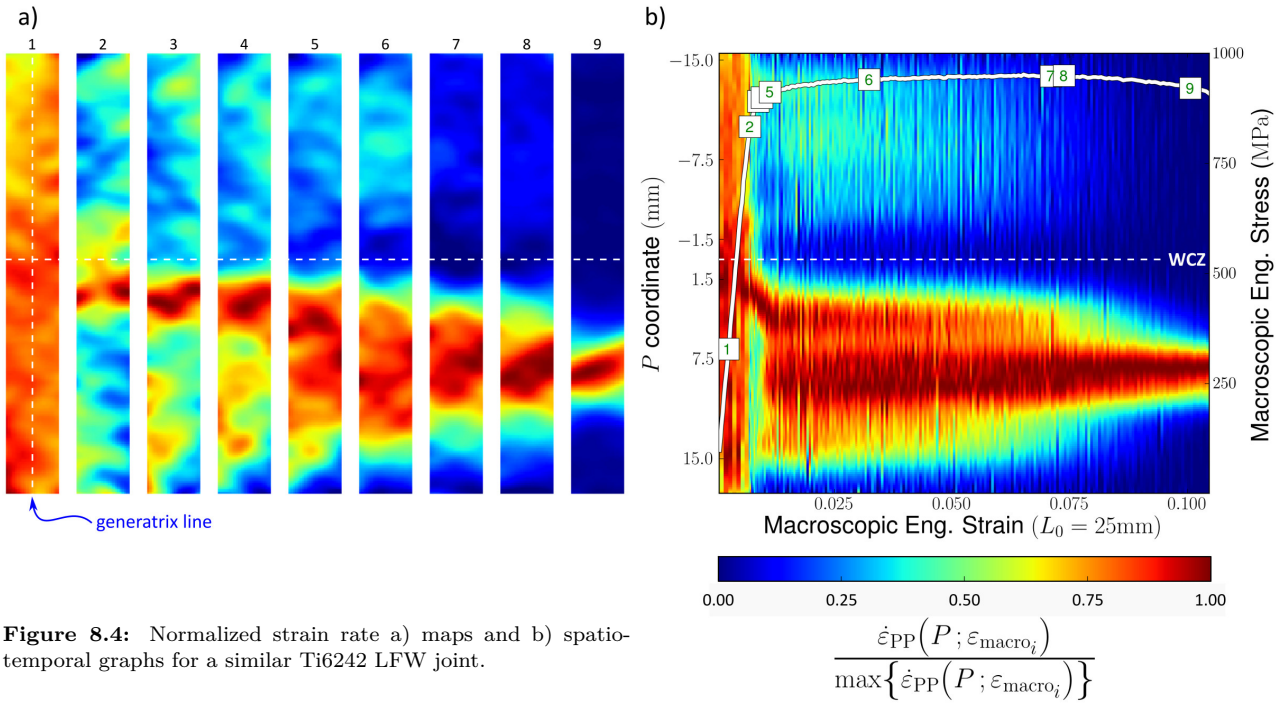

Figure 8.4: Normalized strain rate a) maps and b) spatio-temporal graphs for a similar Ti6242 LFW joint.

the PM's microstructure. It would very interesting to study fatigue crack propagation in terms of the fatigue crack propagation rate and crack path of a PWHTed joint using CT specimens having the notch centred with respect to the interface.

8.2.2 Numerical studies

In Chapters 4 and 6, based on the results of Frankel et al. (2009) and Romero et al. (2009), the early plastic activity observed in the vicinity of the WCZ was attributed to the presence of residual stresses. An interesting way of reinforcing this hypothesis would be by performing simulations of the welding process to obtain a joint containing residual stresses. Thereafter, a numerical tensile specimen containing residual stresses should be virtually machined. Finally, a numerical tensile test should be performed for generating a numerical spatio temporal graph of the normalized strain rate (Fig.8.4). Comparing the numerical and experimental normalized strain rate spatio temporal graph could clarify this matter.

Despite it was advised to perform post weld heat treatments, valuable information has been gathered in this PhD thesis for carrying out an inverse analysis to perform a **constitutive law identification** of the welded zones of the LFW joints in the as welded state using the macroscopic smooth tensile specimens and the notched micro-tensile specimens.

Abstract

English version

The mechanical properties in terms of tensile behaviour, fatigue strength and toughness of Linear Friction Welded (LFW) Titanium (Ti) alloys were studied and compared to the parent materials' (PM) behaviour. LFW is a solid state joining process that could be used for assembling heavily loaded structures in the aerospace industry. Since the Weld Centre Zone (WCZ) of a similar Ti6242 LFW joint exhibited overmatching strength, its fracture mechanisms and ductility were investigated by micro-tensile tests using notched specimens. They revealed some ductility and a mixture of brittle and ductile fracture mechanisms. Local strain and normalized strain rate fields on smooth samples were assessed by Stereo Digital Image Correlation (SDIC) and showed an early plastic activity at yielding in the vicinity of the WCZ, attributed to residual stresses. For the target life of 10^5 cycles, the fatigue strength was slightly reduced but compromised by a strong scatter that was related to prior to welding contamination. The LFW self-cleaning mechanism also failed to extrude the contaminants at the weld interface of a dissimilar Ti17-Ti64 LFW joint that led to pseudo-brittle fracture at a defect layer in the WCZ. For a pre-cleaned dissimilar Ti17-Ti64 LFW joint, ductile rupture was observed sometimes at the Ti64 PM and sometimes at the Ti17 thermo-mechanically affected zone (TMAZ), due to a depletion of the strengthening α phase. Fatigue cracks initiated at the weak Ti17 TMAZ with a reduced fatigue strength compared to the PM. Fracture toughness was significantly reduced and the fracture surface at the TMAZ highlighted unexpected clusters of parallel and elongated voids. These trends were also observed for a similar Ti17 LFW joint. Comparable mechanical properties to those of the Ti17 PM were successfully regained by means of a post-weld heat treatment.

Version en français

Les propriétés mécaniques en termes de comportement monotone, résistance en fatigue et ténacité d'alliages de titane soudés par friction linéaire ont été étudiées et comparées à celles des matériaux de base. Le soudage par friction linéaire est un procédé de soudage à l'état solide qui pourrait être utilisé dans l'industrie aéronautique pour assembler des structures fortement chargées. Étant donné que le noyau de soudure du joint mono-matériau Ti6242 a montré une résistance mécanique supérieure à celle du matériau de base, ses propriétés mécaniques

ont été étudiées en utilisant des éprouvettes entaillées. Elles ont montré une certaine ductilité et une rupture mixte entre des mécanismes ductiles et fragiles. Les champs de déformation locale et de vitesse de déformation normalisée ont été étudiées sur des éprouvettes lisses. Une activité plastique précoce a été observée dans le voisinage du noyau de la soudure et elle a été attribuée aux contraintes résiduelles. Pour la durée de vie visée de 10^5 cycles, la résistance en fatigue a légèrement été réduite mais compromise avec une forte dispersion de la durée de vie reliée à la contamination avant soudage. Le mécanisme auto-nettoyant n'a pas réussi à extruder les contaminants à l'interface d'un joint bi-matériaux Ti17-TA6V et a mené à une rupture fragile au niveau d'une couche de défauts. Pour un joint bi-matériaux Ti17-TA6V nettoyé avant soudage, une rupture ductile a été observée tantôt au niveau du matériau de base TA6V tantôt au niveau de la zone thermo-mécaniquement affectée (TMAZ) côté Ti17, due à un épuisement de la phase durcissante alpha. L'amorce des fissures de fatigue a eu lieu au niveau de la TMAZ Ti17 avec une résistance en fatigue réduite. La ténacité a également été dégradée et le faciès de rupture au niveau de la TMAZ a dévoilé des clusters de cavités allongées et parallèles. Ces tendances ont été observées pour un joint mono-matériau Ti17. Un traitement thermique post soudage a permis de retrouver avec succès des propriétés proches de celles du MB.

A

Computation of stiffness correction factors for fatigue specimens using Castigliano's method

In this appendix, the integral of Eq. 3.2 is solved for the CS beam and the CR and TF fatigue specimens. For all the specimens, the thickness is t, the width of the minimal cross-section is W and the beam span is L_t. The CR and TF fatigue specimens have circular transition zones of radius R which were approximated using first degree polynomials in first instance and finally, using second degree polynomials.

A.1 Bending stiffness of the CS beam

The bending moment in Eq.3.1 and its derivative with respect to the reaction force in the clamps for the CS beam are written in Eqs.A.1.

$$M(x) = F\ (x - L_t/2) \qquad \frac{\partial M}{\partial F} = (x - L_t/2) \tag{A.1}$$

The geometry of the CS beam is shown in Fig.3.1c and can be defined with three parameters: W, the width of the gage length; L_t, the beam span and t, the beam thickness. The cross-section moment of inertia is a constant defined by $I = Wt^3/12$.

Castigliano (1873)'s method is applied by computing the integral of Eq.3.2.

$$\frac{\delta_F}{2} = \int_0^{L_t/2} \frac{M(x)}{E\,I_z(x)} \frac{\partial M}{\partial F} dx = \int_0^{L_t/2} \frac{12F\,(x - L_t/2)^2}{EWt^3} dx = \frac{12F}{EWt^3} \left[\frac{(x - L_t/2)^3}{3} \Bigg|_0^{L_t/2} \right]$$

Finally, the bending form of Hooke's for the CS can be written as stated in Eq.A.2

$$F = \frac{EWt^3}{L_t^3}\,\delta_F \tag{A.2}$$

A.2 Bending stiffness of the TF fatigue specimen

The geometry of the TF fatigue specimen is shown in Fig.3.1a and can be defined with 7 parameters: W, the width of the gage length; L, the length of the uniform test section; C, the width of the ends; R, the radius

of the fillet; b, the distance between the grips; D, the length of the transition zone and the transition zone and t, the specimen thickness (see Fig.3.1a). Two different zones can be distinguished: the heads with a constant width and the test zone with a variable width. The cross-section moment of inertia is defined by piecewise functions in Sections A.2.1 and A.2.2.

A.2.1 Linear approximation of the TF fatigue specimen transition zones.

The bending moment in Eq.3.1 and its derivative with respect to the reaction force in the clamps for the TF fatigue specimen are written in Eqs.A.3. For the sake of simplicity, the distance to the gripped zones is considered to be $b = 0$.

$$M(x) = F\ (x - L_t/2) \qquad \frac{\partial M}{\partial F} = (x - L_t/2) \qquad L_t = (2k_2 + 1)\,L \tag{A.3}$$

If the transition zones of the TF fatigue specimen are approximated using first degree polynomials, the geometry of the specimen can be described by the dimensionless geometric factors $k_1 = C/W$ and $k_2 = D/L$ (see Fig.3.6a), as explained in Section 3.3. The moment of inertia written as a piecewise function with the geometrical parameters k_1 and k_2 can be seen in Eq.A.4.

$$I_z(x) = \frac{W\,t^3}{12}\begin{cases} \frac{(1-k_1)}{k_2\,L}\,x + k_1 & \text{if } 0 < x < k_2\,L \\ 1 & \text{if } k_2\,L < x < (k_2 + 1/2)\,L \end{cases} \tag{A.4}$$

Castigliano (1873)'s method is applied by computing the integral of Eq.3.2.

$$\frac{\delta_F}{2} = \frac{12F}{E\,W\,t^3}\int_0^{k_2 L} \frac{(x - (k_2 + 1/2)L)^2}{\left[\frac{(1-k_1)}{k_2 L}\,x + k_1\right]}dx + \frac{12F}{E\,W\,t^3}\int_{k_2 L}^{(k_2+1/2)L} [x - (k_2 + 1/2)L]^2\,dx$$

$$\frac{E\,W\,t^3\,\delta_F}{24\,F} = \int_0^{k_2 L} \frac{[x - (k_2 + 1/2)L]^2}{\left[\frac{(1-k_1)}{k_2 L}\,x + k_1\right]}dx + \int_{k_2 L}^{(k_2+1/2)L} [x - (k_2 + 1/2)L]^2\,dx$$

The primitive of the first integrand takes two forms depending of the value of k_1. If $k_1 = 1$, the TF specimen becomes the CS beam and its bending stiffness can be computed as described in the Appendix A.1. The primitive of the integrand when $k_1 \neq 1$ can be found by introducing variables α, β and γ.

$$\alpha = (k_2 + 1/2)L \qquad \beta = \frac{(1 - k_1)}{k_2\,L} \qquad \gamma = k_1$$

$$\frac{E\,W\,t^3\,\delta_F}{24\,F} = \int_0^{k_2 L} \frac{(x - \alpha)^2}{(\beta\,x + \gamma)}dx + \int_{k_2 L}^{(k_2+1/2)L} (x - \alpha)^2\,dx$$

$$\frac{E\,W\,t^3\,\delta_F}{24\,F} = \left[\frac{x^2}{2\,B} - \frac{x\,(2\,A\,B + C)}{B^2} + \frac{(A\,B + C)^2}{B^3}\,\ln(B\,x + C)\Big|_0^{k_2 L}\right] + \left[\frac{(x - A)^3}{3}\Big|_{k_2 L}^{(k_2+1/2)\,L}\right]$$

$$\frac{E\,W\,t^3}{L^3}\frac{\delta_F}{F} = \frac{12\,k_2^3}{(1-k_1)^3}\left[(1-k_1)^2 - 2(1-k_1)\left(2\,\frac{(k_2+1/2)(1-k_1)}{k_2}+k_1\right)+ 2\left(\frac{(k_2+1/2)(1-k_1)}{k_2}+k_1\right)^2\ln\left(\frac{1}{k_1}\right)\right]+1$$

The variable L is the length of the gage length. Let the previous equation be written as function of the span of the specimen.

$$L_t = (2k_2+1)\,L$$

$$\frac{E\,W\,t^3}{L_t^3}\frac{\delta_F}{F} = \left\{\frac{12\,k_2^3}{(1-k_1)^3}\left[(1-k_1)^2 - 2(1-k_1)\left(2\,\frac{(k_2+1/2)(1-k_1)}{k_2}+k_1\right)+ 2\left(\frac{(k_2+1/2)(1-k_1)}{k_2}+k_1\right)^2\ln\left(\frac{1}{k_1}\right)\right]+1\right\} : (2k_2+1)^3$$

The second term of the previous equality represents the inverse of the stiffness correction of TF fatigue specimen computed using first degree polynomial approximations for the transition zones. Let the bending form of Hooke's law be written as:

$$F = m_{\mathrm{TF}}\frac{EWt^3}{L_t^3}\delta_F$$

Having:

$$m_{\mathrm{TF}} = (2k_2+1)^3 : \left\{\frac{12\,k_2^3}{(1-k_1)^3}\left[(1-k_1)^2 - 2(1-k_1)\left(2\,\frac{(k_2+1/2)(1-k_1)}{k_2}+k_1\right)+ 2\left(\frac{(k_2+1/2)(1-k_1)}{k_2}+k_1\right)^2\ln\left(\frac{1}{k_1}\right)\right]+1\right\} \tag{A.5}$$

The stiffness correction factor m_{TF} is a function of the dimensionless geometrical factors k_1 and k_2 and its value can be read from the abacus of Fig.3.6b.

A.2.2 Parabolic approximation of the TF fatigue specimen transition zones.

The bending moment (Eq.3.1) and its derivative with respect to the reaction force in the clamps are written in Eqs.A.6.

$$M(x) = F\ (x - L_t/2) \qquad \frac{\partial M}{\partial F} = (x - L_t/2) \qquad L_t/2 = (b + D + L/2) \tag{A.6}$$

By writing the transition zones of the TF fatigue specimen as second degree polynomials, the area moment of inertia of the TF fatigue specimen can be written as stated in Eq.A.7.

$$I_z(x) = \frac{t^3}{12}\begin{cases} C & \text{if } 0 < x < b \\ \frac{[x-(b+D)]^2}{R} + W & \text{if } b < x < b+D \\ W & \text{if } b < x < b+D+L/2 \end{cases} \tag{A.7}$$

Castigliano (1873)'s method is applied by computing the integral of Eq.3.2.

$$\frac{\delta_F}{2} = \frac{12F}{E\,t^3}\left[\int_0^b \frac{(x-L_t/2)^2}{C}dx + \int_b^{b+D} \frac{(x-L_t/2)^2}{\frac{[x-(b+D)]^2}{R}+W}dx + \int_{b+D}^{b+D+L/2} \frac{(x-L_t/2)^2}{W}dx\right]$$

Multiplying both sides by a factor of $\frac{Et^3W}{12FL_t^3}$

$$\begin{aligned}\frac{EWt^3\,\delta_F}{24FL_t^3} =& \left[\frac{W}{CL_t^3}\int_0^b (x-L_t/2)^2\,dx + \frac{RW}{L_t^3}\int_b^{b+D} \frac{(x-L_t/2)^2}{[x-(b+D)]^2+RW}dx\right. \\ &\left. + \frac{1}{L_t^3}\int_{b+D}^{b+D+L/2} (x-L_t/2)^2\,dx\right]\end{aligned} \tag{A.8}$$

Introducing α, β and γ variables for simplifying integration of the second term:

$$\alpha = \frac{L_t}{2} \qquad \beta = b+D = \frac{L_t - L}{2} \qquad \gamma = RW$$

$$\begin{aligned}\frac{RW}{L_t^3}\int_b^{b+D} \frac{(x-L_t/2)^2}{[x-(b+D)]^2+RW}dx =& \frac{\left[\gamma-(\alpha-\beta)^2\right]}{\sqrt{\gamma}}\tan^{-1}\left(\frac{\beta-x}{\sqrt{x}}\right) - \\ &(\alpha-\beta)\log\left((\beta-x)^2+\gamma\right) + x\end{aligned} \tag{A.9}$$

Having $b = \frac{L_t-2D-L}{2}$

$$\begin{aligned}\frac{EWt^3\,\delta_F}{FL_t^3} =& \frac{8W}{CL_t^3}\left[\left(\frac{L_t}{2}\right)^3 - \left(D+\frac{L}{2}\right)^3\right] - \frac{24RW}{L_t^3}\left[\frac{L}{2}\ln\left(\frac{RW}{D^2+RW}\right)\right. \\ &\left. - \frac{(L^2-4RW)}{4\sqrt{RW}}\tan^{-1}\left(\frac{D}{\sqrt{RW}}\right) - D\right] + \frac{L^3}{L_t^3}\end{aligned} \tag{A.10}$$

The second term of the previous equality represents the inverse of the stiffness correction of TF fatigue specimen computed using second degree polynomial approximations for the transition zones. Let the bending form of Hooke's law be written as :

$$F = m_{\text{TF}}\frac{EWt^3}{L_t^3}\delta_F$$

Having:

$$m_{\mathrm{TF}} = \left\{ \frac{8W}{CL_t^3}\left[\left(\frac{L_t}{2}\right)^3 - \left(D+\frac{L}{2}\right)^3\right] - \frac{24RW}{L_t^3}\left[\frac{L}{2}\ln\left(\frac{RW}{D^2+RW}\right) - \frac{\left(L^2-4RW\right)}{4\sqrt{RW}}\tan^{-1}\left(\frac{D}{\sqrt{RW}}\right) - D\right] + \frac{L^3}{L_t^3}\right\}^{-1} \tag{A.11}$$

A.3 Bending stiffness of the CR fatigue specimen

The geometry of the CR fatigue specimen is shown in Fig.3.1b and can be defined with 6 parameters: W, the width of the gage length; L, the length of the gage length, C the width of the ends; R, the radius of the fillet; b, the distance between the grips and the transition zone and t, the specimen thickness (see Fig.3.1b). Two different zones can be distinguished: the heads with a constant width and the test zone with a variable width. The cross-section moment of inertia is defined by piecewise functions in Sections A.3.1 and A.3.2.

A.3.1 Linear approximation of the CR transition zones.

The bending moment in Eq.3.1 and its derivative with respect to the reaction force in the clamps for the CR fatigue specimen are written in Eqs.A.12. For the sake of simplicity, the distance to the gripped area was set to $b = 0$.

$$M(x) = F\ (x - L_t/2) \qquad \frac{\partial M}{\partial F} = (x - L_t/2) \qquad L_t = L \tag{A.12}$$

If the transition zones of the CR fatigue specimen are approximated using first degree polynomials, the geometry of the specimen can be described by the dimensionless geometric factor k_1 (see Fig.3.6c), as explained in Section 3.3. The area moment of inertia of the CR fatigue specimen is written as a piecewise function with the geometrical parameters $k_1 = C/W$, as stated in Eq.A.13.

$$I_z(x) = \frac{Wt^3}{12}\begin{cases} \frac{2}{L_t}(1-k_1)\,x + k_1 & \text{if } 0 < x < \frac{L_t}{2} \\ -\frac{2}{L_t}(1-k_1)\ (x - L_t) + k_1 & \text{if } \frac{L_t}{2} < x < L_t \end{cases} \tag{A.13}$$

Castigliano (1873)'s method is applied by computing the integral of Eq.3.2.

$$\frac{\delta_F}{2} = \frac{12F}{EWt^3}\int_0^{L_t/2}\frac{\left[x - L_t/2\right]^2}{\left[\frac{2}{L_t}(1-k_1)\,x + k_1\right]}dx = \frac{12FL_t}{EWt^3 2(1-k_1)}\int_0^{L_t/2}\frac{\left[x - L_t/2\right]^2}{\left[x + \frac{k_1 L_t}{2(1-k_1)}\right]}dx$$

$$\frac{EWt^3\,\delta_F}{24FL_t} = \frac{1}{2\,(1-k_1)}\int_0^{L_t/2}\frac{\left[x - L_t/2\right]^2}{\left[x + \frac{k_1 L_t}{2(1-k_1)}\right]}dx$$

$$\frac{EWt^3\,\delta_F}{24FL_t} = \frac{1}{2\,(1-k_1)}\left[\left(\frac{L_t}{2} + \frac{k_1 L_t}{2(1-k_1)}\right)^2 \ln\left(1 + \frac{1-k_1}{k_1}\right) - \frac{L_t}{4}\left(\frac{3L_t}{2} + \frac{k_1 L_t}{1-k_1}\right)\Big|_0^{L_t/2}\right]$$

$$\frac{EWt^3\,\delta_F}{FL_t^3} = \underbrace{\frac{12}{(1-k_1)}\left[\left(\frac{1}{2}+\frac{k_1}{2(1-k_1)}\right)^2 \ln\left(\frac{1}{k_1}\right) - \left(\frac{3}{8}+\frac{k_1}{4(1-k_1)}\right)\right]}_{1/m_{\mathrm{CR}}}$$

$$F = m_{\mathrm{CR}}\frac{EWt^3}{L^3}\delta_F$$

Having:

$$m_{\mathrm{CR}} = \left\{\frac{12}{(1-k_1)}\left[\left(\frac{1}{2}+\frac{k_1}{2(1-k_1)}\right)^2 \ln\left(\frac{1}{k_1}\right) - \left(\frac{3}{8}+\frac{k_1}{4(1-k_1)}\right)\right]\right\}^{(-1)} \tag{A.14}$$

The stiffness correction factor m_{CR} is a function of the dimensionless geometrical factor k_1 and its value can be taken from the abacus of Fig.3.6d.

A.3.2 Parabolic approximation of the CR transition zones.

Using second degree polynomials for approximating the transition zones, the moment of inertia of the CR fatigue specimen can be written as stated in Eq. A.15.

$$I_z(x) = \frac{t^3}{12}\begin{cases} C & \text{if } 0 < x < b \\ \frac{[x-(b+L/2)]^2}{R} + W & \text{if } b < x < b + L/2 \end{cases} \tag{A.15}$$

Castigliano (1873)'s method is applied by computing the integral of Eq.3.2.

$$\frac{\delta_F}{2} = \frac{12F}{E\,t^3}\left[\int_0^b \frac{[x-(b+L/2)]^2}{C}dx + \int_b^{b+L/2} \frac{[x-(b+L/2)]^2}{\frac{[x-(b+L/2)]^2}{R}+W}dx\right]$$

Both integrals in the second term constitute a dimensionless factor that depends only on the geometrical parameters of the CR fatigue specimen.

$$\frac{EWt^3\,\delta_F}{24FL_t^3} = \left[\frac{W}{CL_t^3}\int_0^b [x-(b+L/2)]^2\,dx + \frac{RW}{L_t^3}\int_b^{b+L/2} \frac{[x-(b+L/2)]^2}{[x-(b+L/2)]^2+RW}dx\right]$$

$$\frac{EWt^3\,\delta_F}{24FL_t^3} = \frac{W}{CL_t^3}\left[\frac{[x-(b+L/2)]^3}{3}\Big|_0^b\right] + \frac{RW}{L_t^3}\left[\sqrt{RW}\tan^{-1}\left(\frac{b+L/2-x}{\sqrt{RW}}+x\right)\Big|_b^{b+L/2}\right]$$

$$\frac{EWt^3\,\delta_F}{FL_t^3} = \underbrace{\frac{24W}{CL_t^3}\left[\frac{b^3}{3}+\frac{b^2L}{2}+\frac{bL^2}{4}\right] + \frac{24RW}{L_t^3}\left[\frac{L}{2}-\sqrt{RW}\,\tan^{-1}\left(\frac{L}{2\sqrt{RW}}\right)\right]}_{m_{\mathrm{CR}}^{-1}}$$

Finally, the bending form of Hooke's law for the CR can be written as stated in Eq.A.16

$$F = m_{\mathrm{CR}}\frac{EWt^3}{L_t^3}\delta_F \tag{A.16}$$

Having:

$$m_{\mathrm{CR}} = \left\{ \frac{24W}{CL_t^3} \left[\frac{b^3}{3} + \frac{b^2 L}{2} + \frac{bL^2}{4} \right] + \frac{24RW}{L_t^3} \left[\frac{L}{2} - \sqrt{RW}\, \tan^{-1}\left(\frac{L}{2\sqrt{RW}} \right) \right] \right\}^{-1} \tag{A.17}$$

Bibliography

H. Abdesselam, J. Crepin, A. Pineau, A.-L. Rouffie, P. Gaborit, L. Menut-Tournadre, and T.F. Morgeneyer. On the crystallographic, stage I-like, character of fine granular area formation in internal fish-eye fatigue cracks. *International Journal of Fatigue*, 106:132 – 142, 2018. ISSN 0142-1123. doi: https://doi.org/10.1016/j.ijfatigue.2017.09.013. URL http://www.sciencedirect.com/science/article/pii/S014211231730378X.

E. Aeby-Gautier, A. Settefrati, F. Bruneseaux, B. Appolaire, B. Denand, M. Dehmas, G. Geandier, and P. Boulet. Isothermal α formation in β metastable titanium alloys. *Journal of Alloys and Compounds*, 577:S439 – S443, 2013. ISSN 0925-8388. doi: https://doi.org/10.1016/j.jallcom.2012.02.046. URL http://www.sciencedirect.com/science/article/pii/S0925838812003088. SI :ICOMAT2011.

Elisabeth Aeby-Gautier, Benoît Denand, Julien Teixeira, Moukrane Dehmas, Benoît Appolaire, and S Settefrati. Influence of microstructure on tensile properties of beta-metastable ti17 alloy. *JOM*, 63(10):16, Oct 2011. ISSN 1543-1851. doi: 10.1007/s11837-011-0166-3. URL https://doi.org/10.1007/s11837-011-0166-3.

Global Market Forecast Airbus. Growing horizons 2017–2036, 2017.

R.R. Ambriz, D. Chicot, N. Benseddiq, G. Mesmacque, and S.D. de la Torre. Local mechanical properties of the 6061-T6 aluminium weld using micro-traction and instrumented indentation. *European Journal of Mechanics - A/Solids*, 30(3):307 – 315, 2011. ISSN 0997-7538. doi: https://doi.org/10.1016/j.euromechsol.2010.12.007. URL http://www.sciencedirect.com/science/article/pii/S0997753810001452.

M. Y. Amegadzie, O. T. Ola, O.A. Ojo, P. Wanjara, and MC. Chaturvedi. On liquation and liquid phase oxidation during linear friction welding of nickel-base in738 and cmsx superalloys. In *Superalloys 2012*, pages 587–594. John Wiley & Sons, Ltd, 2012. ISBN 9781118516430. doi: 10.1002/9781118516430.ch65. URL https://onlinelibrary.wiley.com/doi/abs/10.1002/9781118516430.ch65.

ASTM E 466-07. 466-07. *Standard Practice for Conducting Force Controlled Constant Amplitude Axial Fatigue Tests of Metallic Materials*, 2007.

ASTM E1012-14e1. E1012-14e1. *Standard Practice for Verification of Testing Frame and Specimen Alignment Under Tensile and Compressive Axial Force Application*, 2014. URL www.astm.org.

ASTM E384-17. E384-17. *Standard Test Method for Microindentation Hardness of Materials, ASTM International, West Conshohocken, PA, 2017.*, 2017. doi: 10.1520/E0384-17. URL http://www.astm.org/cgi-bin/resolver.cgi?E384.

ASTM E8/E8M-16a. E8. *Standard Test Methods for Tension Testing of Metallic Materials*, 2016.

W.A. Baeslack, T.F. Broderick, M. Juhas, and H.L. Fraser. Characterization of solid-phase welds between ti-6al-2sn-4zr-2mo-0.1si and ti-13.5al-21.6nb titanium aluminide. *Materials Characterization*, 33(4):357 – 367, 1994. ISSN 1044-5803. doi: https://doi.org/10.1016/1044-5803(94)90140-6. URL http://www.sciencedirect.com/science/article/pii/1044580394901406.

Dorick Ballat-Durand, Salima Bouvier, Marion Risbet, and Wolfgang Pantleon. Multi-scale and multi-technic microstructure analysis of a linear friction weld of the metastable-β titanium alloy ti-5al-2sn-2zr-4mo-4cr (ti17) towards a new post-weld heat treatment. *Materials Characterization*, 144:661 – 670, 2018. ISSN 1044-5803. doi: https://doi.org/10.1016/j.matchar.2018.08.013. URL http://www.sciencedirect.com/science/article/pii/S1044580318312671.

Dorick Ballat-Durand, Salima Bouvier, Marion Risbet, and Wolfgang Pantleon. Through analysis of the microstructure changes during linear friction welding of the near-α titanium alloy Ti-6Al-2Sn-4Zr-2Mo (Ti6242) towards microstructure optimization. *Materials Characterization*, 151:38 – 52, 2019. ISSN 1044-5803. doi: https://doi.org/10.1016/j.matchar.2019.02.027. URL http://www.sciencedirect.com/science/article/pii/S1044580318332443.

Dipankar Banerjee and J.C. Williams. Perspectives on titanium science and technology. *Acta Materialia*, 61(3):844 – 879, 2013. ISSN 1359-6454. doi: https://doi.org/10.1016/j.actamat.2012.10.043. URL http://www.sciencedirect.com/science/article/pii/S1359645412007902. The Diamond Jubilee Issue.

Srikumar Banerjee and Pradip Mukhopadhyay. *Phase transformations: examples from titanium and zirconium alloys*, volume 12. Elsevier, 2010.

Paul J. Bania. Beta titanium alloys and their role in the titanium industry. *JOM*, 46(7):16–19, Jul 1994. ISSN 1543-1851. doi: 10.1007/BF03220742. URL https://doi.org/10.1007/BF03220742.

Ioannis Bantounas, Trevor C. Lindley, David Rugg, and David Dye. Effect of microtexture on fatigue cracking in ti–6al–4v. *Acta Materialia*, 55(16):5655 – 5665, 2007. ISSN 1359-6454. doi: https://doi.org/10.1016/j.actamat.2007.06.034. URL http://www.sciencedirect.com/science/article/pii/S1359645407004338.

B. Barkia, V. Doquet, J.P. Couzinié, I. Guillot, and E. Héripré. In situ monitoring of the deformation mechanisms in titanium with different oxygen contents. *Materials Science and Engineering:A*, 636:91 – 102, 2015. ISSN 0921-5093. doi: https://doi.org/10.1016/j.msea.2015.03.044. URL http://www.sciencedirect.com/science/article/pii/S0921509315002865.

Meriem Ben Haj Slama, Nabila Maloufi, Julien Guyon, Slim Bahi, Laurent Weiss, and Antoine Guitton. In situ macroscopic tensile testing in sem and electron channeling contrast imaging: Pencil glide evidenced in a bulk β-ti21s polycrystal. *Materials*, 12(15), 2019. ISSN 1996-1944. doi: 10.3390/ma12152479. URL https://www.mdpi.com/1996-1944/12/15/2479.

Gilles Besnard, Sandra Guérard, Stéphane Roux, and François Hild. A space-time approach in digital image correlation: Movie-dic. *Optics and Lasers in Engineering*, 49:71–81, 2011. doi: 10.1016/j.optlaseng.2010.08.012. URL https://hal.archives-ouvertes.fr/hal-00521203.

Jacques Besson and Ronald Foerch. Object-oriented programming applied to the finite element method part I. General Concepts. *Revue Européenne des Éléments Finis*, 7(5):535–566, 1998. doi: 10.1080/12506559.1998.10511321. URL https://doi.org/10.1080/12506559.1998.10511321.

James H. Bevington. Modes of welding the ends of wire and rods, 1891a. US Patent 463,134.

James H. Bevington. Spinning tubes, 1891b. US Patent 444,721.

I. Bhamji, M. Preuss, P. L. Threadgill, and A. C. Addison. Solid state joining of metals by linear friction welding: a literature review. *Materials Science and Technology*, 27(1):2–12, 2011. doi: 10.1179/026708310X520510. URL https://doi.org/10.1179/026708310X520510.

I. Bhamji, A.C. Addison, P.L. Threadgill, and M. Preuss. Appendix: Linear friction welding in aerospace engineering. In M.C. Chaturvedi, editor, *Welding and Joining of Aerospace Materials*, Woodhead Publishing Series in Welding and Other Joining Technologies, pages 384 – 415. Woodhead Publishing, 2012. ISBN 978-1-84569-532-3. doi: https://doi.org/10.1533/9780857095169.appendix. URL http://www.sciencedirect.com/science/article/pii/B9781845695323500162.

H Bomberger and S Seagle. Titanium-base alloy and method of improving creep properties, 1974. US Patent 3,833,363.

R. R. Boyer. Titanium for aerospace: Rationale and applications. *Advanced Performance Materials*, 2(4):349–368, 1995. ISSN 1572-8765. doi: 10.1007/BF00705316. URL https://doi.org/10.1007/BF00705316.

R. R. Boyer. Attributes, characteristics, and applications of titanium and its alloys. *JOM*, 62(5):21–24, May 2010. ISSN 1543-1851. doi: 10.1007/s11837-010-0071-1. URL https://doi.org/10.1007/s11837-010-0071-1.

R.R. Boyer. An overview on the use of titanium in the aerospace industry. *Materials Science and Engineering:A*, 213(1):103 – 114, 1996. ISSN 0921-5093. doi: https://doi.org/10.1016/0921-5093(96)10233-1. URL http://www.sciencedirect.com/science/article/pii/0921509396102331. International Symposium on Metallurgy and Technology of Titanium Alloys.

Clare Breidenich, Daniel Magraw, Anne Rowley, and James W. Rubin. The kyoto protocol to the united nations framework convention on climate change. *The American Journal of International Law*, 92(2):315–331, 1998. ISSN 00029300, 21617953. URL http://www.jstor.org/stable/2998044.

F. Bridier, P. Villechaise, and J. Mendez. Analysis of the different slip systems activated by tension in a α/β titanium alloy in relation with local crystallographic orientation. *Acta Materialia*, 53(3):555 – 567, 2005. ISSN 1359-6454. doi: https://doi.org/10.1016/j.actamat.2004.09.040. URL http://www.sciencedirect.com/science/article/pii/S1359645404005634.

J.-Y Buffière, E Maire, P Cloetens, G Lormand, and R Fougères. Characterization of internal damage in a mmcp using x-ray synchrotron phase contrast microtomography. *Acta Materialia*, 47(5):1613 – 1625, 1999. ISSN 1359-6454. doi: https://doi.org/10.1016/S1359-6454(99)00024-5. URL http://www.sciencedirect.com/science/article/pii/S1359645499000245.

Christophe Buirette, Julitte Huez, Nathalie Gey, Alain Vassel, and Eric Andrieu. Study of crack propagation mechanisms during charpy impact toughness tests on both equiaxed and lamellar microstructures of ti–6al–4v titanium alloy. *Materials Science and Engineering: A*, 618:546 – 557, 2014. ISSN 0921-5093. doi: https://doi.org/10.1016/j.msea.2014.09.048. URL http://www.sciencedirect.com/science/article/pii/S0921509314011538.

W.G. Burgers. On the process of transition of the cubic-body-centered modification into the hexagonal-close-packed modification of zirconium. *Physica*, 1(7):561 – 586, 1934. ISSN 0031-8914. doi: https://doi.org/10.1016/S0031-8914(34)80244-3. URL http://www.sciencedirect.com/science/article/pii/S0031891434802443.

Carlo Alberto Castigliano. Intorno all'equilibrio di sistemi elastici. *Atti della Reale Accademia delle Scienze Di Torino*, vol. X, 1873.

Augustin-Louis Cauchy. *Leçons sur les applications du calcul infinitésimal à la géométrie*, volume 1. de l'Imprimerie Royale, 1826.

L. Ceschini, I. Boromei, G. Minak, A. Morri, and F. Tarterini. Effect of friction stir welding on microstructure, tensile and fatigue properties of the aa7005/10vol. *Composites Science and Technology*, 67(3):605 – 615, 2007. ISSN 0266-3538. doi: https://doi.org/10.1016/j.compscitech.2006.07.029. URL http://www.sciencedirect.com/science/article/pii/S026635380600282X.

R. Chait and T. S. DeSisto. The influence of grain size on the high cycle fatigue crack initiation of a metastable beta ti alloy. *Metallurgical Transactions A*, 8(6):1017–1020, Jun 1977. ISSN 1543-1940. doi: 10.1007/BF02661593. URL https://doi.org/10.1007/BF02661593.

A. Chamanfar, M. Jahazi, J. Gholipour, P. Wanjara, and S. Yue. Maximizing the integrity of linear friction welded waspaloy. *Materials Science and Engineering: A*, 555:117 – 130, 2012a. ISSN 0921-5093. doi: https://doi.org/10.1016/j.msea.2012.06.041. URL http://www.sciencedirect.com/science/article/pii/S0921509312008660.

A. Chamanfar, M. Jahazi, J. Gholipour, P. Wanjara, and S. Yue. Suppressed liquation and microcracking in linear friction welded waspaloy. *Materials & Design (1980-2015)*, 36:113 – 122, 2012b. ISSN 0261-3069. doi: https://doi.org/10.1016/j.matdes.2011.11.007. URL http://www.sciencedirect.com/science/article/pii/S0261306911007679. Sustainable Materials, Design and Applications.

A. Chamanfar, T. Pasang, A. Ventura, and W.Z. Misiolek. Mechanical properties and microstructure of laser welded ti–6al–2sn–4zr–2mo (ti6242) titanium alloy. *Materials Science and Engineering:A*, 663:213 – 224, 2016. ISSN 0921-5093. doi: https://doi.org/10.1016/j.msea.2016.02.068. URL http://www.sciencedirect.com/science/article/pii/S0921509316301836.

Biplab Chatterjee and Sumit Bhowmik. Chapter 9 - evolution of material selection in commercial aviation industry—a review. In Kaushik Kumar, Divya Zindani, and Paulo Davim, editors, *Sustainable Engineering Products and Manufacturing Technologies*, pages 199 – 219. Academic Press, 2019. ISBN 978-0-12-816564-5. doi: https://doi.org/10.1016/B978-0-12-816564-5.00009-8. URL http://www.sciencedirect.com/science/article/pii/B9780128165645000098.

Charlie C Chen. Process for preparation of near-alpha titanium alloys, January 5 1982. US Patent 4,309,226.

Chuan chen ZHANG, Tian cang ZHANG, Ya juan JI, and Ji hua HUANG. Effects of heat treatment on microstructure and microhardness of linear friction welded dissimilar ti alloys. *Transactions of Nonferrous Metals Society of China*, 23(12):3540 – 3544, 2013. ISSN 1003-6326. doi: https://doi.org/10.1016/S1003-6326(13)62898-8. URL http://www.sciencedirect.com/science/article/pii/S1003632613628988.

František Chmelík, Frank B. Klose, Hanno Dierke, Jindřich Šachl, Hartmut Neuhäuser, and Pavel Lukáč. Investigating the portevin–le châtelier effect in strain rate and stress rate controlled tests by the acoustic emission and laser extensometry techniques. *Materials Science and Engineering:A*, 462(1):53 – 60, 2007. ISSN 0921-5093. doi: https://doi.org/10.1016/j.msea.2006.01.169. URL http://www.sciencedirect.com/science/article/pii/S0921509306018624. International Symposium on Physics of Materials, 2005.

A. I. Chudikov. Friction welding, 1956. Russian Patent, RU106270.

A. T. Churchman and Thomas Edward Allibone. The slip modes of titanium and the effect of purity on their occurrence during tensile deformation of single crystals. *Proceedings of the Royal Society of London. Series A. Mathematical and Physical Sciences*, 226(1165):216–226, 1954. doi: 10.1098/rspa.1954.0250. URL https://royalsocietypublishing.org/doi/abs/10.1098/rspa.1954.0250.

Nicolas Clément et al. *Phase transformations and mechanical properties of the Ti-5553 beta-metastable titanium alloy*. PhD thesis, Université catholique de Louvain, 2010. URL http://dial.uclouvain.be/pr/boreal/object/boreal:32266.

James D. Cotton, Robert D. Briggs, Rodney R. Boyer, Sesh Tamirisakandala, Patrick Russo, Nikolay Shchetnikov, and John C. Fanning. State of the art in beta titanium alloys for airframe applications. *JOM*, 67 (6):1281–1303, Jun 2015. ISSN 1543-1851. doi: 10.1007/s11837-015-1442-4. URL https://doi.org/10.1007/s11837-015-1442-4.

Steven J Covey and Paul A Bartolotta. In-plane biaxial failure surface of cold-rolled 304 stainless steel sheets. In *Multiaxial Fatigue and Deformation: Testing and Prediction*. ASTM International, 2000.

E. Dalgaard, P. Wanjara, J. Gholipour, X. Cao, and J.J. Jonas. Linear friction welding of a near-β titanium alloy. *Acta Materialia*, 60(2):770 – 780, 2012a. ISSN 1359-6454. doi: https://doi.org/10.1016/j.actamat.2011.04.037. URL http://www.sciencedirect.com/science/article/pii/S1359645411002898.

E Dalgaard, P Wanjara, J Gholipour, and J J Jonas. Evolution of microstructure, microtexture and mechanical properties of linear friction welded imi 834. *Canadian Metallurgical Quarterly*, 51(3):269–276, 2012b. doi: 10.1179/1879139512Y.0000000014. URL https://doi.org/10.1179/1879139512Y.0000000014.

E.C. Dalgaard. *Evolution of Microstructure, Microtexture and Mechanical Properties in Linear Friction Welded Titanium Alloys*. McGill theses. McGill University Library, 2011.

Ning Dang, Lingyu Liu, Jérôme Adrien, Sophie Cazottes, Wenlong Xiao, Chaoli Ma, Lian Zhou, and Eric Maire. Crack nucleation and growth in / titanium alloy with lamellar microstructure under uniaxial tension: 3d x-ray tomography analysis. *Materials Science and Engineering: A*, 747:154 – 160, 2019. ISSN 0921-5093. doi: https://doi.org/10.1016/j.msea.2019.01.065. URL http://www.sciencedirect.com/science/article/pii/S0921509319300851.

Joseph R Davis et al. *ASM specialty handbook: heat-resistant materials*. Asm International, 1997.

Mark R. Daymond and Neil W. Bonner. Measurement of strain in a titanium linear friction weld by neutron diffraction. *Physica B: Condensed Matter*, 325:130 – 137, 2003. ISSN 0921-4526. doi: https://doi.org/10.1016/S0921-4526(02)01514-4. URL http://www.sciencedirect.com/science/article/pii/S0921452602015144.

N. de Benardos and S Olszewski. Process of and aparatus for working metals by the direct application of the electric current, 1887. US Patent 363,320.

Maarten De Strycker, Pascal Lava, Wim Van Paepegem, Luc Schueremans, and Dimitri Debruyne. Measuring welding deformations with the digital image correlation technique. *Welding Journal*, 90(6), 2011. ISSN 0043-2296.

Loic Debeugny and Guillaume Racineux. *Contribution a la modelisation et a la comprehension du procede de soudage par friction lineaire*. Ecole Central de Nantes, 2013.

Jérome Delfosse. Welds characterisation of linear friction welds for mechanical applications. In *Journees Technologiques Titane*, page 2. EADS, 2012.

Francesco Delloro. *Méthodes morphologique et par éléments finis combinées pour une nouvelle approche de la modélisation 3D du dépôt par projection dynamique par gaz froid (« cold spray »)*. PhD thesis, Ecole des Mines, 2015. URL http://www.theses.fr/2015ENMP0017. Thèse de doctorat dirigée par Jeandin, Michel et Jeulin, Dominique Sciences et génie des matériaux Paris, ENMP 2015 - 2015ENMP0017.

Estelle Parra Denis, Cécile Barat, Dominique Jeulin, and Christophe Ducottet. 3d complex shape characterization by statistical analysis: Application to aluminium alloys. *Materials Characterization*, 59(3):338 – 343, 2008. ISSN 1044-5803. doi: https://doi.org/10.1016/j.matchar.2007.01.012. URL http://www.sciencedirect.com/science/article/pii/S1044580307000320.

Vinod Deshmukh, Raju Kadam, and Suhas S. Joshi. Removal of alpha case on titanium alloy surfaces using chemical milling. *Machining Science and Technology*, 21(2):257–278, 2017. doi: 10.1080/10910344.2017.1284558. URL https://doi.org/10.1080/10910344.2017.1284558.

Shusheng Di, Xinqi Yang, Dapeng Fang, and Guohong Luan. The influence of zigzag-curve defect on the fatigue properties of friction stir welds in 7075-t6 al alloy. *Materials Chemistry and Physics*, 104(2):244 – 248, 2007. ISSN 0254-0584. doi: https://doi.org/10.1016/j.matchemphys.2007.01.023. URL http://www.sciencedirect.com/science/article/pii/S0254058407000545.

Matthew J Donachie. *Titanium: a technical guide*. ASM international, 2000.

Thimothée Duval. /. Theses, ISAE-ENSMA Ecole Nationale Supérieure de Mécanique et d'Aérotechique - Poitiers, December 2013. URL https://tel.archives-ouvertes.fr/tel-00959280.

McLean P. Echlin, Jean Charles Stinville, Victoria M. Miller, William C. Lenthe, and Tresa M. Pollock. Incipient slip and long range plastic strain localization in microtextured ti-6al-4v titanium. *Acta Materialia*, 114: 164 – 175, 2016. ISSN 1359-6454. doi: https://doi.org/10.1016/j.actamat.2016.04.057. URL http://www.sciencedirect.com/science/article/pii/S1359645416303251.

P. S. Effertz, F. Fuchs, and N. Enzinger. Modelling the flash formation of linear friction welded 30crnimo8 high strength steel chains. *The International Journal of Advanced Manufacturing Technology*, 92(5):2479–2486, Sep 2017. ISSN 1433-3015. doi: 10.1007/s00170-017-0338-6. URL https://doi.org/10.1007/s00170-017-0338-6.

Wilfried Eichlseder. Fatigue analysis by local stress concept based on finite element results. *Computers & Structures*, 80(27):2109 – 2113, 2002. ISSN 0045-7949. doi: https://doi.org/10.1016/S0045-7949(02)00273-0. URL http://www.sciencedirect.com/science/article/pii/S0045794902002730.

K. Elangovan, V. Balasubramanian, and S. Babu. Developing an empirical relationship to predict tensile strength of friction stir welded aa2219 aluminum alloy. *Journal of Materials Engineering and Performance*, 17(6):820, Apr 2008. ISSN 1544-1024. doi: 10.1007/s11665-008-9240-6. URL https://doi.org/10.1007/s11665-008-9240-6.

D. Eylon, S. Fujishiro, Pamela J. Postans, and F. H. Froes. High-temperature titanium alloys—a review. *JOM*, 36(11):55–62, Nov 1984. ISSN 1543-1851. doi: 10.1007/BF03338617. URL https://doi.org/10.1007/BF03338617.

D. Eylon, A. Vassel, Y. Combres, R. R. Boyer, P. J. Bania, and R. W. Schutz. Issues in the development of beta titanium alloys. *JOM*, 46(7):14–15, Jul 1994. ISSN 1543-1851. doi: 10.1007/BF03220741. URL https://doi.org/10.1007/BF03220741.

Michael E Fitzpatrick and Alain Lodini. *Analysis of residual stress by diffraction using neutron and synchrotron radiation*. CRC Press, 2003.

Bertrand Flipo, Kathryn Beamish, Bryan Humphreys, and Martin Wood. Linear friction welding of ti−6al−4v for aerostructure applications. *Trends Weld. Res. Proc. 10th Int. Conf., Tokyo, Japan.*, 2016. URL https://www.twi-global.com/technical-knowledge/published-papers/linear-friction-welding-of-ti-6al-4v-for-aerostructure-applications.

J.W. Flowers, K.C. O'Brien, and P.C. McEleney. Elastic constants of alpha-titanium single crystals at 25°c. *Journal of the Less Common Metals*, 7(5):393 – 395, 1964. ISSN 0022-5088. doi: https://doi.org/10.1016/0022-5088(64)90084-0. URL http://www.sciencedirect.com/science/article/pii/0022508864900840.

John W. Foltz, Brian Welk, Peter C. Collins, Hamish L. Fraser, and James C. Williams. Formation of grain boundary α in β ti alloys: Its role in deformation and fracture behavior of these alloys. *Metallurgical and*

Materials Transactions A, 42(3):645–650, Mar 2011. ISSN 1543-1940. doi: 10.1007/s11661-010-0322-3. URL https://doi.org/10.1007/s11661-010-0322-3.

P. Frankel, M. Preuss, A. Steuwer, P. J. Withers, and S. Bray. Comparison of residual stresses in ti–6al–4v and ti–6al–2sn–4zr–2mo linear friction welds. *Materials Science and Technology*, 25(5):640–650, 2009. doi: 10.1179/174328408X332825. URL https://doi.org/10.1179/174328408X332825.

L. Fratini, S. Pasta, and A.P. Reynolds. Fatigue crack growth in 2024-t351 friction stir welded joints: Longitudinal residual stress and microstructural effects. *International Journal of Fatigue*, 31(3):495 – 500, 2009. ISSN 0142-1123. doi: https://doi.org/10.1016/j.ijfatigue.2008.05.004. URL http://www.sciencedirect.com/science/article/pii/S0142112308001151.

FH Froes. *Titanium: physical metallurgy, processing, and applications*. ASM International, 2015.

FH Froes, JC Chesnutt, CG Rhodes, and JC Williams. Relationship of fracture toughness and ductility to microstructure and fractographic features in advanced deep hardenable titanium alloys. In *Toughness and Fracture Behavior of Titanium*. ASTM International, 1978.

R Scott Funderburk. Selecting filler metals: matching strength criteria. *Welding Innovation*, 16(2):10–12, 1999.

A. W. Funkenbusch and L. F. Coffin. Low-cycle fatigue crack nucleation and early growth in ti-17. *Metallurgical Transactions A*, 9(8):1159, Aug 1978. ISSN 1543-1940. doi: 10.1007/BF02652221. URL https://doi.org/10.1007/BF02652221.

Gabriele. World titanium industry supply and demand overview, 2016. TITANIUM USA 2016 Executive Summary.

Antonio M. Mateo García. Blisk fabrication by linear friction welding. In Ernesto Benini, editor, *Advances in Gas Turbine Technology*, chapter 18. IntechOpen, Rijeka, 2011. doi: 10.5772/21278. URL https://doi.org/10.5772/21278.

Juan Manuel García and Thilo F. Morgeneyer. Strength and fatigue strength of a similar Ti–6Al–2Sn–4Zr–2Mo–0.1Si linear friction welded joint. *Fatigue & Fracture of Engineering Materials & Structures*, 42(5):1100–1117, 2019. doi: 10.1111/ffe.12973. URL https://onlinelibrary.wiley.com/doi/abs/10.1111/ffe.12973.

Juan Manuel García, Fabrice Gaslain, Vladimir Esin, and Thilo Frank Morgeneyer. Effect of a thermal treatment on the tensile and fatigue properties of similar ti17 linear friction welds and ti17 parent material. *Materials Characterization*, 2019.

A.F. Gerday, M. Ben Bettaieb, L. Duchêne, N. Clement, H. Diarra, and A.M. Habraken. Material behavior of the hexagonal alpha phase of a titanium alloy identified from nanoindentation tests. *European Journal of Mechanics - A/Solids*, 30(3):248 – 255, 2011. ISSN 0997-7538. doi: https://doi.org/10.1016/j.euromechsol.2010.11.001. URL http://www.sciencedirect.com/science/article/pii/S0997753810001373.

B. Gfeller, M. Zanetti, M. Properzi, A. Pizzi, F. Pichelin, M. Lehmann, and L. Delmotte. Wood bonding by vibrational welding. *Journal of Adhesion Science and Technology*, 17(11):1573–1589, 2003. doi: 10.1163/156856103769207419. URL https://doi.org/10.1163/156856103769207419.

U. Ghosh et al. *Desing of welded steel structures. Principle and practises.* Taylor & Francis Group, 2015.

Charles M. Gilmore, M.Ashraf Imam, and George R. Yoder. On fatigue crack growth in a ti-4.5al-5mo-1.5cr alloy with metastable β-phase. *Engineering Fracture Mechanics*, 21(1):115 – 121, 1985. ISSN 0013-7944. doi: https://doi.org/10.1016/0013-7944(85)90058-X. URL http://www.sciencedirect.com/science/article/pii/001379448590058X.

Yina Guo, Taenam Jung, Yu Lung Chiu, Hangyue Li, Simon Bray, and Paul Bowen. Microstructure and microhardness of ti6246 linear friction weld. *Materials Science and Engineering: A*, 562:17 – 24, 2013. ISSN 0921-5093. doi: https://doi.org/10.1016/j.msea.2012.10.089. URL http://www.sciencedirect.com/science/article/pii/S0921509312015249.

Hiroshi Hayakawa, Nobuo Fukada, Takeshi Udagawa, Masaaki Koizumi, Hirowo G. Suzuki, and Takashi Fukuyama. Solidification structure and segregation in cast ingots of titanium alloy produced by vacuum arc consumable electrode method. *ISIJ International*, 31(8):775–784, 1991a. doi: 10.2355/isijinternational.31.775.

Hiroshi Hayakawa, Nobuo Fukada, Takeshi Udagawa, Masaaki Koizumi, Hirowo G. Suzuki, and Takashi Fukuyama. Solidification structure and segregation in cast ingots of titanium alloy produced by vacuum arc consumable electrode method. *ISIJ International*, 31(8):775–784, 1991b. doi: 10.2355/isijinternational.31.775.

M Hayes. Connexions between the moduli for anistropic elastic materials. *Journal of Elasticity*, 2(2):135–141, 1972.

Lukas Helfen, Feng Xu, Heikki Suhonen, Peter Cloetens, and Tilo Baumbach. Laminographic imaging using synchrotron radiation – challenges and opportunities. *Journal of Physics: Conference Series*, 425(19):192025, 2013. doi: 10.1088/1742-6596/425/19/192025. URL https://doi.org/10.1088%2F1742-6596%2F425%2F19%2F192025.

Samuel Hémery, Van Truong Dang, Loïc Signor, and Patrick Villechaise. Influence of microtexture on early plastic slip activity in ti-6al-4v polycrystals. *Metallurgical and Materials Transactions A*, 49(6):2048–2056, Jun 2018. ISSN 1543-1940. doi: 10.1007/s11661-018-4569-4. URL https://doi.org/10.1007/s11661-018-4569-4.

Michael Herbig, Andrew King, Péter Reischig, Henry Proudhon, Erik M. Lauridsen, James Marrow, Jean-Yves Buffière, and Wolfgang Ludwig. 3-d growth of a short fatigue crack within a polycrystalline microstructure studied using combined diffraction and phase-contrast x-ray tomography. *Acta Materialia*, 59(2):590 – 601, 2011. ISSN 1359-6454. doi: https://doi.org/10.1016/j.actamat.2010.09.063. URL http://www.sciencedirect.com/science/article/pii/S1359645410006403.

Stéphanie Hollande, Jean-Louis Laurent, and Thierry Lebey. High-frequency welding of an industrial thermoplastic polyurethane elastomer-coated fabric. *Polymer*, 39(22):5343 – 5349, 1998. ISSN 0032-3861. doi: https://doi.org/10.1016/S0032-3861(97)10281-6. URL http://www.sciencedirect.com/science/article/pii/S0032386197102816.

L. Huang, P. Kinnell, and P.H. Shipway. Removal of heat-formed coating from a titanium alloy using high pressure waterjet: Influence of machining parameters on surface texture and residual stress. *Journal of Materials Processing Technology*, 223:129 – 138, 2015. ISSN 0924-0136. doi: https://doi.org/10.1016/j.jmatprotec.2015.03.053. URL http://www.sciencedirect.com/science/article/pii/S0924013615001569.

E. Héripré, M. Dexet, J. Crépin, L. Gélébart, A. Roos, M. Bornert, and D. Caldemaison. Coupling between experimental measurements and polycrystal finite element calculations for micromechanical study of metallic materials. *International Journal of Plasticity*, 23(9):1512 – 1539, 2007. ISSN 0749-6419. doi: https://doi.org/10.1016/j.ijplas.2007.01.009. URL http://www.sciencedirect.com/science/article/pii/S074964190700006X.

Shin ichi Matsuoka. Ultrasonic welding of ceramics/metals using inserts. *Journal of Materials Processing Technology*, 75(1):259 – 265, 1998. ISSN 0924-0136. doi: https://doi.org/10.1016/S0924-0136(97)00372-5. URL http://www.sciencedirect.com/science/article/pii/S0924013697003725.

O.M. Ivasishin, P.E. Markovsky, S.L. Semiatin, and C.H. Ward. Aging response of coarse- and fine-grained β titanium alloys. *Materials Science and Engineering:A*, 405(1):296 – 305, 2005. ISSN 0921-5093. doi: https://doi.org/10.1016/j.msea.2005.06.027. URL http://www.sciencedirect.com/science/article/pii/S0921509305006428.

Tomoyuki Iwashita. Method and apparatus for joining, 2003. US Patent 6,601,751.

R.I. Jaffee. The physical metallurgy of titanium alloys. *Progress in Metal Physics*, 7:65 – 163, 1958. ISSN 0502-8205. doi: https://doi.org/10.1016/0502-8205(58)90004-2. URL http://www.sciencedirect.com/science/article/pii/0502820558900042.

Robert I. Jaffee. General physical metallurgy of titanium reviewed. *JOM*, 7(2):247–252, Feb 1955. ISSN 1543-1851. doi: 10.1007/BF03377488. URL https://doi.org/10.1007/BF03377488.

M.N James, D.G Hattingh, and G.R Bradley. Weld tool travel speed effects on fatigue life of friction stir welds in 5083 aluminium. *International Journal of Fatigue*, 25(12):1389 – 1398, 2003. ISSN 0142-1123. doi: https://doi.org/10.1016/S0142-1123(03)00061-6. URL http://www.sciencedirect.com/science/article/pii/S0142112303000616.

Shude Ji, Yue Wang, Jianguang Liu, Xiangchen Meng, Jun Tao, and Tiancang Zhang. Effects of welding parameters on material flow behavior during linear friction welding of ti6al4v titanium alloy by numerical investigation. *The International Journal of Advanced Manufacturing Technology*, 82(5):927–938, Feb 2016a. ISSN 1433-3015. doi: 10.1007/s00170-015-7408-4. URL https://doi.org/10.1007/s00170-015-7408-4.

Yajuan Ji, Yanbing LIU, Tiancang ZHANG, and Chuanchen ZHANG. Structure and mechanical properties of tc4/tc17 linear friction welding joint [j]. *Transactions of the China Welding Institution*, 10, 2012.

Yingping Ji and Sujun Wu. Study on microstructure and mechanical behavior of dissimilar ti17 friction welds. *Materials Science and Engineering:A*, 596:32 – 40, 2014. ISSN 0921-5093. doi: https://doi.org/10.1016/j.msea.2013.10.005. URL http://www.sciencedirect.com/science/article/pii/S0921509313011003.

Yingping Ji, Sujun Wu, and Dalong Zhao. Microstructure and mechanical properties of friction welding joints with dissimilar titanium alloys. *Metals*, 6(5), 2016b. ISSN 2075-4701. doi: 10.3390/met6050108. URL https://www.mdpi.com/2075-4701/6/5/108.

Avinash C. Kak, Malcolm Slaney, and Ge Wang. Principles of computerized tomographic imaging. *Medical Physics*, 29(1):107–107, 2002. doi: 10.1118/1.1455742. URL https://aapm.onlinelibrary.wiley.com/doi/abs/10.1118/1.1455742.

SW Kallee, ED Nicholas, and MJ Russell. Friction welding of aero engine components. In *Proceedings of the 10th World Conference Titanium,(TI-2003), Hamburg, Germany*, pages 13–18, 2003.

Matthew Kasemer, McLean P. Echlin, Jean Charles Stinville, Tresa M. Pollock, and Paul Dawson. On slip initiation in equiaxed α/β ti-6al-4v. *Acta Materialia*, 136:288 – 302, 2017. ISSN 1359-6454. doi: https://doi.org/10.1016/j.actamat.2017.06.059. URL http://www.sciencedirect.com/science/article/pii/S1359645417305360.

Amir Mahyar Khorasani, Moshe Goldberg, Egan H. Doeven, and Guy Littlefair. Titanium in biomedical applications, properties and fabrication: A review. *Journal of Biomaterials and Tissue Engineering*, 5(8):593–619, 2015. ISSN 2157-9083. doi: doi:10.1166/jbt.2015.1361. URL https://www.ingentaconnect.com/content/asp/jbte/2015/00000005/00000008/art00001.

Y. C. Kim, A. Fuji, and T. H. North. Residual stress and plastic strain in ai51 304l stainless steel/titanium friction welds. *Materials Science and Technology*, 11(4):383–388, 1995. doi: 10.1179/mst.1995.11.4.383. URL https://doi.org/10.1179/mst.1995.11.4.383.

U. Kocks and A. Kallend, J.and Biondo. Accurate representations of geneil textures by a set of wetghted grains. *Textures and Microstructures*, 14-18:199–204, 1991. doi: http://dx.doi.org/10.1155/TSM.14-18.199.

Wilhelm Kroll. Method for manufacturing titanium and alloys thereof, June 25 1940. US Patent 2,205,854.

Hiroshi Kuroki, Koji Nezaki, Tsukasa Wakabayashi, and Kenji Nakamura. Application of linear friction welding technique to aircraft engine parts. *IHI Eng Rev*, 47:40–43, 2014.

Hiroshi Kuroki, Yukihiro Kondo, Tsukasa Wakabayashi, Kenji Nakamura, Kikuo Takamatsu, Koji Nezaki, and Mitsuyoshi Tsunori. Fatigue characteristic of linear friction welded ti-6al-4v joints. In Antoni Niepokolczycki and Jerzy Komorowski, editors, *ICAF 2019 – Structural Integrity in the Age of Additive Manufacturing*, pages 3–15, Cham, 2020a. Springer International Publishing. ISBN 978-3-030-21503-3.

Hiroshi Kuroki, Yukihiro Kondo, Tsukasa Wakabayashi, Kenji Nakamura, Kikuo Takamatsu, and Mitsuyoshi Nezaki, Kojiand Tsunori. Fatigue characteristic of linear friction welded ti-6al-4v joints. In Antoni Niepokolczycki and Jerzy Komorowski, editors, *ICAF 2019 – Structural Integrity in the Age of Additive Manufacturing*, pages 3–15, Cham, 2020b. Springer International Publishing. ISBN 978-3-030-21503-3.

B. Lang, T. C. Zhang, X. H. Li, and D. L. Guo. Microstructural evolution of a tc11 titanium alloy during linear friction welding. *Journal of Materials Science*, 45(22):6218–6224, Nov 2010. ISSN 1573-4803. doi: 10.1007/s10853-010-4716-9. URL https://doi.org/10.1007/s10853-010-4716-9.

D. A. LaVan and W. N. Sharpe. Tensile testing of microsamples. *Experimental Mechanics*, 39(3):210–216, Sep 1999. ISSN 1741-2765. doi: 10.1007/BF02323554. URL https://doi.org/10.1007/BF02323554.

K. Le Biavant, S. Pommier, and C. Prioul. Local texture and fatigue crack initiation in a ti-6al-4v titanium alloy. *Fatigue & Fracture of Engineering Materials & Structures*, 25(6):527–545, 2002. doi: 10.1046/j.1460-2695.2002.00480.x. URL https://onlinelibrary.wiley.com/doi/abs/10.1046/j.1460-2695.2002.00480.x.

T. Le Jolu, T.F. Morgeneyer, A. Denquin, and A.F. Gourgues-Lorenzon. Fatigue lifetime and tearing resistance of AA2198 Al–Cu–Li alloy friction stir welds: Effect of defects. *International Journal of Fatigue*, 70:463 – 472, 2015. ISSN 0142-1123. doi: https://doi.org/10.1016/j.ijfatigue.2014.07.001. URL http://www.sciencedirect.com/science/article/pii/S0142112314001844.

Thomas Le Jolu, Thilo F. Morgeneyer, Anne Denquin, Mohamed Sennour, Anne Laurent, Jacques Besson, and Anne-Françoise Gourgues-Lorenzon. Microstructural characterization of internal welding defects and their effect on the tensile behavior of fsw joints of aa2198 al-cu-li alloy. *Metallurgical and Materials Transactions A*, 45(12):5531–5544, Nov 2014. ISSN 1543-1940. doi: 10.1007/s11661-014-2537-1. URL https://doi.org/10.1007/s11661-014-2537-1.

L. Lecarme, E. Maire, A. Kumar K.C., C. De Vleeschouwer, L. Jacques, A. Simar, and T. Pardoen. Heterogenous void growth revealed by in situ 3-d x-ray microtomography using automatic cavity tracking. *Acta Materialia*, 63:130 – 139, 2014. ISSN 1359-6454. doi: https://doi.org/10.1016/j.actamat.2013.10.014. URL http://www.sciencedirect.com/science/article/pii/S1359645413007659.

Yung-Li Lee, Jwo Pan, Richard Hathaway, and Mark Barkey. *Fatigue testing and analysis: theory and practice*, volume 13. Butterworth-Heinemann, 2005.

Christoph Leyens and Manfred Peters. *Titanium and titanium alloys*. Wiley Online Library, 2003.

Rui Zhe Li, Chun Feng, Long Jiang, and Ya Qiong Cao. Research status and development of titanium alloy drill pipes. In *Functional and Functionally Structured Materials III*, volume 944 of *Materials Science Forum*, pages 903–909. Trans Tech Publications Ltd, 2 2019. doi: 10.4028/www.scientific.net/MSF.944.903.

W.-Y. Li, T. Ma, Y. Zhang, Q. Xu, J. Li, S. Yang, and H. Liao. Microstructure characterization and mechanical properties of linear friction welded ti-6al-4v alloy. *Advanced Engineering Materials*, 10(1-2):89–92, 2008. doi: 10.1002/adem.200700034. URL https://onlinelibrary.wiley.com/doi/abs/10.1002/adem.200700034.

Wen-Ya Li, Tiejun Ma, and Siqian Yang. Microstructure evolution and mechanical properties of linear friction welded ti-5al-2sn-2zr-4mo-4cr (ti17) titanium alloy joints. *Advanced Engineering Materials*, 12(1-2):35–43, 2010. doi: 10.1002/adem.200900185. URL http://onlinelibrary.wiley.com/doi/abs/10.1002/adem.200900185.

Wenya Li, Hui Wu, Tiejun Ma, Changlin Yang, and Zhongwei Chen. Influence of parent metal microstructure and post-weld heat treatment on microstructure and mechanical properties of linear friction welded ti-6al-4v joint. *Advanced Engineering Materials*, 14(5):312–318, 2012. doi: 10.1002/adem.201100203. URL https://onlinelibrary.wiley.com/doi/abs/10.1002/adem.201100203.

Wenya Li, Juandi Suo, Tiejun Ma, Yan Feng, and KeeHyun Kim. Abnormal microstructure in the weld zone of linear friction welded ti–6.5al–3.5mo–1.5zr–0.3si titanium alloy joint and its influence on joint properties. *Materials Science and Engineering:A*, 599:38 – 45, 2014. ISSN 0921-5093. doi: https://doi.org/10.1016/j.msea.2014.01.071. URL http://www.sciencedirect.com/science/article/pii/S0921509314001026.

Wenya Li, Achilles Vairis, Michael Preuss, and Tiejun Ma. Linear and rotary friction welding review. *International Materials Reviews*, 61(2):71–100, 2016. doi: 10.1080/09506608.2015.1109214. URL https://doi.org/10.1080/09506608.2015.1109214.

Rong Liang, Yingping Ji, Shijie Wang, and Shuzhen Liu. Effect of microstructure on fracture toughness and fatigue crack growth behavior of ti17 alloy. *Metals*, 6(8), 2016. ISSN 2075-4701. doi: 10.3390/met6080186. URL http://www.mdpi.com/2075-4701/6/8/186.

H. Lombard, D.G. Hattingh, A. Steuwer, and M.N. James. Optimising fsw process parameters to minimise defects and maximise fatigue life in 5083-h321 aluminium alloy. *Engineering Fracture Mechanics*, 75(3):341 – 354, 2008. ISSN 0013-7944. doi: https://doi.org/10.1016/j.engfracmech.2007.01.026. URL http://www.sciencedirect.com/science/article/pii/S0013794407000549. International Conference of Crack Paths.

S. Lomolino, R. Tovo, and J. dos Santos. On the fatigue behaviour and design curves of friction stir butt-welded al alloys. *International Journal of Fatigue*, 27(3):305 – 316, 2005. ISSN 0142-1123. doi: https://doi.org/10.1016/j.ijfatigue.2004.06.013. URL http://www.sciencedirect.com/science/article/pii/S0142112304001537.

Marc Long and H.J Rack. Titanium alloys in total joint replacement—a materials science perspective. *Biomaterials*, 19(18):1621 – 1639, 1998. ISSN 0142-9612. doi: https://doi.org/10.1016/S0142-9612(97)00146-4. URL http://www.sciencedirect.com/science/article/pii/S0142961297001464.

D. Lunt, J. Quinta da Fonseca, D. Rugg, and M. Preuss. Microscopic strain localisation in ti-6al-4v during uniaxial tensile loading. *Materials Science and Engineering:A*, 680:444 – 453, 2017. ISSN 0921-5093. doi: https://doi.org/10.1016/j.msea.2016.10.099. URL http://www.sciencedirect.com/science/article/pii/S0921509316313260.

P. F. Luo, Y. J. Chao, M. A. Sutton, and W. H. Peters. Accurate measurement of three-dimensional deformations in deformable and rigid bodies using computer vision. *Experimental Mechanics*, 33(2):123–132, 1993. ISSN 1741-2765. doi: 10.1007/BF02322488. URL https://doi.org/10.1007/BF02322488.

Gerd Lütjering and James Case Williams. *Titanium*, volume 2. Springer, 2003.

G. Lütjering. Influence of processing on microstructure and mechanical properties of (α+β) titanium alloys. *Materials Science and Engineering:A*, 243(1):32 – 45, 1998. ISSN 0921-5093. doi: https://doi.org/10.1016/S0921-5093(97)00778-8. URL http://www.sciencedirect.com/science/article/pii/S0921509397007788.

T J Ma, W Y Li, B Zhong, Y Zhang, and J L Li. Effect of post-weld heat treatment on microstructure and property of linear friction welded ti17 titanium alloy joint. *Science and Technology of Welding and Joining*, 17(3):180–185, 2012. doi: 10.1179/1362171811Y.0000000079.

Yazid Madi, Juan-Manuel Garcia, Thilo Frank Morgeneyer, Henry Proudhon, Lukas Helfen, and Jacques Besson. On the origin of the anisotropic damage of x100 line pipe steel. *Polymer Testing*, 2019.

Rick Martin and Daniel Evans. Reducing costs in aircraft: The metals affordability initiative consortium. *JOM*, 52(3):24–28, Mar 2000. ISSN 1543-1851. doi: 10.1007/s11837-000-0096-y. URL https://doi.org/10.1007/s11837-000-0096-y.

A. Mateo, M. Corzo, M. Anglada, J. Mendez, P. Villechaise, J.-P. Ferte, and O. Roder. Welding repair by linear friction in titanium alloys. *Materials Science and Technology*, 25(7):905–913, 2009. doi: 10.1179/174328408X363380. URL https://doi.org/10.1179/174328408X363380.

R Maurya and J Kauzlarich. Reciprocating friction bonding apparatus. *Patent nos. US3420428-A, DE1552871-A, CA844858-A*, 1969.

Anthony R. McAndrew, Paul A. Colegrove, Adrian C. Addison, Bertrand C. D. Flipo, and Michael J. Russell. Energy and force analysis of ti-6al-4v linear friction welds for computational modeling input and validation data. *Metallurgical and Materials Transactions A*, 45(13):6118–6128, 2014. ISSN 1543-1940. doi: 10.1007/s11661-014-2575-8. URL https://doi.org/10.1007/s11661-014-2575-8.

Anthony R. McAndrew, Paul A. Colegrove, Adrian C. Addison, Bertrand C.D. Flipo, and Michael J. Russell. Modelling the influence of the process inputs on the removal of surface contaminants from ti–6al–4v linear friction welds. *Materials & Design*, 66:183 – 195, 2015. ISSN 0261-3069. doi: https://doi.org/10.1016/j.matdes.2014.10.058. URL http://www.sciencedirect.com/science/article/pii/S0261306914008462.

Fraser J McMaster and Peter C McKeighan. Spectrum coupon testing of fatigue-resistant fasteners for an aging military aircraft. *Journal of ASTM International*, 1(8):1–15, 2004.

GW Meetham. *The Development of Gas Turbines*. Springer, 1981.

Suresh D. Meshram and T. Mohandas. A comparative evaluation of friction and electron beam welds of near-α titanium alloy. *Materials & Design*, 31(4):2245 – 2252, 2010. ISSN 0261-3069. doi: https://doi.org/10.1016/j.matdes.2009.10.012. URL http://www.sciencedirect.com/science/article/pii/S0261306909005548. Design of Nanomaterials and Nanostructures.

MTS Systems Corporation. Series 609. *Series 609 Alignment Fixture Product Information*, 2008. URL http://www.manualsdir.com/manuals/567919/mts-series-609-alignment-fixture.html?page=17.

Design Improvements of the EJ 200 HP Compressor: From Design Verification Engine to a Future All Blisk Version, volume Volume 1: Aircraft Engine, Marine, Turbomachinery, Microturbines and Small Turbomachinery of *Turbo Expo: Power for Land, Sea, and Air*, 06 2001. MTU Aero Engines. doi: 10.1115/2001-GT-0283. URL https://doi.org/10.1115/2001-GT-0283.

Y. Murakami, T. Nomoto, T. Ueda, and Y. Murakami. On the mechanism of fatigue failure in the superlong life regime (n>107 cycles). part ii: influence of hydrogen trapped by inclusions. *Fatigue & Fracture of Engineering Materials & Structures*, 23(11):903–910, 2000. doi: 10.1046/j.1460-2695.2000.00343.x. URL https://onlinelibrary.wiley.com/doi/abs/10.1046/j.1460-2695.2000.00343.x.

Yukitaka Murakami. *Metal fatigue: effects of small defects and nonmetallic inclusions*. Elsevier, 2002.

Takeshi Naito, Hideo Ueda, and Masao Kikuchi. Fatigue behavior of carburized steel with internal oxides and nonmartensitic microstructure near the surface. *Metallurgical Transactions A*, 15(7):1431–1436, 1984. ISSN 1543-1940. doi: 10.1007/BF02648572. URL https://doi.org/10.1007/BF02648572.

Kazuhiro Nakata, Young Gon Kim, Masao Ushio, Takenori Hashimoto, and Shigetoshi Jyogan. Weldability of high strength aluminum alloys by friction stir welding. *ISIJ International*, 40(Suppl):S15–S19, 2000. doi: 10.2355/isijinternational.40.Suppl_S15.

J.B. Newkirk and A.H. Geisler. Crystallographic aspects of the beta to alpha transformation in titanium. *Acta Metallurgica*, 1(3):370 – 374, 1953. ISSN 0001-6160. doi: https://doi.org/10.1016/0001-6160(53)90113-8. URL http://www.sciencedirect.com/science/article/pii/0001616053901138.

T.E. Norgate, S. Jahanshahi, and W.J. Rankin. Assessing the environmental impact of metal production processes. *Journal of Cleaner Production*, 15(8):838 – 848, 2007. ISSN 0959-6526. doi: https://doi.org/10.1016/j.jclepro.2006.06.018. URL http://www.sciencedirect.com/science/article/pii/S0959652606002320. From Cleaner Production to Sustainable Production and Consumption in Australia and New Zealand: Achievements, Challenges, and Opportunities.

ME Nunn. Aero engine improvements through linear friction welding. In *1st International conference on innovation and integration in aerospace sciences*, pages 4–5. CEIA, Queen's University Belfast Northern Ireland, UK, 2005.

Erik Oberg, Franklin D Jones, Holbrook L Horton, Henry H Ryffel, and James H Geronimo. *Machinery's handbook*, volume 200. Industrial Press New York, 2004.

T. L Oberle, C. D. Loyd, and M. R. Calton. Caterpillar's inertia weld process. In *National Powerplant and Transportation Meetings*. SAE International, feb 1966. doi: https://doi.org/10.4271/660470. URL https://doi.org/10.4271/660470.

A.O. Payne. The fatigue of aircraft structures. *Engineering Fracture Mechanics*, 8(1):157 – 203, 1976. ISSN 0013-7944. doi: https://doi.org/10.1016/0013-7944(76)90085-0. URL http://www.sciencedirect.com/science/article/pii/0013794476900850.

Maxime Pelerin, Andrew King, Lucien Laiarinandrasana, and Henry Proudhon. Development of a versatile mechanical testing device for in situ synchrotron tomography and diffraction experiments. *Integrating Materials and Manufacturing Innovation*, Jun 2019. ISSN 2193-9772. doi: 10.1007/s40192-019-00143-6. URL https://doi.org/10.1007/s40192-019-00143-6.

Michael A. Sutton Perng-Fei Luo, Yuh J. Chao. Application of stereo vision to three-dimensional deformation analyses in fracture experiments. *Optical Engineering*, 33(3):981 – 990 – 10, 1994. doi: 10.1117/12.160877. URL https://doi.org/10.1117/12.160877.

M Peters, G Ziegler, and G Lütjering. Control of microstructures of($\alpha + \beta$)-titanium alloys. *Zeitschrift für Metallkunde*, 74:274–282, 1983.

Jean Petit and C. Sarrazin-Baudoux. Some critical aspects of low rate fatigue crack propagation in metallic materials. *International Journal of Fatigue*, 32(6):962 – 970, 2010. ISSN 0142-1123. doi: https://doi.org/10.1016/j.ijfatigue.2009.10.013. URL http://www.sciencedirect.com/science/article/pii/S0142112309003065. Selected Papers of the 17th European Conference of Fracture (ECF 17).

Tom Petit, Claire Ritter, Jacques Besson, and Thilo F. Morgeneyer. Impact of machine stiffness on "pop-in" crack propagation instabilities. *Engineering Fracture Mechanics*, 202:405 – 422, 2018. ISSN 0013-7944. doi: https://doi.org/10.1016/j.engfracmech.2018.08.007. URL http://www.sciencedirect.com/science/article/pii/S0013794418305496.

H. R. Piehler and W. A. Backofen. A theoretical examination of the plastic properties of bcc crystals deforming by ⟨111⟩ pencil glide. *Metallurgical Transactions*, 2(1):249–255, Dec 1971. ISSN 1543-1916. doi: 10.1007/BF02662665. URL https://doi.org/10.1007/BF02662665.

André Pineau and Stephen D. Antolovich. Probabilistic approaches to fatigue with special emphasis on initiation from inclusions. *International Journal of Fatigue*, 93:422 – 434, 2016. ISSN 0142-1123. doi: https://doi.org/10.1016/j.ijfatigue.2016.09.002. URL http://www.sciencedirect.com/science/article/pii/S0142112316302687. Gigacycle Fatigue-Theory and Applications Dedicated to the Memory of Professor Claude Bathias.

I.J. Polmear. 6 - titanium alloys. In I.J. Polmear, editor, *Light Alloys (Fourth Edition)*, pages 299 – 365. Butterworth-Heinemann, Oxford, fourth edition edition, 2005. ISBN 978-0-7506-6371-7. doi: https://doi.org/10.1016/B978-075066371-7/50010-4. URL http://www.sciencedirect.com/science/article/pii/B9780750663717500104.

PJ Postans and RH Jeal. Titanium for fuel efficient gas turbines. *Metallurgical Society/AIME, Titanium for Energy and Industrial Applications*, pages 183–197, 1981.

Antoine Potet, Katia Mocellin, and Lionel Fourment. Numerical simulation of linear friction welding of aeronautical alloys. *AIP Conference Proceedings*, 1896(1):110007, 2017. doi: 10.1063/1.5008134. URL https://aip.scitation.org/doi/abs/10.1063/1.5008134.

E. Pouillier, A.-F. Gourgues, D. Tanguy, and E.P. Busso. A study of intergranular fracture in an aluminium alloy due to hydrogen embrittlement. *International Journal of Plasticity*, 34:139 – 153, 2012. ISSN 0749-6419. doi: https://doi.org/10.1016/j.ijplas.2012.01.004. URL http://www.sciencedirect.com/science/article/pii/S0749641912000058.

B. Predel. Cu-zn (copper-zinc): Datasheet from landolt-börnstein - group iv physical chemistry · volume 5d: "cr-cs – cu-zr" in springermaterials, 1994. URL https://materials.springer.com/lb/docs/sm_lbs_978-3-540-47417-3_1134.

M. B. Prime. Cross-Sectional Mapping of Residual Stresses by Measuring the Surface Contour After a Cut . *Journal of Engineering Materials and Technology*, 123:162–168, 11 2000. ISSN 0094-4289. doi: 10.1115/1.13455263. URL https://doi.org/10.1115/1.1345526.

H.J. Rack and J.I. Qazi. Titanium alloys for biomedical applications. *Materials Science and Engineering: C*, 26(8):1269 – 1277, 2006. ISSN 0928-4931. doi: https://doi.org/10.1016/j.msec.2005.08.032. URL http://www.sciencedirect.com/science/article/pii/S0928493105002237. Proceedings of the First TMS Symposium on Biological Materials Science.

Sicong Ren, Matthieu Mazière, Samuel Forest, Thilo F. Morgeneyer, and Gilles Rousselier. A constitutive model accounting for strain ageing effects on work-hardening. application to a c–mn steel. *Comptes Rendus Mécanique*, 345(12):908 – 921, 2017. ISSN 1631-0721. doi: https://doi.org/10.1016/j.crme.2017.09.005. URL http://www.sciencedirect.com/science/article/pii/S1631072117301900.

W. Ritcher. Herbeifuehrung einer haftverbindung zwischen plaettchen aus werkzeugstahl und deren traegern nach art einer schweissung oder loetung, 05 1929. URL https://www.lens.org/lens/patent/DE_476480_C.

W.T. Roberts. Preferred orientation and anisotropy in titanium. *Journal of the Less Common Metals*, 4(4): 345 – 361, 1962. ISSN 0022-5088. doi: https://doi.org/10.1016/0022-5088(62)90004-8. URL http://www.sciencedirect.com/science/article/pii/0022508862900048.

J. Romero, M.M. Attallah, M. Preuss, M. Karadge, and S.E. Bray. Effect of the forging pressure on the microstructure and residual stress development in ti–6al–4v linear friction welds. *Acta Materialia*, 57(18): 5582 – 5592, 2009. ISSN 1359-6454. doi: https://doi.org/10.1016/j.actamat.2009.07.055. URL http://www.sciencedirect.com/science/article/pii/S135964540900490X.

F. Rotundo, L. Ceschini, A. Morri, T.-S. Jun, and A.M. Korsunsky. Mechanical and microstructural characterization of 2124al/25vol.joints obtained by linear friction welding (lfw). *Composites Part A: Applied Science and Manufacturing*, 41(9):1028 – 1037, 2010. ISSN 1359-835X. doi: https://doi.org/10.1016/j.compositesa.2010.03.009. URL http://www.sciencedirect.com/science/article/pii/S1359835X10000977. Special Issue on 10th Deformation & Fracture of Composites Conference: Interfacial interactions in composites and other applications.

F. Rotundo, A. Marconi, A. Morri, and A. Ceschini. Dissimilar linear friction welding between a sic particle reinforced aluminum composite and a monolithic aluminum alloy: Microstructural, tensile and fatigue properties. *Materials Science and Engineering:A*, 559:852 – 860, 2013. ISSN 0921-5093. doi: https://doi.org/10.1016/j.msea.2012.09.033. URL http://www.sciencedirect.com/science/article/pii/S0921509312013470.

Christine Sarrazin-Baudoux, Sandrine Lesterlin, and Jean Petit. Atmospheric influence on fatigue crack propagation in titanium alloys at elevated temperature. In *Elevated temperature effects on fatigue and fracture*. ASTM International, 1997.

C Sauer and G Lütjering. Influence of α layers at β grain boundaries on mechanical properties of ti-alloys. *Materials Science and Engineering:A*, 319-321:393 – 397, 2001. ISSN 0921-5093. doi: https://doi.org/10.1016/S0921-5093(01)01018-8. URL http://www.sciencedirect.com/science/article/pii/S0921509301010188.

Hubert Schreier, Jean-José Orteu, and Michael A Sutton. *Image correlation for shape, motion and deformation measurements*. Springer US, 2009.

F. Schroeder, R. Mark Ward, R. P. Turner, A. R. Walpole, M. M. Attallah, J.-C. Gebelin, and R. C. Reed. Validation of a model of linear friction welding of ti6al4v by considering welds of different sizes. *Metallurgical and Materials Transactions B*, 46(5):2326–2331, Oct 2015. ISSN 1543-1916. doi: 10.1007/s11663-015-0396-9. URL https://doi.org/10.1007/s11663-015-0396-9.

S. L. Semiatin, V. Seetharaman, and I. Weiss. The thermomechanical processing of alpha/beta titanium alloys. *JOM*, 49(6):33–39, Jun 1997. ISSN 1543-1851. doi: 10.1007/BF02914711. URL https://doi.org/10.1007/BF02914711.

Yang Shen, Thilo F. Morgeneyer, Jérôme Garnier, Lucien Allais, Lukas Helfen, and Jérôme Crépin. Three-dimensional quantitative in situ study of crack initiation and propagation in aa6061 aluminum alloy sheets via synchrotron laminography and finite-element simulations. *Acta Materialia*, 61(7):2571 – 2582, 2013. ISSN 1359-6454. doi: https://doi.org/10.1016/j.actamat.2013.01.035. URL http://www.sciencedirect.com/science/article/pii/S1359645413000621.

J. Sieniawski, W. Ziaja, K. Kubiak, and M. Motyka. Microstructure and mechanical properties of high strength two-phase titanium alloys. In Jan Sieniawski and Waldemar Ziaja, editors, *Titanium Alloys*, chapter 4. IntechOpen, Rijeka, 2013. doi: 10.5772/56197. URL https://doi.org/10.5772/56197.

KT Slattery. Structural assembly's eg wing, preform for eg aircraft, has set of structural members connected by linear friction weld joint to base member, where each structural member defines connection surfaces. *Patent: Boeing Co, US2007186507-A1*, 2007.

Saeed Solaymani. Co2 emissions patterns in 7 top carbon emitter economies: The case of transport sector. *Energy*, 168:989 – 1001, 2019. ISSN 0360-5442. doi: https://doi.org/10.1016/j.energy.2018.11.145. URL http://www.sciencedirect.com/science/article/pii/S0360544218323569.

Abkowitz Stanley. Heat treated titanium-aluminumvanadium alloy, September 29 1959. US Patent 2,906,654.

J.C. Stinville, F. Bridier, D. Ponsen, P. Wanjara, and P. Bocher. High and low cycle fatigue behavior of linear friction welded ti–6al–4v. *International Journal of Fatigue*, 70:278 – 288, 2015. ISSN 0142-1123. doi: https://doi.org/10.1016/j.ijfatigue.2014.10.002. URL http://www.sciencedirect.com/science/article/pii/S0142112314002539.

Vijay K Stokes. Joining methods for plastics and plastic composites: an overview. *Polymer Engineering & Science*, 29(19):1310–1324, 1989.

Subra Suresh. *Fatigue of materials*. Cambridge university press, 1998.

MA Sutton, WJ Wolters, WH Peters, WF Ranson, and SR McNeill. Determination of displacements using an improved digital correlation method. *Image and vision computing*, 1(3):133–139, 1983.

S. Tamirisakandala, Steve C. Medeiros, William G. Frazier, and Y. V. R. K. Prasad. Strain-induced porosity during cogging of extra-low interstitial grade ti-6al-4v. *Journal of Materials Engineering and Performance*, 10(2):125–130, Apr 2001. ISSN 1544-1024. doi: 10.1361/105994901770345114. URL https://doi.org/10.1361/105994901770345114.

B.H. Tao, Q. Li, Y.H. Zhang, T.C. Zhang, and Y. Liu. Effects of post-weld heat treatment on fracture toughness of linear friction welded joint for dissimilar titanium alloys. *Materials Science and Engineering:A*, 634:141 – 146, 2015. ISSN 0921-5093. doi: https://doi.org/10.1016/j.msea.2015.03.003. URL http://www.sciencedirect.com/science/article/pii/S0921509315002087.

Geoffrey Ingram Taylor. Section a. -mathematical and physical sciences. - the deformation of crystals of β-brass. *Proceedings of the Royal Society of London. Series A, Containing Papers of a Mathematical and Physical Character*, 118(779):1–24, 1928. doi: 10.1098/rspa.1928.0032. URL https://royalsocietypublishing.org/doi/abs/10.1098/rspa.1928.0032.

The American Society for Testing and Materials (ASTM). E837-99: Standard test method for determining residual stresses by the hole-drilling strain-gage method, 1992.

The American Welding Society. Standard welding terms and definitions: Including terms for bazing, soldering thermal spraying and thermal cutting, 1985.

Wayne M Thomas, Edward D Nicholas, James C Needham, Michael G Murch, Peter Temple-Smith, and Christopher J Dawes. Friction welding, October 24 1995. US Patent 5,460,317.

Stephen Prokofevich Timoshenko. *Strength of materials*, volume 210. van Nostrand New York, 1956.

RD Trask, SH Goetschius, and SA Hilton. Process for linear friction welding–comprises providing two members to be joined to one another at an interface by linear friction welding, where one of the two members is stub, etc. *Patent nos. EP850718-A, EP850718-A1, JP10193141-A, US5865364-A, EP850718-B1, DE69734232-E, DE69734232-T2*, 1998.

R. Turner, J.-C. Gebelin, R.M. Ward, and R.C. Reed. Linear friction welding of ti–6al–4v: Modelling and validation. *Acta Materialia*, 59(10):3792 – 3803, 2011. ISSN 1359-6454. doi: https://doi.org/10.1016/j.actamat.2011.02.028. URL http://www.sciencedirect.com/science/article/pii/S1359645411001224.

A. Vairis and M. Frost. High frequency linear friction welding of a titanium alloy. *Wear*, 217(1):117 – 131, 1998. ISSN 0043-1648. doi: https://doi.org/10.1016/S0043-1648(98)00145-8. URL http://www.sciencedirect.com/science/article/pii/S0043164898001458.

A Vairis and M Frost. On the extrusion stage of linear friction welding of ti 6al 4v. *Materials Science and Engineering:A*, 271(1):477 – 484, 1999. ISSN 0921-5093. doi: https://doi.org/10.1016/S0921-5093(99)00449-9. URL http://www.sciencedirect.com/science/article/pii/S0921509399004499.

A. Vairis and M. Frost. Modelling the linear friction welding of titanium blocks. *Materials Science and Engineering:A*, 292(1):8 – 17, 2000. ISSN 0921-5093. doi: https://doi.org/10.1016/S0921-5093(00)01036-4. URL http://www.sciencedirect.com/science/article/pii/S0921509300010364.

Achilles Vairis. *High frequency linear friction welding.* PhD thesis, University of Bristol, 1997.

Vadim Ivanovich Vill. *Friction welding of metals*, volume 1. American Welding Society; trade distributor: Reinhold Pub. Co., 1962.

W. F. Ranson W. H. Peters. Digital imaging techniques in experimental stress analysis. *Optical Engineering*, 21(3):427 – 431 – 5, 1982. doi: 10.1117/12.7972925. URL https://doi.org/10.1117/12.7972925.

Q. G. Wang, P. N. Crepeau, C. J. Davidson, and J. R. Griffiths. Oxide films, pores and the fatigue lives of cast aluminum alloys. *Metallurgical and Materials Transactions B*, 37(6):887–895, Dec 2006. ISSN 1543-1916. doi: 10.1007/BF02735010. URL https://doi.org/10.1007/BF02735010.

Xinyu Wang, Wenya Li, Tiejun Ma, Xiawei Yang, and Achilles Vairis. Microstructural evolution and mechanical properties of a linear friction welded two-phase ti-6.5al-3.5mo-1.5zr-0.3si titanium alloy joint. *Materials Science and Engineering:A*, 743:12 – 23, 2019. ISSN 0921-5093. doi: https://doi.org/10.1016/j.msea.2018.11.059. URL http://www.sciencedirect.com/science/article/pii/S0921509318315855.

P. Wanjara and M. Jahazi. Linear friction welding of ti-6al-4v: Processing, microstructure, and mechanical-property inter-relationships. *Metallurgical and Materials Transactions A*, 36(8):2149–2164, 2005. ISSN 1543-1940. doi: 10.1007/s11661-005-0335-5. URL https://doi.org/10.1007/s11661-005-0335-5.

Priti Wanjara, Elvi Dalgaard, Javad Gholipour, Xinjin Cao, Jonathan Cuddy, and John J. Jonas. Effect of pre- and post-weld heat treatments on linear friction welded ti-5553. *Metallurgical and Materials Transactions A*, 45(11):5138–5157, Oct 2014. ISSN 1543-1940. doi: 10.1007/s11661-014-2475-y. URL https://doi.org/10.1007/s11661-014-2475-y.

G.A. Webster and A.N. Ezeilo. Residual stress distributions and their influence on fatigue lifetimes. *International Journal of Fatigue*, 23:375 – 383, 2001. ISSN 0142-1123. doi: https://doi.org/10.1016/S0142-1123(01)00133-5. URL http://www.sciencedirect.com/science/article/pii/S0142112301001335.

Gerhard Welsch, Rodney Boyer, and EW Collings. *Materials properties handbook: titanium alloys*. ASM international, 1993.

G.D. Wen, T.J. Ma, W.Y. Li, J.L. Li, H.Z. Guo, and D.L. Chen. Cyclic deformation behavior of linear friction welded ti6al4v joints. *Materials Science and Engineering:A*, 597:408 – 414, 2014. ISSN 0921-5093. doi: https://doi.org/10.1016/j.msea.2014.01.006. URL http://www.sciencedirect.com/science/article/pii/S0921509314000239.

J. C. Williams and M. J. Blackburn. The identification of a non-basal slip vector in titanium and titanium-aluminum alloys. *physica status solidi (b)*, 25(1):K1–K3, 1968. doi: 10.1002/pssb.19680250146. URL https://onlinelibrary.wiley.com/doi/abs/10.1002/pssb.19680250146.

JC Williams. Critical review–kinetics and phase transformations. *Titanium Science and Technology,*, 3, 1973.

P.J. Withers and H.K.D.H. Bhadeshia. Residual stress. part 1 – measurement techniques. *Materials Science and Technology*, 17(4):355–365, 2001. doi: 10.1179/026708301101509980. URL https://doi.org/10.1179/026708301101509980.

M. Wojtaszek, T. Sleboda, A. Czulak, G. Weber, and W.A. Hufenbach. Quasi-static and dynamic tensile properties of ti-6al-4v alloy. *Archives of Metallurgy and Materials*, 58(4):1261 – 1265, 2013. URL https://content.sciendo.com/view/journals/amm/58/4/article-p1261.xml.

P. Xie, H. Zhao, and Y. Liu. Measuring residual stresses in linear friction welded joints composed by dissimilar titanium. *Science and Technology of Welding and Joining*, 21(5):351–357, 2016. doi: 10.1080/13621718.2015.1115158. URL https://doi.org/10.1080/13621718.2015.1115158.

U. Zerbst, R.A. Ainsworth, H.Th. Beier, H. Pisarski, Z.L. Zhang, K. Nikbin, T. Nitschke-Pagel, S. Münstermann, P. Kucharczyk, and D. Klingbeil. Review on fracture and crack propagation in weldments – a fracture mechanics perspective. *Engineering Fracture Mechanics*, 132:200 – 276, 2014. ISSN 0013-7944. doi: https://doi.org/10.1016/j.engfracmech.2014.05.012. URL http://www.sciencedirect.com/science/article/pii/S0013794414001763.

Haoyu Zhang, Chuan Wang, Siqian Zhang, Ge Zhou, and Lijia Chen. Evolution of secondary α phase during aging treatment in novel near β ti-6mo-5v-3al-2fe alloy. *Materials*, 11(11), 2018. ISSN 1996-1944. doi: 10.3390/ma11112283. URL http://www.mdpi.com/1996-1944/11/11/2283.

Pengkang Zhao and Li Fu. Strain hardening behavior of linear friction welded joints between tc11 and tc17 dissimilar titanium alloys. *Materials Science and Engineering:A*, 621:149 – 156, 2015. ISSN 0921-5093. doi: https://doi.org/10.1016/j.msea.2014.10.044. URL http://www.sciencedirect.com/science/article/pii/S0921509314012878.

Caizhi Zhou, Xinqi Yang, and Guohong Luan. Effect of root flaws on the fatigue property of friction stir welds in 2024-t3 aluminum alloys. *Materials Science and Engineering:A*, 418(1):155 – 160, 2006. ISSN 0921-5093. doi: https://doi.org/10.1016/j.msea.2005.11.042. URL http://www.sciencedirect.com/science/article/pii/S0921509305014644.

N. Özdemir. Investigation of the mechanical properties of friction-welded joints between aisi 304l and aisi 4340 steel as a function rotational speed. *Materials Letters*, 59(19):2504 – 2509, 2005. ISSN 0167-577X. doi: https://doi.org/10.1016/j.matlet.2005.03.034. URL http://www.sciencedirect.com/science/article/pii/S0167577X0500323X.

RÉSUMÉ

Les propriétés mécaniques en termes de comportement monotone, résistance en fatigue et ténacité d'alliages de titane soudés par friction linéaire ont été étudiées et comparées à celles des matériaux de base. Le soudage par friction linéaire est un procédé de soudage à l'état solide qui pourrait être utilisé dans l'industrie aéronautique pour assembler des structures fortement chargées. Étant donné que le noyau de soudure du joint mono-matériau Ti6242 a montré une résistance mécanique supérieure à celle du matériau de base, ses propriétés mécaniques ont été étudiées en utilisant des éprouvettes entaillées. Elles ont montré une certaine ductilité et une rupture mixte entre des mécanismes ductiles et fragiles. Les champs de déformation locale et de vitesse de déformation normalisée ont été étudiées sur des éprouvettes lisses. Une activité plastique précoce a été observée dans le voisinage du noyau de la soudure et elle a été attribuée aux contraintes résiduelles. Pour la durée de vie visée de 10^5 cycles, la résistance en fatigue a légèrement été réduite mais compromise avec une forte dispersion de la durée de vie reliée à la contamination avant soudage. Le mécanisme auto-nettoyant n'a pas réussi à extruder les contaminants à l'interface d'un joint bi-matériaux Ti17-TA6V et a mené à une rupture fragile au niveau d'une couche de défauts. Pour un joint bi-matériaux Ti17-TA6V nettoyé avant soudage, une rupture ductile a été observée tantôt au niveau du matériau de base TA6V tantôt au niveau de la zone thermo-mécaniquement affectée (TMAZ) côté Ti17, due à un épuisement de la phase durcissante alpha. L'amorce des fissures de fatigue a eu lieu au niveau de la TMAZ Ti17 avec une résistance en fatigue réduite. La ténacité a également été dégradée et le faciès de rupture au niveau de la TMAZ a dévoilé des amas de cavités allongées et parallèles. Les mêmes tendances ont été observées pour un joint mono-matériau Ti17. Un traitement thermique *post*-soudage de celui-ci a permis de retrouver avec succès des propriétés proches de celles du MB.

MOTS CLÉS

Soudage par friction linéaire, essai de traction, fatigue, stéréo-corrélation d'images

ABSTRACT

The mechanical properties in terms of tensile behaviour, fatigue strength and toughness of Linear Friction Welded (LFW) Titanium (Ti) alloys were studied and compared to the parent materials' (PM) behaviour. LFW is a solid state joining process that could be used for assembling heavily loaded structures in the aerospace industry. Since the Weld Centre Zone (WCZ) of a similar Ti6242 LFW joint exhibited overmatching strength, its fracture mechanisms and ductility were investigated by micro-tensile tests using notched specimens. They revealed some ductility and a mixture of brittle and ductile fracture mechanisms. Local strain and normalized strain rate fields on smooth samples were assessed by Stereo Digital Image Correlation (SDIC) and showed an early plastic activity at yielding in the vicinity of the WCZ, attributed to residual stresses. For the target life of 10^5 cycles, the fatigue strength was slightly reduced but compromised by a strong scatter that was related to prior to welding contamination. The LFW self-cleaning mechanism also failed to extrude the contaminants at the weld interface of a dissimilar Ti17-Ti64 LFW joint that led to pseudo-brittle fracture at a defect layer in the WCZ. For a pre-cleaned dissimilar Ti17-Ti64 LFW joint, ductile rupture was observed sometimes at the Ti64 PM and sometimes at the Ti17 thermo-mechanically affected zone (TMAZ), due to a depletion of the strengthening α phase. Fatigue cracks initiated at the weak Ti17 TMAZ with a reduced fatigue strength compared to the PM. Fracture toughness was significantly reduced and the fracture surface at the TMAZ highlighted unexpected clusters of parallel and elongated voids. These trends were also observed for a similar Ti17 LFW joint. Comparable mechanical properties to those of the Ti17 PM were successfully regained by means of a post-weld heat treatment.

KEYWORDS

Linear Friction Welding, Tensile test, Fatigue, Digital Image Correlation